DEPARTMENT OF CONTINUUM MECHANICS AND THEORY OF STRUCTURES
SCHOOL OF CIVIL ENGINEERING
TECHNICAL UNIVERSITY OF MADRID

USE OF HEADED REINFORCEMENT BARS IN CONSTRUCTION

A THEORETICAL APPROACH TO DETERMINE THE DIMENSIONS OF ANCHORAGE PLATES AND EXPERIMENTAL TESTS ON KNEE JOINTS SUBJECTED TO A CLOSING MOMENT

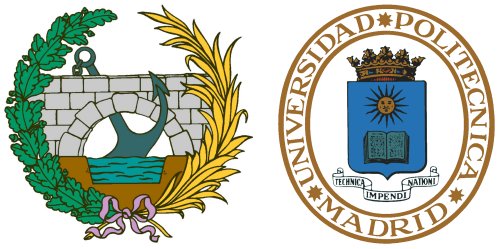

PHD DISSERTATION

FRANCESCO MARCHETTO
MEng MSc in Civil Engineering

2015

Francesco Marchetto: *Use of Headed Reinforcement Bars in Construction*
PhD Dissertation, © April 2015

SUPERVISOR:
Alejandro Pérez Caldentey
Dr. Ingeniero de Caminos, Canales y Puertos

LOCATION:
Madrid, Spain

This dissertation is dedicated to my wife Romina, who patiently supported me during the years needed to complete my work.

I am enormously grateful to Alejandro Pérez Caldentey, for his kindness and his patient guidance, as well as for the many illuminating suggestions he gave me throughout my time here as a PhD student.

I would also like to thank Hugo Corres Peiretti and Javier León González for their encouragement and valuable contributions to my academic and professional formation within the Structural Concrete Research Group.

Many thanks also to my colleagues Alejandro Giraldo Soto, Giancarlo Groli, Freddy Ariñez, Leonardo Todisco, Rodrigo Martínez Arribas, Miguel Ángel Peña Cobos and Isidro Garcia Martín for their precious help with designing and performing the laboratory tests.

The roots of education are bitter, but the fruit is sweet.

— Aristotele

Although to penetrate into the intimate mysteries of nature and thence to learn the true causes of phenomena is not allowed to us, nevertheless it can happen that a certain fictive hypothesis may suffice for explaining many phenomena.

— Leonhard Euler, 1707 – 1783

ABSTRACT

In order to reduce costs and time while improving quality, durability and sustainability in structural concrete constructions, a widely used material nowadays, special care must be taken in some crucial phases of the project and execution, including the structure design and calculation, the dosage, dumping and curing of concrete: another important aspect is the proper design and execution of assembly plans and construction details.

The framework, a name designating the whole reinforcement bars cage already assembled as shown in the drawings, can be made up of several components and implies higher or lower industrialization degree. The framework costs constitute about one third of the price per cubic meter placed in concrete works. The best solutions from all points of view are clearly those involving an easier processing to achieve the same goal, and consequently carrying a high degree of industrialization, meaning quality and safety in the work.

This thesis aims to provide an indepth analysis of a relatively new type of anchoring by plate known as *headed reinforcement bars*, which can potentially replace standard or L-shaped hooks, improving the cleaning of construction details and enabling a faster, more flexible, and therefore a more economical assembly. A literature review on the topic and an overview of typical applications is provided, followed by some examples of specific applications in real projects.

Since a strict theoretical formulation used to provide the design plate dimensions has not yet been put forward, an equation is proposed for the side-face blowout strength of the anchorage, based on the capacity of concrete to carry concentrated loads in cases in which no transverse reinforcement is provided. The correlation of the calculated ultimate load with experimental results available in the literature is given. Besides, the proposed formulation can be expanded to cases in which a certain development length is available: using a software for nonlinear finite element analysis oriented to the study of reinforced concrete, numerical tests on the bond-bearing interaction are performed.

The thesis ends with a testing of eight corner joints subjected to a closing moment, held in the Structures Laboratory of the Polytechnic University of Madrid, aiming to check whether the design of such plates as stated is adequate for these elements and whether an element with plate-anchored reinforcement is equivalent to one with a traditional construction detail.

RESUMEN

Con el objetivo de reducir costes, acortar plazos y a la vez mejorar la calidad, durabilidad y sostenibilidad de realizaciones en hormigón estructural, material de construcción por excelencia de nuestro tiempo, es preciso tener especial cuidado en fases cruciales del proyecto y de la ejecución, entre ellas la concepción de la estructura y su cálculo, la dosificación, el vertido y el curado del hormigón: otro aspecto no menos importante por su trascendencia es el correcto diseño y ejecución de los planes de armado y de los detalles constructivos.

La ferralla, nombre con que el que se designa el conjunto de armaduras montado y dispuesto según los planos, puede ser constituida por varios elementos y comportar un menor o mayor grado de industrialización, y constituye alrededor de un tercio del precio del metro cúbico de hormigón armado colocado en obra. Queda claro que las soluciones mejores bajo todos los puntos de vista serán aquellas que para conseguir el mismo objetivo comporten un menor número de manipulaciones y conlleven un elevado grado de industrialización, sinónimo de calidad y seguridad en la obra.

En esta tesis se analiza en detalle los anclajes mediante placa, que potencialmente pueden sustituir los comunes anclajes por gancho o patilla mejorando la limpieza de los detalles constructivos y permitiendo un montaje más rápido, más flexible y por ende más económico. Se presenta el estado del arte y una reseña de aplicaciones típicas en la que podría plantearse una solución de este tipo, seguida de algunos ejemplos de aplicaciones específicas surgidas en proyectos reales.

Dada la ausencia de una formulación teórica rigurosa que proporcione las dimensiones de la placa de diseño, se propone una ecuación para el cálculo de la capacidad del anclaje frente a estallido lateral, basada en la resistencia del hormigón frente a cargas concentradas en casos en los que no se haya dispuesto armadura de difusión, y se analiza su correlación con los resultados experimentales disponibles en literatura. Asimismo, el método propuesto puede extenderse a los casos en que se disponga de una cierta longitud de anclaje: para ello, se realizan ensayos numéricos con un programa para análisis no lineales de elementos finitos dedicado al estudio del hormigón armado.

Se concluye con la descripción de ocho ensayos sobre nudos de esquina armados para momentos negativos, realizados en el Laboratorio de Estructuras de la Escuela de Caminos de la Universidad Politécnica de Madrid, que tienen como objetivo comprobar si el diseño de placas tal como se ha establecido es adecuado y si un elemento armado con barras ancladas es equivalente a otro con un detalle de armado tradicional.

PUBLICATIONS

Some ideas and figures have appeared previously in the following publications:

2013 **Plate-anchored Reinforcement Bars:**
A New Simple and Physical Model for Practical Applications
Alejandro Pérez Caldentey, Francesco Marchetto, Hugo Corres Peiretti, Jesús Iglesias Villareal, *In Engineering Structures*.
Volume 52, pp. 168 - 178.

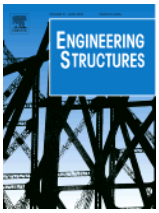

ACKNOWLEDGMENTS

These studies have been carried out within the framework of the research project titled *Investigación y desarrollo de un nuevo método de anclaje de barras de acero corrugadas en hormigón y estudio de sus aplicaciones en la construcción* lead by GRUPO ARMATEK and partially funded by a grant from Centro de Desarrollo Tecnológico Industrial (CDTI) an organism of the Spanish Government, under Project Number IDI-20110631.

The assistance of Fernando García Martín from *Grupo Cementos Portland Valderrivas* by supplying the concrete used for experimental tests is greatly appreciated.

AGRADECIMIENTOS

Este trabajo ha sido llevado a cabo en el marco del proyecto de investigación titulado *Investigación y desarrollo de un nuevo método de anclaje de barras de acero corrugadas en hormigón y estudio de sus aplicaciones en la construcción* liderado por el GRUPO ARMATEK y parcialmente financiado por el Centro de Desarrollo Tecnológico Industrial (CDTI), número de proyecto IDI-20110631.

Se agradece la inestimable ayuda de Fernando García Martín de *Grupo Cementos Portland Valderrivas* por proveer el hormigón necesario para llevar a cabo la campaña experimental.

CONTENTS

LIST OF FIGURES

LIST OF TABLES

ACRONYMS

ACI American Concrete Institute

AOGA Alaska Oil and Gas Association

Caltrans CALifornia department of TRANSportation

CAESAR Center for Advanced Engineering Structural Assessment and Research

CCD Concrete Capacity Design

CEN Comité Européen de Normalisation

Condeep CONcrete DEEP water structure

ECCP European Climate Change Programme

ERICO Electric Railway Improvement COmpany

fib Fédération Internationale du Béton

GBS Gravity Based Structure

GCPV Grupo Cementos Portland Valderrivas

HRC Headed Reinforcement Corporation

LNG Liquified Natural Gas

LVDT Linear Variable Displacement Transducer

MPU Multi Purpose Unit

PEER Pacific Earthquake Engineering Research Group

TLP Tension Leg Platform

TXDOT TeXas Department Of Transportation

NOTATIONS

Roman lower case letters

a	Smallest concrete block side
a_1	Smallest plate side
b	Largest concrete block side
b_1	Largest plate side
b_{ef}	Effective width
c	Clear cover
c'	Clear cover to the bolt
c_1	Smallest side cover: distance to the closest free edge to the centre of the bar
c_2	Largest side cover
c_{sp2}	Clear spacing between headed bars
d_b	Bar diameter
d_s	Stud or bolt outer diameter
e_1	Plate thickness
e_a	Eccentricity in a-direction
e_b	Eccentricity in b-direction
f_{bc}	Equibiaxial compressive strength of concrete
f_{bd}	Design bond strength
$f_{bd,o}$	Basic bond strength (MC)
f'_c	Specified compressive strength of concrete (ACI)
f_c	Cylinder compressive strength of concrete
f_{cb}	Bearing strength of concrete
$f_{cc,200}$	Concrete compressive strength for a 200 mm cube
f_{cd}	Design compressive strength of concrete
f_{ck}	Characteristic compressive strength of concrete
f_{cm}	Mean compressive strength of concrete
f_{ct}	Split cilinder tensile strength of concrete
f_{ctd}	Desing value of the axial tensile strength of concrete
f_{ctm}	Mean value of the axial tensile strength of concrete
f_{cu}	Cube compressive strength of concrete
f_y	Specified yield strength of reinforcement (ACI)
f_{yd}	Design strength of reinforcement (EC2, MC)

h	Concrete block height
h_d	Embedment depth
l_b	Bond length (MC)
l_{bd}	Design anchorage length (EC2)
l_{dh}	Development length for deformed bars in tension terminating in a standard hook (ACI)
l_{dt}	Development length for headed reinforcement bars in tension (ACI)

Roman capital letters

A_1	Plate area
A_b	Reinforcement bar area
A_{brg}	Net bearing area of the head (ACI)
A_c	Concrete area
A_e	Effective concrete area
A_n	Net bearing area of the head
$N_{Rd,1}$	Load which produces compression failure
$N_{Rd,2}$	Load which produces side-blowout failure
$N_{Rk,cb}$	Characteristic resistance due to local blowout failure (CEB)
N_{Sd}	Force to be anchored over the design anchorage length
N^*_{Sd}	Part of force that does not need to be deflected
N_u	Ultimate load
$P_{U0,s}$	Basic concrete breakout capacity for shallow embedment tests (DeVries)
$P_{U0,d}$	Basic concrete blowout capacity for deep embedment tests (DeVries)
P_U	Ultimate blowout capacity of a bar or a group of bars for deep embedment tests (DeVries)
T_{Rd}	Tensile force resisted by concrete
T_{Sd}	Tensile force generated by the spreading out of the compression stresses

Greek letters

α_{mod}	Diffusion angle
β	Lateral diffusion angle
γ_c	Material safety factor for concrete
γ_{cb}	Partial safety coefficient for bond (MC)
γ_s	Material safety factor for steel
σ_d	Uniform compression achieved in a concrete block
ρ_{sl}	Main or longitudinal reinforcement ratio
ρ_{st}	Transverse reinforcement ratio
ω_s	Mechanical reinforcement ratio
ω_i	Beam reinforcement index

Statistics

$\bar{x}$	Sample mean
σ^2, σ	Variance, Standard deviation
s^2, s	Sample variance, Sample standard deviation
CoV	Coefficient of Variation
R^2	Sample correlation coefficient

INTRODUCTION

«Scientists study the world as it is, engineers create the world that has never been»

—Theodore Von Karman *(1890-1947)*

In reinforced concrete structures, the traditional detailing problems related to the anchorage of reinforcement bars are often of great importance due to the long development lengths and large bend radii required for straight or hooked bars. Alternatives to conventional detailing — not so common in ordinary structures but with a long history in heavily reinforced structures — have been developed since the middle of the XXth century. Known as mechanical anchorages, they are particularly useful in presence of large bar diameters, because they can achieve the anchorage by a combination of development length and a plate anchor that can be fixed to the rebar contributing to the total anchorage capacity. Therefore, the use of plate-anchored reinforcement bars reduces the development length needed and simplifies the detailing of congested areas, also reducing significantly the placing times.

In this thesis, a new sound formulation based on simple physical considerations allowing the calculation of the concrete capacity to carry concentrated loads is proposed. A comparison with available experimental results shows the adequacy of the proposed model with respect to this problem and some numeric tests confirm the expected behavior of a mechanical anchorage in pullout tests. Finally, a specifically designed laboratory campaign is described, whose objective is to verify the results obtained by application of the theoretical model. The preparation and execution of the tests are described with the experimental results reported and their intrepretation undertaken.

The work is organized into seven chapters and four appendix:

CHAPTER ONE presents a review of the state of the art on mechanical anchorages and related concepts such as bearing strength and joint detailing, with particular regard to the laboratory tests related to their behavior and to the existing code provisions. An introduction about the mechanics of bond is also provided;

CHAPTER TWO goes into specific headed reinforcement bar applications with emphasis on their first application fields and other more common, general applications in which an increase of the use of headed bars is expected due to the many advantages they

provide, for instance the simpler and more flexible cage assembly or reduced congestion of the details. Mechanically anchored reinforcement is also increasingly used because it allows the shortening of the connection between prefabricated elements;

CHAPTER THREE describes the proposed design methodology. The capacity of concrete to carry concentrated loads without transverse reinforcement is assessed by a simple strut-and-tie model and compared against some available experimental evidence and existing models. The safety level is also evaluated with a view for the model inclusion in code provisions;

CHAPTER FOUR provides more comparisons with available bearing and headed bolt tests and some capacity graphs for side or corner positioning. Also, a realistic simulation performed with the commercial software ATENA reproduces the blowout failure mechanics and provides an estimation of the relative importance of the two collaborating mechanisms of stress transfer;

CHAPTER FIVE describes the objectives of the experimental campaign, the materials used and the fabrication of the specimens. It also provides some drawings about the setup of the laboratory tests;

CHAPTER SIX provides an interpretation of the experimental campaign results and concludes the dissertation;

CHAPTER SEVEN presents the conclusions of the thesis and a proposal for future works;

APPENDIX A reports on statistical concepts and formulas used throughout the work;

APPENDIX B reports additional data table regarding laboratory tests on bearing strength of concrete loaded over limited areas;

APPENDIX C describes general concepts of continuum mechanics and failure criteria usually adopted for brittle and ductile materials, with a view for the concrete material available in ATENA;

APPENDIX D reports extensively the test results.

Part I

STATE OF THE ART

1 BACKGROUND

«The Hand of God is in the details»

— John E. Breen
2012 ACI Convention

In reinforced concrete structures, mechanical anchorages have been used to simplify design and construction of complex details. They are increasingly used to replace conventional reinforcement bars, but despite their advantages, they are still far from being widely used in traditional concrete structures. However, research over the last fifty years has led not only to understand their behavior, but also to confirm their great effectiveness when compared to traditional solutions.

The core of this chapter is dedicated to the description of the previous research on mechanical anchorages. A review of the literature on the matter is presented here, with extensions to related phenomena that can help understand the problem in its whole complexity, with particular regard to laboratory tests. For a better comprehension of the core topic, the problem will be approached starting with a brief introduction on the mechanics of bond and other related topics.

1.1 BACKGROUND ON BOND

Reinforced concrete is a material manufactured by combination of other materials. The obtention of a new material whose properties are better than those of the individual components themselves is its reason of being. It takes advantage of the concrete compressive strength and the ability of steel to resist tensile stresses, integrating both materials into a composite one and thereby achieving economy.

The connection between the materials inside the structural elements is made automatically through bond, i. e., no devices are needed to link the parts together, as it may be the case in steel or wood structures, but the stresses generated in the steel due to external forces are transmitted to the concrete by a combination of resistant mechanisms that oppose relative movement between the two materials. Wherever steel and concrete strains differ, a relative displacement (slip) does occur, as a consequence of the localized strains in the concrete layer closest to the reinforcement.

Bond is a critical feature of any reinforced concrete structure. Thus it is not surprising that, because of its relevance, it was extensively in-

vestigated in the past decades and it is now well understood. Notwithstanding, it is still an attractive field for many researchers (see Gambarova [46]), who are filling the gaps regarding bond at high or low temperatures, bond in high-strength or lightweight concrete, in aggressive environments or regarding fiber-reinforced concrete.

The steel-to-concrete bond is based on some well-known mechanisms, as reported by the *fib*[1] *bulletin 10: Bond of reinforcement in concrete* [1]:

- Chemical adhesion, the product of the interaction between steel and hydration products of the cement paste is the first mechanism that develops. The resistance resulting from this mechanism is small; it is lost rapidly when slipping between the reinforcement and the concrete starts. When an additional displacement is produced, the next mechanism is activated.

- Mechanical adhesion, dependent on the surface shape of the bar, is activated when chemical adhesion breaks down. In this phase, the lugs induce bearing stresses on concrete and simultaneously transverse microcracks originate. The inclined forces resulting from the action of the ribs spread radially outwards in the concrete, as shown in Figure 1.1. The total stress is usually separated into two orthogonal components: a longitudinal component, called bond stress, and a radial component, called normal or splitting stress.

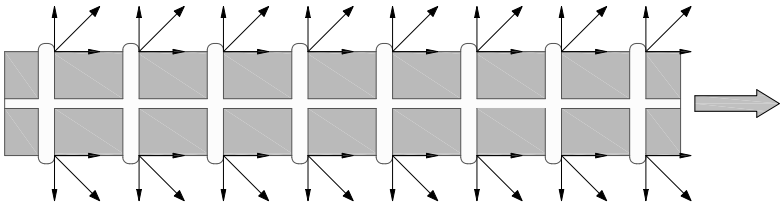

Figure 1.1: Bond and splitting in reinforced concrete

- Once higher bond stress values have been reached, the wedging action is increased by the concrete situated in front of the lugs, as shown in Figure 1.2b. The crushed paste changes the bond angle as the bar acquires load, thus resulting in creation or increase of the splitting cracks (Figure 1.2a). When the cracks reach the outer surface of the concrete member two phenomena can be observed:

  - In the case of light-to-medium transverse reinforcement, longitudinal cracks break out and a more or less sudden splitting failure occurs whenever the development length provided is insufficient. With increasing slip values, the

[1] Fédération Internationale du Béton

bond stresses reach a peak and start decreasing. Even at very high slip values a residual bond can be measured;

– In the case of heavy transverse reinforcement or large concrete cover, splitting is prevented and limited to a core around the bar. Hence, splitting failure cannot occur and bond failure is governed by pull-out.

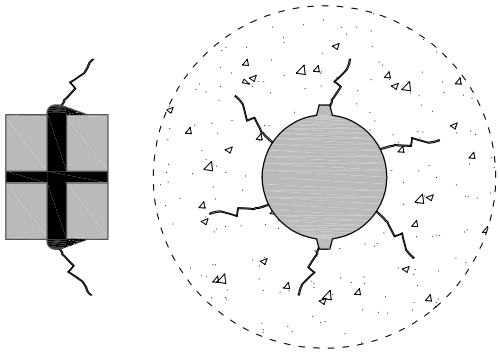

(a) *Radial splitting cracks*

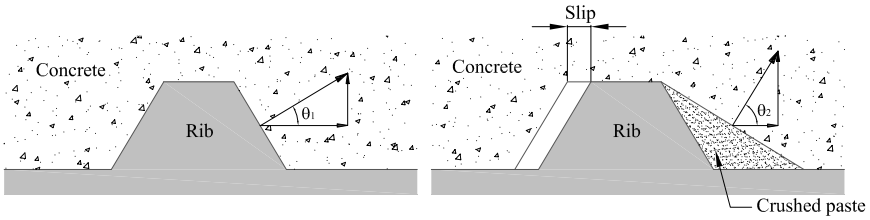

(b) *Bar-concrete slip and wedging action of the bar*

Figure 1.2: Bar-concrete interaction

These two modes of failure, shown in Figure 1.3, have been traditionally recognized: the former is ascribable to the longitudinal splitting of the concrete while the latter is mostly due to shearing failure of concrete between lugs. This deteriorates the bond capacity of the element, and it may originate a phenomenon known as *blowout*, consisting in a violent outbreak of the concrete surrounding the bar.

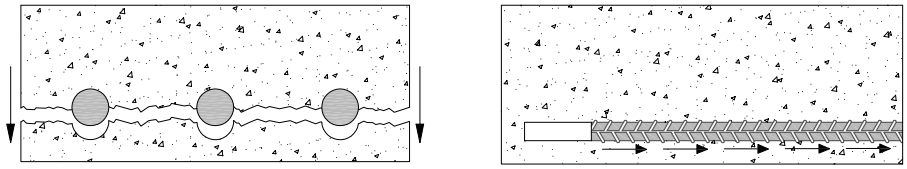

Figure 1.3: Main failure modes: splitting and pull-out

1.1.1 Influence of concrete properties on bond

The splitting failure depends on the concrete tensile strength, hence the mechanical properties of the concrete are the first variables to be

considered. The use of lightweight or recycled concrete can reduce the tensile strength resulting in bond properties which are weaker than those of a normal concrete.

Another important factor is the casting position, as recognized by many code writing bodies such as ACI[2] [5], European Committee for Standardization (CEN[3]) [9] and fib [4]. The reason is the following: when the concrete is being poured and vibrated, the heavier components settle to the bottom while the lighter ones rise up forming a layer of inferior concrete below the bar with poorer bond quality (see Figure 1.4). The concrete over the steel is locally restrained from settling by the reinforcing bar itself, while the adjacent concrete continues to settle and plastic settlement cracks may form over the restraining element. The amount of settlement as well as the deterioration of bonding tend to be related to the depth of concrete beneath the reinforcement. Hence, top cast bars, situated near the top surface of formworks, will generally[4] have poorer bond qualities than bottom cast bars.

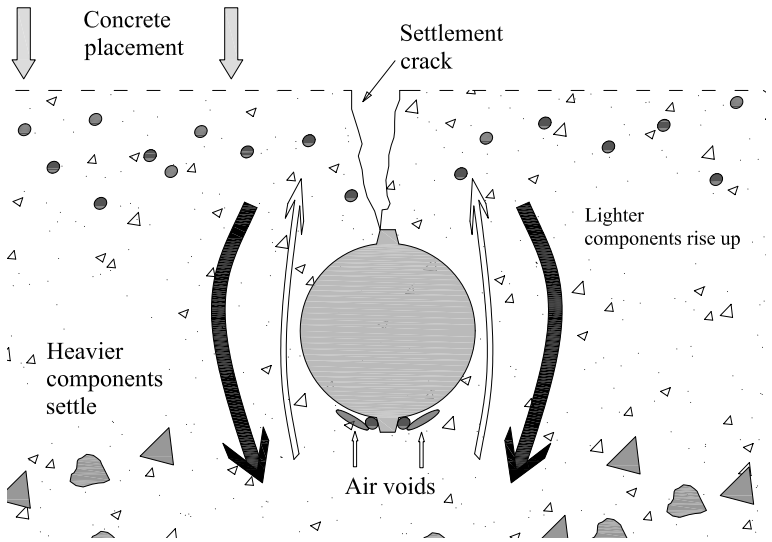

Figure 1.4: Top cast bar effect

Finally, as explained above, the confinement degree of the concrete surrounding the bar influences the mode of failure.

1.1.2 Measurement of bond stress

One of the methods traditionally used to measure bond is the classic pullout test (Figure 1.5), in which a single bar is cast in a concrete block and loaded in tension.

[2] American Concrete Institute
[3] Comité Européen de Normalisation
[4] If normal-strength concrete is used [1].

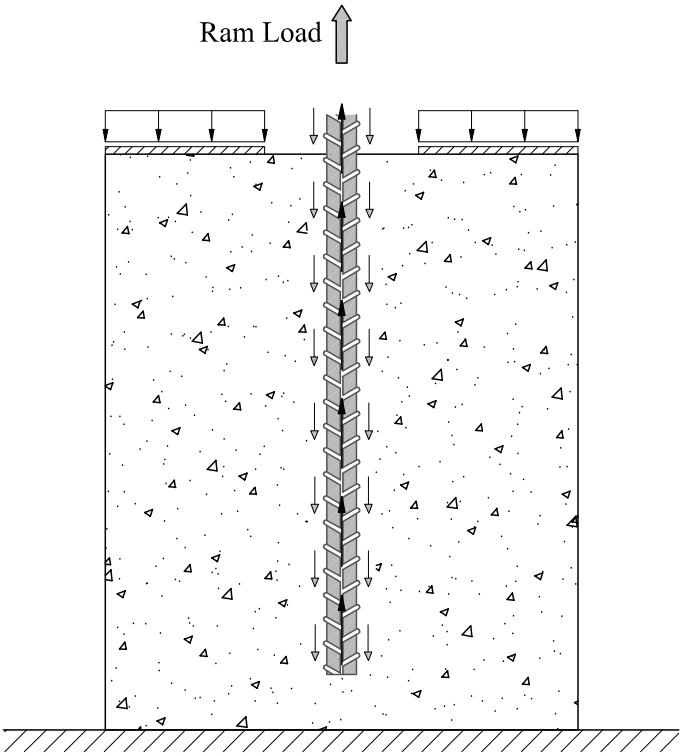

Figure 1.5: Typical arrangement of a pullout test

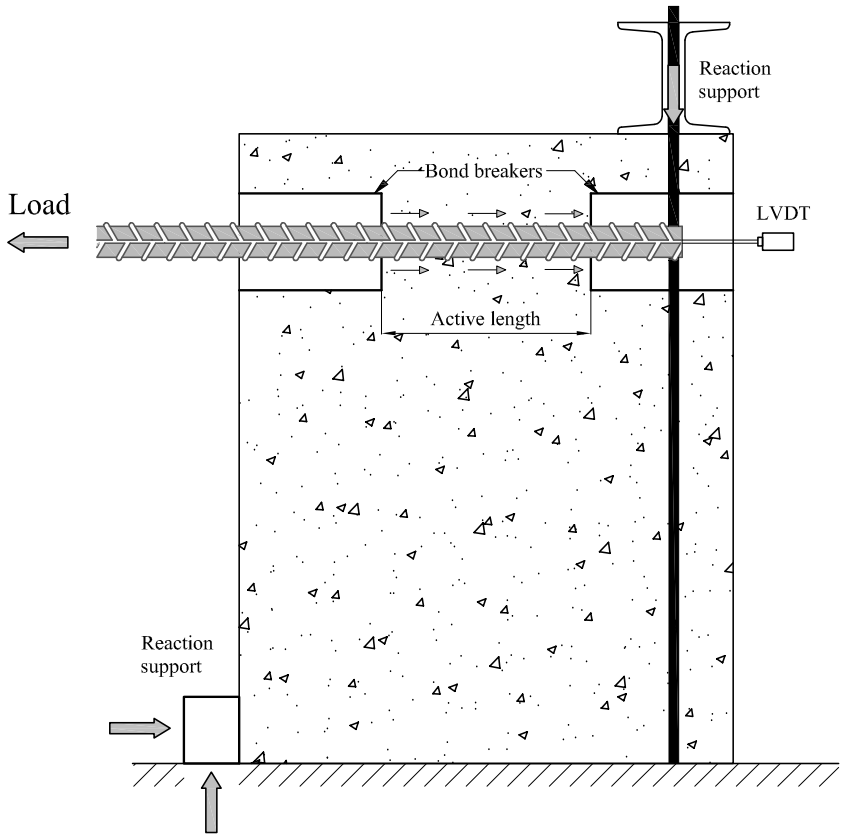

Figure 1.6: Typical arrangement of a beam-end test

Splitting tensile stresses balance the inclined compressive forces spreading outward. In case of small concrete covers, these ring stresses cannot be resisted by the surrounding concrete and a splitting failure may occur, although pullout failure is more prone to occur if a well confined concrete is used (MC2010 considers a well confined concrete a concrete with cover $\geqslant 5\phi$ and clear spacing between bars $\geqslant 10\phi$. Transverse pressure and stirrups can also improve the confinement).

In a standard pullout test, bar force and slip can be measured directly, making this method one of the simplest ways to test anchorages. However, the concrete is compressed against the reaction plate, and such influence can vary during the test or between different tests. This leads to a possible over-estimation regarding conditions found in practice, when such compression is low or even absent.

The well-known beam test is more reliable as a more accurate representation of bar anchorage. In fact, it reproduces the stress state obtained in reinforced concrete members, but it is more expensive in terms of material, cost and space. A compromise specimen is the beam-end specimen represented in Figure 1.6, whose main disadvantage is the complex load arrangement required.

1.1.3 Code provisions

The anchorage of a reinforcement bar is usually calculated with simplified models included in code provisions, in terms of development length. Only provisions for standard hooks in tension are discussed here.

1.1.3.1 *Hooked bars*

Hooked bars achieve the anchorage by a combination of bond along the straight portion of the bar[5] and bearing of the hook on concrete. At failure, Minor [88] observed a loss of bond on the outer radius and the presence of crushed concrete on inner bend radius, as represented in Figure 1.7a).

ACI 318-08 [5] explains in paragraph 12.5 — Development of standard hooks in tension — that "splitting of the concrete cover in the plane of the hook is the primary cause of failure and that splitting originates at the inside of the hook where the local stress concentrations are very high" (see Figure 1.7b). Development length for de-

[5]Usually, the development length provided by code provisions for bent bars is measured to the outside of a hook or bend.

formed bars in tension terminating in a standard hook, l_{dh}, shall be (§12.5.2)[6]:

$$l_{dh} = \frac{0{,}02\ \psi_e f_y}{\lambda\sqrt{f'_c}} d_b \geqslant \max(8\ d_b; 6 \text{ inches or } 152{,}4 \text{ mm}) \qquad (1.1)$$

ψ_e takes into account the influence of epoxy-coated reinforcement and λ the use of lightweight concrete. Both factors increase development length.

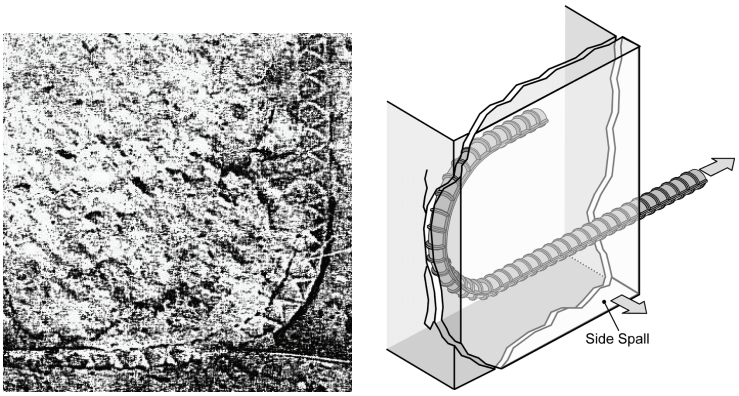

(a) *Loss of bar bond and crushing at bend [58]*

(b) *Side spall failure of a hooked bar [118]*

Figure 1.7: Failure of a hooked reinforcement bar

The development length in Equation 1.1 can be reduced by applicable modification factors which basically consider the presence of confinement, in form of adequate cover (passive confinement) or presence of stirrups (active confinement), which both have a beneficial effect. In fact, they enhance bond strength reducing splitting stresses on concrete and, thus, the possibility of a sudden, brittle failure, like the splitting-type failure is reduced.

MODEL CODE 2010 [4] introduces in paragraph 6.1.3 — Anchorage and lapped joints of reinforcement — a basic concept valid for many types of devices: "Reinforcement may be anchored by bond alone, or by a combination of bond along the straight portion of a bar together with a resistance provided by" other mechanisms. In the case of a hook or bend, a contribution given by the following equation is considered:

$$F_h = 60\ f_{bd} A_b \qquad (1.2)$$

where A_b is the bar area and the design bond strength f_{bd} can be determined as a function of the basic bond strength $f_{bd,o}$, enhanced with some factors depending on passive (concrete cover) and active

[6] The coefficient is 0,24 if using SI units (MPa and mm)

(transverse reinforcement) confinement, and on an eventual compression stress perpendicular to the potential splitting failure surface (p_{tr}). The basic bond strength, considered as an average stress, is:

$$f_{bd,o} = \eta_1\eta_2\eta_3\eta_4 \left(f_{ck}/25\right)^{0,5} / \gamma_{cb} \tag{1.3}$$

in which the η factors take into account respectively the influence of bar surface ($\eta_1 = 1{,}75$ for ribbed reinforcement, 0,90 for unribbed bars), casting position ($\eta_2 = 1{,}0$ for good bond conditions, 0,7 for other conditions and 0,5 for unribbed bars), bar diameter (for $d_b > 25$ mm, $\eta_3 = (25/d_b)^{0,3}$) and strength of steel reinforcements ($\eta_4 = 1{,}0$ for $f_{yk} = 500$, 1,2 for $f_{yk} = 400$ and lower than 1,0 for $f_{yk} > 500$). γ_{cb} is taken as 1,5. The design bond strength is then calculated as:

$$\begin{aligned} f_{bd} &= (\alpha_2 + \alpha_3) f_{bd,o} - 2\ p_{tr} \\ &< 2{,}0\ f_{bd,o} - 0{,}4\ p_{tr} \\ &< (1{,}5/\gamma_{cb})\ \sqrt{f_{ck}} \end{aligned} \tag{1.4}$$

The influece of passive confinement from cover and from transverse reinforcement is represented, respectively, by means of factors α_2 and α_3. For the comparison shown in Figure 1.8 the use of the conservative values $\alpha_2 = \alpha_3 = 1{,}0$ was adopted. Finally, the stress to be anchored is:

$$\sigma_{sd} = \alpha_1 f_{yd} - (F_h/A_b) \tag{1.5}$$

where α_1 is the ratio between the reinforcement area required by design and the one provided, assumed equal to 1,0 in this comparison. Finally, the design anchorage length may be calculated using the following equation:

$$l_b = \frac{d_b \sigma_{sd}}{4\ f_{bd}} \geqslant l_{b,min} \tag{1.6}$$

where

$$l_{b,min} = \max\left(0{,}3\frac{d_b f_{yd}}{4\ f_{bd}}; 10\ d_b; 100\ \text{mm}\right) \tag{1.7}$$

EUROCODE [9] in paragraph 8.4.2 — Ultimate bond stress — defines the design value of the ultimate bond stress, f_{bd}, for ribbed bars as:

$$f_{bd} = 2{,}25\ \eta_1\eta_2 f_{ctd} \tag{1.8}$$

As in Model Code 2010, the η factors take into account the influence of casting position and bar diameter in a similar way. $\eta_1 = 1{,}0$ for good positions and $\eta_2 = (132 - \phi)/100$ for bars whose diameter is greater than 32 mm, being otherwise 1,0. The basic required anchorage length, $l_{b,rdq}$ can be estimated as a function of the ultimate bond stress.

$$l_{b,rdq} = \frac{\phi \sigma_{sd}}{4\ f_{bd}} \tag{1.9}$$

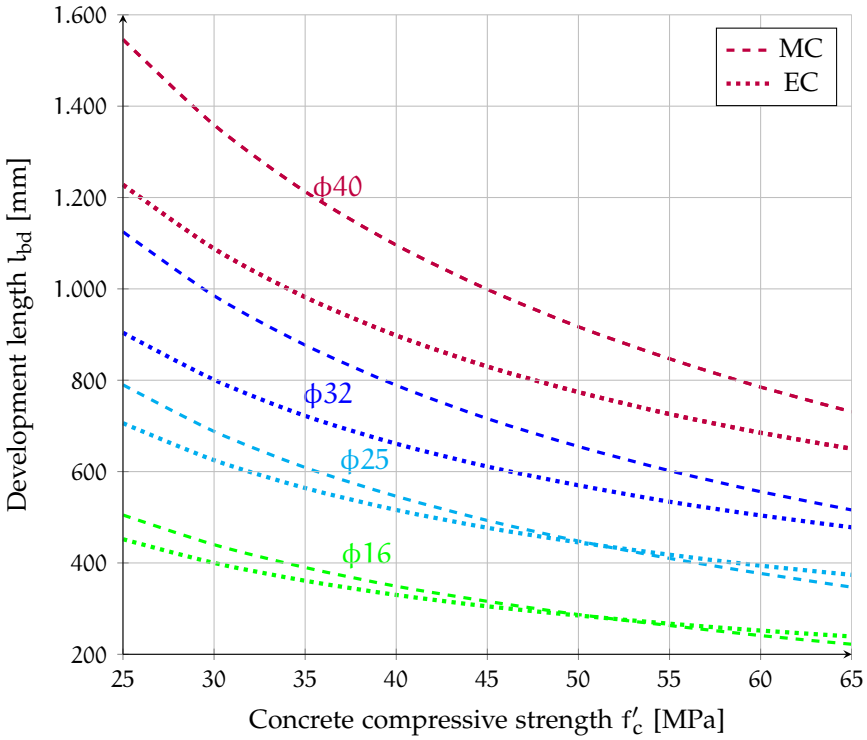

Figure 1.8: Development length of standard hooks for some common diameters (16, 25, 32, 40 mm) using the MC2010 and the EC2

Finally, the design anchorage length, l_{bd}, is:

$$l_{bd} = \alpha_1 \alpha_2 \alpha_3 \alpha_4 \alpha_5 l_{b,rdq} \geqslant l_{b,min} \tag{1.10}$$

where α_1 takes into account the shape of the bar (0,7 for hooked bars), α_2 the passive confinement, α_3 the active confinement, α_4 the presence of welded transverse bars and α_5 the effect of the transverse pressure, in a way similar to Model Code 2010. In Figure 1.8 conservative values for all factors others than α_1 have been adopted (α_i=1,0).

As can be seen in the above graph (Figure 1.8), the development length needed for a proper anchorage of a hooked bar has a very similar shape in both cases, with a 20% maximum difference in terms of absolute value between EC and MC 2010 curves (ϕ40).

If the same graph is plotted in terms of bar diameters l_{bd} ranges from $14d_b$ to $40d_b$ for the concrete strength range considered. ACI Code allows smaller values, but the difference is due to the absence of a resistance factor for bond[7], as commented at paragraph 9.3.3: "Development length specified in Chapter 12 does not require a ϕ-factor".

Calculating the curves provided by EC and MC without material safety factors ($\gamma_s = \gamma_c = 1{,}0$), as in Figure 1.9, it can be seen that the ACI curve lies approximately between EC and MC curves.

[7]In the ACI code the material partial safety factors used in other codes are replaced by strength modification factors called ϕ.

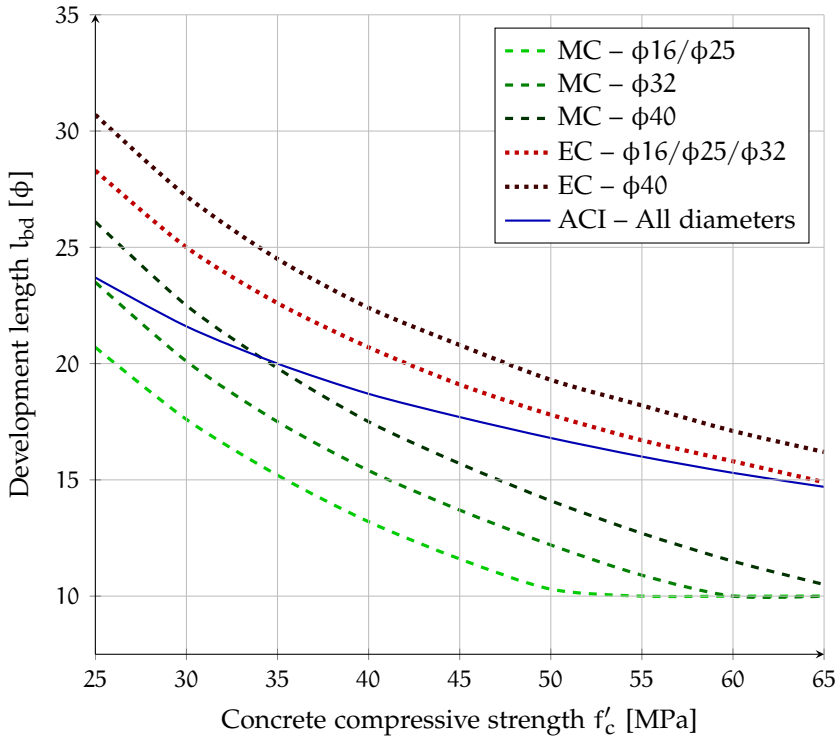

Figure 1.9: Development length of standard hooks: comparison between MC2010, EC2 and ACI expressed in terms of bar diameters. No material safety factors have been used.

1.2 BACKGROUND ON MECHANICAL ANCHORAGES

A somewhat more recent development in reinforcing steel technology is the use of headed reinforcing bars as an alternative to standard hook terminations. Headed bars are ordinary reinforcing bars with steel plates or nuts attached to one or both ends, as schematically depicted in Figure 1.10. The bearing area of the plate acting on the surrounding concrete contributes to anchor the tensile force in the bar.

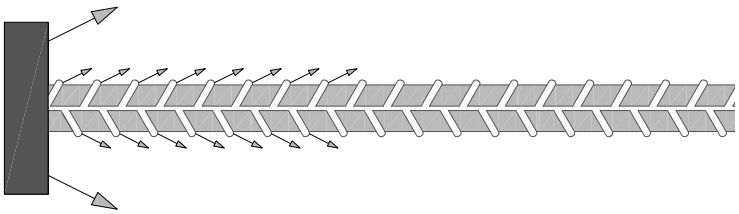

Figure 1.10: Headed Reinforcement Bar concept

In many cases, these mechanical anchorages represent a viable option and often a better solution with respect to traditional bent or hooked bars. The need of a proper anchorage can require bends with

very large radii and long development lengths, thus resulting in a complicated assembly especially in congested areas in which concreting conditions are poor. The advantages provided by the use of this relatively new type of reinforcement make this technique attractive for many common construction problems.

1.2.1 Historical development

The history of mechanical anchorages in reinforced concrete structures, also known as headed bars or headed reinforcement bars, began in the 1960's, when an extensive research [25, 60, 110, 111] on headed stud anchors was carried out in the field of concrete slab-steel beam composite construction.

In 1973 McMackin et al. [84] from Lehigh University introduced the pullout cone design method for anchors under combined shear and tension loading. The embedment length was among the factors affecting the ultimate strength of a headed steel anchor stud. Stoker et al. [113] also performed in 1974 a study for Caltrans[8] whose aim was to determine a method for anchoring large bar diameters with a reduced development length.

In a 1981 work, Dilger and Ghali [36] from the University of Calgary proposed the use of double-headed ties as punching shear reinforcement in slabs. The solution proved to be better than welding the existing shear studs to flat plates creating studrails. They also recommended a head size 10 times the bar area, which, in their opinion, was necessary for proper anchorage. Being one of the first studies regarding the use of welding plates to reinforcement bars, it has often been considered as a reference by many researchers. As a consequence of this research, a product similar to studrail, with 10 : 1 head-to-stem cross-sectional area ratio was patented and is still sold by Decon, being the primary product commercialized by them. Following this work, many years later they investigated the use of double-headed studs to substitute the difficult-to-place stirrups as ties for wall or slab elements [37].

AOGA[9] began to study the technology interested in the potential use of headed reinforcement as shear reinforcement in heavily reinforced concrete offshore platforms. AOGA was also considering the possibility of improving highly congested details and recommending the use of headed bars to Norwegian Contractors, who were interested in mass production to be applied to their field of work, the design and construction of offshore oil platforms.

Norwegian Contractors joined a partnership with a specialist engineering company serving the marine and industrial sectors, Metalock, and an independent research organisation in Scandinavia, the

[8] CALifornia department of TRANSportation
[9] Alaska Oil and Gas Association

SINTEF group. As a result of this cooperation, a friction-welding technology was patented, and an American subsidiary of Metalock was founded, the HRC[10], the first supplier of headed reinforcement bars. Much research was carried out by HRC in Norway, for instance the study published by Fynboe and Thorenfeldt [45] which analyzed the behavior of static pullout tests aiming to "give a basis for the future use of the T-headed bars in concrete structures". However, most research on this topic is proprietary and has not been published.

Some results from previous investigations and some insight on proprietary tests by AOGA and SINTEF were presented by Berner et al. [15], who have also been the first to describe many of the possible applications of this innovative typology of reinforcement bars.

By 2009, fib [3] reports that "T-headed bars have been used instead of conventional shear reinforcement on several offshore projects to reduce the congestion of small diameter stirrups and facilitate the placing of concrete. T-heads may also be used to anchor larger bars".

Meanwhile, ERICO[11] had been developing its own headed bar technology, and would start selling in Europe in the 1980's. ERICO and HRC were for a long time the only producers of this kind of products which, today, are provided by a series of firms.

Although the earliest works were targeted to the offshore oil industry, in the last decades designers have acknowledged the high potential of using headed bars for some more common construction problems. The focus is primarily on seismic and retrofit applications but the application field is potentially very wide and continuously expanding.

Recent works at the University of Texas at Austin have explored many of the potential applications and have proposed anchorage provisions, within the Project 1855 funded by TXDOT[12] [118] and some of them have been included in the ACI 318 Building Code.

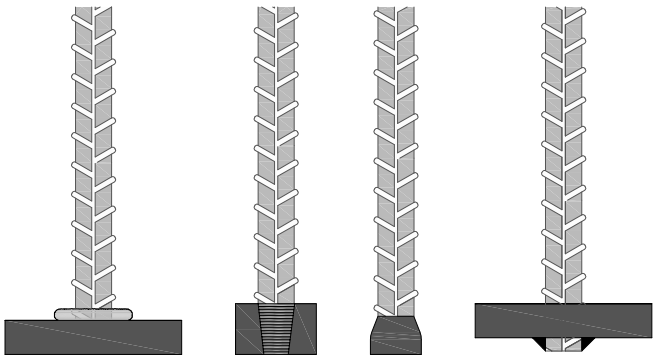

Figure 1.11: Mechanical anchorage details. From the left to the right: friction-welding, threaded connection, forging, traditional weld

[10] Headed Reinforcement Corporation
[11] Electric Railway Improvement COmpany
[12] TeXas Department Of Transportation

1.2.2 Processing technologies

As seen in the previous section, there are various technologies allowing to achieve the connection between the bar and the plate, the main ones being related to some form of welding or threading. Some of the technologies used today are reviewed in the following paragraphs. A schematic representation of some possible details is shown in Figure 1.11.

1.2.2.1 *Friction-welded heads*

Friction-welding technology was the first method to be used in plate-anchored reinforcement production. It is a class of solid-state welding, a reliable and economic welding process in which the head is rotated up to about 1500 rpm and a bar is pressed against it. The heat resulting from the friction welds the parts together.

This process is widely used in the automotive or in the aerospace industries, and one of its advantages is that it allows dissimilar materials to be joined. At the junction between two materials, softened material begins to extrude creating a torus of upset[13] steel during the process. This excess material is known as flashing.

This is the only process capable of welding alloys or metals of different nature. Futhermore, it is a fast and reliable process.

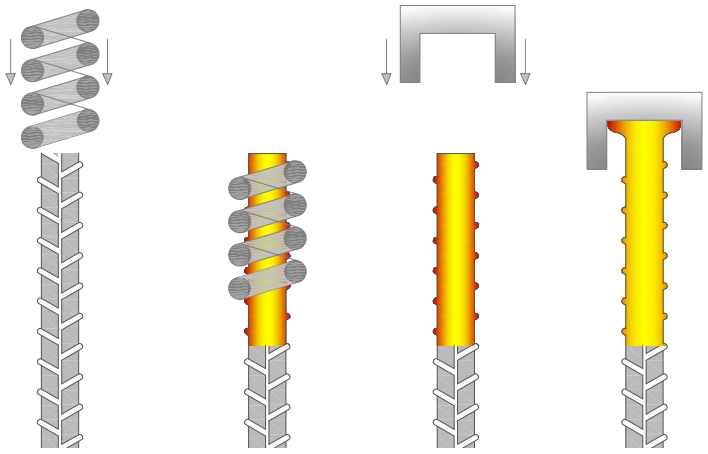

Figure 1.12: Manufacturing process: forged head by induction heating

1.2.2.2 *Threaded heads*

The union between a bar and a plate is performed via a cylindrical or conical thread, although the conical thread allows a more efficient transmission of forces. It is the same system adopted for mechanical couplers, when rods of large diameter have to be coupled but the transmission of forces by splicing is not possible.

[13] An upset is a class of forging process in which the length decreases, while the cross-section increases.

1.2.2.3 *Forged heads*

Forging is a manufacturing process involving the shaping of metal using localized compressive forces. According to the temperature at which is performed, it can be a cold or a heat forming process. It is one of the oldest known metalworking processes.

In headed bar production, the forging process is usually preceeded by an induction heating, like the one represented in Figure 1.12, therefore the resultant process is called induction forging. The high frequency induction is a non-contact process which uses a strong varying magnetic field in order to produce a potential difference, therefore producing heat through the material. In this process, a reinforcement bar is introduced into a solenoid, then, once the desidered temperature has been reached, the object is pushed against a mold where it takes the desired form.

Sometimes, usually for cold working processes involving the use of a die, the term *swaging* is used to describe the forging process.

1.2.2.4 *Traditional weld*

While traditional weld is a potential technology to manufacture mechanical reinforcement, it is not suitable for a mass production and for this reason no further reference to this technology is made in this work.

1.2.3 Manufacturers

As previously described, HRC and ERICO were the first manufacturers of headed reinforcement bars. In the following paragraphs some of the products available on the market are briefly described, although the list is not meant to be complete.

1.2.3.1 *HRC*

HRC is the principal distributor of mechanical anchorages, called *T-Headed bar* or *T-Heads*. HRC uses mainly the welding-friction patented and provides four typologies of plates: square, rectangular, circular, oval. A_1 being the plate area and A_b the bar area, all of the T-heads in the HRC catalog comply with the following limitations:

$$9{,}6 \leqslant \frac{A_1}{A_b} \leqslant 12{,}4$$

The plate thickness varies but in general it can be said that it is smaller than the bar diameter. Figure 1.13 represents some products manufactured by the corporation and Table 1.1 reports head dimension and thickness for some bar diameters of HRC 100 series. HRC 200 series, with forged heads, is presented as an improvement for fatigue loads with respect to the friction-welded heads [53].

Figure 1.13: The HRC 100 and 555 Series, with reduced size heads [53]

d_b	Rectangular			Square			Circular			
	$a_1 \times b_1$	A_1/A_b	e_1	$a_1 \times b_1$	A_1/A_b	e_1	ϕ	A_1/A_b	e_1*	e_1**
16	35 × 60	10,4	16	50 × 50	12,4	12	50	9,8	12	20
20	40 × 80	10,2	18	60 × 60	11,5	14	65	10,6	16	25
25	50 × 100	10,2	20	70 × 70	10,0	16	80	10,2	20	30
32	65 × 120	9,7	25	90 × 90	10,1	20	100	9,8	25	40
40	-	-	-	110 × 110	9,6	25	-	-	-	-

Table 1.1: HRC 100 series for Europe and Canada. * = forged; ** = threaded

1.2.3.2 *ERICO*

ERICO has a unique typology of mechanical anchorage called *Lenton Terminator*, which consists of a rebar with a tapered thread termination which is screwed onto a circular enlarged head, as shown in Figure 1.15a. Plates anchoring large diameters ($\geqslant$ 40 mm) present an intermediate ring before reaching the external diameter (Figure 1.14). Series D14 (full size) in ERICO's catalog respects for a variety of diameters the following plate-to-bar area ratio:

$$10{,}0 \leqslant \frac{A_1}{A_b} \leqslant 12{,}6$$

while the D16 series, with reduced head sizes, has a mean ratio about 5,0. This last series is suitable for cases when it can be possible to combine the bearing capacity of the plate with the bond along the straight part of the bar. The plate thickness varies but in general it can be said that it is greater than the bar diameter and also greater than the one of the HRC circular plate.

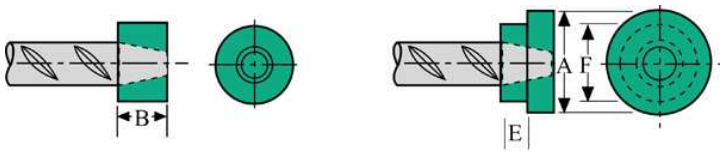

Figure 1.14: ERICO Lenton Terminator: the standard version and the one with an intermediate ring, for large bars. [40]

1.2.3.3 *Dextra Group*

Dextra Group produces a mechanical anchoring system very similar to ERICO's, consisting of a circular plate screwed on the bar termination, although it can have other forms under specific order. The

system, shown in Figure 1.15b, is called Bartec End Anchor and is adapted from the same coupling system used in standard splicing.

The plate area is between 5 and 10 times the bar area: smaller heads are able to operate by combining the bearing strength of the plate with the bond along the bar[14]; large heads achieve yield without exceeding the capacity of concrete, provided that the compressive strength is at least 40 MPa. The plate thickness is similar to that of HRC.

(a) *Lenton Terminator*

(b) *Bartec End Anchor*

(c) *BAR-US Anchor Nut*

(d) *Dayton D158B*

(e) *BPI-Grip Buttonhead*

Figure 1.15: Some products available on the market

1.2.3.4 *Barsplice*

Barsplice provides a product called BPI-Grip Buttonhead with an octagonal plate (Figure 1.15e) . Plate thickness is greater than bar diameter. The bar is not threaded and the connection is manufactured through a cold swaging process. The necessary equipment can be rented or purchased. The head area is 5 times the bar area (BNH series) or 10 times the bar area (BNX series). The company manufactures another product called BPI Doughnut, with a threaded connec-

[14] As in the previous cases, the limitation $A_1/A_b = 10$ for the full size heads may derive from the first available products, the HRC series, which in turn, may derive from either the Calgary recommendations or from SINTEF proprietary studies.

tion, reduced or full size heads and a thickness similar to that of the octogonal plate.

1.2.3.5 *Other manufacturers*

Dayton Superior provides the full size head series called D-158-B (Figure 1.15d). BAR-US is a Turkish firm which produces cylindrical threaded bars sold under the trade name Anchor-Nut (Figure 1.15c). Dai-Ichi High Frequency Company, a Japanese firm whose main field of activity is the high frequency induction technology, produces mechanical anchorages using this procedure.

Other countries may be interested in similar products, given their seismicity. Some institutions in Korea [27, 29, 30, 28, 61, 62, 64], Taiwan [26, 67, 123] and Japan [109, 124] are currently doing research on the topic and have published experimental results.

1.2.4 Previous research

In this section the main research carried out on the topic of mechanical anchorages is discussed, with emphasis on the most important studies. The proposed design equations are also reported, pointing out the ones which have been incorporated in structural codes.

1.2.4.1 *Behavioral tests*

UNIVERSITY OF TEXAS STUDY An extensive research was sponsored by HRC and conducted by three PhD students: De Vries, Bashandy and Thompson. DeVries [35] conducted the first phase of the study with over 140 pullout tests on headed reinforcement bars embedded in concrete blocks in which many variables were tested to determine their influence resulting in a comprehensive study of the topic. The pullout campaign was divided in two main categories, depending on the ratio between embedment depth (h_d in Figure 1.17a) and clear cover, which was chosen to be less than five in the shallow embedment pullout tests and more than this figure in the deep pullout tests. The goal of the research was to produce design recommendations to predict the anchorage capacity of headed reinforcement.

Of the 21 shallow embedment tests, 18 resulted in a pullout-cone failure — as in Figure 1.17a — and the remaining 3 failed by bar fracture. DeVries found out that:

- The embedment depth generally increased the capacity;
- A head aspect ratio[15] greater than one (as it is for rectangular plates) did not affect the anchorage capacity;

[15]The aspect ratio is defined as b_1/a_1. This is lower or equal than two in the case of HRC rectangular heads.

- The presence of transverse reinforcement did not affect the ultimate strength of the anchorage.

The CCD[16] method was used by DeVries to estimate the capacity using the applicable modification factors for edge or corner placement. The procedure, developed for studs, bolts and expansion anchors by Fuchs et al. [42], assumes a four-sided pyramidal failure surface projected from the head, measuring $3h_d$ on each side, hence giving a slope of the failure surface of about 35 degrees. A distribution of tensile stresses in the concrete over the failure surface resists the tension in the bar. The basic concrete breakout capacity was estimated with the formula:

$$P_{U0,s} = k\, {h_d}^{1,5} \sqrt{f'_c} \tag{1.11}$$

The failure area can be less than that previously described when an anchor is placed near to a corner or an edge (Figure 1.16a). For this reason the CCD method considers a reduction coefficient, the ratio between the failure area A_N and the assumed failure area A_{N0}:

$$A_N = (c_1 + 1{,}5h_d)(c_2 + 1{,}5h_d) \leqslant 9{h_d}^2$$

with $c_1, c_2 \leqslant 1{,}5h_d$

$$A_{N0} = 9{h_d}^2$$

$$P_{U,s} = \frac{A_N}{A_{N0}} P_{U0,s} \tag{1.12}$$

However, Equation 1.12 slightly underestimated the experimental results as a consequence of the larger heads typically found on plate-anchored bars. For this reason, DeVries proposed two solutions: adjust the coefficient k in the formula or change the definition of the failure surface A_N to take into account the head size (Figure 1.16b) rather than head perimeter (Figure 1.16a). The second option resulted in better predictions.

Focusing now on deep embedment specimens, a total of 129 pull-out tests were performed. 123 on single bars and the remaining six on closely spaced bars. Primary tested variables were bar diameter (20 to 35 mm), development length l_d/d_b (6,1 to 18,3), head orientation, head geometry, head area A_1/A_b (2,2 to 13,0), shape, aspect ratio (max 3,0) and thickness e_1/d_b (0,46 to 1,0), transverse reinforcement, concrete strength (19 to 44 MPa), concrete cover, corner or edge bars and closely spaced bars.

Eighteen concrete cubes were constructed, each of them with 4 to 12 headed bars cast around the perimeter. Each bar was tested monotonically in tension until failure. 15 tests resulted in an unexpected

[16] Concrete Capacity Design

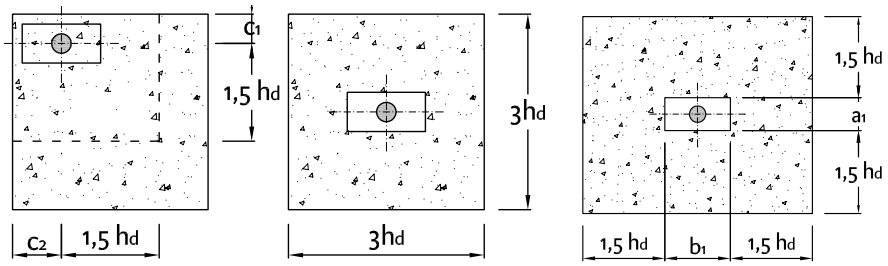

(a) A_n *based on head axis (as in CCD method) Left: edge placement; Right: center placement*

(b) A_n *Based on head perimeter (as in DeVries' proposal)*

Figure 1.16: Projected failure surface

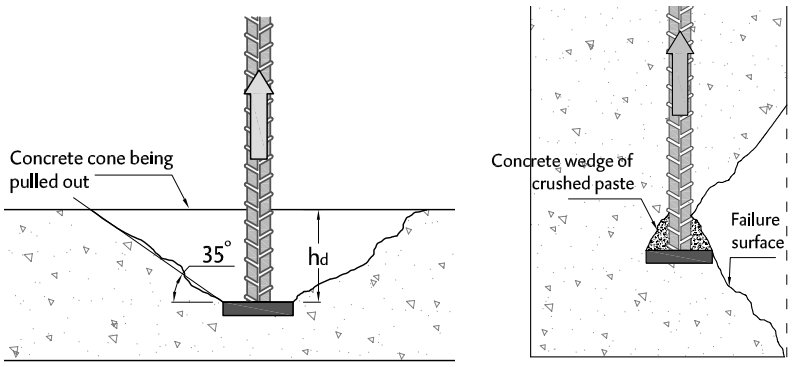

(a) *Shallow embedment*

(b) *Deep embedment side blow-out-type failure*

Figure 1.17: Expected failure modes

failure of the top surface under the applied load. Of the 114 remaining, 35 had a PVC tubes sheathing the bars, in order to control the amount of development length. Of the 79 with no bond contribution, 57 were edge bars, 16 were corner bars and 6 were paired bars[17]. All the specimens failed by a side-blowout failure — as represented in Figure 1.17b — with crushing of the concrete over the head. These are some of the conclusions drawn by DeVries:

- The critical variables affecting the blowout capacity were edge distance, concrete strength and the net bearing area of the head. Head shape and orientation, as well as the aspect ratio for rectangular heads, had no noticeable influence on the capacity;
- For bars with high embedment depth, a side-blowout failure or a bar failure is expected. Additional embedment depth did not further enchance anchorage capacity;
- Development length increases the anchorage capacity, in a measure predictable by standard provisions. At failure, approximately 33% of the total load was carried by the development

[17]Complete data are reported in Chapter 3.

length, but this data is based on only six tests equipped with strain gauges and thus, it seems conservative to ignore the increase in strength.

- Transverse reinforcement did not increase the ultimate capacity but it had the effect of substantially increasing the ductility and the residual strength maintained after blowout failure.
- Although tests seemed to indicate that head thickness does not affect the anchorage capacity, DeVries proposed that the head should be designed to prevent yielding in bending under a uniform stress ditribution.
- Corner placement and close spacing of bars reduced the anchorage capacity of the reinforcement.

A nonlinear multivariable regression analysis formula was used and a power function of the primary variables was proposed. The regression produced the following best-fit equation:

$$P_{U0,d} = 0{,}0252\ {c_1}^{0{,}609} {A_n}^{0{,}577} {f'_c}^{0{,}671} \tag{1.13}$$

A so-called physical model was proposed, based on the size of the failure surface and the tensile stresses to be resisted by concrete, that is, the bursting force — referred to by the author as the *driving force* — caused by the spreading of the applied concentrated force.

$$P_{U0,d} = 0{,}0107\ {c_1}^{1{,}33} {A_n}^{0{,}333} {f'_c}^{0{,}667} \tag{1.14}$$

Notwithstanding, neither equation was considered suitable for design, since the exponents for the variables had to be simplified. For instance, the use of square root for the concrete strength was considered an acceptable simplification as the tensile strength is usually considered as a function of the square root of the compressive strength. The area was also found more appropriate with a 0,5 exponent, while the influence of edge distance was taken linear.

The proposed design equation is based on a characteristic blowout capacity for a common situation of a single headed bar not affected by edges or spacing. Additional factors can be applied in other cases accordingly to the following equation for the ultimate blowout capacity of a bar or a group of bars:

$$P_U = \Psi \frac{A_{bo}}{A_{bon}} \frac{c_1 \sqrt{A_n f'_c}}{80} \tag{1.15}$$

This last equation has been included in HRC catalogs. The simplified formula has the same structure as the one previously proposed by Furche and Eligehausen for headed bolts (see Section 1.3.1.1) and the partial factors are taken from the CEB bulletin [8], being:

Ψ a factor, called by DeVries *radial disturbance factor*, which takes into account the lower capacity of bars placed on corners, calculated as:

$$\Psi = 0{,}7 + 0{,}3\frac{c_2}{3c_1} \leqslant 1 \tag{1.16}$$

$\frac{A_{bo}}{A_{bon}}$ a factor that takes into account geometric effects of edge distance in the second direction and the presence of closely spaced bars (see Figure 1.18).

In CEB nomenclature these two factors are named $\Psi_{s,Nb}$ and $\Psi_{A,Nb}$.

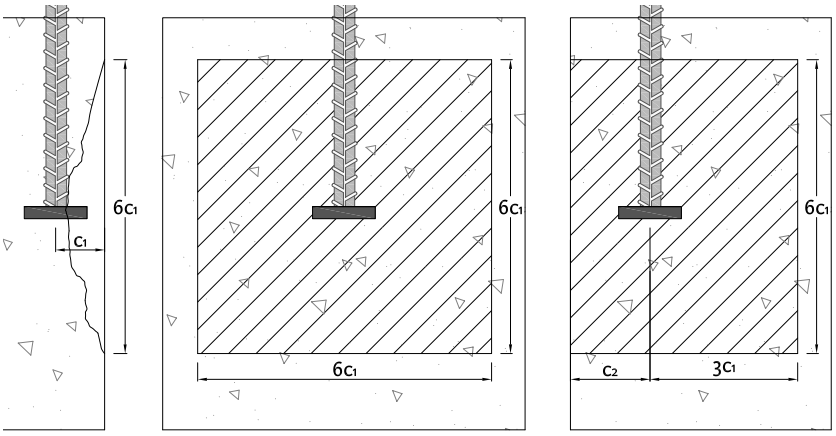

Figure 1.18: Blowout areas for various configurations. Left: side view; middle and right: basic blowout area (A_{bon}) and blowout area (A_{bo}) for a corner placement. For other conditions, such as presence of closely spaced bars, see the original sources [8][35]. See also Section 1.3.1.1

In the second phase of the research, Bashandy [14] studied the possibility of using plate-anchored bars as shear reinforcement and the effects of cyclic load in 14 additional pullout tests designed in a similar way to DeVries' tests, all of them with 35 mm rebars. He found out that:

- Cyclic loading, between 5% and 80% of the ultimate capacity, up to 15 cycles[18], was recognized as not having a significative influence on the anchorage capacity;
- Placing a crossing bar in the head anchorage zone positively affects the ultimate anchorage capacity, acting as a lateral restraint against blowout failure and increasing the effective bearing area of the head, except for cases in which a small head is restrained

[18]The number of cycle is oriented at estimating damage resulting from earthquake forces, not really cyclic loads.

by a bar with a larger area. For this reason, Bashandy suggested a conservative limitation on the increase on capacity to 25% for head with a *positive anchorage*[19]. As DeVries concluded that the presence of transverse reinforcement did not increase the ultimate capacity of the anchorage, it should be noted that a crossing bar has the additional effect of increasing the effective bearing area of the head, which leads to lower bearing stresses.

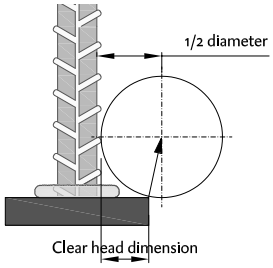

Figure 1.19: Deviation forces resulting from a head without a *positive anchorage*

- The 11 exploratory tests regarding the use of plate-anchored bars as a confinement reinforcement provided results indicating a great potential for this use.

Bashandy also tested 32 large specimens — shown in Figure 1.20 — simulating exterior beam-column joints and he confirmed some of the observations by DeVries. The beam was not cast with the specimens, but was simulated by a tensile force on the headed bars and a compressive zone on a block which provides a uniform bearing surface. Tested variables were bar diameter (25 or 35 mm), head area A_1/A_b (3,0 to 8,1), head aspect ratio, head orientation and concrete strength (22,1 to 40,0 MPa). Also, the embedment length h_d (measured from the column face to the end of the bar) was provided using columns with variable dimensions (229 to 457 mm), and the effects of confinement were evaluated providing additional concrete cover or confinement reinforcement.

More than half of the specimens failed with a side blow-out failure. Another 14 failed in shear, some of them with heads not anchored behind longitudinal bars of the column.

In specimens with a side-blowout failure, a longitudinal splitting crack first initiated at the face of the column and radially propagated from the bar to the surface along embedment length. As the load increased, a diagonal crack initiated at the head and propagated towards the compressive zone. At failure, the side cover spalled, in some cases completely, and removing the damaged layer a crushed concrete wedge could be detected on the bearing side of the head.

Specimens which failed in shear had a similar cracking pattern, but the failure was due to the increasing width of the first diagonal

[19] According to Bashandy, positive anchorage means that the clear head dimension is at least equal to half the crossing bar diameter. This specification excludes cases in which a small plate interacts with a very large bar, a situation in which a side-blowout failure is favored, as shown in Figure 1.19.

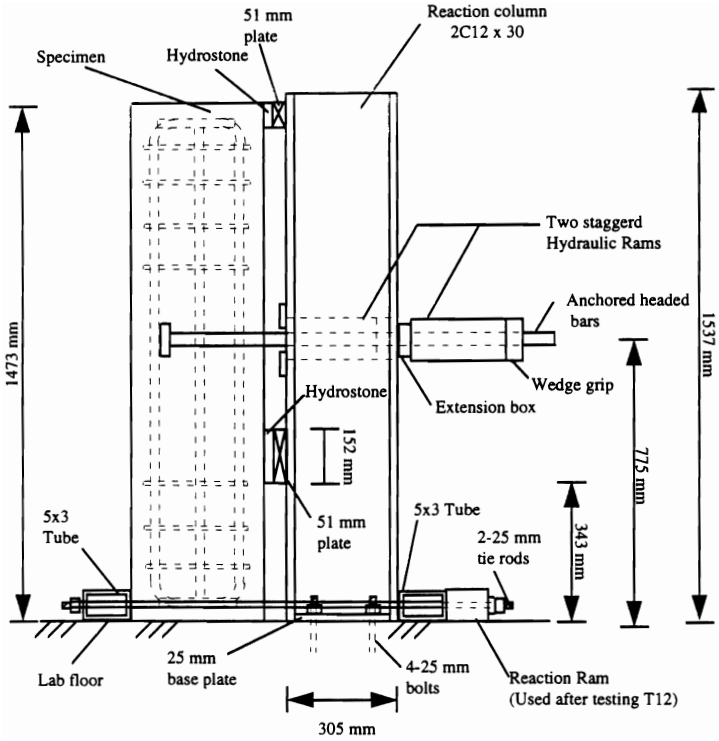

Figure 1.20: Setup of Bashandy beam-column joints [14]

crack and failure occurred along the plane of the crack without side spalling. In some tests, in which heads were anchored behind the column longitudinal bars, he recognized a significantly higher shear capacities[20]. There will be no further references to these tests.

Bashandy drew the following conclusions:

- The resistant mechanism is a composition of bearing stress on the head and anchorage along the bar;
- Head aspect ratio and orientation do not have significant effect;
- Increasing head area or side cover improved ultimate capacity;
- Transverse steel confinement placed parallel to the axis of the headed bars improved the ultimate capacity restraining side cover from blowout and confining the concrete beneath the head to improve bearing capacity;
- Ultimate capacity increased linearly with embedment depth: less of the total capacity was carried by the head as the length was increased;

[20]The design of the specimens was aiming to reproduce early tests on hooked rebars carried out by Marques and Jirsa [58], who concluded that the position of the column longitudinal bars did not affect the stress-slip behavior of the anchorage. Additionally, in order to develop a design equation any possible beneficial effect is neglected.

- Comparing the data to DeVries' deep embedment tests, the capacity in these tests was 14-44% less. It should be remarked that the heads used were relatively small, in order to avoid bar yielding before failure (Only two tests reached the steel tensile strength, the average stress being 0,8 f_y); consequently, only some specimens were able to resist an increase of the applied load after the deterioration of bond, when the applied load was carried entirely by the head.

  Bashandy attributed the difference to concrete cracking in the joint region, which would have a direct influence on the shape of the side blowout area.

  Thompson [117] offered a good explanation for this results pointing out that tests with greater embedment length to cover ratio had better measured/predicted ratios. These tests had an embedment length to cover ratio lower than 5,0, which was the limit specified by DeVries for deep embedment tests. Therefore, the mode of failure was somehow an intermediate mode between the concrete breakout and the side blow-out.

  He also pointed out the important distinction between embedment length and anchorage length. The anchorage length is measured from the head to the intersection between the edge of the strut and the bar: if this length is considered instead of the embedment length, the effective embedment would be even more reduced.

- The overall performance of headed bars was at least equivalent to and frequently better than analogous hooked bars.

Some years later, in 2002, Thompson [117] presented his dissertation. The aim of his work was to continue and conclude the researches started separately by Young and Ledesma about the use of headed reinforcement bars in CCT node specimens and in lap splice tests. They analyzed in detail some preeminent characteristics of these common uses of mechanically anchored bars.

Regarding the first part of his work, a total of 64 CCT node specimens were tested. The basic load setup was essentially a beam resting on two supports with an hydraulic ram applying the load through a bearing plate, as shown in Figure 1.21. The specimens were instrumented with strain gages to provide information about the development of the force in the bar and about strains in concrete and in confining reinforcement. Primary variables were anchorage type (straight, headed or hooked bars), relative head area A_n/A_b (0,0 to 10,4), strut angle (30, 45 or 55 degrees), bar size (#8 or #11) and level of confinement (none or closed stirrups placed at 6 in. or 3 in.).

Failure was due to crushing or splitting of the compression strut transversely, with a lateral rupture similar to the side-blowout failure observed by DeVries. Similarly to what DeVries had done previously,

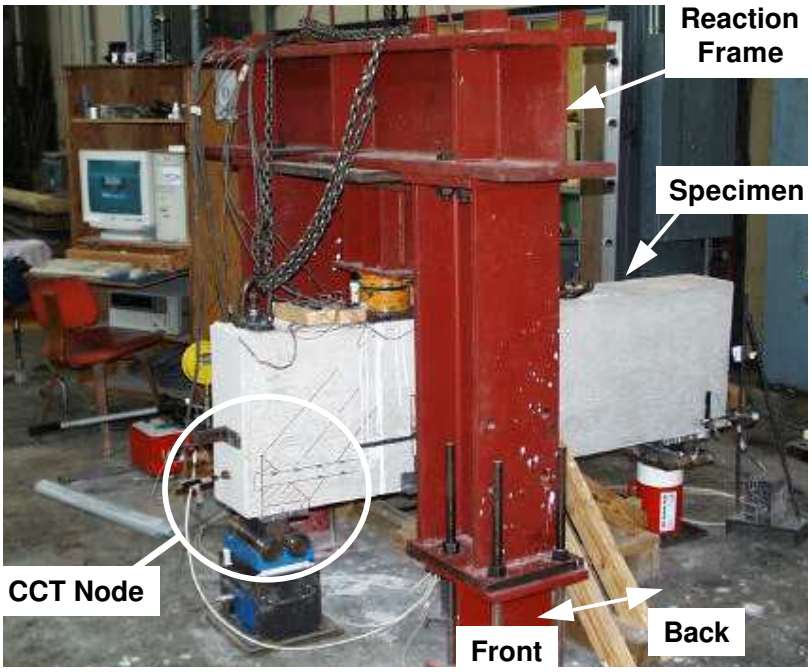

Figure 1.21: Setup of Thompson's CCT tests [117]

after an extensive investigation Thompson proposed two formulas for the estimation of the bearing capacity of headed bars. The structure is similar to the DeVries' formula, since primary variables are taken into account with the same exponents, except for concrete strength that is considered to have a linear influence on total capacity[21].

$$P_U = A_n \left(0{,}9\, \Psi \frac{2c_1}{\sqrt{A_n}} f'_c \right) \quad \text{with } \Psi = 0{,}6 + 0{,}4 \frac{c_2}{c_1} \leqslant 2{,}0 \qquad (1.17)$$

Thompson adopted a Ψ factor to take into account the bar position, equal to 1,0 when a bar is close to a corner and increasing when a bar approaches an edge condition, unlike what was done by DeVries with his disturbance factor. A minimum anchorage length of $6d_b$ is required[22]. The following observations were also made:

- Head capacity increased with the ratio c_2/c_1 with an upper limit between 3 and 4;
- Head orientation wass found out not to have visible effects on capacity, up to an aspect ratio of 3;
- Decrease in the strut angle resulted in a longer development length for the bar (see Figure 1.22), allowing a greater contribution from bond and therefore the use of smaller head sizes.

[21] He also proposed another formula with a variable exponent for concrete strength but only Equation 1.17 is reported here as it is considered much more simple.

[22] The limitation arises from the strain gages placed to measure bas stresses from $1d_b$ (next to the head) to $7d_b$ (close to the critical crack) along the bar.

The critical development point is estimated at the intersection of the tie with the edge of the strut, while changes in confinement can increase the anchorage length modifying the strut-and-tie mechanism;

- Anchorage is achieved through composition of bond and bearing: the capacities provided by each can be determined separately and added to find the total anchorage capacity. Thompson suggested that the larger the head, the smaller the bond contribution to the total anchorage force at failure. The relationship was linear with a minimum bond stress of 30%. He suggested applying a head size reduction factor to the bond in order to estimate the bond stress at failure:

$$\chi = 1{,}0 - 0{,}7\left(\frac{A_n/A_b}{5{,}0}\right) \geqslant 0{,}3 \tag{1.18}$$

- The anchorage process consists of two stages. First, anchorage is carried almost entirely by bond stress. When it reaches its peak, the deterioration of the bond allows the stress to be transferred to the head. Final anchorage was achieved by peak head capacity and diminished bond capacity;
- The capacity was not improved by confinement, although it appears to help sustain bond stresses;
- Head shape and aspect ratio had no significant influence on capacity;
- Headed bars provide a feasible substitute for hooks;
- The limitation for stress in nodes imposed by code provisions may be conservative or even unnecessary.

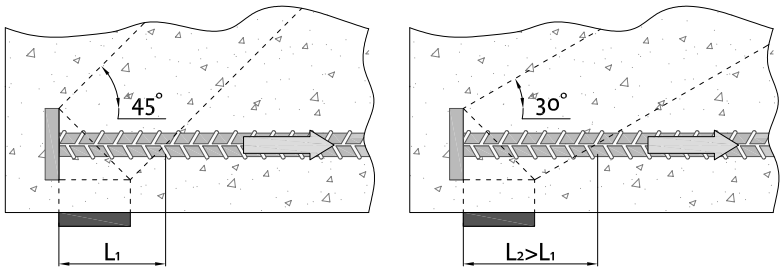

Figure 1.22: Influence of strut angle on development length

Regarding the second part of Thompson's work, 27 lap splice specimens were constructed and tested as represented schematically in Figure 1.23. The primary reinforcement was spliced at midspan of the slab, in the constant moment zone. The variables in the study were: relative head area A_{nh}/A_b (0,0 to 4,7), lap length l_d/d_b (3

to 14), bar spacing s_b/d_b (6 or 10) and others such as staggered or adjacent lap, debonded or bonded bars and confinement type. The following conclusions were drawn:

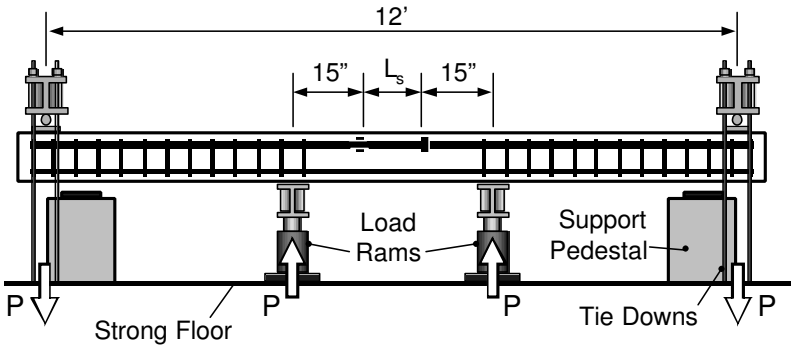

Figure 1.23: Setup of Thompson's lap splice tests [117]

- The stress is transferred by a strut acting on an anchorage length less than the lap length. The struts were observed to act at an angle of about 55 degrees, as shown in Figure 1.24a. Thus, the resultant equation for lap splices is:

$$L_s = L_a + s_b \tan 35° \tag{1.19}$$

- Less bond stress and greater head capacity are expected in case of epoxy coated bars;
- Smaller bar spacing results in reduced head capacity;
- Transverse confining bars over the splices (Figure 1.25b) provide the best confinement for lapped bars, with a significant improvement in capacity, while hairpins (Figure 1.25a) were less effective and did not change the fundamental mechanism of force transfer in the lap zone.

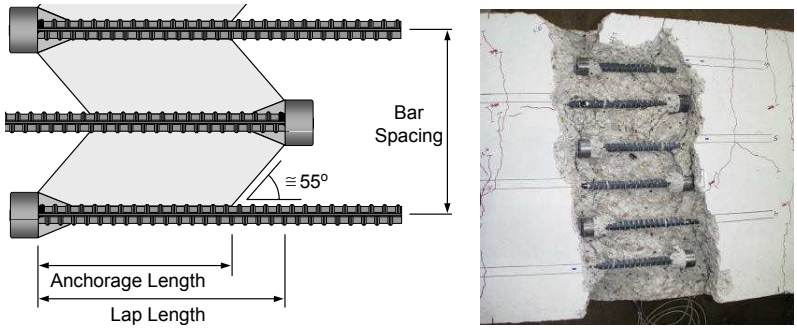

(a) *Strut model for lap splices* **(b)** *A tested specimen*

Figure 1.24: Strut model for lap splices. Source: [118]

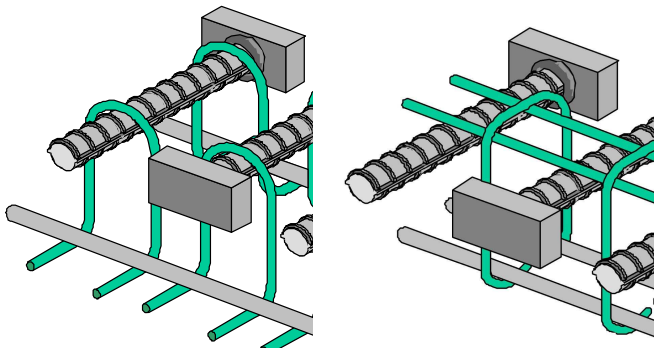

(a) *Harpin confinement*

(b) *Transverse tie-down confinement*

Figure 1.25: The two types of confinement details tested [117]

UNIVERSITY OF KANSAS STUDY Wright and McCabe [122] tested 70 beam-end specimens with single bars in each, with a setup similar to the one shown in Figure 1.6. The bars were non-hooked, hooked, or friction-welded headed bars. The work aimed at determining a formula for the development length of headed bars. Primary variables were: concrete cover (2 or 3 d_b), bar exposure (bar sheated or not) and transverse reinforcement, with the four different stirrup arrangement reported in Figure 1.26. Throughout the study the same bar diameter (25 mm), an embedment length of 12'' ($\simeq$ 30 cm) and the HRC's standard square head of 3×3 inches were used.

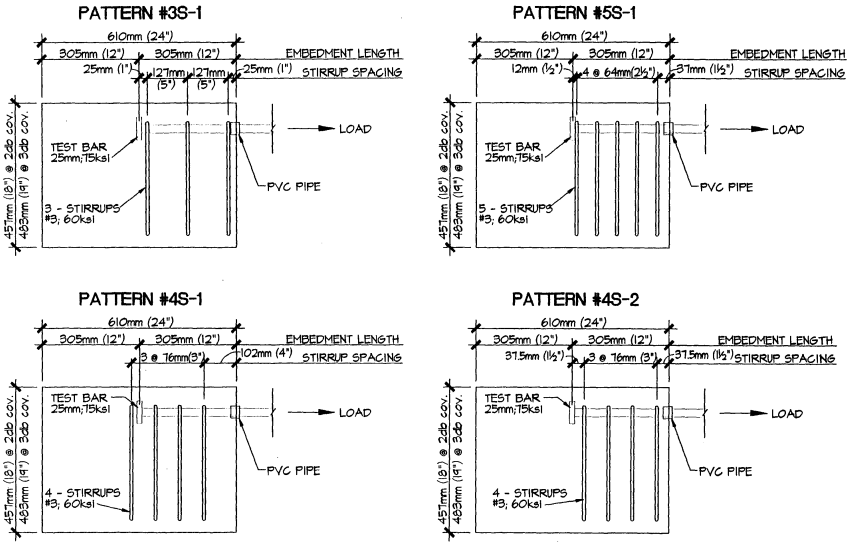

Figure 1.26: Stirrup spacing patterns [122]

The following conclusions were reported:

- Headed bars fail at equal or higher loads than hooked bars. Both exhibit similar behavior and are affected by the inclusion of transverse reinforcement in a similar way;

- An increase in cover increased ultimate capacity;
- The more transverse reinforcement was provided, the smaller was the increase in the ultimate load consequent to an increase in cover;
- A compression strut spread out by the head with a diffusion angle α. As the use of PVC sheating eliminates the wedging action of the bar, somehow it reduces the strut angle α, thus increasing the axial load capacity of the specimens. The use of transverse stirrups, which eliminate the lateral wedge forces, appear to lower the strut angle too. As the sheating and the stirrups fulfill the same function, the use of PVC covering is most effective in providing additional capacity when no transverse reinforcement is used (capacity increased by a 32% on specimens with 2 d_b cover)[23];
- The use of PVC sheating implies a significantly smaller amount of cracks associated with bond, improving the ability of concrete to carry forces by the head. On specimens with PVC sheating, if transverse reinforcement is used the additional capacity is approximately 26%, but the effect of additional cover on these bars is minimal;
- Stirrup configuration pattern #5S-1, the only one with two stirrups intersecting the strut (as shown in Figure 1.27), provided the highest average load capacity among all specimens with a 2 or 3 d_b. In the author's opinion, the closer a stirrup is placed to the head, the higher the ultimate load of the specimen.

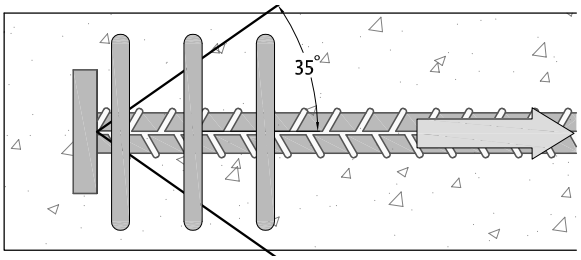

Figure 1.27: Strut-Tie Pattern of specimen #S1

[23]This statement is obviously in contrast with DeVries and Thompson's conclusions. The reason is that the set-up of Wright and McCabe's tests cannot be compared with the previous ones, since in the latter study the specimen ends abruptely after the bonded length, while in the former the presence of concrete after the bonded length guarantees a higher level of confinement: in fact, the deterioration of bond required by the anchorage process to transfer the stress to the head is materialized with a crack which starts at the face of the specimen and progresses towards the head. Hence, the lack of confinement in this zone can determine a greater damage and consequently a lower strength of the bearing mechanism. Equivalently, it can be stated in a more concise form that the embedment length provided seems not enough to classify these specimens within the *deep embedment* category.

Wright and McCabe also performed a regression analysis and provided a proposed code addition with a formula to calculate the development length of a headed bars similar to the one used for straight bars:

$$l_{dt} = 0{,}0116 \frac{f_y}{\sqrt{f'_c}} d_b (\alpha\beta\lambda\psi\delta) \geqslant \max(6d_b; 6 \text{ inches}) \tag{1.20}$$

Apart from the Greek letters, designed as different modification factors to be determined in future researches, this provision is essentially 60% of the existing ACI formula for hooked bars (Eq. 1.1). The authors also proposed a minimum concrete cover of $3d_b$ and gave a formula to determine the minimum amount of transverse reinforcement to be positioned within the development length if the concrete cover is less than $5d_b$.

1.2.4.2 *Joint tests*

KNEE JOINTS McConnell and Wallace [83] investigated the effects of confinement reinforcement, joint shear stress and anchorage type on the seismic performance of knee joint and compared the response to cyclic loading of joints constructed using T-headed bars or conventional reinforcement anchorages. A total of eighteen beam-column

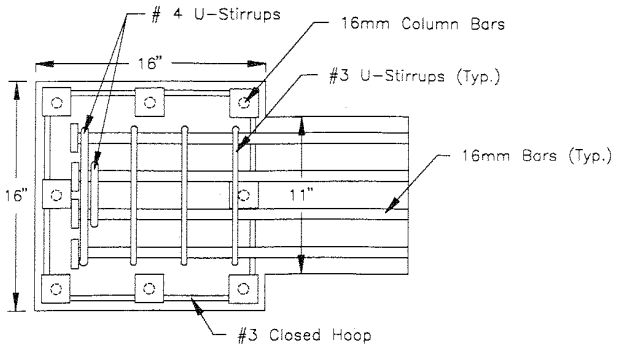

(a) *Plan View*

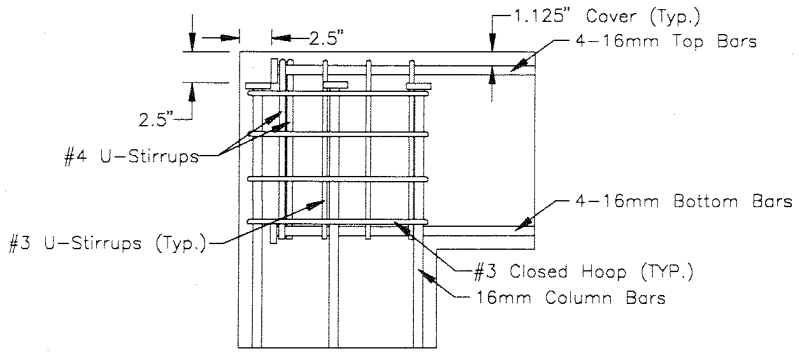

(b) *Elevation View*

Figure 1.28: Joint detailing for specimen KJ17 [83]

roof joints were tested under both opening and closing moments. The results indicated that the performance of joints constructed with headed bars is as good as, or superior to, similar joints with conventional hooked anchorages. The greater stiffness observed in specimens with headed reinforcement can be a consequence of the smaller slip in the anchorage experimented for headed reinforcement.

The use of mechanical reinforcement also alleviates congestion and makes placement easier, being a viable alternative to current construction practice. As can be observed in Figure 1.28, the presence of four vertical U-shaped stirrups has been noticed to be effective in restraining against the pullout of the upper bars of the beam and this practice is included within the design recommendations made by the author.

Ingham et al. [54] tested a bridge knee joint with headed reinforcement and concluded that the functionality of these details for regions where a limited embedment length is available was clearly demonstrated. In addition, the use of headed bars can favor a sound understanding of the force transfer mechanisms and the associated detailing requirements. The feasability for footings and column-footing connection was also demonstrated.

BEAM–COLUMN JOINTS Many authors followed the first behavioral study by Bashandy about applying headed reinforcement in beam-column joints. Some of them are presented in the following paragraphs.

Naito et al. [95] noted that the higher design requirements subsequent to the 1989 Loma-Prieta Earthquake could result in congested details. Aiming to improve constructability, they tested four subassembly large-sclae beam-column joints with headed longitudinal and transverse reinforcement under simulated seismic loading. The use of headed transverse reinforcement in the joint produced a behavior comparable to that of conventionally reinforced joints, while headed longitudinal column reinforcement experienced less slip.

Choi [27] tested 32 pullout specimens with relatively deeply embedded bars in reinforced concrete column-like members. The objective of the study was to determine the minimum embedment depth necessary for a safe design using headed bars. Concrete strength was 30,7 or 32,4 MPa while steel strength was 420 MPa. Small threaded heads ranging from 3,5 to 4,0 A_1/A_b were used. Other primary variables were the center-to-center distance between adjacent heads and the amount of supplementary reinforcement. The specimens were subjected to a concrete cone type failure as in the shallow embedment tests described in Paragraph 1.2.4.1. The tests revelead the following:

- A development length of $10d_b$ is not sufficient to fully develop closely installed headed bars;
- A group effect reduces the pullout strength of a individual headed bar if it is placed in a closely spaced bar group;

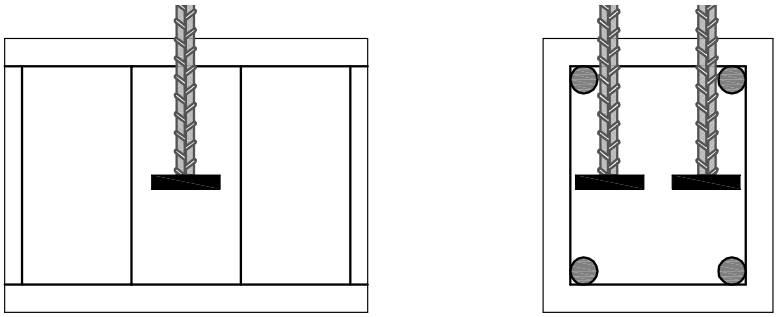

Figure 1.29: Setup of Dong-Uk Choi's Pullout tests

- The pullout strength increases with the use of supplementary transverse or main reinforcement;
- For center-to-center distance between adjacent heads less than $4{,}5d_b$ — the lower distance in Choi's tests — he recommended the use of a longitudinal reinforcement ratio $\rho_{sl} \geqslant 1\%$ and a transverse reinforcement ratio $\rho_{st} \geqslant 0{,}6\%$. Complying with these values, if the embedment depth is at least $13d_b$ a pullout strength over $1{,}25f_y$ and a ductile load-displacement behavior is guaranteed.

Chun and Kim [29] tested two sets of exterior beam-column joints with same geometric and material properties, one with 90 degrees standard hooks and the other with threaded headed bars, both tested against cyclic lateral loads applied to the beam, as shown in Figure 1.30. The behavior of the specimens was very similar and the mechanical anchor was shown to has enough anchorage capacity. In addition, the ductility ratio and the energy dissipation were better in specimens with mechanical anchorages.

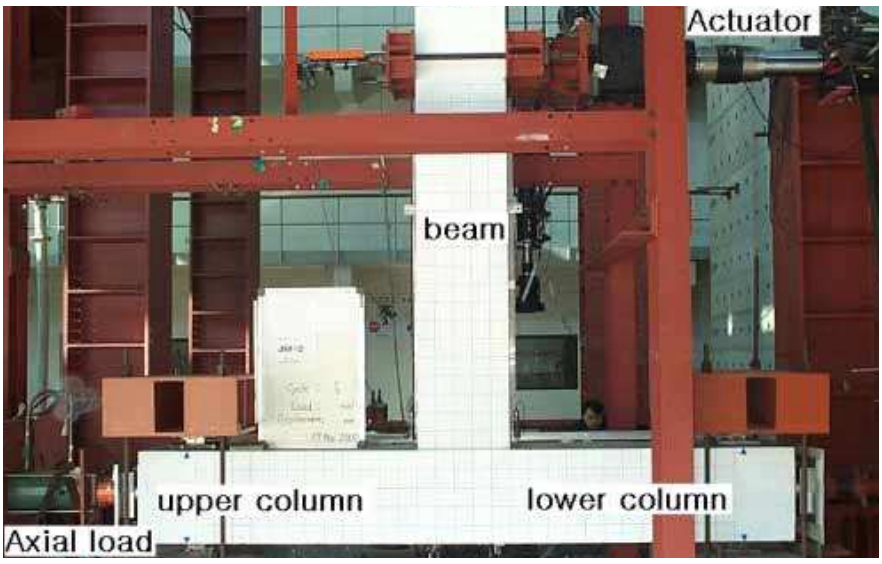

Figure 1.30: Test Setup [29]

Chun et al. [30] tested nine inter-story and five roof-level joint specimens under reversed cyclic loading. The results indicated that the hysteretic behavior of joints constructed with mechanical anchorages was equal or better than joints constructed with hooked bars.

Head size with a net area to bar area ratio between three and four was adequate to anchor the beam reinforcement effectively within the joint. The bond along the bar and bearing of the head contribute approximately equally to the anchorage capacity. The test results also indicate that transverse reinforcement is required throughout the joint to ensure that the joint strength is mantained after cracking. Furthermore, to provide improved behavior it is recommended to add vertical U-bars at roof joints and extend the heads on column bars beyond the beam top bars to avoid concrete spalling caused by top beam bars.

ACI 352R-02 recommendations are appropriate for the large diameters bar tested (#11 or 36 mm) and should be used instead of the recommendations of the ACI349-01 for Nuclear Safety-Related Concrete Structures, whose predicted capacities were less than 1/4 of the measured anchorage capacities.

CODE PROVISIONS FOR JOINTS DESIGN ACI 352R-02 [6] — Recommendations for Design of Beam-Column Connections in Monolithic Reinforced Concrete Structures — collected some previous results and reported the following recommendations about the use of mechanical anchorages:

- Headed bars (or hooked bars) should be located in the confined core within 2 in. (50 mm) from the back of the confined core[24];
- The development length l_{dt} of a headed bar should be taken as 3/4 of the value computed for hooked bars, l_{dh}, where, for non-seismic joints:

$$l_{dh} = \frac{f_y d_b}{4{,}2\sqrt{f'_c}}[\text{MPa}] \tag{1.21}$$

- Headed bars having a side cover less than $3d_b$ should be transversely restrained, the strength of the loop being at least half the yield strength of the bar (1/4 for non-seismic joints);
- Additionally, for Type 2 connections (seismic joints) with a discontinuous column[25], inverted U-bars along the top face of the joint should be provided in addition to hoops and crossties.

[24] "The tails of the hooks should face into the joint to promote the development of a diagonal compression strut within the joint, which is the main joint-resisting mechanism relied on."

[25] The usual case of discontinuous columns is at the roof level.

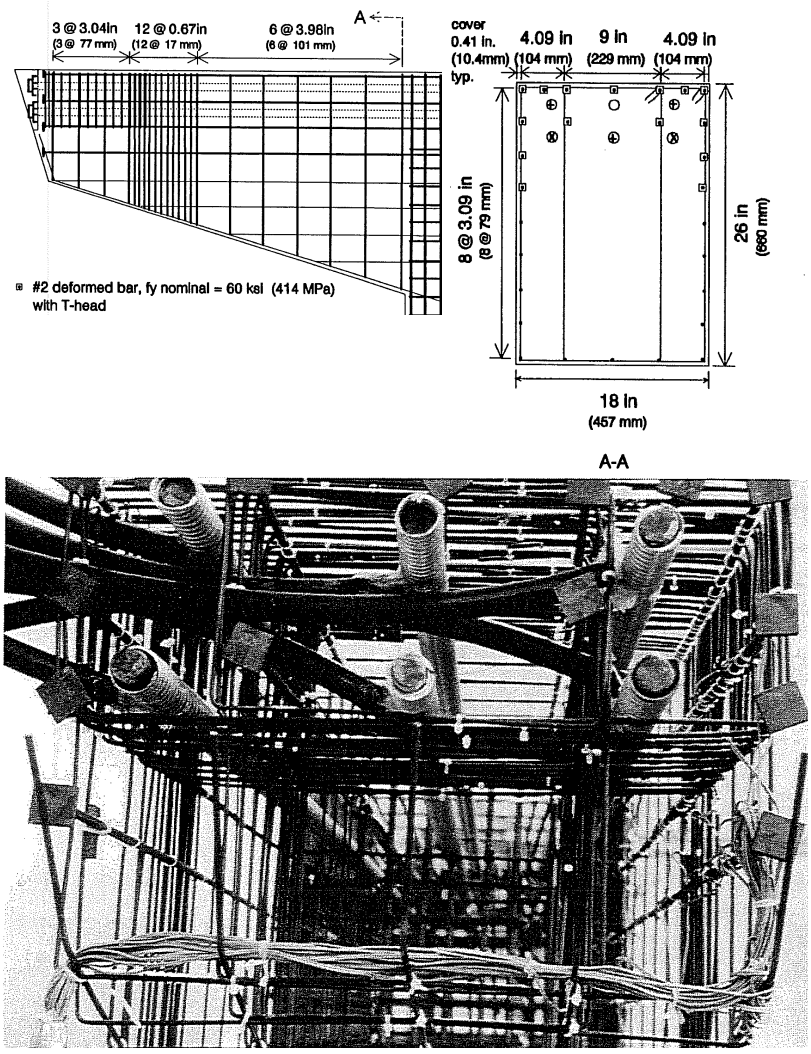

Figure 1.31: Reinforcing cage of a cap beam specimen [101]

The last two points refer to the already described tests performed by McConnell and Wallace [83] (see again Figure 1.28): the described confinement resulted in a performance as good as the one obtained with conventional reinforcement.

PIER CAP BEAM A pier is generally designed to support a deck that is wider than the pier, thus a cap is cast at the top of the pier to support the full width and to distribuite loads. A pier cap is a cantilever beam that can be subjected to high loads. In a work of Pereira [101], from the University of Texas, six cap beams with prestressed and mild reinforcement were tested under static loading using a mechanical anchorage for the main flexural reinforcement. The specimens were scaled down by a 5,5 factor and the reinforcement used in one of them can be seen in Figure 1.31. In this work, the author points out the following results about mechanical anchorages:

- Headed reinforcement bars improved significantly the constructability of the cages, reducing the construction time by at least 30%. Placement and tying were also improved. The author also asserts that congestion in anchorage was reduced by one half, although is not clear how this value was obtained.

- The behavior using either standard hooks or headed bars was practically the same. No improvement was noticed regarding crack control at service load levels.

The use of a precast bent cap supported by precast columns is also possible. Pullout tests of epoxy-coated[26] upset-headed bars[27] simulating typical grouted connections were conducted by Waggoner [119], from the University of Texas. Tests results showed that adequate anchorage can be achieved and that straight or headed reinforcing bars can be designed for use in grout pocket connections in a precast bent cap system. However, bars in a grout pocket are expected to achieve a capacity slightly smaller (approx. 20%) than cast-in-place bars, as noted by Matsumoto [81].

PILE-TO-DECK CONNECTIONS It can be argued that some of the beam-column joint tests shown in Section 1.2.4.2, for instance the one by Chun and Kim, are almost equivalent to other connection typologies described in this paragraph.

Earthquakes are a big concern for port structures, having both immediate and long-term consequences, as understood after Loma Prieta, Kobe and other seismic events. Particularly, the moment connection between the wharf deck and piles is often severely damaged by the horizontal loads generated during the seismic activity. The large economic investments and the large losses that can be generated as a result of shipping interruptions entail a big interest in improving the connection performance and mitigate the pile and deck damage resulting from seismic activity, especially in the common case of precast pile connections. These considerations can be easily extended to other cases of pier-to-deck and pile-to-foundation links.

As commented in a PEER[28] Report by Roeder et al. [104], early connections were designed employing dowel bars bent outward into the top of wharf deck oriented in a radial or orthogonal pattern (Figure 1.32a). This type of connection is still widely used in its multiple variations, altough some of them are infrequent, for instance, the outward orthogonal pattern of columns rebars is often preferred to the fan pattern, as the former also inhibits the placement of the wharf flexural reinforcement.

[26] The use of epoxy-coated bars is a typical choice in grouted connections, where the deterioration of the connection region may have major implications.

[27] The upset-headed bars are a HRC product with a A_1/A_b ratio of 1,4.

[28] Pacific Earthquake Engineering Research Group

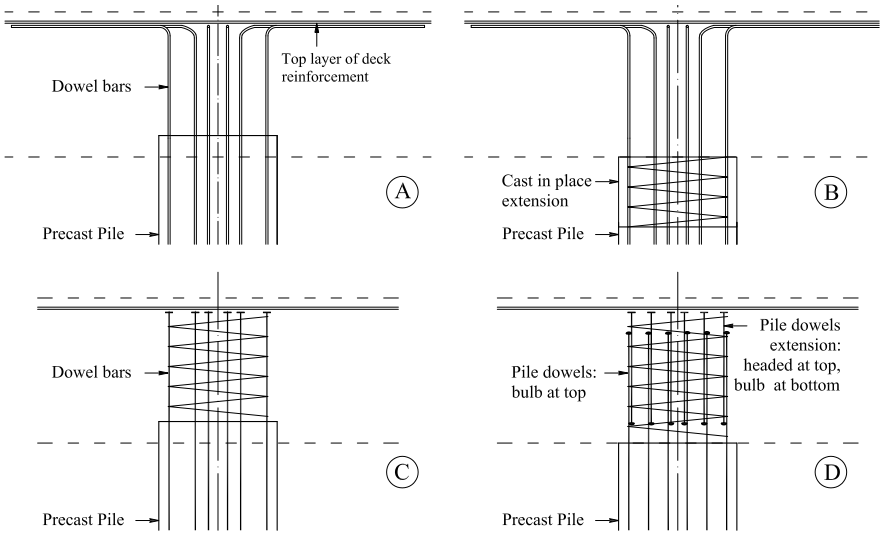

Figure 1.32: Some typical pile-deck connections: a) Dowel bars bent outward connection; b) Extended dowel bars bent outward connection; c) T-headed dowel bar connection; d) Bond bar connection. Redrawn from [104]

The extended dowel connection (Figure 1.32b) is similar to the previous one described, but in this case, instead of extending itself into the deck, the precast pile ends before. A short length is left to be cast in place and allows the positioning of a spiral reinforcement in order to confine the pile extension zone. Other connections, for instance the ones made with bond bars with bulbous ends (Figure 1.32d) or with headed bars (Figure 1.32c), concentrate the reinforcing bars into the connection zone and reduce the interference with the deck flexural reinforcement. In this zone it is also easier to employ spiral reinforcement.

Eight pile-wharf connections were tested at the University of Washington Structural Research Laboratory. Connection details exhibited significant differences in behavior, especially between precast pile connections and extended pile connections. The latter had better distribution of deformation and maximum local strains smaller than the outward connections. T-headed bar connections provided comparable performance to other connection types.

In another work from the University of Washington, four full-size specimens were tested under cyclic loading by Lehman et al. [70]. The specimens used were octogonal precast concrete piles with T-headed connections. The inelastic deformation was concentrated in a short zone, and a significant spalling of the pile and the deck due to the rocking[29] was observed, even with relatively small rotations.

The Controlled Rotation connection (or CR connection – see Figure 1.33) proposed resulted in significantly less damage to the pile

[29]Seismic response involving uplift of the major portion of the base.

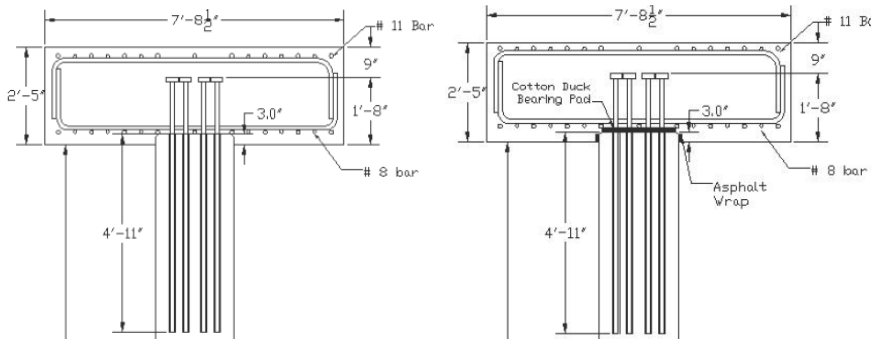

Figure 1.33: Reference specimen and CR connection [70]

and deck at given deformation levels. To achieve these results, two changes on the reference model were made:

1. the dowel bars were unbonded within the connection for 375 mm, allowing to extend the length of yielding of the bars in the connection;

2. a cotton duck bearing pad (CDP) — an elastomeric pad consisting of thin layers of elastomer interlaid with closely spaced layers of cotton duck fabric — strong in compression but more deformable than concrete, was employed at the interface with the pier to reduce the edge loading on the pile and consequently the spalling, improving the overall performance of the system with its significant shear capacity[30] [68].

1.2.4.3 *Shear tests*

As already discussed in Section 1.2.1 the first shear tests on mechanical reinforcements were conducted by Dilger and Ghali aiming to substitute the conventional single-leg stirrups with double headed studs, as illustrated in Figure 1.34. In their 1997 paper [37], they tested five column specimens — representing reduced size walls — in order to compare the effectiveness of small size double-headed reinforcement against cross ties. They found that the anchorage of the crossties was not sufficient to develop yield stress in the ties, while double-headed studs exhibited large strains beyond yield at failure load of the column. Columns and walls exhibit more ductile behavior and higher ultimate strength when double heads are used to replace conventional crossties.

Other authors investigated this possibility, for instance, Bashandy reported in his dissertation [14] that Collins and Gupta tested 14 beams subjected to shear and high compression, up to $0{,}9f'_c$ in a study

[30] CDPs tolerate limited shear deformation, howeve, since a significant translational capacity is often needed, a polytetrafluorethylene (PTFE) sliding surface is placed at the top of the bearing in order to avoid the rupture of the CDP due to friction or the transmission of higher moments and forces to the column.

(a) *The conventional and double-headed bars detailing in a slab*

(b) *Wall of a nuclear waste containment structure*

Figure 1.34: Use of headed bars in walls and slabs [53]

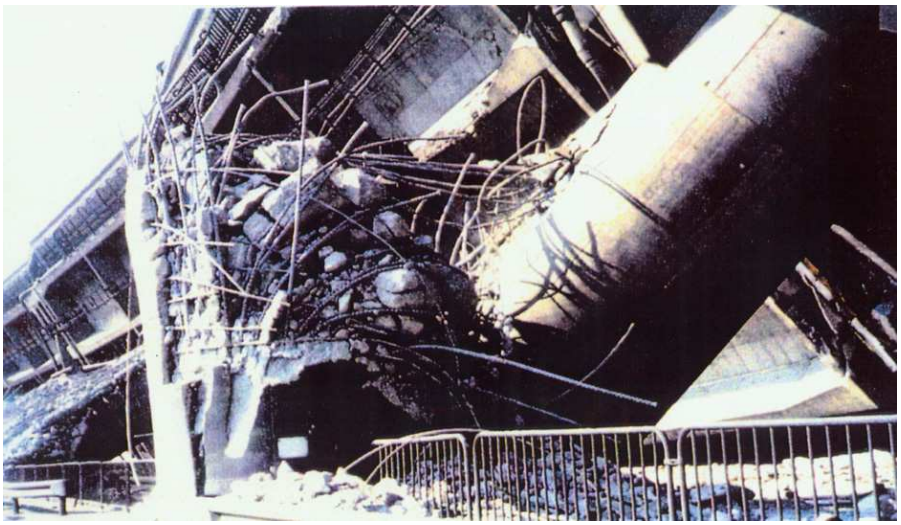

Figure 1.35: Shear failure of a RC column in the 18-span Fukae Viaduct. Courtesy of Center for Advanced Engineering Structural Assessment and Research, Japan.

sponsored by Metalock. Some specimens had no shear reinforcement, while others had standard 90° stirrups or headed reinforcement bars used for shear reinforcement. Headed stirrups were more effective restraining the longitudinal steel against buckling, that is, at large strain levels the 90° hooks opened.

Jakobsen et al. [56] performed full scale tests on a tricell wall after the failure of Sleipner A platform. Of the ten specimens tested, seven were reinforced as in Sleipner A, one with elongated T-headed bars in the haunch, while two specimens were changed according to the new design of Sleipner A2 (a more extensive description is provided in Section 2.2.1).

After the Hyogo-ken Nanbu earthquake in 1996, also known as Great Hanshin earhquake or Kobe earthquake, much research was done worldwide about the causes of the registered collapsed structures across the city (see Figure 1.35) and the premature flexural-shear

failure near the column midheight resulted the main cause of the collapse of bridges along the Hanshin expressway. This was the consequence of the pre-1996 design specifications that led to splice the reinforcement at midheight with a short development length. The revised Japanese design code increased the amount of shear reinforcement for civil structures, and consequently the congested arrangement produced by the new specifications aroused interest in plate-anchored reinforcements. The generalized use of high-strength concrete, by which the column sections become smaller and wall paneling structures or beam-column connections present overcrowded arrangements, is another factor favoring the widespread use of headed bars.

Shioya et al. [109], from Shimizu Corporation and Dai-ichi High Frequency Company, conducted shear, flexure and compressive tests using T-headed bars. The shear capacity of the beam using T-headed stirrups was almost the same as the one with 180° hook sitirrups. The same conclusion can be drawn for the flexural capacity and the compressive test results.

Kim et al. [64] constructed four beam-like specimens — see Figure 1.36 — representing a heavily reinforced concrete portion of a wall used in civil construction and tested them with repeated loading. The two specimens with standard 90° stirrups were not able to develop strains much above yielding as a a consequence of the anchorage loss due to splitting and crushing of concrete. On the contrary, the two other specimens using double headed reinforcement were able to develop strain hardening in the stirrups. The heads were also useful in delaying the buckling of the main reinforcement. Comparing the two typologies, the one with headed stirrups dissipated a significantly greater amount of energy and showed a greater residual strength after the maximum load had been reached.

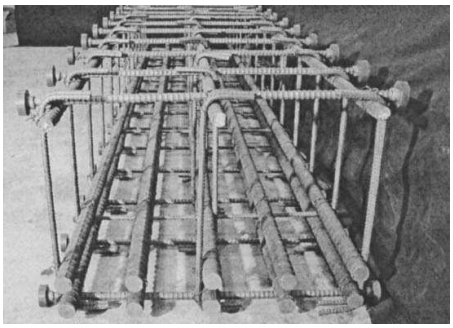

Figure 1.36: Section detail of one specimen [64]

In another article by Japanese professionals Yoshitake et al. [124], two issues related to railway structures were tackled. Flexural tests with high shear reinforcement ratio and fatigue tests were carried out to verify the sufficiency of headed reinforcement bars as shear reinforcement under both conditions. The first series of tests resulted in an equivalent performance of the two details, while the fatigue performances of lapped headed bars and the U-shaped headed bars was shown to be superior to the one of semicircular

hooks, which in the author's opinion proves the safety of structures using this technique against the railway loads.

Headed bars used as shear reinforcement also act as a good confinement in columns and wall elements subjected to axial loading, as shown experimentally in 2013 by Mitchell et al. [89], although further research on reversed cyclic loading is needed.

1.2.4.4 *Rehabilitation and retrofit studies*

Earthquake damaged bridge columns may require repair or replacement of damaged regions. Various repair schemes were evaluated by Lehman et al. [69] in an experimental program in which four columns were tested. Three of them with longitudinal reinforcement ratios of 0,75%, 1,5% and 3,0% were previously severly damaged. Repairs used headed reinforcement, mechanical couplers and newly cast concrete. The repair schemes were considered successful and proved the potential of mechanical reinforcement to be used for seismic rehabilitation.

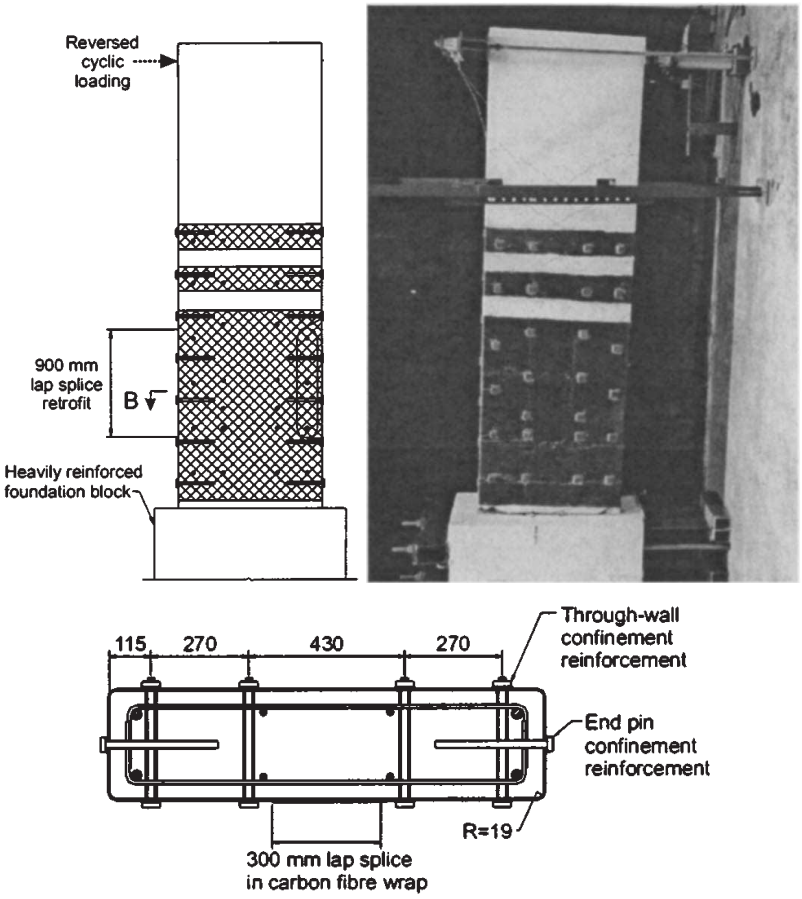

Figure 1.37: Retrofit details of a tested specimen [100]

In another work of Paterson and Mitchell [100], a series of four shear wall specimens was tested in order to determine the effective-

ness of the combined use of headed reinforcement bars for a concrete collar at the base of a specimen and carbon fiber wrap (see Figure 1.37), in order to improve the overall ductility of poorly detailed walls. The combination was shown to be effective in increasing both the anchorage of the transverse reinforcement and the confinement of the wall boundary regions.

1.2.4.5 *Prefabrication*

As seen in Section 1.2.4.2 prefabrication is a field suitable for the use of reinforcement bars anchored by plates. The use of headed bars for lap splices seen in Paragraph 1.2.4.1, for instance, is also suitable for precast panels in which the cast-in-place closure strips can be reduced by the same measure in which the anchorage length needed is shortened by using headed rebars. The use of headed reinforcement is also suitable in *in situ* staged excavation processes in which the whole work is subdivided into many trenches in order to execute the task in a gradual way, usually for security reasons. To guarantee the connection between parts a temporary void has to be left, and mechanical anchorages make this part smaller increasing the process speed and enabling greater freedom of movement.

Another application case in this field can be the design of precast columns with a corbel/bracket, in which the tie bars may not be anchored properly within the space available, given the reduced corbel depth.

Double-headed bars can also be used for confining reinforcement of post tensioning cables, reducing at the same time the vibration and potential concreting defects which may arise from the use of conventional hairpins or spiral reinforcement.

1.2.5 Code provisions

Plate-anchored reinforcement bars achieve anchorage by a combination of bond along the straight portion of the bar and bearing of the plate on concrete. Codes recognize this behavior but usually they limit their provisions to full size heads, being quite vague about the reduced size heads.

1.2.5.1 *ACI 318-08*

In paragraph 12.6 — *Development of headed and mechanically anchored deformed bars in tension* — a formula for the development length of headed bars in tension, l_{dt}, is provided[31]:

$$l_{dt} = 0{,}016 \, \frac{\psi_e f_y}{\sqrt{f'_c}} d_b \geqslant \max(8 \; d_b; 6 \text{ inches or } 152{,}4 \text{ mm}) \quad (1.22)$$

[31] The coefficient is 0,192 if using SI units (MPa and mm).

This length is the 80% of the development length of a standard hook in tension, l_{dh} (see Paragraph 1.1.3.1). ψ_e is an amplification factor which takes into account the influence of epoxy-coated reinforcement. A series of additional conditions have to be respected when using headed bars:

- f_y shall not exceed 60 000 psi (413,7 MPa);
- Bar size shall not exceed #11 ($\simeq \phi 35$);
- Concrete shall be normalweight;
- Net bearing area of head A_{brg} shall not be less than $4A_b$;
- Clear cover for bar shall not be less than $2d_b$;
- Clear spacing between bars shall not be less than $4d_b$.

These restrictions are a consequence of the empirical character of the formulation which is based on a limited number of tests. This type of formulation does not allow extrapolation outside the tested ranges of the parameters without significant risk of over-predicting resistance.

The word *development* in the previous paragraph describes cases in which the force in the bar is transferred to the concrete through a combination of a bearing force at the head and bond forces along the bar. If the force in the bar is transferred through bearing to the concrete at the head alone, design requirements are the same given for anchors in Appendix D (paragraph D.5.4.1.). The maximum side-face blowout strength of an anchor is based on reccomendations by Furche and Eligehausen [44] (equation 1.26 in Section 1.3.1.1).

ON THE CURRENT LIMITATIONS ASTM A970 [7] standard specifications state that "the head is intended to be sized so as to provide an anchorage capable of resisting the nominal tensile strength of the bar by the head". Additionally, designers should check that "the steel and concrete stresses are not excessive for the loadings, and that the detailing of the connection is consistent with the intended usage".

These general concepts are in contrast with a head size specification, as included in 1997 edition of the standard. The minimum size specification ($A_1/A_b \geqslant 10$) was considered by Thompson [117] as controversial: indeed, the determination of the head size should be carried out by structural engineers since a specific dimension cannot be adequate for all possible applications, or, if it were, it would be over-conservative in many cases.

In order to clarify the ideas outlined above, a summary of the ongoing research that deals with expanding the boundary of the current ACI formulation is presented:

- Experiments with lap splices anchored by high-strength headed bars ($f_y = 600$ MPa) were conducted by Chun and Lee [28]

in order to investigate their anchorage behavior. The products used for the experiments were provided by the Korean company Boowon B.M.S. The threaded heads, known as *BMS-Terminator*, have a net head area four times the bar area[32]. They concluded that current design provisions do not give a conservative result for high-strength reinforcing bars, especially, without transverse reinforcement.

- No guidance is provided for bars larger than #11. Mihaylov et al. [87] tested and evaluated the behavior of a large deep beam[33] without stirrups, reinforced with a single #18 bar ($\phi \simeq 57$ mm) in comparison to the behavior of a more conventional specimen with six #8 bars.

  Clear cover was 110 mm, almost $2d_b$ (114 mm) as required by ACI. The beam failed in shear before yielding, due to the bond degradation caused by splitting cracks, after which the head began to carry load. At failure, the 88% of the total force was carried by the head. The plate diameter was 180 mm, resulting in a A_1/A_b ratio of 10.

  They concluded that despite the extreme detailing of the specimen with a single bar, the test with the large bar performed similarly to the others, which demonstrates that anchor heads are effective even for bar sizes larger than #11.

- The assumption that plate area should be greater than five times the bar area ($A_1/A_b \geqslant 5{,}0$) motivated the already cited experimental campaigns performed by Choi [27] (see Section 1.2.4.2), in which threaded heads with plate area ranging from 3,5 to 4,0 A_b were used and yielding of the rebars was achieved.

  Kang et al. [62] performed 12 pullout tests and two full-scale exterior beam-column joints. Headed bars with small heads (A_1/A_b from 3,6 to 3,8) were used. Tests showed a satisfactory anchorage behavior even after significant bond deterioration, although the clear cover and the bar spacing tested were $3{,}6d_b$ and $4{,}2d_b$, respectively, greater than the required minimum values ($2{,}0d_b$ and $4{,}0d_b$). Hence, the author concluded that "additional research would be needed to assess current restrictions on such parameters".

[32] Personal correspondence between the author, PhD candidate at Polytechnic University of Madrid, and Dr. Sung Chul Chun, Assistant Professor at Mokpo National University.

[33] A deep beam is a beam with a relatively small span-to-depth ratio, whose behavior is dominated by shear deformations. It carries most of the load by direct diagonal compression between the loading and support points, as in arch (or strut) action. The longitudinal reinforcement develops almost constant tension from support to support and almost the total anchorage force must be provided by the head at failure.

- In order to mobilize bond resistance, ACI requires that the clear spacing between headed bars be not less than $4d_b$. Moreover, in case of parallel non-headed bundled bars, paragraph 7.6.6.5 states: "Where spacing limitations or concrete cover requirements are based on bar diameter, d_b, a unit of bundled bars shall be treated as a single bar of a diameter derived from the equivalent total area". Therefore, a group of four bundled bars should have a clear spacing equal to twice that of a single bar.

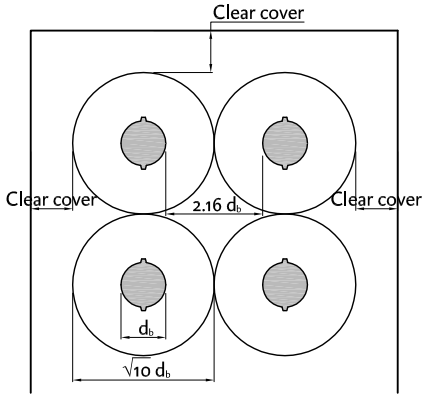

Figure 1.38: A group of four bundled bars

Ghali and Gayed [48] have shown experimentally that if the anchorage relies exclusively on bearing, in a group of 3 or 4 bundled headed bars the heads can be in contact, that is, with a clear spacing of only $2{,}16d_b$ (as drawn in Figure 1.38), since the maximum stress in the ties exceeded the nominal yield stress value in the two beams and the two corbels tested.

1.2.5.2 *Model Code 2010*

Model Code 2010 establishes two different approaches:

- If the full capacity must be provided entirely by the head, a minimum diameter of $3{,}0d_b$ and a minimum clear cover from the end of the plate of $2{,}0d_b$ are required. Other requests include a spacing between bar centers not less than $6{,}0d_b$ and $f_{cd} > f_{yd}/24$.
- If the reinforcement is anchored by a combination of bond along the bar and bearing on the plate, then the anchorage capacity can be evaluated in one of the following ways:
  - Determining it by laboratory tests;
  - As the capacity of the head alone, neglecting any contribution from bonding (this is a conservative approach);
  - As if it were a bar terminated by a hook or bend, providing that the net-projected area of the head is equal to that of a standard bend.

> In all cases the head must have sufficient embedment to avoid a premature concrete cone-type failure. These provisions seem to provide good design rules but they do not provide guidance on situations in which the limiting parameters cannot be fulfilled. There is therefore a need to develop a general model which can be applied to specific design situations.

1.2.5.3 *Eurocode*

The Eurocode has no section regarding the use of plate-anchored reinforcement.

1.3 BACKGROUND ON RELATED TOPICS

1.3.1 Headed anchor bolts

Several studies on anchorage behavior of deeply embedded anchor bolts have been published. In the 1960's Lee and Breen [66] performed a limited study on six factors affecting the development of high strength anchor bolts. They found out that concrete cover and concrete strength were primary variables affecting ultimate strength and behavior, while the geometry of the concrete surrounding the anchors did not significantly affect ultimate strength or slip. Most of the specimens failed in the splitting failure mode, as shown in Figure 1.39.

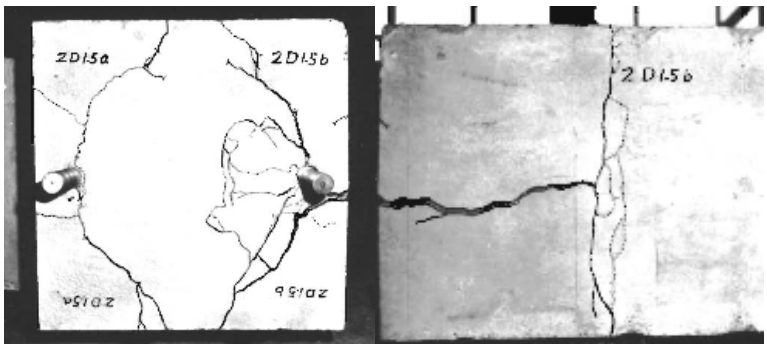

Figure 1.39: Splitting failure [66]

Some years later, using similar specimens Hasselwander et al. [49] observed a similar behavior. They also considered the bearing area of the head among the primary variables affecting bolt capacity. Furthermore, they found out that transverse reinforcement provides lateral restraint once cover splits away from the bolt, improving the strength and ductility in anchor bolts with small cover. The proposed equation was based on 48 pullout tests on anchors in heavily reinforced concrete specimens:

$$N_u = 140\, A_n \sqrt{f'_c} \left[0{,}7 + \ln\left(\frac{2c}{d_s - d_b}\right)\right] \tag{1.23}$$

Furche and Eligehausen [44] observed that concrete breakout or side blowout were the two principal concrete-related failure modes. According to their study, the expected failure mode can be inferred on the basis of two parameters: the cover to embedment depth ratio (c_1/h_d) and the embedment depth to net area ratio (h_d/A_n). This delimitates three different behaviors:

1. When c_1/h_d is large in relation to h_d/A_n, a concrete breakout failure is expected. That is the case of the shallow embedment headed anchors, which fail by formation of a breakout cone as represented in Figure 1.17a;

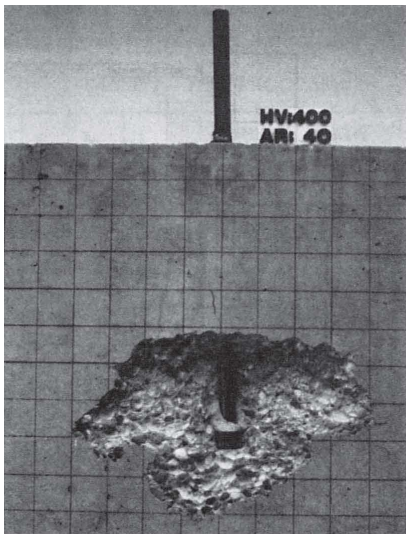

Figure 1.40: Typical local blowout failure at the side of the specimen [44]

2. When the opposite occurs, as in the case of deep embedment headed anchors, the expected failure mode is side spalling of the concrete, or what is known as side blow-out failure. A typical blow-out failure is depicted in Figure 1.40;

3. Finally, a splitting of the concrete member can be expected if the member dimensions are too small.

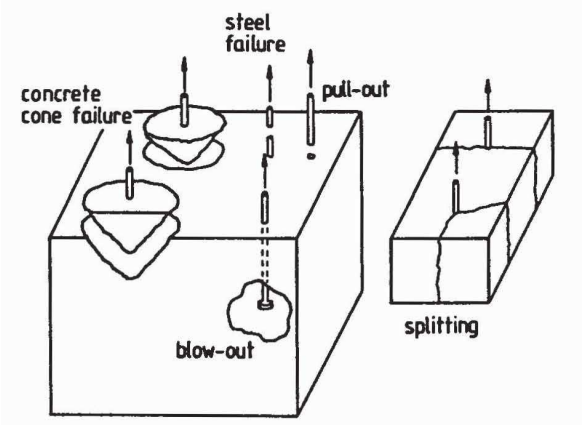

Figure 1.41: Failure modes of a single fastening [44]

Other possible failure modes are by rupture of the steel or by anchor pullout, with all possibilities represented in Figure 1.41.

1.3.1.1 *Formulas and code provisions for headed bolt*

Side blowout failure governs concrete capacity when the side cover is small and the embedment depth is large if compared to the edge distance. Otherwise a concrete cone breakout failure can be expected. For instance, CEB [8] proposed that for an edge distance greater than

half the embedment depth "it may be assumed that a local blowout failure will not occur".

Many authors proposed formulas to estimate the blowout capacity through an approximation of the bursting force at failure. Furche and Eligehausen, who performed tests on single headed studs[34], suggested [44] describing the average test results with the formula:

$$N_u = 31\ c_1 {A_n}^{1/3} {f_{cc,200}}^{2/3} \tag{1.24}$$

where c_1 denotes the side cover to the free edge, A_n is the net bearing area of the head $\left(a_1 b_1 - \pi {d_b}^2/4\right)$ and $f_{cc,200}$ is the concrete compressive strength measured in a 200 mm cube. For an anchor group, in case of small spacing, the estimated failure surfaces can overlap.

They also argued that the influence of the net bearing area was underestimated and the concrete tensile strength is generally taken as a function of the square root of the concrete compressive strength. Consequently, they performed a new regression analysis. From this analysis, the following formula emerged:

$$N_u = 16{,}8\ c_1 \sqrt{A_n f_{cc,200}} \tag{1.25}$$

Assuming that the blowout capacity can be modeled, taking into account stochastic variability, by a normal law, for a 5% fractile a characteristic design value can be defined, given by the following formula:

$$N_u = 13{,}4\ c_1 \sqrt{A_n f_{cc,200}} \tag{1.26}$$

although in a subsequent book by the same author [39], the coefficient in Equations 1.24 and 1.25 became respectively 27 and 15.

Hofmann and Eligehausen [51] performed extensive numerical investigations with edge anchors, corner anchors and with multiple anchors along a free edge. They proposed the formula:

$$N_u = 18{,}5\ {c_1}^{0{,}75} {A_n}^{0{,}5} {f_{cc,200}}^{0{,}75} \tag{1.27}$$

The general formula proposed by the CEB guide for fastenings [8] (§2.1.2.6) has a similar structure to the ones used for other failure modes. The characteristic resistance of a single anchor or a row of anchors due to a local blowout failure, $N_{Rk,cb}$, is:

$$N_{Rk,cb} = N^0_{Rk,cb}\ \Psi_{A,Nb}\ \Psi_{s,Nb}\ \Psi_{ec,Nb}\ \Psi_{ucr,Nb} \tag{1.28}$$

in which:

$N^0_{Rk,cb}$ is the characteristic resistance of a single anchor, estimated as $8\ c_1 d_b {f_{ck}}^{0{,}5}$;

[34] The experimental basis used to obtain these formulas is not clear. The authors inform that in the experimental investigation 35 studs were tested, of which 28 resulted in blowout failure. However, from this source DeVries reported only 20 tests. Furthermore, in the evaluation of the test results, a total of 51 tests with blowout failure was considered available but, as in the first case, the data were not reported.

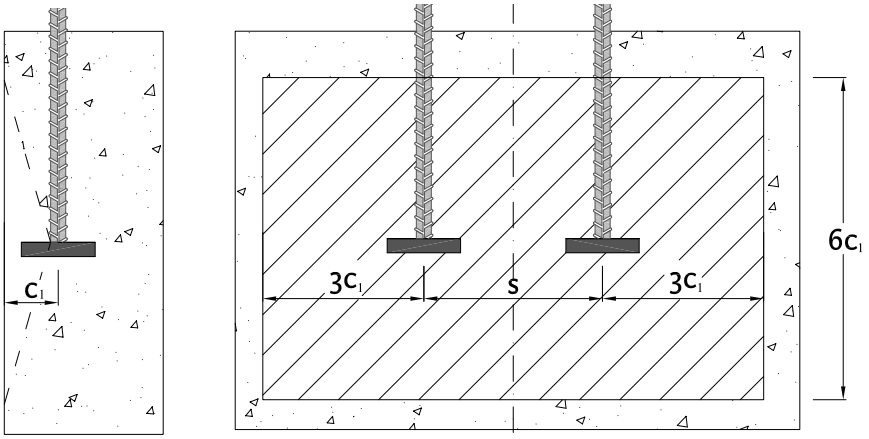

(a) *Side view*

(b) *Two anchors at the edge:* $s \leqslant 6c_1$

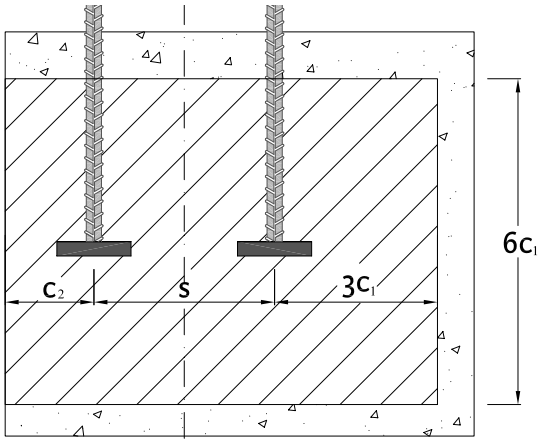

(c) *Two anchors at a corner:* $s \leqslant 6c_1$ *and* $c_2 \leqslant 3c_1$

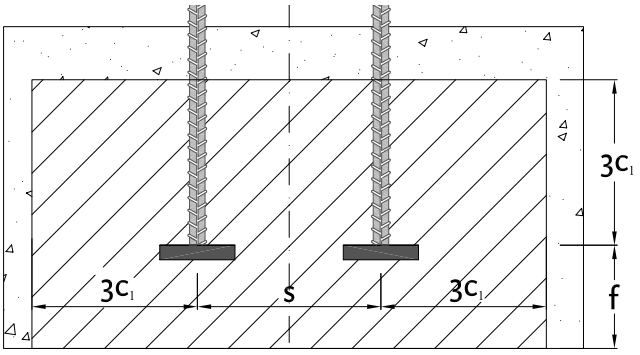

(d) *Two anchors in a thin member:* $s \leqslant 6c_1$ *and* $f \leqslant 3c_1$

Figure 1.42: Actual areas of idealized concrete cones for anchors loaded in tension

$\Psi_{A,Nb}$ is an amplifying factor which takes into account the possibility of an overlapped failure surface, calculated as the ratio $\frac{A_{c,Nb}}{A^0_{c,Nb}}$ in which $A^0_{c,Nb}$ is the area of concrete cone of a single anchor[35] and $A_{c,Nb}$ is the actual concrete cone area, computed as in Figure 1.42;

$\Psi_{s,Nb}$ is a reduction factor for corner positioning:

$$\Psi_{s,Nb} = 0{,}7 + 0{,}3\frac{c_2}{3c_1} \leqslant 1{,}0 \tag{1.29}$$

$\Psi_{ec,Nb}$ is a reduction factor which allows for the consideration of the group effect when different tension loads are acting on the anchors, e_N being the eccentricity of the resulting tension force with respect to the center of gravity of the anchors:

$$\Psi_{ec,Nb} = \frac{1}{1 + 2e_N/6c_1} \tag{1.30}$$

$\Psi_{ucr,Nb}$ is an amplifying factor for fastenings in non-cracked concrete, equal to 1,4.

As already pointed out in Section 1.2.4.1, the correction factors used in DeVries' formula are taken from the CEB bulletin, while the basic capacity of the anchor is estimated by means of a slightly modified version of Equation 1.25.

1.3.2 Bearing strength of concrete

The bearing action resembles very much the behavior of the bearing action of a plate embedded in a concrete block. Therefore it seems interesting to review some notable research on this topic.

Hawkins [50] and Niyogi [97, 98] performed hundreds of tests on concrete cubes and cilinders with many specimens of different sizes and shapes, plate sizes and shapes, concentric or eccentric loading, and others. The failure is originated by splitting stresses caused by a crushed paste concrete wedge formed below the load plate, as shown in Figure 1.43. Hawkins recognized this behavior and developed approximate theoretical expressions for bearing strength, while Niyogi recommended an empirical expression. They both provided design equations based on the analysis of experimental data: Hawkins used both f_c and $\sqrt{f_c}$, Niyogi used only f_c. While Hawkins recommended an effective area to be concentric with the loaded area, Niyogi noted that the bearing capacity of eccentrically loaded blocks was greater than the capacity predicted using a concentric reduced area.

[35] $A^0_{c,Nb} = 36{c_1}^2$ according to Furche and Eligehausen's experimental observations [44].

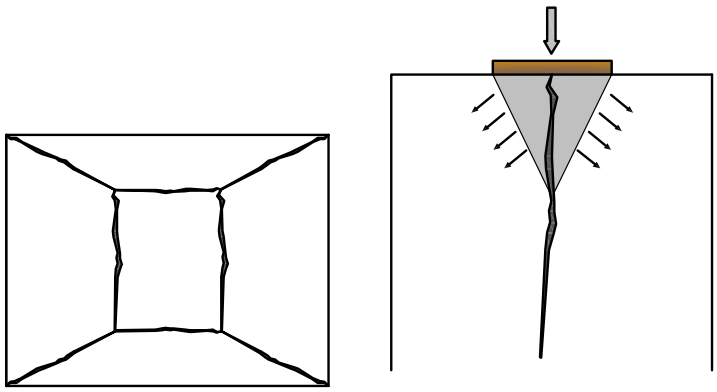

(a) *Top view* **(b)** *Front view*

Figure 1.43: Bearing failure as observed in tests

In 1979 Williams [121] carried out an extensive experimental campaign and collected data from other authors, including both Niyogi and Hawkins. He concluded that for the specimens exhibiting bearing failures the best-fit equation is:

$$f_{cb} = 6{,}92\, f_{ct} \left(\frac{A_1}{A_e}\right)^{-0{,}47} \tag{1.31}$$

while the greatest lower bound curve is:

$$f_{cb} = 3{,}3\, f_{ct} \left(\frac{A_1}{A_e}\right)^{-0{,}5} \tag{1.32}$$

where A_e is the effective area, concentric to the applied load. He argued that the capacity was determined by the resistance of the specimens to splitting, rather than by compressive strength.

1.3.3 Ends of prestressed concrete beams

Many researchers have been investigating this topic since the middle of the 20th century, when after the World War II the high price of steel gave rise to the development of the prestressed concrete technique that had been patented by Eugène Freyssinet in 1928.

The first study about the stress distribution in a concrete block was developed in 1924 by Mörsch [92], who used a truss analogy to find the stresses in eccentrically loaded concrete blocks. Mörsch's approach is part of a group of analytical procedures referred to as the *simplified methods*, which use an equilibrium approach in combination of some approximate assumptions and provide a relatively accurate and simple solution.

Magnel [77] — who also developed his own prestressing system — proposed an approximate solution to calculate stresses in the anchorage zone of a post-tensioned beam, assuming that the distribution of

transverse stresses can be represented by a cubic parabola, as shown in Figure 1.44. The procedure is lengthy because it implies the calculation of the tension principal stresses in each point.

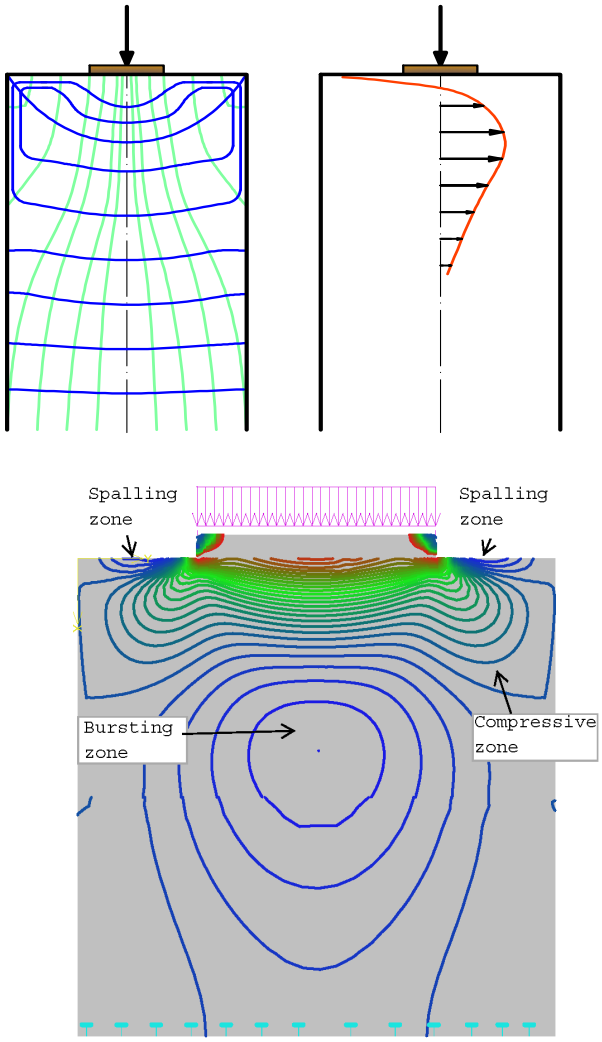

Figure 1.44: Left: tensile and compressive stress trajectories; Right: bursting forces along beam axis; Bottom: Stresses normal to the force (contour lines obtained with a FEM software)

For bidimensional problems, photoelasticity was used in order to obtain experimentally the elastic stress distributions through direct measurement, using the property known as birefringence or double refraction[36]. As explained by Fernández Casado in a 1932 divulgative paper [41], at that time the first useful results were being obtained at Laboratories in Paris and Zurich. He also stated that this was the only method capable of analyzing structures exhibiting geometric complexity and he described the diffusion of concentrated forces in a concrete block as a problem which could be solved by this technique.

[36]The decomposition of a ray of light into two rays when it passes through a material.

In the 1940's and 1950's great emphasis was placed on elastic methods of analysis and design, often based on the two-dimensional Airy stress function[37], which satisfies equilibrium in the absence of body forces with a scalar potential function used to find the stress tensor. The envelope of the tangent direction to the principal stresses in each point of a body defines the isostatic lines, a family of curves with mutual orthogonality. Procedures of this type were developed by Guyon, Douglas, Sleech, Trahair among others, as cited by Leonhardt and Mönnig [72], but a rigourous solution for simply supported rectangular plates was found only in 1969 by Iyengar and Prabhakara [55], using a Galerkin vector approach, the components being expressed as double Fourier series chosen to satisfy boundary conditions. Abeles et al. [10] made a review of the existing methods. According to them, "Mörsch's method appears to be the simplest solution".

In 1958, Base [13], who was aiming to determine the variability of transmission length, collected data about the longitudinal deformations as a function of the end distance. He observed that deformed sections were not plane, but they were at a distance slightly greater than the section depth, that is, Saint-Venant hypothesis was met with surprising accuracy.

Field studies and laboratory investigations reported longitudinal cracks in the anchorage zones of prestressed concrete beams and this motivated investigations such as the one carried out by Welsh and Sozen [120]. According to these investigations, cracks in anchorage zones result from the transverse tensile stresses produced as the prestressing force *flows* from the load application region to the zone in which the stresses are linearly distributed (see again Figure 1.44). Two zones have been identified as prone to cracking:

THE BURSTING STRESS ZONE, situated at a short distance from the beam end, on the axis of the applied force;

THE SPALLING ZONE, situated on the end face of the beam at some distance from the axis of the applied force, in the supposedly "dead vertices".

While a formation of a bursting crack generally occurs simultaneously with the failure of the anchorage zone, spalling cracks are not detrimental as long as transverse reinfocement is present and the width and the extension of the crack is limited. Transverse reinforcement has also been used to postpone the formation of bursting cracks.

Finally, there is a third zone in which a failure can be expected: the contact zone between the plate and the concrete where high pressure is acting. If the body is protected against bursting stresses[38], a

[37] The Airy stress function φ is biharmonic: $\nabla^4 \varphi = 0$.

[38] This may be provided by the presence of a spiral or another transverse reinforcement, by the large dimensions of the body, or finally by the existence of an exterior compression.

localized conical shape failure is expected, as noted by Hawkins (see Section 1.3.2). In fact, right under the load surface, a double state of compression is acting, i. e. there is a triaxial compression state. This problem has been studied by Spieth [112], who determined the pressure distribution in concrete and derived a relation for allowable bearing stress:

$$N_u = \sqrt{\frac{A_c}{A_1}} f_{cu} \leqslant 9\, f_{cu} \tag{1.33}$$

Spieth also recommended a safety factor of 3.

One of the first studies on concrete under compressive stresses applied in two or three directions was the one conducted by Richart et al. [102] in 1928, who also provided stress strain curves for concrete with and without confinement. The active confinement was provided by "a liquid pressure to the sides of a cylinder which was loaded in the axial direction in a testing machine". Two of the principal stresses were always kept equal. In the next decades many researchers have studied this topic: a recent State-of-the-Art can be found, for instance, in Samani and Attard [106] or in Montoya et al. [90].

Several analytical models for the stress-strain relationship of confined concrete have been proposed by many authors. For instance, Menétrey and Willam [86] proposed a triaxial failure criterion in which the yield surface is undefined along the hydrostatic axis and plastic potential surfaces are formulated in terms of Haigh-Westergaard stress space[39]. This surface has parabolic meridians and a variable shape on the deviatoric plane, from triangular to almost circular with increasing confinement. Papanikolaou and Kappos [99] analyzed the adequacy of the proposed model to a variety of experimental results and they found generally a reasonable correlation, "especially for low and moderate levels of confinement".

Recent triaxial tests were conducted in Grenoble by Malecot et al. [78] by means of a high-capacity hydraulic triaxial press called *GIGA machine*[40]. The results confirmed that concrete compressive strength can reach very high values with respect to uniaxial concrete compressive strength. Furthermore, the strain in correspondence of the peak stress can change from 0,2% — a typical value in an unconfined specimen — to 4% or more in a highly confined specimen. That is, with a high confinement, concrete behaves like a ductile material, with a diffused damage at failure.

[39] A tridimensional space in which the principal stresses are used in order to define cylindrical coordinates (ξ, ρ, θ) as the measure of distance along the coordinate axes.

[40] This experimental device can generate stress levels up to 1 GPa.

1.3.4 Strut-and-Tie modeling

The Strut-and-Tie modeling is one of the most useful design methods for discontinuity regions in reinforced concrete members, in which traditional beam equations do not apply. The first reference to the method dates back to Karl Culmann and Karl Wilhelm Ritter.

Culmann [33] (Figure 1.45) introduced graphic statics[41] in the second half of the 19th century. He considered drawing the true language of engineers, because it allowed the visualization of structural relations using diagrams of forces, as opposed to analytical methods.

Ritter [103] formulated his truss theory and applied it to a structure imagined in the interior of an apparently continuous body like a concrete beam. The calculation of the forces in the ties allows to design the reinforcement, and the capacity of the strut is controlled at the nodes.

Emil Mörsch, manager of the Engineering office Wayss & Freytag[42], developed a similar idea almost at the same time. In 1903 and in the following years he arranged four tests on T-beams in order to study the influence of shear stresses and presented his results in the following years.

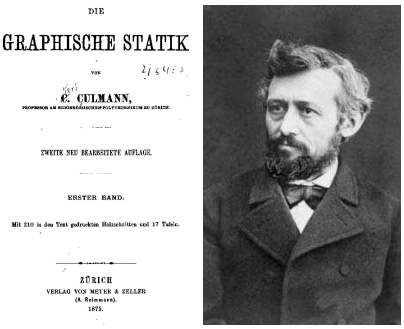
DIE

GRAPHISCHE STATIK

von

C. CULMANN,

ZWEITE NEU BEARBEITETE AUFLAGE.

ERSTER BAND.

ZÜRICH

VERLAG VON MEYER & ZELLER

Figure 1.45: Culmann and the frontpage of his work

He wrote [91]: "Such shear tests are suitable for setting up general design rules [...] a reinforced concrete beam of constant depth can then be compared to a single or double intersection truss or one of higher order". Mörsch's work was refined and expanded by other academics, among them the Swiss engineer Marti [80], and the German engineers Leonhardt [71] and Schlaich [108], from Stuttgart University. In particular the work carried out by the latter, "generalizes the truss analogy in order to apply it in the form of strut-and-tie models to every part of the structure". Recently, a systematic approach for the choice of a suitable truss model has been proposed by Muttoni et al. [93]. It is a general method that develops stress fields, allowing the consideration of a predefined reinforcement layout. Currently, the Swiss Standard SIA 262 implements this method for the design and verification of structural concrete elements [105, 94].

[41] Techniques of graphic nature aimed at solving problems of equilibrium of bodies and systems of bodies.

[42] Wayss & Freytag bought the first patent from Monier and made Mörsch Chief Engineer, responsible for the research in the firm.

1.3.5 Knee Joints

A reinforced concrete knee joint, sometimes simply named a corner, is composed of one beam and one column connected at their ends, forming usually a 90° angle. The positioning of the reinforcing steel in the adjoining members is usually determined on the basis of their flexural resistance.

While the behavior of beam-column connections has been explored fairly well, and specifications have been incorporated in design codes around the world, little work has been done regarding the behavior of knee joints. Angelakos [11] observed that "very little work has been done on modeling the behavior of knee joints" and Johansson [59] noted that "The detailing of corners in reinforced concrete frame structures represents a relatively untouched field".

Only the static case of knee joints subjected to negative (closing) moments is discussed here. A sketch of the forces acting on the body is shown in Figure 1.46 and a brief review on this subject is provided in the following paragraphs.

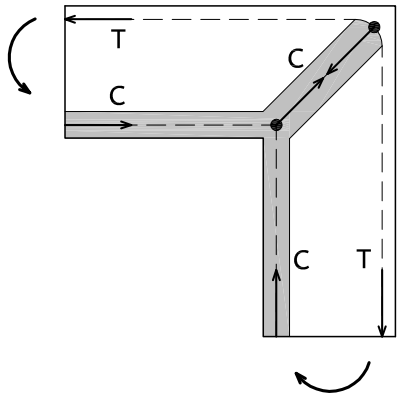

Figure 1.46: Free body diagram for a knee joint subjected to closing moments

1.3.5.1 *Behavior of frame concrete subjected to closing moments*

If the corner is designed properly, failure is expected to occur as a consequence of bending in the sections adjacent to the corner, with yielding of the reinforcements. The internal lever arm increases at the corner, thus a joint region in a closing corner may appear always stronger than the members adjoining in. However, it has been shown that the corner can fail before yielding of the reinforcement. According to Stroband and Kolpa [114] there are three possible failure modes:

CRUSHING IN THE COMPRESSIVE ZONE

A corner subjected to closing moment presents large compressive stresses at the inner part of the corner. A biaxial compressive state is expected as a result of the compressive stresses coming from both sides of the corner, or even a triaxial stress state

if lateral deformations are restricted, such as in the case of wall-slab connections.

This type of failure can occur in case of high mechanical reinforcement ratios but usually the corner has the strength required to resist concrete crushing, thanks to the favourable multiaxial compressive state of stress that substantially improves the material strength, as discussed in Section 1.3.2.

CRUSHING IN THE DIAGONAL STRUT

Tensile forces from each side of the corner are balanced by a compressive strut. If the stress in this diagonal becomes large, crushing of the concrete may occur. In this case, the favourable stress state seen in the previous case is no longer present, unless confining stirrups are positioned within the corner. For large values of mechanical reinforcement ratios a compressive failure of the strut is likely to occur.

In order to avoid this mode of failure, Stroband and Kolpa suggested to limit the mechanical reinforcement ratio to:

$$\omega_s = \frac{A_s f_{yd}}{b d f_{cd}} < 0{,}240 \tag{1.34}$$

BEARING FAILURE AT THE BEND OF THE REINFORCEMENT

High concentrated forces are generated along the inside of the bend, with a possible spalling of the side concrete cover and consequent anchorage failure of the reinforcement.

In correspondence with the reinforcement bent, radial compressive stresses are present. When these compressive stresses spread, tensile stresses act out of the plane of the bar axis generating splitting cracks when the concrete tensile strength is reached. This kind of failure is more likely to occur when a reinforcement bar is positioned near a free edge.

In case of a wall-slab connection, the corner region will be confined in the transverse direction. In a beam-column joint, however, side concrete spalling may become a major problem and this kind of failure cannot be ignored, especially if there is a reduced number of longitudinal bars.

Furthermore, a fourth type of premature failure can occur when the reinforcements are spliced within the corner: an anchorage failure can take place if a minimum splice length is not provided, as in the case of ordinary beams with insufficient lap splices.

1.3.5.2 *Monotonic tests of knee joints under closing action*

Many researchers adopted a description of the behavioral response of knee joints in terms of the ratio of the moment reached at joint failure

to the yield moment of the weakest adjacent flexural member: this is called *efficiency factor*. Values higher than one are desirable, as they imply a safe design, with a failure by flexure of the adjoining members. The joint should not be a weak link, because its behavior can influence the whole structure in terms of both strength and deformability. The philosophy of this *hierarchy*, that designers should always keep in mind, is to encourage ductile modes of failure avoiding other brittle mechanisms suchs shear-related failures.

Kemp and Mukherjee [63] tested four portal frames and four L-shaped specimens subjected to a closing moment. Test results showed low efficiencies for specimens with high reinforcement ratios. Failure was related to the formation of diagonal cracks across the joint starting from the outside of the corner.

Swann [116] performed tests under monotonic closing action on five knee joint specimens with a tensile reinforcement ratio of about 3%. As a results of loading conditions, there was no axial load acting on the adjoining members. Efficiencies between 0,75 and 1,00 were obtained.

Mayfield et al. [82] tested a number of knee joint specimens under closing action and they obtained efficiencies greater than 1,0 for almost all of their tests. The difference when compared to the previuosly published work of other authors may be attributed to the lower reinforcement ratio for the main tensile reinforcement, of about 1%.

More studies on knee joints were motivated by the damage occurred during the Loma-Prieta Earthquake in San Francisco in 1989. Zouzou and Haldane [125] tested two large scale knee joint specimens. One of them had confining stirrups in the joint region, that allowed to preserve the diagonal strut and caused the cracks in the joint region to relocate outside the strut core, improving the overall ductility of the joint. The failure mode seemed to change from the splitting tensile failure of the compressive strut to the flexural failure of the adjoining members.

Luo et al. [76] tested 27 full scale knee joint specimens. They used the bend radius to column effective depth ratio (R/d_c) and the beam reinforcement index[43] as the key parameters to delimitate three failure regions:

1. with an high reinforcement index, a crushing failure of the diagonal strut is likely to occur;

2. with a low reinforcement index, when the bend radius is small in relation to the column effective depth a splitting failure in the plane of the bars can be expected;

[43] Defined as $\omega = \frac{\rho f_y}{f_c}$, with $\rho = A_s f_y$ taken as the reinforcement ratio of the beam with b, d respectively being the beam width and the beam effective height.

3. with a low reinforcement index, when the bend radius is high in relation to the column effective depth a flexural failure can be achieved.

Recently, the Swedish Shelter Regulations and the Swedish Road Administration have promoted the study of different detailing of the corner reinforcement. The former aims at establishing an easier design for shelters, that must be able to withstand dynamic loads such as impacts or bombs. The latter aims at simplifying the reinforcement detailing in frame corners, since splicing in corners was not allowed and had caused complicated reinforcement layouts difficult to apply correctly. Lundgren [75] investigated whether splicing of the reinforcement can be allowed or not within a corner region, at least for closing moments. The results show that splicing the reinforcement in the middle of the corner has advantages over splices placed outside the bend of the reinforcement. Johansson [59] suggested that perhaps "the best method, if using high reinforcement ratios and full efficiency still is to be achieved, is to increase the concrete strength within the corner. Fiber-reinforced concrete is then believed to be especially advantageous".

1.3.5.3 *Modeling the behavior of reinforced concrete knee joints*

One approach that may be used to model knee joint behavior under static loads is strut-and-tie idealization. Finite Element modelling is another possible choice: even when analisys may not describe the response quite correctly, it can often give the user a basic idea of what behavior may be expected in a given situation. Maybe the best approach for a detailed study is combining laboratory tests with finite element modelling.

1.4 SUMMARY

The available knowledge on mechanical anchorages used in reinforced concrete structures has been presented, with particular regard to previous notable research and other related topics. This relatively new solution has been tested in a wide range of applications, such as: beam primary and transverse reinforcement, beam-column or roof joints, pile-wharf and pile-to-foundation connections, transverse reinforcement in walls or slabs. Its use has also been studied for lap splices and in prefabrication industry.

Experimental studies and code provisions have been analyzed with the aim of applying this knowledge in the development of a design formulation through the clear understanding of the mechanism that allows the transferring of the force between headed rebar and surrounding concrete.

From the above review, the following conclusions can be drawn:

- The use of plate-anchored reinforcement bars is often noticed to be as good as or better than conventional reinforcement anchorages;
- Deeply embedded headed bars fail by a side blowout failure with spalling of the concrete over the head;
- Corner placement results in a lower capacity, as occurs with a close spacing that can overlap the failure surface;
- The total capacity of reinforcement bars anchored with end plates is achieved through composition of two mechanisms: the anchorage provided by bearing on the head plus the contribution of the bond along the bar. Many authors have focused on the calculation of the head contribution and their findings can be summarized as follows:
  - Side cover, concrete strength and head area are the primary factors affecting the blowout capacity. An increase of any variable increases the anchorage capacity in some measure. An increase in second cover dimension also increases the capacity: however, this increase is limited to a second cover dimension of 3-4 times the smaller cover dimension;
  - Head shape and orientation do not affect significantly the total anchorage capacity;
  - Transverse reinforcement does not increase the capacity per se, but helps to restrain side cover from blowout. In this sense, its active confinement role is similar to the passive confinement exherted by cover, although the active confinement can be regarded as more important because it starts acting in correspondence with the growing of the bursting crack. After the failure of the passive confinement, the presence of a transverse reinforcement allows to sustain the load after failure in a significantly higher measure.
- For what concerns the contribution of the bond to the total capacity, authors who have studied the problem concluded that development length increases the anchorage capacity and the increase is predictable by standard code provisions, although few tests were performed to study this contribution. The anchorage process consists of two stages: after a first phase in which the anchorage is carried by bond stress, a deterioration in bond allows some slip and the stress is progressively transferred to the head. At failure, anchor relies on peak head capacity and diminished bond capacity.

2 APPLICATIONS

2.1 GENERAL APPLICATIONS

In this chapter some typical applications of headed reinforcement bars in reinforced concrete structures will be presented, with a special emphasis on their first and main application field, the offshore industry. Since the 1970s a considerable number of large concrete structures have been constructed for the oil industry and now, at the turn of 21st century, there is an increasing interest in robust structures suitable for extreme environments, such as LNG[1] terminals and coastal engineering projects, among others.

Although the application of mechanical anchorages has been mostly limited to very large and very heavily reinforced elements, the advantages of this type of reinforcement in terms of assembly, material savings and sustainability make this technique attractive for some more common construction problems such as short span bridges, foundation slabs, pile caps, concrete box underpasses, or anchoring of column reinforcement in roof slabs. Therefore, an outline on other application fields is provided, with special attention to very common structures in which the use of plate-anchored bars instead of conventional detailing is recommended or even is the only possible choice, and with a view to early historical applications. The chapter ends with an overview of some recent examples of the use of headed reinforcement bars in real structures.

2.1.1 Early examples

Greek monumental buildings were almost exclusively based on trabeated[2] wall construction. Instead of mortar, in ancient architecture iron cramps[3] and dowels were generally used in order to fasten together the blocks of stone, as reported by Mark [79]. Usually, it was made of wood but it could also be made of marble or iron and sometimes was fixed with a lead coating which prevented oxydation and enhanced the flexibility of the joint.

A typical cramp was the bow-tie shaped piece represented in Figure 2.1a, which was fixed into the carved rock and connected the blocks. These double dovetail cramps were the most common cramps in Roman bridges and they could last for centuries: two hardwood

[1] Liquified Natural Gas
[2] Having horizontal beams or lintels rather than arches.
[3] A cramp is a piece used to hold stones together, usually made of metal.

cramps were discovered during the last restoration works between the granite blocks of the Alcántara Bridge, in Spain, in 1859 [38].

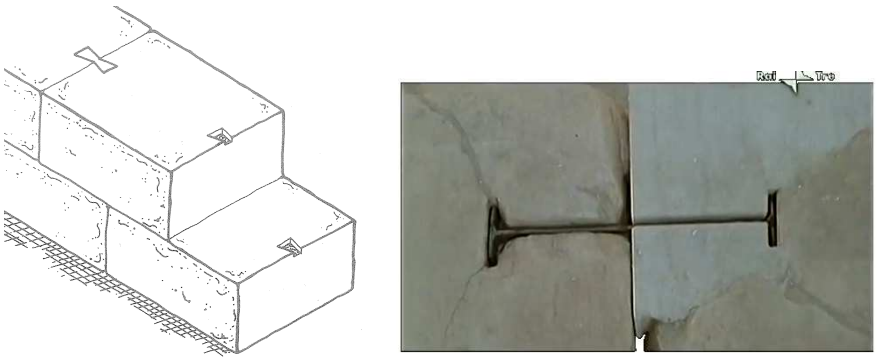

(a) *Bow-tie cramps in Greek temple construction [79]*

(b) *Headed cramp in Parthenon architraves*

Figure 2.1: Some early examples of headed bars in ancient architecture[4]

Similarly, in Figure 2.1b another tipology of connection between blocks can be seen, in this case in the Parthenon of the Periclean Athens. Although it was generally believed that such big marble blocks would not move after precise positioning, for safety, the constructors connected them with cramps. Inserted into specially carved slots they would hold together the blocks providing a safeguard against potential shifts due to earthquakes or foundation settlements. Sometimes lead connections were used instead of iron connections, in which case, given the lower melting temperature, it was possible to directly pour the melted lead into the previously carved mould, although was still more common to pour it into a mold of similar dimensions.

Sadly, the presence of the metals probably was more harmful in the long run than useful. In fact, during hundreds of years seekers of metals left holes in many structures, favoring their degradation. Furthermore, iron is subjected to oxydation: after the process was begun, the increase in volume can result simply in local damages or more likely in the beginning of a generalized corrosion process.

2.1.2 Offshore and coastal structures

The first offshore structures were probably the Maunsell Forts, shown in Figure 2.2b, small fortified towers built in the Thames and Mersey estuaries during the Second World War to help defend the United Kingdom from German air raids. But, it was in 1973 that the first big platform for the oil industry was constructed. It was the Ekofisk Platform, situated in the North Sea and many other offshore structures were constructed afterwards.

[4]Credits: b) Le meraviglie del British Museum – Italy's national public broadcasting company.

Today, most part of the major concrete platforms currently operating worldwide are GBSs[5], a type of structure that lies on the sea floor and remains stable thanks to its massive weight. Generally, it consists of a caisson structure and a number of straight or tapered shafts supporting the topside. The drilling and production equipment can be housed in the interior of the shafts. Most of the construction can be carried out at an inshore location. Then, the almost completed structure is towed-out and sunk at its final destination.

Usually, in moderate water depths and with benign climate conditions, the use of welded tubular steel jackets can result in fewer construction and decommissioning costs and the concrete concept may not be the best option. However, in hostile environments and remote areas a GBS offers a longer life time and requires little or no maintenance. GBSs can achieve large depths. In fact, some of them have a heigth of more than 300 meters. These strcutres are also called Condeep[6]. The Troll A platform is the largest Condeep to date. With a total height of 472 meters it was the tallest structure ever constructed when built. For the construction of the Troll A Condeep, 245 000 m^3 of concrete and 100 000 tons of reinforcing steel were used. Some examples of GBSs are shown in Figure 2.11.

Although the GBS concept is mainly used in oil extraction sites, engineering solutions for concrete gravity base foundations are also being studied for wind farms, since a substantial increase in the number of offshore facilities in European waters is expected as a result of the ECCP[7] that requires a substantial increase in the use of renewable energies.

Nowadays the first examples of a new concept have already appeared. One of them consists in a floating platform connected to the ground with chains or pipes (known as TLP[8]). This is a consequence of the constantly increasing perforation depth needed to exploit new oil fields and that is why in these days offshore concrete structures are usually not only related to the oil industry but also to other industries. A partial list of existing offshore concrete structures is reported in Table 2.1

Marine concrete structures are located at various and very different parts of the world and are usually subjected to severe loads during their life. In fact, as reported by fib [3] "particularly, the float out of the shallow base and the submergenge prior to inshore deck mating have a significant influence on the design". Typical important loads for marine concrete structures are the dead weight, enviromental and accidental loads such waves or ice and differential pressures. Usually marine structures are shaped to behave as a membrane, offering an

[5]Gravity Based Structures
[6]CONcrete DEEP water structure
[7]European Climate Change Programme
[8]Tension Leg Platform

Year	Field	Platform Type	Depth [m]	Concrete [m^3]	Location
1973	Ekofisk	Caisson	71	80 000	North Sea (N)
1976	Brent D	GBS 3 shafts	140	68 000	North Sea (UK)
1986	Gullfaks A	GBS 4 shafts	135	125 000	North Sea (N)
1987	Gullfaks B	GBS 3 shafts	141	101 000	North Sea (N)
1988	Oseberg A	GBS 4 shafts	109	11 600	North Sea (N)
1989	Gullfaks C	GBS 4 shafts	216	244 000	North Sea (N)
1992	Sleipner A	GBS 4 shafts	82	77 000	North Sea (N)
1993	Draugen	GBS monotower	251	85 000	North Sea (N)
1995	Troll A	GBS 4 shafts	303	245 000	North Sea (N)
1997	Hibernia	GBS 4 shafts	80	165 000	Canada
2008	Adriatic LNG	LNG terminal	29	95 000	Adriatic Sea (I)

Table 2.1: Offshore Concrete Structures for Oil and Gas Industry. Source: [3].

economic way to resists the important stresses originated by differential pressures.

Impacts from ice, icebergs, ships or supply boats may be causes of substantial local damages to a shaft. The icebergs or the sea ice driven by wind and tide from the Arctic during the summer melt period, can generate high local pressures and the behavior of the platform can be difficult to predict. As an example, the Confederation Bridge, linking Prince Edward Island to continental Canada, is the world's longest bridge on ice covered waters. During the design process, ice forces became the primary lateral load on piers, that were designed with a 52° conical ice shield at the waterline which lifts the ice and breaks it in bending, as shown in Figure 2.2a. Brown [18] reported that years of observations and measurements following its construction have proven the efficiency of the design.

The Confederation bridge is also a remarkable example of modular bridge technology, based on the use of prefabricated modules with large dimensions. Although the author is not aware whether headed bars were used or not in this specific bridge, this high-growing sector is potentially suitable for the employment of the headed bar concept, as seen in Chapter 1.

(a) *The Confederation Bridge*

(b) *The Red Sands Maunsell sea fort*

Figure 2.2: Some examples of offshore structures[9]

As a consequence of the severe load conditions, high densities of reinforcement are used on most offshore structures. Densities of 300-400 kg/m^3 are common and may even reach 700-1000 kg/m^3 in some special cases (see, for instance, [115, 15]). Therefore, large diameter bars and small aggregate sizes are used to improve the concrete placing and compaction. Headed reinforcement bars have been used extensively instead of conventional shear reinforcement to anchor large bars. Generally, offshore structures are also heavily prestressed.

Some code provisions about offshore concrete structures have been written in the past years. Det Norske Veritas made early efforts to provide design rules for concrete offshore structures, and ISO 19903:2006 "Petroleum and natural gas industries – Fixed offshore concrete structures" has been adopted as a European Standard. The Norwegian Code NS 3472, the American Code ACI357 and the Canadian Standard S474 are also used as national standards. A general and more complete overview about this topic can be found, for instance, in Melchers and Hough [85] and in Nawy [96].

2.1.3 Underpasses

An underpass is a crossing beneath a road or railway, allowing users to reach the other side in safety, and may also be constructed for the benefit of wildlife. This type of structure — depicted in Figure 2.3 — is totally or partially confined by the ground cover and by the embankment or the natural soil situated below.

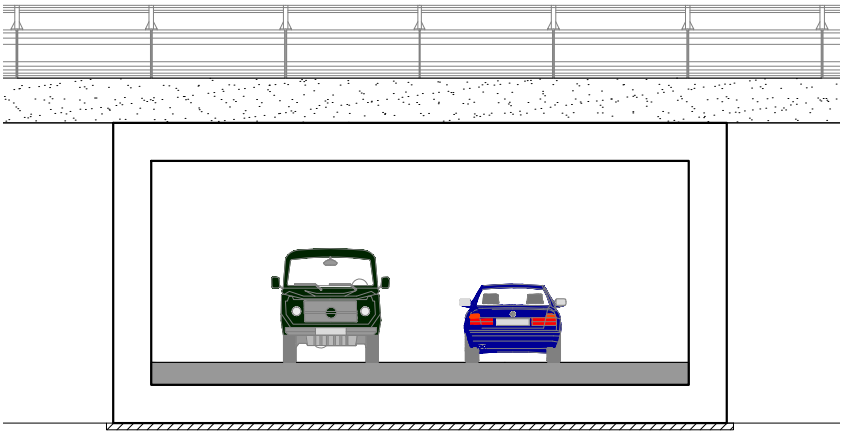

Figure 2.3: A sketch of a typical road underpass

The structure is formed by an upper slab connected to supporting walls, which in turn are connected to a bottom slab. The top slab-wall connection is monolithic in many cases. This structure can be

[9]Credits: a) Photo taken by Ron MacKay on february 29, 2012 ©. Reproduced by permission of the author; b) Imaged published By Russss via Wikimedia Commons (CC BY-NC-SA 3.0).

calculated by means of a plane model, due to the large length of the structure normal to the top traffic flow. The dominating loads are traffic loads and earth pressure.

If the connection between slabs and walls is monolithic, the maximum bending moment is found at the corner joints. This makes an underpass an ideal candidate for the use of plate-anchored bars. Figure 2.4 shows reinforcement details for both lower and upper knee joints. On the left side a conventional reinforcement solution is represented, while on the right side an equivalent detail using headed bars is proposed.

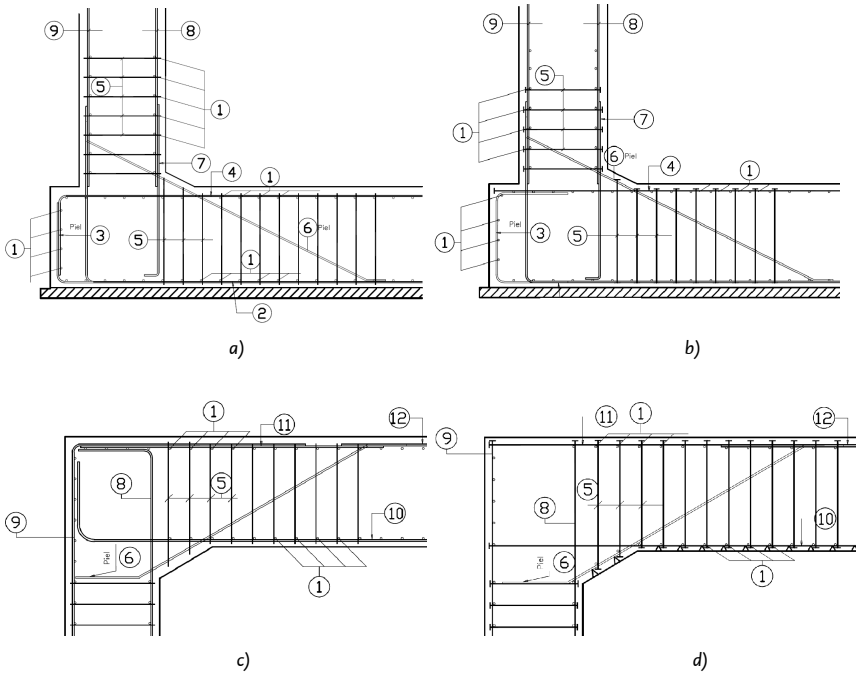

Figure 2.4: Reinforcement details for knee joints using either hooked bars or headed bars

It is clear that the first advantage of using mechanical anchorages is less congestion. In the upper corner, it is not necessary to bend the transverse reinforcement of the upper slab nor those of the walls. At the same time, the use of headed reinforcement permits an easier assembly allowing the placing of the upper slab reinforcement without interference from bent bars coming from the walls, which might, otherwise, be of a considerable length (more than 2 meters for large diameter bars – see bar number 11 in figure). For what concerns the foundation slab, the only advantage here consists in saving steel, the complications related to the assembly of the cage being similar in both cases.

If shear reinforcement is needed, the use of double headed bars instead of stirrups enables a much more flexible assembly of the framework, since in this case they can be placed regardless of the positioning order. In fact, conventional stirrups are not suitable to

be introduced after the positioning of slab rebars, but they should be already assembled when the positioning takes place.

2.1.4 Overpasses

An overpass or flyover is a road or railway that crosses over another road or railway. The structure may consist of several spans. The most common overpass is formed by three or four spans, one or two main spans and two compensation spans of smaller length, as represented in Figure 2.5a. In this example, the deck is supported by circular piers, and the whole structure is built on deep foundations.

In this example the possible applications of mechanical anchorages on a prestressed hollow-core girder bridge, which is a very common typology within the usual range of spans (see Figure 2.5b), are analyzed.

Starting from the bottom, each pile has a reinforcement that requires a certain development length. The circular geometry leads to an important congestion of reinforcement, as shown in Figure 2.6a. The equivalent detail using headed bars, illustrated in Figure 2.6b, is cleaner than the conventional one. Regarding the bottom and top reinforcements of the pile cap, especially if many layers are superposed, it can be stated that, again, the use of headed reinforcement improves substantially constructability, even if a small amount of skin reinforcement has to be placed. Before concrete is poured into the pile cap, starter bars are left in order to connect the slab with the pier reinforcement. These bars can be anchored by a plate, reducing the congestion and simplifying the assembly (Figure 2.7). The substitution of the hooked bars in the pile-deck connection is more interesting, due to the congestion produced by the presence at that location of the pier diaphragm (Figure 2.8a and 2.8b). Using headed reinforcement bars, the development length of the pier reinforcement, which can be longer than two meters, can be avoided.

Furthermore, double headed bars can take the place of transverse stirrups. If one considers that the reinforcement does not allow the positioning of the prestressing sheath within a distance from the upper surface, the traditional solution involves an important reduction of the maximum eccentricity, that would not occur with the alternative detail. With regard to the deck, the use of headed bars would allow a much more flexible placement of the reinforcement, since the shear reinforcement can be placed before or after the upper reinforcement, as already noted in Section 2.1.3, again obtaining a cleaner solution. Notwithstanding, this is not a significant saving since the longitudinal reinforcement of the deck needs to be supported in order to remain in the predetermined position, hence the stirrups cannot simply be removed but should be replaced by omega-shaped elements.

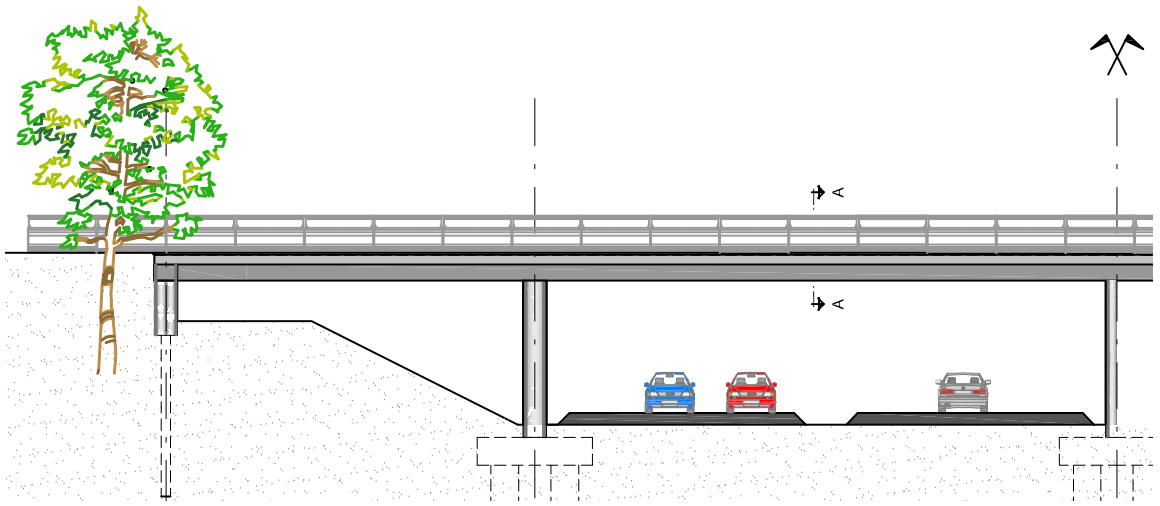

(a) *Elevation view*

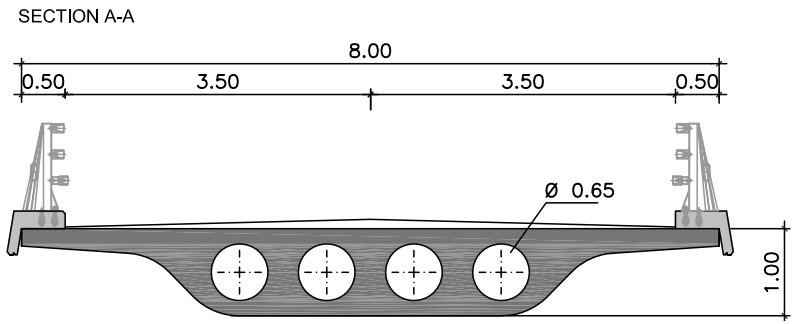

(b) *Transverse Section*

Figure 2.5: A highway overpass

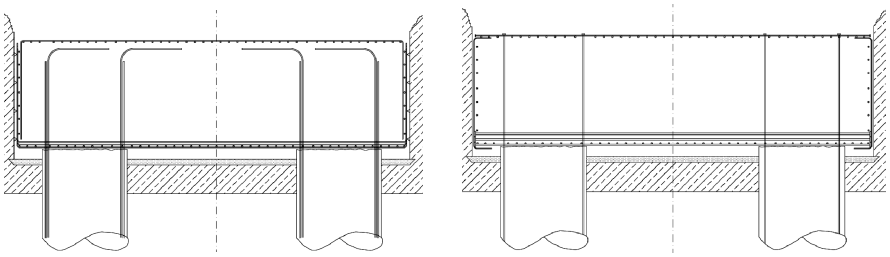

(a) *Conventional reinforcement* **(b)** *Alternative reinforcement*

Figure 2.6: Pile reinforcement details

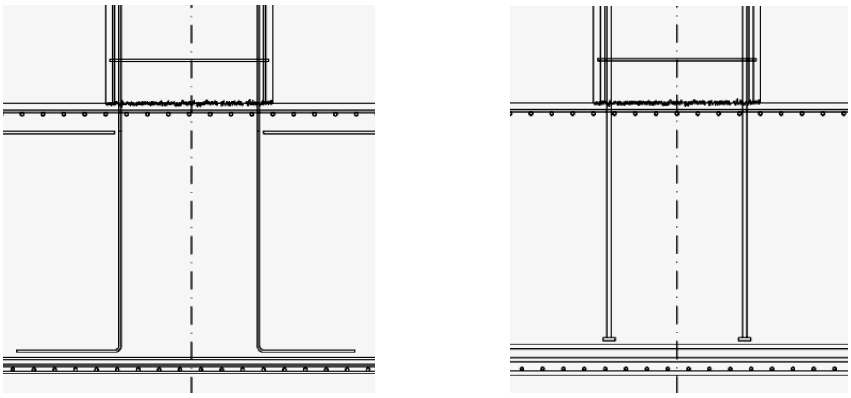

Figure 2.7: Reinforcement details for pile-to-foundation connection

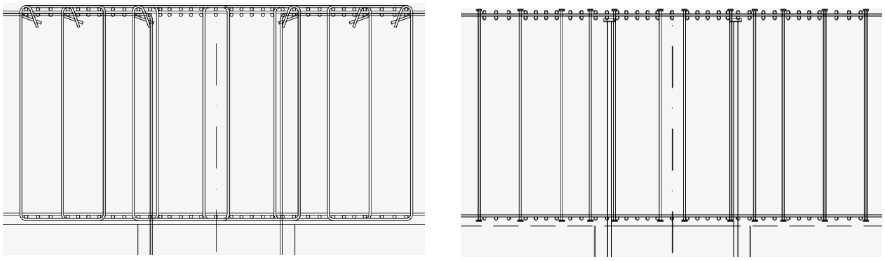

(a) *Conventional reinforcement* **(b)** *Alternative reinforcement*

Figure 2.8: Pier-deck connection – Strut reinforcement details

Finally, double headed bars are potentially suitable as splitting reinforcement at anchors of prestressed concrete structures. In this way, a concentration of U bars not properly anchored is avoided. On the other hand, as seen previously, the presence of a transverse diaphragm normal to the tendons is cause for concern, since it complicates the pouring leading possibly to voids between aggregates (honeycombing), an undesirable defect in prestressing anchor zones.

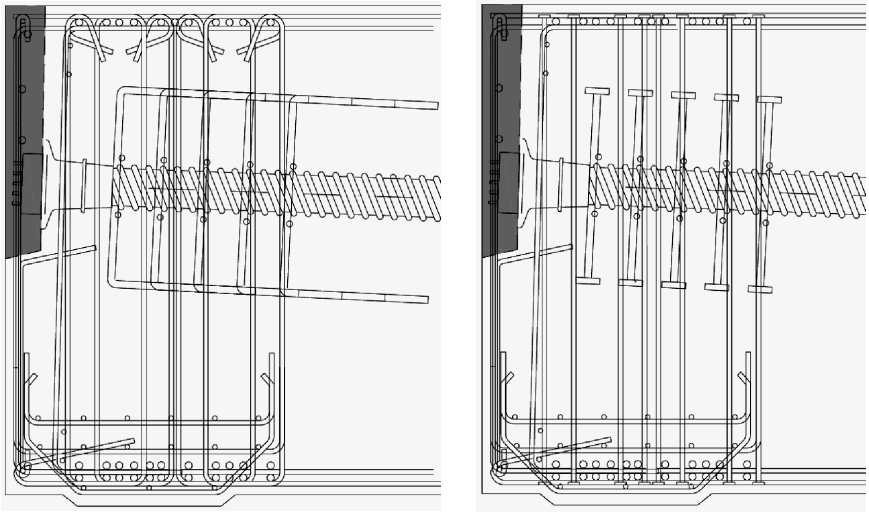

(a) *Conventional reinforcement* **(b)** *Alternative reinforcement*

Figure 2.9: Prestressed anchor zone – Reinforcement details

In Figure 2.9a there are 10ϕ25 bars in both directions, with a 60 cm anchorage legs. This results in the superposition of many bars causing difficulties in positioning. The detail shown in Figure 2.9b is thus a better solution, since it eliminates overlaps.

2.1.5 Buildings

As pointed out in Section 1.2.1, among the first applications for mechanically anchored reinforcement was the use of double-headed ties as punching shear reinforcement in slabs.

In the example of Figure 2.10, lower and upper reinforcement consists of ϕ12/0,20, plus a supplementary layer of ϕ16/0,20 for negative moments in a length of about 1/3 of the span, and a supplementary layer of ϕ12/0,20 for positive moments in a length of about 80%, only along column strips. Figure 2.10a shows the reinforcement drawings of a conventional layout of bars in a typical floor. In Figure 2.10b an alternative option is represented, in which studrails or double-headed bars are used.

The use of headed bars to anchor supplementary reinforcement would save a development length, but it has no particular advantages in terms of assembly. On the contrary, the assembly of punching

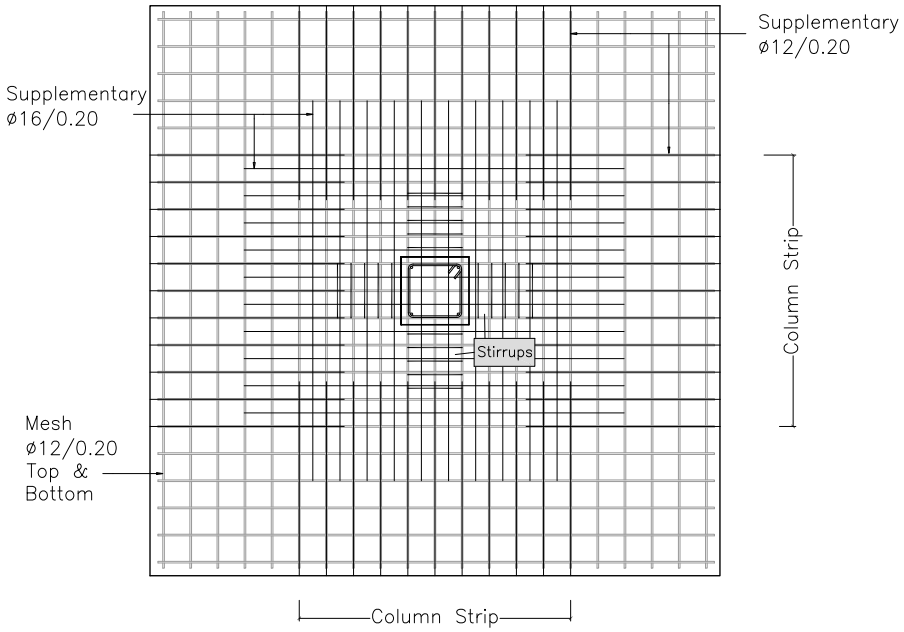

(a) *Conventional punching reinforcement*

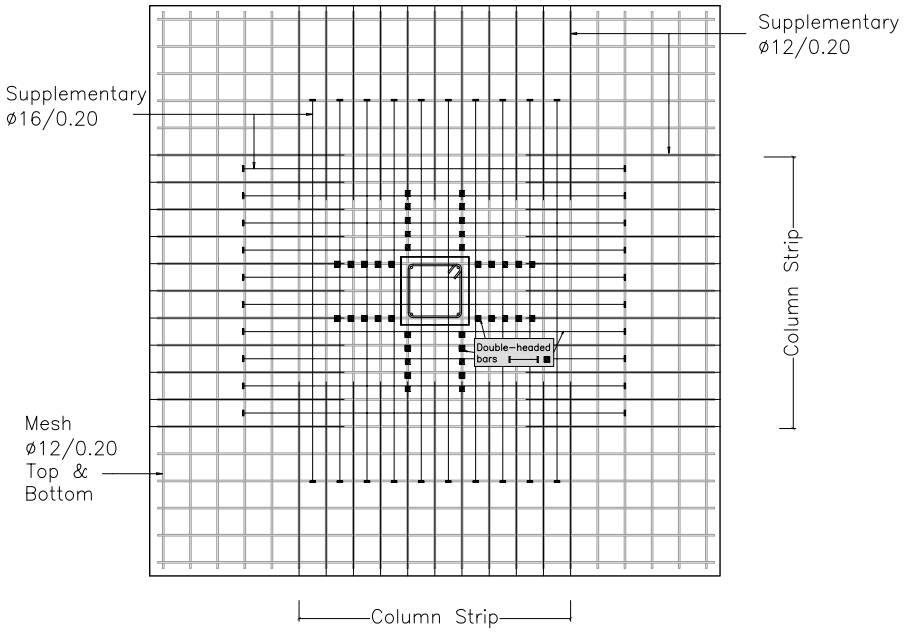

(b) *Double-headed punching reinforcement*

Figure 2.10: Typical reinforcement drawings of a floorplan

reinforcement does present the convenience of making the assembly independently from the rest of the reinforcement cage, as already noted in Section 2.1.3.

Another possible application of headed bars can be in the roof-column connection, whose hooked bars would be replaced saving the corresponding development length and improving the constructability of the corner joint.

2.2 SPECIFIC APPLICATIONS

In this section some specific applications of headed reinforcement bars in real structures will be presented, starting with a closer view of the Norwegian experience and following with some examples of its use in other application fields.

2.2.1 The Norwegian experience

Seventeen large offshore concrete structures were built at the construction site of Aker Kværner near Stavenger in Norway. Dr. techn. Olav Olsen designed the concrete substructures. In terms of concrete volume, Sandvik et al. [107] said that approximately half of the total volume of concrete used in the world to build offshore structures comes from this construction site.

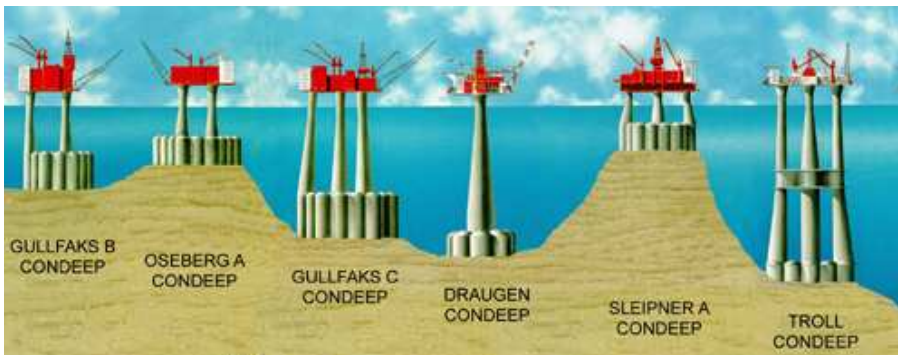

Figure 2.11: Some of GBS constructed in Norway.[10]

A large platform is usually partially built in a dry-dock situated in a protected area or in a fjord and then, after the flooding of the dry dock the structure is towed-out to a deep water area for completion near its final position. There, slipformed construction extends the structure upward as the buyoancy cells are ballasted with gravel and flooded with water so the base of the structure can go deeper into the sea.

The critical phase is the deck-mating phase, in which the top deck of the platform is floated over the substructure. After that, the ballast water is pumped out of the cells and the structure rises and lifts the deck, coupling with it. After deck-mating, the completed platform can be towed-out to the field and lowered to its final destination, generally during a forecast weather window. Little or no preparation of the sea floor is required.

Large quantities of headed bars were used in the Oseburg Platform A, in the Snorre Foundation and Draugen Platform [53, 15, 117] as well as in the Gullfaks, Sleipner and Ibernia platforms, whose description is provided in the following paragraphs.

[10] Picture taken from Dr. techn. Olav Olsen's website.

GULLFAKS PLATFORM C The Gullfaks C consists of four shafts supported by 24 cells with an inner diameter of 28 m. The shafts are placed in a T configuration with a total height of more than 160 m while the height of the total structure measured from the sea floor is 380 meters. The reinforcement content was higher than all Condeeps ever built with a mean of 320 kg/m^3 and peaks of 1000 kg/m^3, in addition to the presence of prestressing tendons, plates and other embedded elements. It was the heaviest structure ever transported [85] with a weight of 1 500 000 tons (Figure 2.12a).

(a) *The Gullfaks C being towed-out* **(b)** *The Hibernia GBS*

Figure 2.12: Some pictures of the tow-to-field phase[11]

Within the technical improvements achieved during the project, Svensvik and Kepp [115] cite the "rationalization of ordinary reinforcement by application of T-headed bars as confinement in highly congested areas". Standard stirrups were replaced by the T-headed bars produced by HRC, with the advantage of less space required and improved constructability. In fact, due to bendability of rebars, usually the standard stirrups are ϕ12, while headed stirrups can be produced with a diameter of 25 mm, replacing four conventional stirrups. 80 000 T-headed bars were used on top of the shafts, to relieve steel congestion and on top of the sludge and the surfactant tanks, to reduce development lengths and provide better anchorage. The material cost appears to be comparable with conventional reinforcement, but the placement was achieved in 1/12 of the time [15].

SLEIPNER PLATFORM A This platform was part of a crude storage program set by the Norwegian government off the coast of Stavanger. The Norwegian government discovered very rich oil fields near its shores, furthermore, the Norwegian industry was producing high quantities of microsilica, a very useful mineral for the production of high strength concrete. Therefore, the government decided to conduct a major investigation on the use of high strength concrete for

[11] Credits. a) Kvaerner's official YouTube channel; b) Offshore Magazine 57.

the construction of offshore platforms and construct a network of platforms suitable for the explotation of the oil fields.

Sadly, the Sleipner A platform is known for its catastrophic failure, being one of the biggest accidents in the history of construction, as claimed by Calavera Ruiz [19] in his review of five mayor catastrophes in structural engineering.

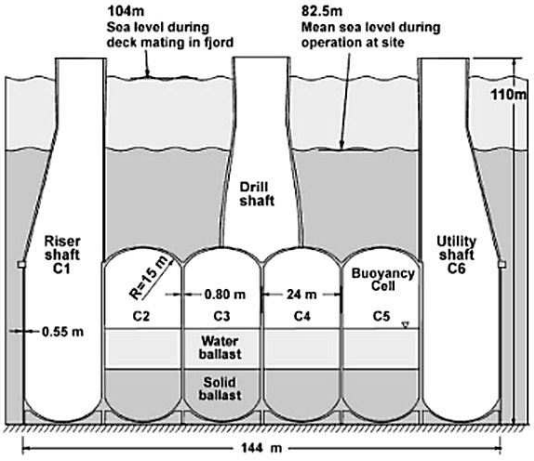

(a) *Elevation of base structure*

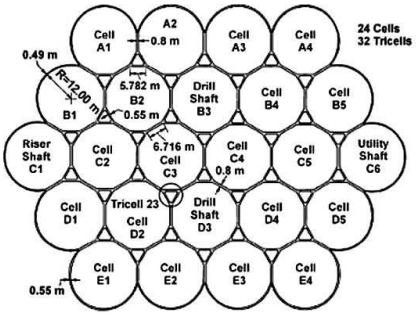

(b) *Section trough buoyancy cells*

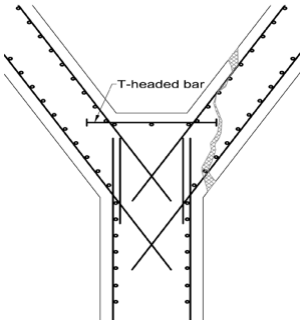

(c) *Tri-cell joint reinforcement detailing and assumed shear failure with spalling of concrete*

Figure 2.13: Failure of Sleipner A platform[12]

The structure was 110 meters high and consisted of a cluster of 24 cells, four of which extended upwards forming the shafts. There were 32 small triangular voids between cells, called tricells. The walls of the tricells had to resist a substantial hydrostatic pressure but could not be too thick in order to float and to be hydrostatically stable.

On August 23rd, 1991, during the progressive lowering of the platform into the Gandsfjord in preparation for deck-mating, at a depth of about 60 meters a shear-related failure of a tricell wall occurred, and the structure collapsed and sank into the ocean, with a rumble of a magnitude comparable to that of a small earthquake. Collins et al.

[12]Credits: a) and b) fib [2]; c) Illustration by Ksenia Tretiakova.

[32], from the University of Toronto, were contracted by the Norwegian consulting Dr. techn. Olav Olsen to investigate the causes of the accident. After running a series of nonlinear finite elements analysis, experts discovered some numerical errors which implied an underestimate of the design shear by almost 50%, leading to no shear reinforcement in the two arms of the Y panel. A plate-anchored bar could have acted as the critical shear reinforcement and intercept the fatal crack if it had had enough length. With losses of hundreds of millions of dollars, it is probably the most expensive shear failure ever occurred.

The Sleipner A platform was rapidly reconstructed with the new name Sleipner A2 and it is still in function. The amount of shear reinforcement used in the new tricell walls was bigger and the double-headed bars used at the haunch were longer than the previuos ones. As reported by fib [2], tests made by SINTEF proved that this reinforcement detailing had 70% greater capacity than the specimens with the original reinforcing scheme.

HIBERNIA PLATFORM The Hibernia GBS is the world's largest offshore oil platform in terms of weight, with a total of 1,2 million tons. About 100 000 tons of reinforcing steel were employed in its construction.

Located more than 300 km off the coast of Canada, the structure — designed by Doris Engineering — was the first one designed against iceberg collisions. In order to achieve this objective a concrete star-shape pedestal was designed to contain in its interior the four 17-meters diameters shafts of the GBS structure, while with its teeth (see Figure 2.12b) it is able to withstand impact from coming icebergs with a mass of over 4 million tons .

As consultant on the most suitable shear reinforcement for the walls of the Hibernia GBS, Amin Ghali proposed double-headed studs with head area equal to 10 times the cross-sectional area of the stud. Ben Gerwick [15] conducted tests to validate these bars as shear reinforcement in walls, but most of them are proprietary and have not been released. Subsequently, several major offshore tank-platforms in the North Sea used studs with heads 10 times the bar area to resist shear and for other purposes[13]

Gerwick [47] reported that the platform was designed to resist the impact of large icebergs: local punching shear, acting over a limited area anywhere on the external of the structure would need special attention. Consequently, after extensive research and testing, T-headed bars were arranged to extend through the wall at close spacing.

[13] Personal correspondence between the author, PhD candidate at Polytechnic University of Madrid, and Dr. Amin Ghali, Professor Emeritus at the University of Calgary.

2.2.2 LNG Adriatic Terminal

ExxonMobil, Qatar Petroleum and Edison Gas are currently developing a facility to receive, store and regasify LNG in the Adriatic Sea off the coast of Italy. The gas will be piped from Qatar through the Suez channel to be stored and sold in the Italian market. The concrete structure of the LNG storage tanks and the regasification plant has been constructed by Acciona Infraestructuras in Algeciras, Spain and was towed to the Adriatic Sea in 2008 in a 22 day trip.

The use of 4100 tons of post-tensioning tendons has reduced the amount of mild steel for a structure of this type. In spite of this, the placement of the rebars was a complex technical problem due to the presence of plates, embedded elements and densely reinforced areas in the foundation and around anchoring heads. Finally, another factor to be considered was the construction process used for the walls, continuous slipforming, which does not allow positioning errors of the reinforcement cage, because, once started, it should not be detained.

About 27 000 tons of B500SD steel and 60 000 anchor plates were used. The reinforcing bars were provided by a subcontractor, Armacentro. The plates, friction–welded to the steel rebars, were assembled by the Armacentro staff but the process was not feasible without the help of HRC regarding the welding process. For this reason, two machines were ordered in Norway and the Armacentro staff was trained in order to use them.

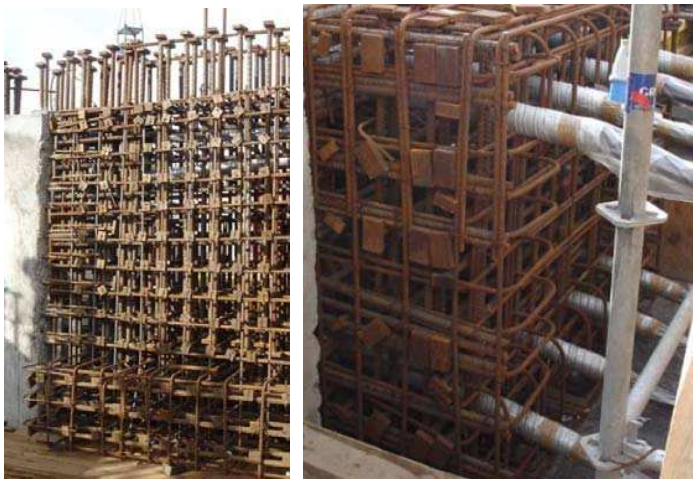

Figure 2.14: The use of the T-Heads on walls and as additional reinforcement in the prestressing anchorage zone[14].

[14] Project Information: Adriatic LNG Terminal. Credits: ☞ http://www.hrc-europe.com

Plate-anchored reinforcement was used for many purposes in these structures. Figure 2.14 illustrates some of these uses.

2.2.3 MPU Heavy lifter

International regulations put constraints on the use of the oceans. Particularly, the 1998 OSPAR (OSlo-PARis) convention established that all platforms in the North Sea should be removed after completion of their duties, with the exception of concrete structures, since the remotion would be too complex. However, the convention requires that at least the topside of the concrete platforms should be removed.

This requirement gave impulse to the development of an entirely new field, potentially with a market value of some billions dollars for the North Sea alone. This led to the conception of a semi-submersible structure that uses the principle of Archimedes in order to perform heavy offshore lifting operations.

A paper by Ludescher et al. [74] provides insight into the detailed design of the MPU[15] heavy lifter[16]. Lightweight concrete was used, and even being sensitive to concentrated loading after early tests, headed reinforcements were used consistently, and even exclusively in the joints (see Figure 2.15). A full-scale test was carried out on a knee joint confirming that bending was the governing failure mode and the resultant behavior was very ductile despite the high reinforcement ratio and the brittleness of the material.

2.2.4 Underwater car park Tjuvholmen

A multistory underwater parking garage has been constructed in Oslo city center by the contractor Skanska. The structure consists of four concrete caissons installed on piles.

Mechanically anchored reinforcement was used primarily in the supporting corbels for caissons and as short connections between prefabricated elements. As usual, they were also used as shear reinforcement or as additional confinement around prestressing tendons.

2.2.5 Railway Genova-Ventimiglia

Genova-Ventimiglia railway is one of the most important Italian railways. Completed in 1872, it follows the coastal line ending on the French border at Ventimiglia. The original track was situated almost at the sea level, parallel to the Via Aurelia, and was composed of only one railway to limit construction costs, but, in the XXth century the line was manifestly inadequate in relation to increasing traffic. Then,

[15] Multi Purpose Unit

[16] MPU is a trademark for the floating U-shaped concrete unit developed by MPU Enterprise to removing used or abandoned offshore structures.

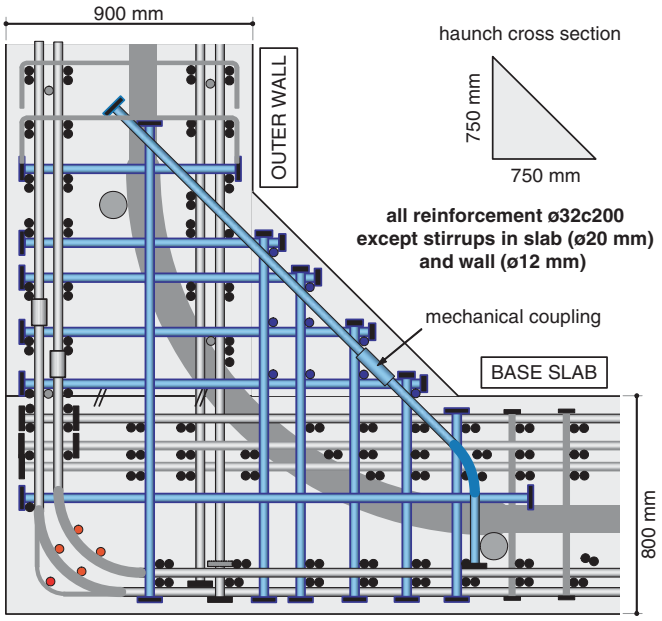

Figure 2.15: Mechanical anchorages are used extensively in the MPU lifter corner [74]

the construction of a new line started, in most of its length independent of the old line, thereby liberating the cities from the presence of the old line that in many cases became a promenade.

FHECOR Consulting Engineers is currently collaborating with FERROVIAL's technical department in order to work-out a series of non-conformities (see Figure 2.16) produced during the tunnel execution in the section Andora–San Lorenzo al Mare.

A procedure has been proposed for the substitution of a ring segment, in which, as a result of a manufacturing defect, design loads cannot be absorbed with full code compliance by the segment itself. The substitution of the vault would be executed as a staged construcion, as a cheaper alternative with respect to the execution of a complete shielding ring. Plate-anchored reinforcement would play here a key-role, allowing the replacing of the ring by means of successive substitutions. Figure 2.17 schematically shows the proposed procedure.

2.2.6 Bankia tower

The same basic conditions that favor the use of mechanical anchorages, e. g. the large amount of reinforcement and the presence of congested areas, can be present in most of tall or supertall modern skyscrapers, especially in foundations but also in columns or diaphragm walls when a high reinforcement ratio is needed.

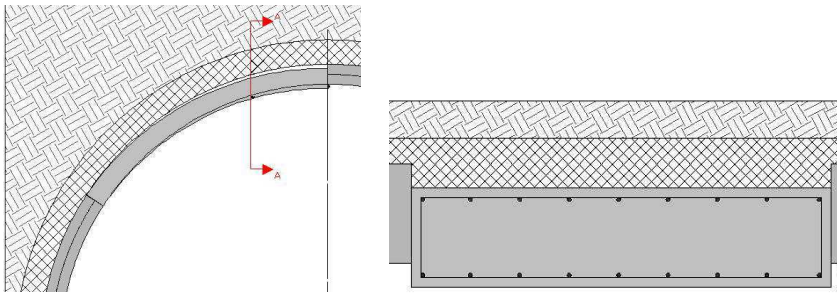

(a) *Elevation* **(b)** *Section A-A*

Figure 2.16: Section of the tunnel with the observed manufacturing defect

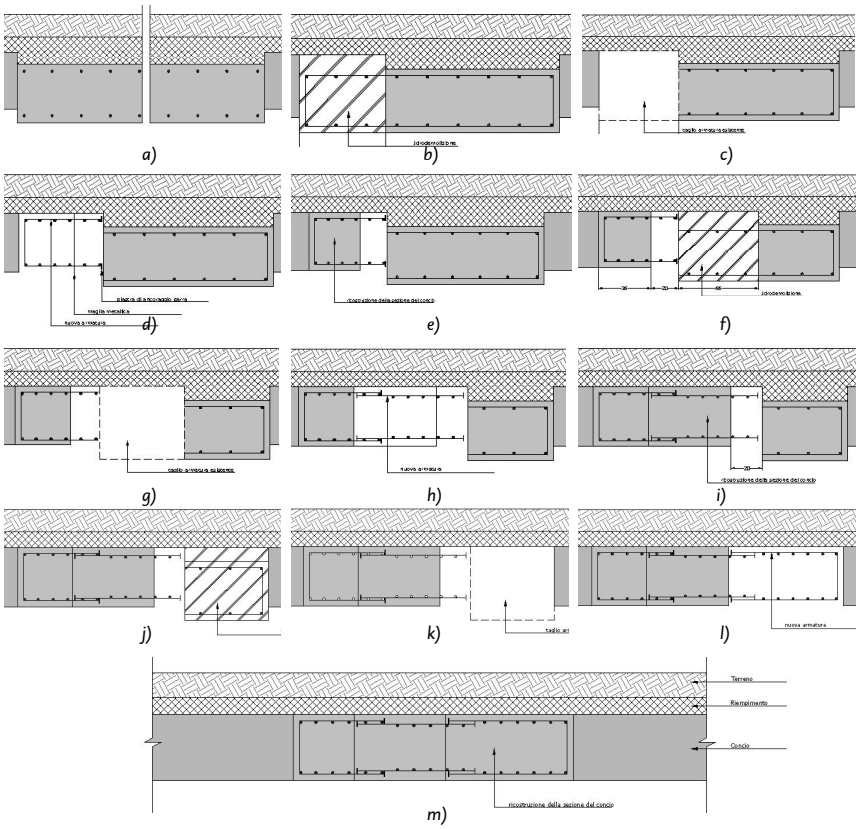

Figure 2.17: a) Drainage of the extrados by means of drills
b) Hydrodemolition of an existing segment
c) Cutting of the existing reinforcement
d) Placing of a new reinforcement in the first part
e) Reconstruction of the first part
f) Hydrodemolition of the second part of the segment
g) Cutting of the existing reinforcement
h) Placing of a new reinforcement in the second part
i) Reconstruction of the second part
j,k,l,m) Repetition of the whole process for the last part

The Bankia Tower[17] is the tallest building in Spain. Designed by Norman Foster, it has a total heigth of 250 m. The heavily reinforced mat foundation measures 43,80 by 72 meters and has 5 meters of depth. It was planned to pour 600 m^3 of concrete a day, subdividing the whole slab in 18 blocks with a 2,50 m depth. About 3000 tons of steel reinforcement were placed in up to 13 bottom layers and 8 top layers. The shear reinforcent consists of 25 000 ϕ25 which made impossible the introduction of bent or hooked bars into the reinforcement grid. Therefore, a plate-anchored shear reinforcement was designed for this purpose, as shown in Figure 2.18b.

(a) *View of the tower*[18]

(b) *Plate-anchored shear reinforcement*

Figure 2.18: Bankia Tower

2.3 SUMMARY

In this chapter some general and specific applications of headed reinforcement bars in RC structures have been presented. Starting from the earliest examples of metal devices connecting stones together, a brief review of its main application field — offshore structures — has been provided, together with some remarkable examples of real large concrete structures in which the massive use of mechanical anchorages is described in literature.

An overview of potential uses for this relatively new product has also been included. Many common structures, such as underpasses, overpasses or buildings present some construction problems for which mechanical anchorages are very suitable. They can potentially replace standard or L-shaped hooks, improving construction details and enabling a faster, flexible, and therefore a more economical assembly.

[17] First Repsol Tower and then Caja Madrid Tower.
[18] Credit: Luis Garcia.

Nowadays, the use of plate-anchored rebars in common structures is not yet widespread. Following first occasional uses by senior engineers in special structures, common structures can be the launching pad for these reinforcing rebars, making them more popular among young engineers.

Part II

FORMULATION OF A DESIGN METHODOLOGY

3 PROPOSED DESIGN METHODOLOGY

3.1 INTRODUCTION

It has been shown in Chapter 1 that some authors have already proposed design formulas based on experimental results, but, all of them are basically empirical or semi-empirical formulations similar to the ones used for headed anchor bolts. Particularly, the extensive studies carried out at University of Austin, Texas, have given way to design recommendations included in ACI code and to the design equations included in HRC catalogs, as explained in Section 1.2.4.

In all codes which comprise a section regarding mechanical anchorages, a series of limiting parameters that must be complied with is normally added to the design requirements, and no guidance is provided on situations in which the limiting parameters cannot be fulfilled (see Section 1.2.5). This is an undesirable situation, since there is a wide consensus in the technical community in preferring a physical model to an empirical or semi-empirical one. In fact, a general model could provide adequate results even in cases which fall outside of the experimental basis, therefore there is a need to develop a more rigorous model.

In order to develop a theoretical model, simple physical considerations on the capacity of concrete to carry concentrated loads are made, allowing the assessment of the contribution of the plate to total anchor capacity. In line with the Model Code approach for hooked bars, the total anchor capacity should be taken as a combination of the capacity provided by bond along the straight part of the bar with the capacity provided by the anchor plate. The proposed formulation is easy to use and allows the consideration of all relevant data in the design of anchor plates for specific conditions.

The proposed model is then compared to available experimental evidence and to existing models. The safety of the proposed model is evaluated applying the standard Eurocode format, though an equivalent safety level can be achieved usign the North American safety format.

3.2 DESCRIPTION OF THE PROPOSED MODEL

The problem of stresses generated by rebars anchored with plates is a deep anchorage problem, where failure may occur by side blowout (also traditionally know as bursting) due to tension stresses generated by the diffusion of compression forces from the plate to the concrete around it or by uniaxial compression, if the plate dimensions are close to the actual concrete block dimensions, or by triaxial compression if the plate dimensions are very small.

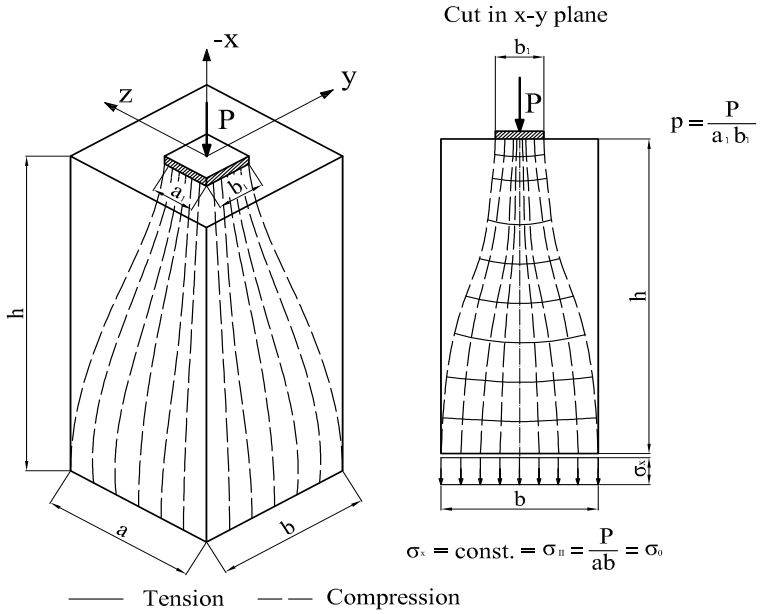

Figure 3.1: The problem of concentrated loads. Redrawn from [72].

The forces acting on concrete due to the plate anchor can be analyzed by using the classical formula for concentrated loads acting on a concrete block — the problem represented in Figure 3.1. The expressions date back to research carried out by Leonhardt and others, as already discussed in Sections 1.3.2 and 1.3.3. This problem is solved in most modern design codes (EN-1992-1-1, MC-2010, ACI-318) by strut-and-tie modeling using the model of Figure 3.2.

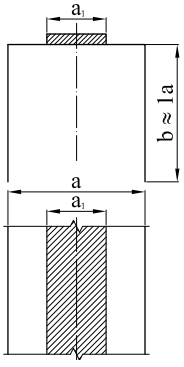

Considering a uniaxial problem, in which the load is applied along a strip (see scheme at the right), the force, which is concentrated within the area of the bearing, will spread out until uniform compression (σ_{Sd}) is achieved in the concrete block at a distance of approximately one block depth, a. Not all the force has to spread out since a part of it — that which is already distributed within the bearing width (a_1) — can follow a straight path.

The total force N_{Sd}, can be expressed as in the following equation:

$$N_{Sd} = \sigma_{Sd} a \tag{3.1}$$

The part of this force that does not need to be deflected, N^*_{Sd}, can be determined as in the following equation:

$$N^*_{Sd} = \sigma_{Sd} a_1 \tag{3.2}$$

Therefore the force that needs to be deflected can be determined as:

$$N_{Sd} - N^*_{Sd} = \sigma_{Sd}(a - a_1) = N_{Sd}\frac{a - a_1}{a} \tag{3.3}$$

Force $N_{Sd} - N^*_{Sd}$, located at the center of the block, has to be transferred to a distance of $a/4$ from the center of the block.

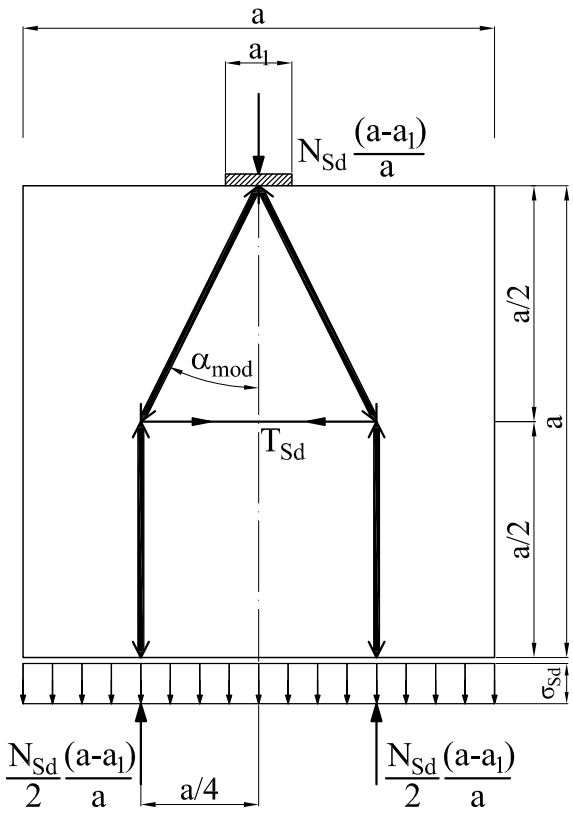

Figure 3.2: Strut-and-tie modeling for concentrated loading. Redrawn from [72].

It is assumed that this is accomplished in a distance equal to the width of the block, the center of gravity of the force being located at $a/2$. More generally a certain diffusion angle α_{mod} can be assumed. The value of the tangent of this angle, if the diffusion distance is taken as a, as in the case represented in Figure 3.2, would be $\tan \alpha_{mod} = 0{,}5$. More generally, the tensile force generated by the spreading out of the compression stresses can be expressed as in the following equation:

$$T_{Sd} = \frac{N_{Sd}}{2} \tan \alpha_{mod} \left(\frac{a - a_1}{a}\right) = \frac{N_{Sd}}{2} \tan \alpha_{mod} \left(1 - \frac{a_1}{a}\right) \tag{3.4}$$

For a three-dimensional problem, with a bearing plate of dimensions $a_1 \times b_1$ and a concrete block of dimensions $a \times b_{ef}$ (see definition of b_{ef} in next paragraph), this equation can be generalized as in Equation 3.5 where the geometric mean of the ratio between plate and block areas is used, instead of the ratio a_1/a.

$$T_{Sd} = \frac{N_{Sd}}{2} \tan \alpha_{mod} \left(1 - \sqrt{\frac{a_1 b_1}{a b}}\right) \tag{3.5}$$

In the case of a plate-anchored rebars, no transverse reinforcement is provided, so that this tensile force must be taken by the tensile resistance of concrete. For this, it may be assumed[1] that the area of concrete resisting this force has a depth of one block dimension (a) and an effective width, b_{ef}, which will be dependent on the width of the bearing plate and, again, on the height of the resisting section, a, and can be expressed as in the Equation 3.6:

$$b_{ef} = b_1 + \beta a \leqslant b \tag{3.6}$$

where β is a model parameter as is α_{mod}. Finally it must be taken into account that the distribution of tensile stresses within this area will not be uniform as shown on the right hand side of Figure 1.44. Therefore the mean admissible tensile stress can be expressed as κf_{ctd}, where κ is a stress distribution factor which must be smaller than 1,0 and f_{ctd} is the design tensile strength of concrete. If necessary, f_{ctd} may be obtained using formulations which take into account size effect (see for instance Cedolin and Cusatis [20]).

$$T_{Sd} \leqslant T_{Rd} \tag{3.7}$$

$$\frac{N_{Sd}}{2} \tan \alpha_{mod} \left(1 - \sqrt{\frac{a_1 b_1}{a b_{ef}}}\right) \leqslant \kappa f_{ctd} a b_{ef} \tag{3.8}$$

With these definitions, the resistance condition can expressed in terms of the ultimate load which produces side blowout failure, $N_{Rd,2}$, as in the following equations:

$$N_{Rd,2} = N_{Sd} \tag{3.9}$$

$$N_{Rd,2} = \frac{2\kappa f_{ctd} a b_{ef}}{\tan \alpha_{mod} \left(1 - \sqrt{\frac{a_1 b_1}{a b_{ef}}}\right)} \tag{3.10}$$

Equation 3.10 provides an expression for the resistance of the concrete block to side blowout failure. The model parameter values which will be adopted are the following:

[1] Other more complex assumptions are possible, such as modeling the failure surface with a pyramidal shape as proposed by DeVries in his *physical model* [35]. However, due to the uncertainties regarding stress distribution in concrete within the failure surface, such an assumption only leads to more complexity which is not rewarded by a better fit as shown in Section 3.4.

$\tan\alpha_{mod}$ will be taken as 0,5 as is normally done in code standards;

κ will be taken as 2/3 assuming a parabolic distribution of tensile stresses;

β will be taken as 1,0 assuming a lateral diffusion angle within the resisting section also equal to α_{mod} at failure. This value is consistent with the assumed diffusion angle in the perpendicular direction:

With these values Equation 3.10 simplifies to:

$$N_{Rd,2} = \frac{8}{3} f_{ctd} \frac{a b_{ef}}{1 - \sqrt{\frac{a_1 b_1}{a b_{ef}}}} \qquad f_{ctd} = 0{,}21 \sqrt[3]{f_{ck}^2} \tag{3.11}$$

Besides the blow-out failure, two types of compression failures need to be checked, as contemplated in all code standards with regard to concentrated loads. If the loading plate is very small, failure can occur in triaxial compression at the plate surface. If the plate is large with respect to the concrete block and the force too high, a uniaxial compression failure can occur. These failure modes are expressed in the well known equation:

$$N_{Rd,1} = \min\left(\sqrt{\frac{a b}{a_1 b_1}}; k_{ct}\right) a_1 b_1 f_{cd} \tag{3.12}$$

The value of k_{ct} normally adopted by code provisions, including EN 1992-1-1, is 3,0 or 3,3. In addition, the value given in codes implicitly includes a total safety factor of 3, as explained by Leonhardt and Mönnig [72]. Moreover, the original source used the cubic compressive strength, as pointed out in Section 1.3.3 (see also Spieth [112]). This is consistent with the well known fact that the capacity in triaxial loading of concrete is very high and that, for hydrostatic compression, failure would never be reached. See, for example, the model by Menétrey and Willam [86], the model proposed by Samani and Attard [106] or Montoya et al. [90].

Additionally, a reduction of the plate area considered in Eq. 3.12 is needed: in fact, the proposed model is derived from the classical formulation for concentrated loads, while, in the case of a rebar anchored by plate, the total force is applied only through the portion of plate in contact with the surrounding concrete[2]. Hence, the proposed equation for the compression failure is[3]:

$$N_{Rd,1} = \min\left(\sqrt{\frac{A_c}{A_n}}; 7{,}0\right) A_n f_{cd} \tag{3.13}$$

[2]No change is applied to the side blowout criterion, since in both cases the spread of the compression forces starts from the plate width.

[3]$A_n = a_1 b_1 - A_b$

The capacity of the anchor is the minimum between the two failure modes:

$$N_{Rd} = \min(N_{Rd,1}; N_{Rd,2}) \tag{3.14}$$

For uniaxial compression failure, the actual block dimensions are taken, since any reduction thereof significantly reduces correlation to test data. Even though design codes recommend to use a concrete resisting area having a similarity relationship to the plate dimensions, the application of such criteria to the experimental data available would predict compression failure in almost all cases whereas side blowout was the type of failure observed in all the tests carried out by DeVries. More on this discussion is given in Section 3.3. Also, experimental observation by Niyogi [97] confirms that defining the effective concrete area resisting compression as a homothetic figure of the load plate (as suggested by EN1992) tends to under-predict the measured capacities of eccentric specimens. Furthermore, testing a series of concrete blocks with a varying widths, Hawkins [50] observed that "the effective width of concrete contributing to the bearing capacity of the specimen can be as high as eight times the actual loaded width".

With regard to the block dimensions to be considered, these are determined either by the proximity of the edges from the center of the bar or by the proximity of other plate anchors. In order to illustrate this definition, Figure 3.3 shows two cases. In a) the block dimensions are determined by the spacing between bars, c_{sp2}, in b) the block dimensions are determined by the side cover.

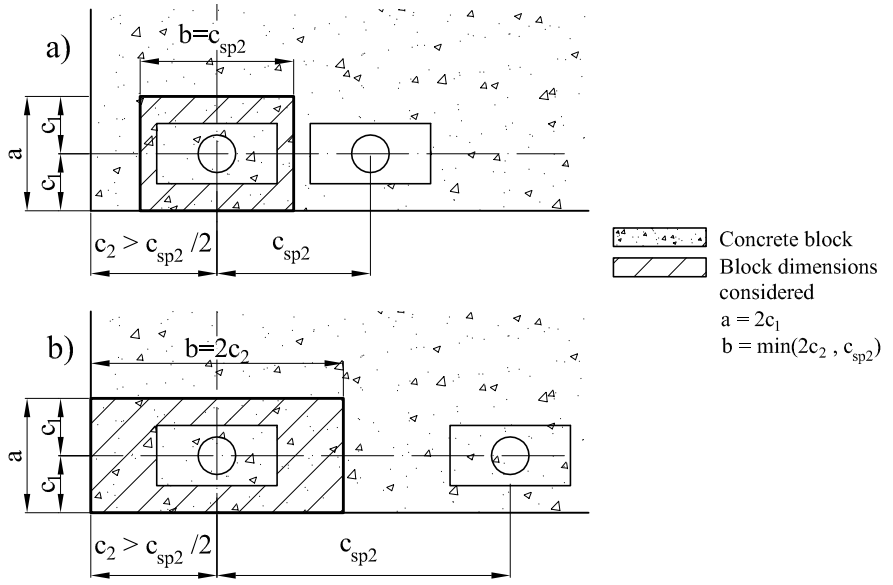

Figure 3.3: Block dimensions to be considered.
a) $c_{sp2}/2 < c_2$; b) $c_{sp2}/2 > c_2$

Another important point is that the model assumes uniform distribution of stresses on the plate and therefore it should be ensured that the plate is rigid. This condition can be met by providing a plate depth greater than half the distance between the bar edge and the plate edge. In such conditions, following the classical approach proposed by Brown [17], the flexibility factor of a circular foundation, K_f, can be defined as:

$$K_f = \frac{E_f}{E_s}\left(\frac{t}{a}\right)^3 \tag{3.15}$$

where E_f and E_s are, respectively, the foundation and soil modulus, t, a are the foundation thickness and radius. Assuming that the foundation is made of steel and the soil is made of concrete, with the proposed minimum geometric ratio of $t/a = 1/2$ the minimum foundation stiffness equals to:

$$K_f = \frac{E_s}{E_c}\left(\frac{1}{2}\right)^3 = \frac{E_s}{E_c}\cdot\frac{1}{8} \simeq 7/8 \tag{3.16}$$

This value implies an intermediate flexibility ($0{,}01 < K_f < 10$), close to the limit usually considered for rigid foundations ($K_f > 10$). Note that, for a flexible footing, the settlement at the edge is lower than the settlement of the center. For a square or rectangular footing, the corner settlements of a flexible foundation are $1/2$ those at the centerpoint. In the present case, the ratio can be calculated as:

$$\frac{s_{edge}}{s_{center}} = 1 - \frac{2.3}{4,6 + 10K_f} \simeq 0{,}83 \tag{3.17}$$

from the equations above, it can be stated that the aformentioned distinction between flexible and rigid plates is accurate enough for the purpose, since the stress distribution on the plate is almost uniform.

In the above derivation, no mention has been made regarding the contribution of bond to the anchorage of the bar. However the model can be easily extended to cover this case simply by summing the anchorage capacity of the plate to the anchorage of the bonded anchorage length. This additive model is supported by the experimental evidence of DeVries [35] and by the provisions of ACI-318-08 [5], which allows the use of relatively small anchorage plates provided that at least $1/3$ of the force is anchored by bond. It should also be pointed out the MC 2010 adopts a more cautious approach to this problem, as already reported in Chapter 1.

3.3 EXPERIMENTAL VALIDATION

The expression proposed in Section 3.2 has been tested against the data provided by the work of DeVries [35] and Niyogi [97]. DeVries carried out pull-out tests of plate-anchored bars embedded in large concrete blocks studying various parameters, among them, the effect of combining plate anchorages with bond between concrete and steel. In DeVries' tests, the connection between plate and bar was achieved by friction welding, and all tests considered are deep embedment-type tests. Since the amount of force taken by bond is not easy to determine experimentally, the proposed model is compared only to the 79 deep embedment tests having no bonded length.

For the comparison, the mean concrete strength was used and the maximum compressive stress under triaxial loading was considered as $7{,}0 \times f_c$ instead of $3{,}0 \times f_c$, for the reasons explained in the previous Section. Figure 3.4, Tables 3.1, 3.2 and 3.3 show the comparison of these test results with the model described in Section 3.2. In the tables, f_c is the mean concrete strength on the day the specimen was tested and c_1 and c_2 are covers measured from the center of the rebar to the closest edges, c_{sp2} is the distance between bars in cases where two bars were placed close together and tested simultaneously. Also given in the table are the block dimensions of the proposed model, a and b_{ef}. As can be seen, excellent agreement between the experimental data and the proposed model is obtained.

The correlation line has a slope close to 1,00 and a very high correlation coefficient. It can also be observed in the tables that the large errors concentrate in elements in which the compression condition is critical. In Figure 3.4 it can also be seen that significant relative errors are concentrated in elements with low capacity as is to be expected, whereas for larger resistances the relative error is small.

Niyogi [97] carried out an extensive experimental campaign on concrete blocks subjected to concentrated loads. For this comparison, only tests with block depth to side cover ratio greater than or equal to 2,0 were considered. This limitation avoids shorter prisms, that present a substantial reduction in tension stresses due to the constrained lateral strain. Complying with the restriction imposed, 383 tests were used.

A comparison of these test results and a statistical evaluation for the proposed model described in Section 3.2 is given in Figure 3.5 for Niyogi's tests. As can be seen, excellent agreement between the experimental data and the proposed model has been obtained. Further details on Niyogi's tests and disaggregated statistics are reported in Section 4.2.

#	Test ID	d_b [mm]	f_c [MPa]	a_1 [mm]	b_1 [mm]	c_1 [mm]	c_2 [mm]	c_{sp2} [mm]	Location	$N_{u,Exp}$ [kN]	a [mm]	b_{ef} [mm]	$N_{Ru,Model}$ [kN]	$N_{Ru,Model}$ / $N_{u,Exp}$
1	C1B1	25	25	70	70	35	457	–	Edge	239	70	140	229	0,96
2	C1B2	25	25	70	70	48	457	–	Edge	283	96	166	245	0,86
3	C1B3	25	25	70	70	48	457	–	Edge	272	96	166	245	0,90
4	C2B1	25	25	70	70	35	35	–	Corner	97	70	70	116	1,20[c]
5	C2B2	25	25	70	70	48	48	–	Corner	179	96	96	159	0,89[c]
6	C2B3	25	25	70	70	48	48	–	Corner	157	96	96	159	1,02[c]
7	C2B4	25	25	70	70	60	60	–	Corner	197	120	120	199	1,01[c]
8	C3B1	35	29	100	55	51	457	–	Edge	285	102	157	292	1,03
9	C3B2	35	29	55	100	51	457	–	Edge	284	102	202	322	1,13
10	C3B3	35	29	100	55	64	457	–	Edge	330	128	183	343	1,04
11	C3B4	35	29	55	70	64	457	–	Edge	335	128	228	389	1,16
12	C3B6	20	29	35	70	18	48	–	Corner	55	36	96	79	1,43[c]
13	C3B7	20	29	35	90	30	35	–	Corner	64	60	70	87	1,36[c]
14	C4B1	35	29	90	90	45	457	–	Edge	403	90	180	418	1,04
15	C4B2	35	29	90	90	51	457	–	Edge	476	102	192	414	0,87
16	C4B3	35	29	90	90	64	457	–	Edge	491	128	218	457	0,93
17	C4B4	35	29	90	90	76	457	–	Edge	512	152	242	523	1,02
18	C4B6	25	29	40	80	33	53	–	Corner	59	66	106	126	2,14[c]
19	C4B7	25	29	40	80	45	65	–	Corner	106	90	130	163	1,54[c]
20	C5B5	20	21	50	50	38	38	–	Corner	67	76	76	75	1,11[c]
21	C7B1	35	24	90	90	89	457	–	Edge	589	178	268	540	0,92
22	C7B2	35	24	90	90	102	457	–	Edge	609	204	294	631	1,04
23	C7B3	35	24	100	55	102	457	–	Edge	460	204	259	519	1,13
24	C7B4	35	24	55	100	102	457	–	Edge	464	204	304	588	1,27
25	C7B5	25	24	40	80	58	78	–	Corner	158	116	156	168	1,06[c]
26	C7B6	25	24	40	80	71	91	–	Corner	193	142	182	201	1,04[c]

Table 3.1: Date of tests by DeVries and comparison (tests from 1 to 26). Source: [35] (c = test controlled by compression condition)

#	Test ID	d_b [mm]	f_c [MPa]	a_1 [mm]	b_1 [mm]	c_1 [mm]	c_2 [mm]	c_{sp2} [mm]	Location	$N_{u,Exp}$ [kN]	a [mm]	b_{ef} [mm]	$N_{Ru,Model}$ [kN]	$N_{Ru,Model}$ / $N_{u,Exp}$
27	C7B7	25	24	40	80	46	91	–	Corner	87	92	172	162	1,86[c]
28	C8B1	35	24	90	90	89	89	–	Corner	355	178	178	361	1,02[c]
29	C8B2	35	24	90	90	127	127	–	Corner	502	254	254	515	1,03[c]
30	C8B3	35	24	100	55	89	89	–	Corner	283	178	178	288	1,22[c]
31	C8B4	35	24	100	55	127	127	–	Corner	411	60	254	411	1,00[c]
32	C8B5	20	24	35	70	30	457	–	Edge	127	90	130	118	0,93
33	C8B6	20	24	70	35	45	457	–	Edge	177	90	125	140	0,79
34	C8B7	20	24	35	70	45	457	–	Edge	155	50	160	163	1,05
35	C12B5	25	25	40	80	25	457	102	Edge	135	50	102	168	1,24
36	C12B6	25	25	40	80	25	457	152	Edge	182	76	130	149	0,82
37	C12B7	25	25	40	80	38	457	102	Edge	167	76	102	148	0,89
38	C12B8	25	25	40	80	38	457	152	Edge	188	90	152	167	0,89
39	C15B1	35	19	57	57	45	305	–	Edge	162	90	147	149	0,92
40	C15B2	35	19	40	80	45	305	–	Edge	185	90	170	161	0,87
41	C15B3	35	19	70	70	45	305	–	Edge	221	90	160	197	0,89
42	C15B4	35	19	49	99	45	305	–	Edge	217	90	189	208	0,96
43	C15B5	35	19	55	100	45	305	–	Edge	194	90	190	225	1,16
44	C15B6	35	19	80	80	45	305	–	Edge	283	90	170	247	0,87
45	C15B7	35	19	90	90	45	305	–	Edge	374	90	180	315	0,84
46	C16B1	25	19	33	33	45	305	–	Edge	93	90	123	80	0,86[c]
47	C16B2	25	19	57	57	45	305	–	Edge	154	90	147	149	0,97
48	C16B3	25	19	57	57	45	305	–	Edge	168	90	147	149	0,89
49	C16B4	25	19	57	57	45	305	–	Edge	176	90	147	149	0,85
50	C16B5	25	19	40	80	45	305	–	Edge	162	90	170	161	0,99
51	C16B6	25	19	40	80	45	305	–	Edge	163	90	170	161	0,99
52	C16B7	25	19	40	80	45	305	–	Edge	180	90	170	161	0,89

Table 3.2: Date of tests by DeVries and comparison (tests from 27 to 52). Source: [35] (c = test controlled by compression condition)

#	Test ID	d_b [mm]	f_c [MPa]	a_1 [mm]	b_1 [mm]	c_1 [mm]	c_2 [mm]	c_{sp2} [mm]	Location	$N_{u,Exp}$ [kN]	a [mm]	b_{ef} [mm]	$N_{Ru,Model}$ [kN]	$N_{Ru,Model}$ / $N_{u,Exp}$
53	C16B8	25	19	40	80	45	305	–	Edge	149	90	170	161	1,08
54	C17B1	25	19	33	98	45	305	–	Edge	144	90	188	171	1,19
55	C17B2	25	19	33	98	45	305	–	Edge	165	90	188	171	1,04
56	C17B3	25	19	33	98	45	305	–	Edge	199	90	188	171	0,86
57	C17B4	25	19	70	70	45	305	–	Edge	238	90	160	197	0,83
58	C17B5	25	19	70	70	45	305	–	Edge	235	90	160	197	0,84
59	C17B6	25	19	70	70	45	305	–	Edge	222	90	160	197	0,89
60	C17B7	25	19	49	99	45	305	–	Edge	222	90	189	208	0,94
61	C17B8	25	19	55	100	45	305	–	Edge	233	90	190	225	0,97
62	C17B9	25	19	80	80	45	305	–	Edge	285	90	170	247	0,87
63	C17B10	25	19	80	80	45	305	–	Edge	331	90	170	247	0,75
64	C17B11	25	19	70	70	45	305	–	Edge	183	90	160	197	1,08
65	C17B12	25	19	77	77	45	305	–	Edge	193	90	167	230	1,19
66	C18B1	35	44	55	100	45	305	–	Edge	411	90	190	394	0,96
67	C18B2	35	44	55	100	51	305	–	Edge	432	102	202	425	0,98
68	C18B3	35	44	55	100	64	305	–	Edge	517	128	228	514	0,99
69	C18B4	35	44	90	90	45	305	–	Edge	555	90	180	551	0,99
70	C18B5	35	44	40	80	45	305	–	Edge	238	90	170	281	1,18
71	C18B6	35	44	40	80	64	305	–	Edge	330	128	208	406	1,23
72	C18B7	25	44	40	80	25	457	102	Edge	204	50	102	245	1,20
73	C19B1	35	44	70	70	45	305	–	Edge	360	90	160	345	0,96
74	C19B2	35	44	70	70	64	305	–	Edge	470	128	198	451	0,96
75	C19B3	25	44	40	80	45	305	–	Edge	287	90	170	281	0,98
76	C19B4	25	44	40	80	25	305	–	Edge	196	50	130	217	1,11
77	C19B5	25	44	57	57	45	305	–	Edge	295	90	147	262	0,89
78	C19B6	25	44	57	57	30	305	–	Edge	261	60	117	219	0,84
79	C19B7	25	44	40	80	25	457	152	Edge	224	50	130	217	0,97

Table 3.3: Date of tests by DeVries and comparison (tests from 27 to 52). Source: [35]

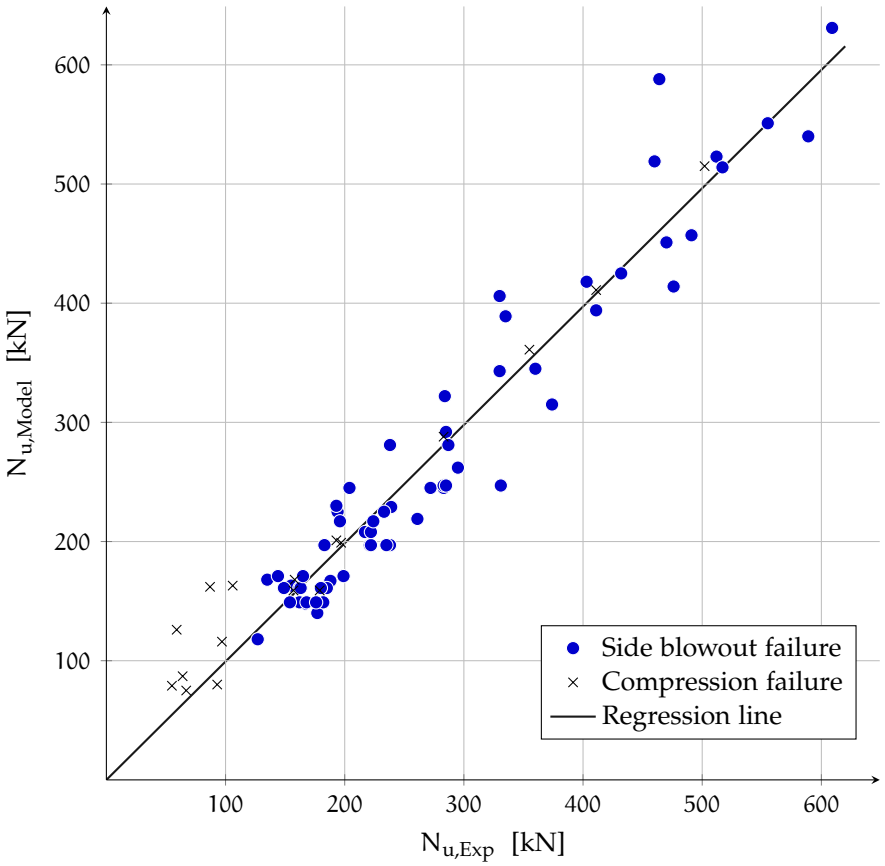

Statistics

Regression line	$N_{u,Model}/N_{u,Exp}$	max(Err)	124,0
	$\bar{x} = 1{,}0294$	min(Err)	−84,2
$m = 0{,}9929$	$s = 0{,}2157$	mean(Err)	−0,3
$R^2 = 0{,}9351$	$CoV = 0{,}2095$	s(Err)	34,44

Figure 3.4: Tests by DeVries: Comparison of predicted ultimate values and measured ultimate values. Statistics defined in Appendix A

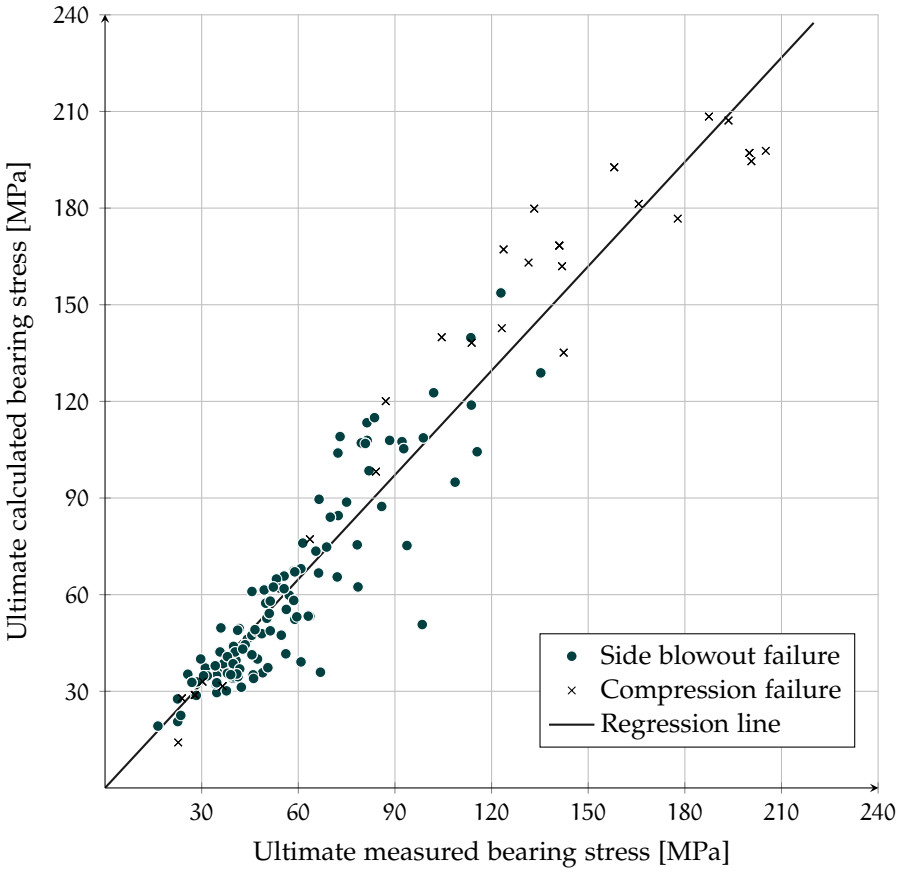

Statistics

Regression line	$N_{u,Model}/N_{u,Exp}$	max(Err)	46,6
	$\bar{x} = 1{,}0534$	min(Err)	−47,8
$m = 1{,}0796$	$s = 0{,}1861$	mean(Err)	5,0
$R^2 = 0{,}9171$	$CoV = 0{,}1766$	s(Err)	14,67

Figure 3.5: Tests by Niyogi: Comparison of predicted ultimate values and measured ultimate values. Statistics defined in Appendix A

3.4 COMPARISON TO OTHER MODELS

DeVries has proposed [35] three models to deal with the anchorage capacity of deeply embedded bars with plate anchorages. These models are also included in [39], and one of them is the basis for the design which has been used in recent years by HRC [53].

The first model presented in reference [35] is a *best fit model* using only 57 edge tests (no corner bars) assuming the main parameters are side cover, net area of the plate and concrete strength. This model is limited in its application because it is fitted to a very particular experimental set with exponents having three digits. DeVries also proposes two other models, a similar model with less extravagant exponents, the so-called *physical model* (having exponents of 1,33 for cover or 0,333 for plate area) and a third model (referred to by DeVries as *simplified model*) obtained through simplification of the exponents for the net bearing area, A_n, the side cover c_1 and for the compressive stress. The *physical model* is a semi-empirical model, which assumes the blow-out surface to have a pyramidal shape with a height equal to the side cover of the bar. The *simplified model*, includes a generalization to take into account corner positioning by applying expressions taken from CEB bulletin No. 226 [8] as explained in Section 1.3.1.1. This last equation has been included in HRC catalogs [53]. These models are given in the following equations:

$$P_{u,\text{best fit}} = 0{,}0252\ {c_1}^{0{,}609} {A_n}^{0{,}577} {f_c}^{0{,}671} \tag{3.18}$$

$$P_{u,\text{physical model}} = 0{,}0107\ {c_1}^{1{,}33} {A_n}^{0{,}333} {f_c}^{0{,}667} \tag{3.19}$$

$$P_{u,\text{HRC}} = \Psi \frac{A_{bo}}{A_{bon}}\ 0{,}017\ c_1 \sqrt{A_n f'_c} \tag{3.20}$$

where $A_n = a_1 b_1 - A_b$ and

$$\Psi = 0{,}7 + 0{,}3\frac{c_2}{3c_1} \leqslant 1{,}0 \tag{3.21}$$

$$\frac{A_{bo}}{A_{bon}} = \frac{A_{bo}}{36{c_1}^2} \tag{3.22}$$

Equation 3.20 is different with respect to Equation 1.15 because the former is the characteristic equation, whereas the latter is the design equation (see Section 1.2.4).

These expressions are compared to the proposed model, using various statistical evaluations, to the 63 edge tests detailed in Tables 3.1, 3.2 and 3.3, in Table 3.4 and to all 79 deep embedment tests in Table 3.5.

The tables include the slope of the regression curve, which should approach 1,00, the correlation coefficient R^2, the maximum and minimum error, the mean value of the error, the mean value of the ratio

			$N_{u,Model} - N_{u,Exp}$				$N_{u,Model}/N_{u,Exp}$		
Model	m	R^2	Max(Err)	Min(Err)	mean(Err)	s(Err)	Mean	s	**CoV** [%]
Best fit model	1,02	0,95	130	−52	−14	30,43	1,04	0,112	**11**
Physical model	1,01	0,80	146	−172	0	58,15	0,96	0,210	**22**
Simple model	0,98	0,88	126	−112	7	47,51	0,97	0,153	**16**
Proposed model	0,99	0,93	124	−84	−5	34,81	0,98	0,123	**13**

Table 3.4: Comparison of models with DeVries tests (only 63 edge tests)

			$N_{u,Model} - N_{u,Exp}$				$N_{u,Model}/N_{u,Exp}$		
Model	m	R^2	Max(Err)	Min(Err)	mean(Err)	s(Err)	Mean	s	**CoV** [%]
Best fit model	1,08	0,80	130	−163	−29	43,74	1,23	0,448	**37**
Physical model	1,14	0,64	146	−526	−29	105,24	1,15	0,449	**39**
Simple model	0,98	0,90	123	−87	8	38,40	1,00	0,191	**19**
Proposed model	0,99	0,94	124	−84	0	34,40	1,03	0,215	**21**

Table 3.5: Comparison of models with DeVries tests (all 79 tests)

between predicted ultimate axial load and the corresponding experimental value $N_{u,Model}/N_{u,Exp}$, its standard deviation and its coefficient of variation (CoV). It can be seen that the Best fit model is indeed just that for the edge tests. It can also be seen that the proposed model follows closely. When examining, however, all 79 deep embedment tests, the Best Fit model's performance is much less impressive and leans to the unsafe side, while this proposal achieves the best results in most statistical categories. This is a good example of the need for good physical models and of the danger involved in extrapolating outside of the empirical basis of empirically-based formulae.

Figure 3.6 shows the comparison between the De Vries' simplified model (HRC design equation) and the 79 deep embedment tests with no bonded length. Comparison between this figure and Figure 3.4 clearly shows a better behavior of the proposed model.

3.5 THE QUESTION OF SAFETY: AMERICAN MODEL VS EUROPEAN MODEL

With regard to the introduction of safety into the model of plate anchors proposed in this document, the expressions derived in Section 3.2 follow the approach of EN 1992-1-1-§8.4 for the anchorage of longitudinal reinforcement in which the design force in the bar is compared to the bond capacity of concrete using the design tensile strength. Basically this means that the bar strength is calculated using the yield strength of steel divided by the material safety factor for steel γ_s, and the tensile strength of concrete used is the lower-bound characteristic value divided by the material safety factor for concrete γ_c.

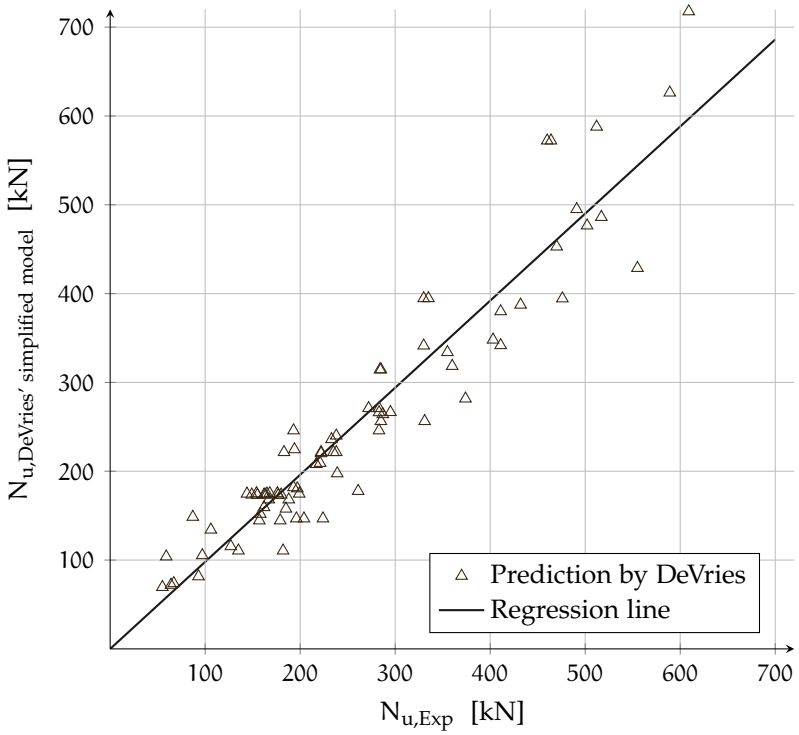

Figure 3.6: Comparison of formula adopted by HRC — the DeVries' simplified expression — to all 79 deep embedment tests (to be compared with Figure 3.4)

For the ACI-318-08 approach, the material strengths are used with their characteristic values while the strength of the anchorage is reduced by multiplying the ultimate load by a strength reduction factor ϕ. This factor is not explicitly given for anchorage problems in ACI-318-08 [5]. However, it may be assumed that the value used for a strut-and-tie models and bearing areas in such models in paragraph 9.3.2.6, of $\phi = 0{,}75$, may be adequate. It should be noted that with this definition the global safety is basically the same for the American and European approaches since $\gamma_s/\gamma_c = 1{,}15/1{,}50 = 0{,}77 \simeq \phi$.

Figure 3.7 compares the design resistance predicted by the proposed model to the experimental results by De Vries. The design resistance is obtained by dividing the lower-bound tensile strength of concrete by the material safety factor (γ_c = 1,5) and considering the characteristic compressive strength of concrete, estimated as the mean strength minus 8 MPa. As can be seen the proposed model provides an adequate safety margin, with a mean value of $1/0{,}39 = 2{,}56$. All results, except one which falls very close to the limit, are within the safety zone.

The same comparison is presented in Figure 3.8 for Niyogi's tests. Results are analogous to the previous ones and all points are within the safety zone.

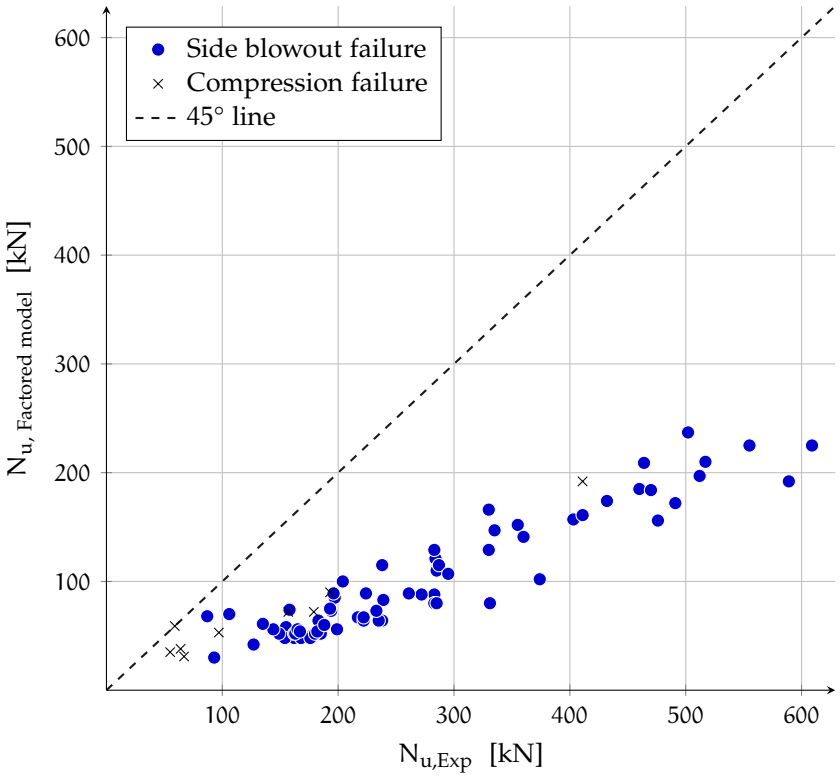

Figure 3.7: Comparison of factored model capacity to tests by DeVries

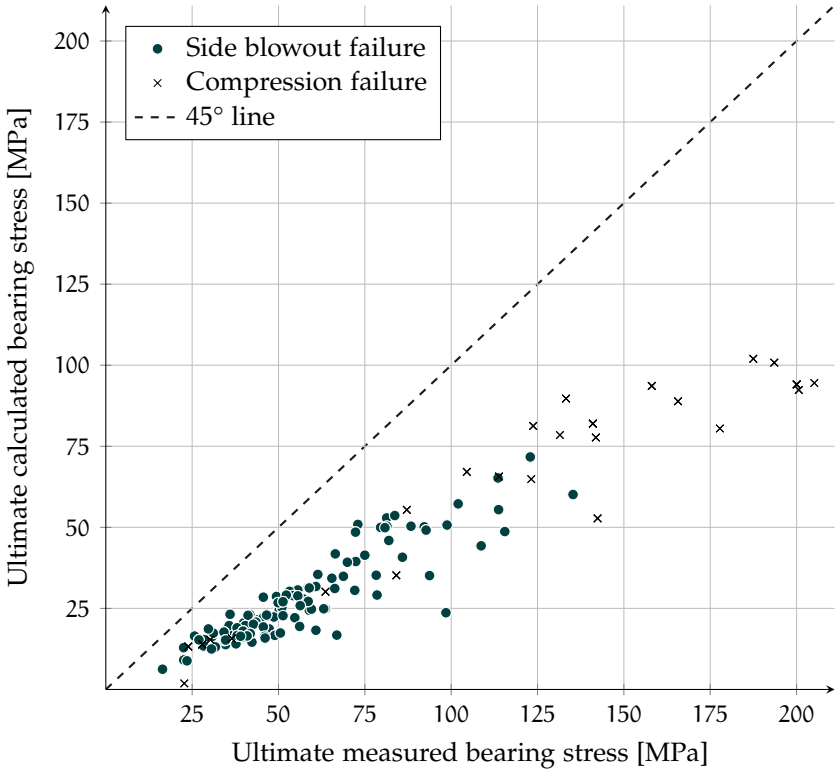

Figure 3.8: Comparison of factored model capacity to tests by Niyogi

3.6 APPLICATION EXAMPLE

In order to illustrate the use of the proposed equation, an example is provided using one of the tests carried out by DeVries (Test ID: C12B7 – see Figure 3.9). In this test, two bars are placed along the edge of a concrete block, with a side cover of $c_1 = 38$ mm and a spacing of 102 mm. The distance to the other edge of the block measured from the center of each bar is 457 mm. The dimensions of the plate are $a_1 \times b_1 = 40 \times 80$ mm. A blow-out failure occurred at a load of 167 kN.

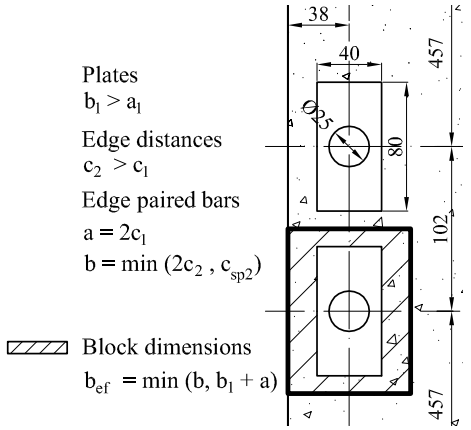

Figure 3.9: Design example: detail of test 37 (Test ID: C12B7)

3.6.1 Calculation with mean values

3.6.1.1 *Verification of side blowout failure*

For this verification the dimensions to be considered for the concrete block are:

$$a = 2c_1 = 2 \cdot 38 = 76 \text{ mm}$$

$$b = \min(2c_2; c_{sp2}) = \min(2 \cdot 457; 102) = 102 \text{ mm}$$

$$b_{ef} = b_1 + \beta a \leqslant b$$

$$b_{ef} = 80 + 1{,}00 \cdot 76 = 156 \leqslant 102$$

$$N_{Rd,2} = \frac{8}{3} \cdot 0{,}3 \cdot 25^{2/3} \cdot \frac{76 \cdot 102}{1 - \sqrt{\frac{40 \cdot 80}{76 \cdot 102}}} = 148 \text{ kN}$$

3.6.1.2 *Verification of compression failure*

For the verification of the compression failure, in this case, the two anchorages need to be considered as a whole. The width corresponding to each plate would be half of the width of the block.

$$a = 2c_1 = 2 \cdot 38 = 76 \text{ mm}$$
$$b = \frac{2 \cdot 457 + 102}{2} = 508 \text{ mm}$$
$$A_n = a_1 \cdot b_1 - A_b = 40 \cdot 80 - 491 = 2709 \text{ mm}^2$$
$$N_{Rd,1} = \min\left(\sqrt{\frac{76 \cdot 508}{2709}}; 7{,}0\right) \cdot 2709 \cdot 25 = 256 \text{ kN}$$

The expected failure mode is side blowout, with a load of 148 kN. The ultimate load of specimen C12B7 was, as already stated, 167 kN.

3.6.2 Calculation with design values

$$N_{Rd,1} = \min\left(\sqrt{\frac{76 \cdot 508}{2709}}; 7{,}0\right) \cdot 2709 \cdot \frac{25 - 8}{1{,}5} = 116 \text{ kN}$$
$$N_{Rd,2} = \frac{8}{3} \cdot \frac{0{,}21 \cdot (25 - 8)^{2/3}}{1{,}5} \cdot \frac{76 \cdot 102}{1 - \sqrt{\frac{40 \cdot 80}{76 \cdot 102}}} = 54 \text{ kN}$$

The design failure mode is side blowout, with a load of 54 kN.

3.7 SUMMARY

From the above considerations, the following conclusions can be drawn:

- A new and simple physical model has been proposed for the analysis of bars anchored by a steel plate, taking into account all relevant parameters: edge cover, plate dimensions and material strengths of concrete and steel.

  Even though model parameters have been chosen according to rational criteria, avoiding curve-fitting, the comparison to experimental data is more than satisfactory. The model shows very close performance to a best fit equation, included in Reference [35] for edge tests performed by DeVries. The model also performs well when corner and edge results are mixed together showing significant improvement when compared to other existing models.

- The safety format proposed is consistent with Eurocode. The model can also be adapted to fit a North American-type safety format without altering the global safety factor. The model

safety has been evaluated considering characteristic concrete strength and a material safety factor for the tensile strength of concrete (γ_c) equal to 1,5. With this format all examined experimental values fall within the safety zone with the exception of one value with falls very close to the limit of this safety zone. It can, therefore, be stated that the proposed formula is adequate, using standard safety format.

4 ON THE PROPOSED DESIGN FORMULATION

4.1 INTRODUCTION

A simple design formulation for the assessment of the anchorage capacity of headed reinforcement bars has been presented in Chapter 3. Comparisons with the DeVries' deep embedment tests, the most extensive pullout campaign in literature, have been reported in order to show the adequacy of the model to the experimental results. Niyogi's bearing tests were also reported given the analogy between the bearing strength of a concrete block and the anchorage capacity of a plate-anchored reinforcement bar, although they did not deal exactly with the same problem.

However, no disaggregated results were presented for Niyogi's campaign: for this reason, in the first part of the chapter the tests used for the comparison are listed in detail. Some other well-known studies on the bearing strength of concrete [50, 97, 121] are also incorporated to the experimental database used for the comparison. Good agreement is again found between the proposed formula and these, independent, experimental tests. The proposed formula is also compared to deep embedded anchor bolt tests [42, 49], again providing a good approximation.

In the second part of this chapter, the design formula has been plotted in order to obtain capacity curves showing the anchorage capacity as a function of the plate dimensions and positioning, and *en passant* illustrating the domain of each failure criterion. Typically, the dominant criterion for plate dimensions of about one half of the block dimension is the blowout failure.

Finally, the influence of the development length on the total anchorage capacity is analyzed with the aid of the advanced finite element software ATENA. The problem of bond and bearing interaction is commented in relation to others authors' proposals and code provisions.

4.2 BEARING CAPACITY

A total of 1126 tests were selected for the comparison among the work cited in Section 1.3.2, of which 387 are related to different test conditions, each of them being repeated from two up to eight times. Statistics for all bearing capacity tests are collected in Table 4.4.

Two limitations to the theoretical model are considered. Tests which does not respect these limitations are excluded from the comparison:

- The first limitation, already introduced in the previous chapter (see Section 3.3), regards tests with depth to side cover ratio lower than 2,0. The limitation is introduced because the proposed formulation aims at designing deep embedded plate: since Niyogi's tests show that the bearing strength increases with decreasing height of the specimens[1], it was preferable to remove such data from the database.

- The second limitation is applied to circular plates with $d \leqslant 25$ mm or rectangular plates with a minimum side smaller than 22 mm. This limitation aims at excluding very small loading area, out of the range normally met by commercial anchorage plates.

Complete data tables are available in Appendix B. Omitted tests according to both conditions are highlighted in gray, while the minimum value between the two failure criteria is reported in red.

4.2.1 Niyogi

Niyogi's [97] campaign is detailed in Table 4.1 in order to clarify the database used for the comparison in the previous chapter. The specimens were tested in a different number of samples, from two to six tests each. Niyogi provided data for both tensile and compressive concrete strength, which are taken for the comparison as mean values. Many tests in subgroups from one to three (strip loading) have a plate aspect ratio (b_1/a_1) greater than three, up to 16. A small increase of calculated[2]/measured ratios can be observed for specimens with higher aspect ratios, however, the proposed formula is conservative for aspect ratios lower than 3,0, a limit normally met by commercial plate-anchored rebars. Table 4.2 illustrates this behavior subdividing strip tests according to the aspect ratio of their loading plate. Complete data from Niyogi's tests are reported in Tables B.1 to B.9.

[1] Especially in the range of A/A_1 below 8, to which many tests belong. The increase in strength was probably due to the greater influence of base friction.

[2] Values are calculated with the proposed formula, using Equations 3.11 to 3.14.

NIYOGI TESTS			
1	Strip loading	30	tests on cube specimens
2	Strip loading	25	tests on rectangular block specimens
3	Strip loading	34	tests on square prism specimens
4	Rectangular plate loading	55	tests on cube specimens
5	Rectangular plate loading	16	tests on square prism specimens
6	Concentric loading	55	tests on cube specimens
7	Concentric loading	46	tests on square prism specimens
8	Uniaxial eccentric loading	53	tests on square prism specimens
9	Biaxial eccentric loading	69	tests on square prism specimens
TOTAL		383	tests (139 different)

Table 4.1: Disaggregated quantities for Niyogi's tests.
19 tests — cube specimens with square steel plate — were added to series #6 from [98] (8 different). Plate of other materials were not considered

	Aspect ratio (a_1/b_1)						
	$\leqslant$ 2,0	$\leqslant$ 3,0	$\leqslant$5,0	$\leqslant$ 10,0	3,0 - 5,0	5,0 - 10,0	10,0 - 16,0
mean($N_{u,Model}/N_{u,Exp}$)	0,99	1,00	1,04	1,05	1,11	1,13	1,31
s($N_{u,Model}/N_{u,Exp}$)	0,19	0,17	0,17	0,12	0,14	0,15	0,14
CoV%($N_{u,Model}/N_{u,Exp}$)	19	17	16	12	12	13	11
Number of tests	19	28	44	72	16	28	17

Table 4.2: Influence of plate aspect ratio in Niyogi's tests (subgroup 1)

WILLIAMS TESTS			
1	Variation in height	48	tests on square prism
2	Central loading on prism and cubes	183	tests on prism and cubes
3	Square, rectangular or strip loading	120	tests on 102 mm cubes with eccentricity
4	Square, rectangular or strip loading	99	tests on 152 mm cubes with eccentricity
5	Effective width phenomenon	54	tests on prism
TOTAL		504	tests (168 different)

Table 4.3: Disaggregated quantities for Williams' tests

4.2.2 Hawkins

Hawkins [50] tested 239 specimens subjected to concentric and eccentric loading, with the setup shown in Figure 4.1.

The concrete strength ranged between 12 and 52 MPa, similarly to Niyogi's tests. As in the previous case there were only 80 different geometries, with two to eight identical specimens. Hawkins provided only compressive strength: the mean tensile strength is calculated here accordingly to the EC formula $f_{ctm} = 0{,}3\ f_{ck}^{2/3}$. Comparisons be-

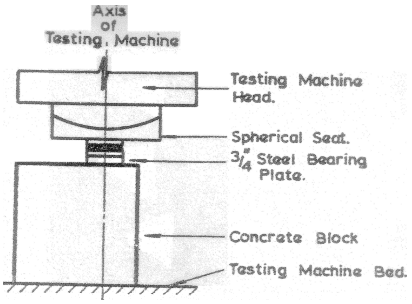

Figure 4.1: Test arrangement for eccentric loading [50]

tween measured and predicted stress are shown in Figure 4.3 and Figure 4.4, in which good agreement between measured and calculated values can be observed. Complete data are reported in Table B.10 and B.11, while statistics are reported in Table 4.4.

4.2.3 Williams

Williams [121] tested over 1000 specimens of concrete loaded over limited areas, under 382 different test conditions, with the setup shown in Figure 4.2. In this work only 187 different test conditions are considered[3], each of them repeated three times. From the first subgroup are excluded 6 different tests, given the low heigth of the concrete block (first limitation), while from the next three subgroups are excluded 13 different tests, given the very reduced plate dimension (second limitation). Both tensile and compressive concrete strengths are available.

The campaign is summarized in Table 4.3 and in Figures 4.5 to 4.8 are shown the corresponding scatter plot. A total of 4 tests fall outside the safety zone (see Figure 4.7), lying very close to the 45° line. Tests with an estimated failure mode by compression criteria are depicted with filled markers.

[3]The excluded tests are related to variables not considered in the present work, as the effect of low-friction base, the effect of loading medium, microconcrete specimens and others.

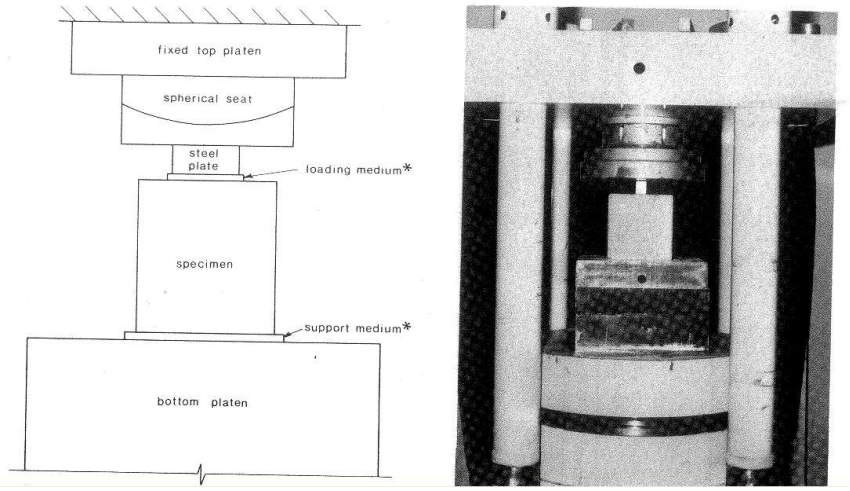

Figure 4.2: The 2000 kN test frame, set up for a strip loading test [121]

4.3 HEADED BOLTS

In this section some comparisons of estimated ultimate loads and experimental results of studies on deep embedded anchor bolts — introduced in Section 1.3.1 — are presented.

Furche and Eligehausen [44] tested many deep embedment anchors, but only 20 of them are reported in Table B.18, whose data are taken from DeVries' dissertation.

The bolt diameter (25 mm), the concrete strength (26,4 MPa) and the splitting tensile strength (2,5 MPa) were kept constant. Plate area to bar area ratio varies from 1,5 up to 3,2, small ratios typical of headed studs. The result of the comparison is plotted in Figure 4.9, while in Figure 4.10 is shown a zoom of the previous figure.

Hasselwander et al. [49] tested 48 specimens with plate area to bar area ratio ranging from 2,9 to 12,2. The result of the comparison is plotted in same graph of the previous series. Full data are reported in Table B.19.

All tests fall within the safety zone, as shown in Figure 4.11–4.12. Statistics are reported in Table 4.4 while complete data are available in Appendix B. Although the experimental data from Furche-Eligehausen are not estimated with great accuracy by the proposed formula (CoV=25%), statistics are affected by three bolt with very reduced net area (only 3 mm of difference between external diameter and bar diameter). For this reason, statistics has been calculated also for a reduced subgroup of seventeen tests, showing a significantly improvement.

					$N_{u,Model} - N_{u,Exp}$				$N_{u,Model}/N_{u,Exp}$		
Tests	Different	Model	m	R^2	Max(Err)	Min(Err)	mean(Err)	s(Err)	Mean	s	CoV [%]
30	9	Niyogi (1)	1,19	0,91	32	−1	6,7	11,2	1,10	0,148	13
25	12	Niyogi (2)	1,07	0,76	15	−7	2,1	6,3	1,05	0,143	13
34	17	Niyogi (3)	1,27	0,89	36	−9	10,2	11,9	1,18	0,220	19
55	18	Niyogi (4)	1,21	0,92	47	−3	17,4	16,3	1,17	0,149	13
16	8	Niyogi (5)	1,05	0,40	10	−7	3,3	6,2	1,07	0,118	11
55	15	Niyogi (6)	1,06	0,94	27	−7	5,5	10,5	1,07	0,116	11
46	19	Niyogi (7)	1,06	0,94	32	−13	6,8	13,2	1,07	0,165	15
53	17	Niyogi (8)	1,00	0,83	31	−48	−2,7	19,4	0,94	0,222	24
69	24	Niyogi (9)	1,00	0,91	24	−22	−2,5	10,7	0,94	0,157	17
383	139	Niyogi – all tests	1,08	0,92	47	−48	5,0	14,7	1,05	0,186	18
103	38	Hawkins – concentric loading	1,14	0,93	66	−20	11,3	19,6	1,10	0,164	15
136	42	Hawkins – eccentric loading	0,91	0,84	27	−42	−7,8	15,9	0,87	0,190	22
239	80	Hawkins – all tests	1,04	0,89	66	−42	0,5	17,6	0,97	0,214	22
48	16	Williams (1)	1,07	0,59	32	−34	9,4	10,8	1,18	0,257	22
183	61	Williams (2)	1,25	0,87	113	−12	22,5	20,7	1,25	0,272	22
120	40	Williams (3)	1,02	0,82	37	−35	4,7	8,8	1,11	0,203	18
99	33	Williams (4)	1,10	0,80	92	−42	6,7	13,3	1,11	0,267	24
54	18	Williams (5)	0,83	0,46	23	−58	−7,7	14,4	1,00	0,362	36
504	168	Williams – all tests	1,13	0,81	113	−58	10,7	15,6	1,15	0,275	24
20	5	Furche - Eligehasuen	0,89	0,48	29	−63	−16,5	28,5	0,88	0,221	25
17	4	Furche - Eligehasuen	0,92	0,34	29	−63	−9,5	24,8	0,95	0,143	15
48	43	Hasselwander et al.	1,23	0,92	334	−70	112,3	125,9	1,12	0,242	22

Table 4.4: Comparison of proposed model with bearing tests and headed bolt tests. Data in [MPa] for bearing tests, in [kN] for haded bolt tests

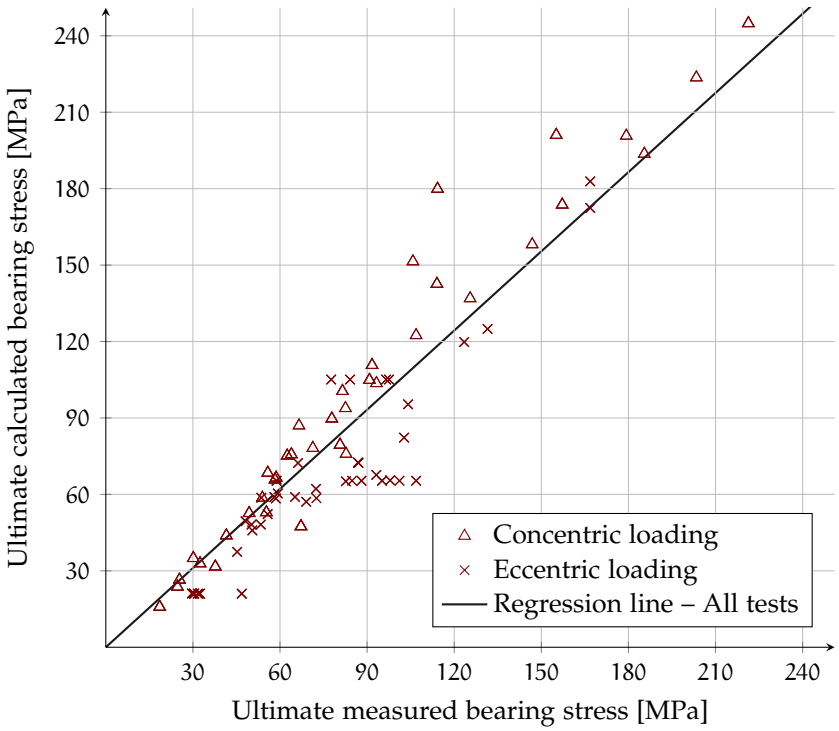

Figure 4.3: Tests by Hawkins: comparison of predicted ultimate values and measured ultimate values

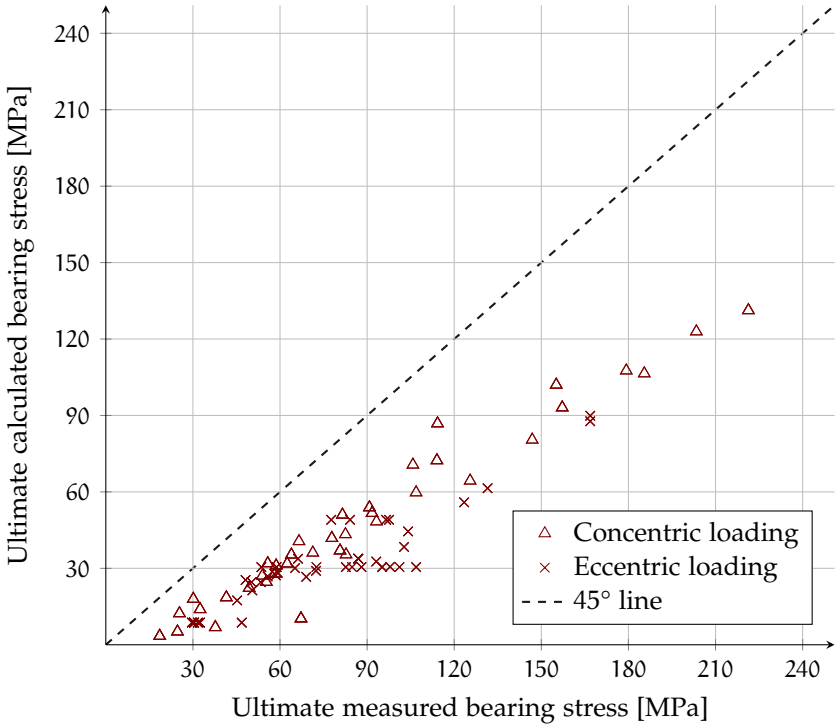

Figure 4.4: Comparison of factored model capacity to tests by Hawkins

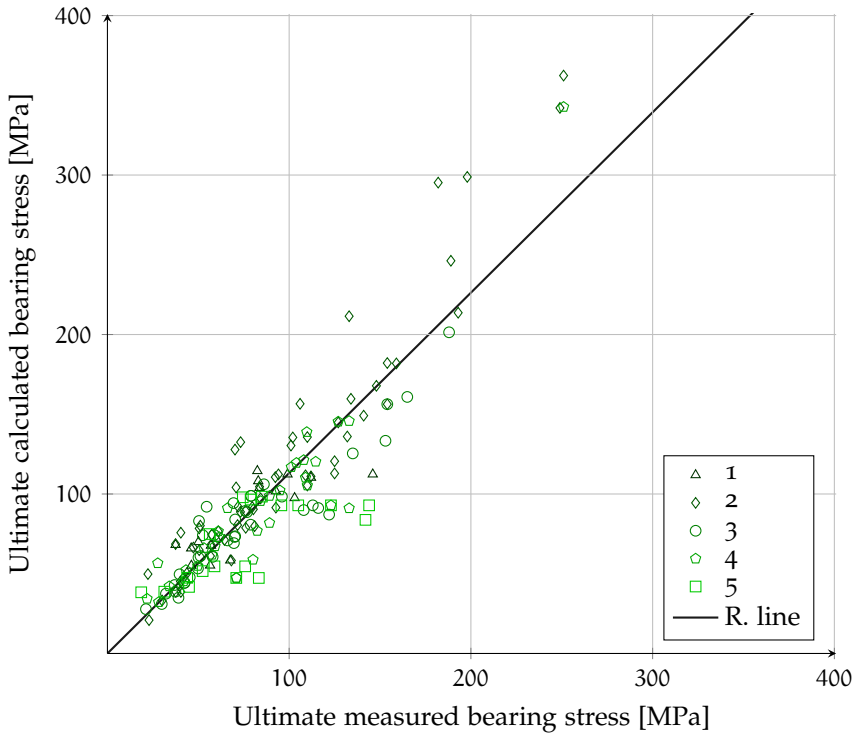

Figure 4.5: Tests by Williams: comparison of predicted ultimate values and measured ultimate values

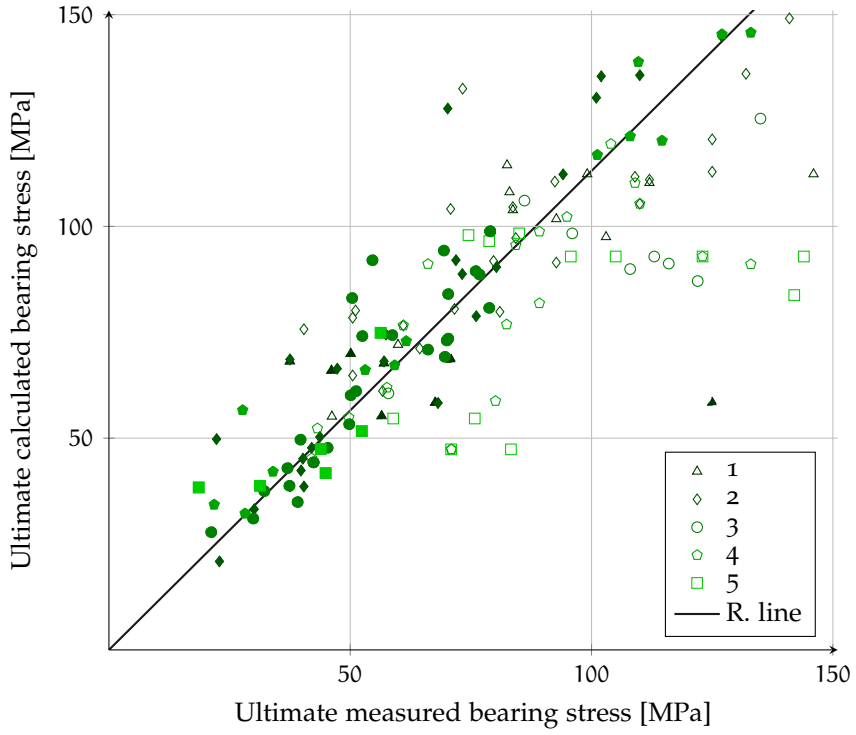

Figure 4.6: Zoom of the previous figure. Filled markers denote that the predicted failure mode is by compression criterion

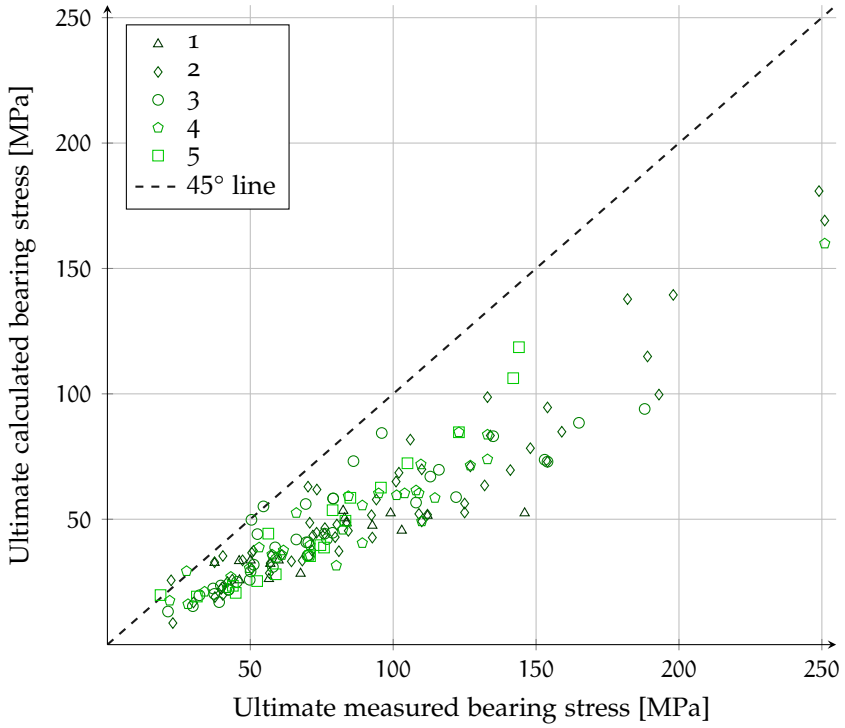

Figure 4.7: Comparison of factored model capacity to tests by Williams

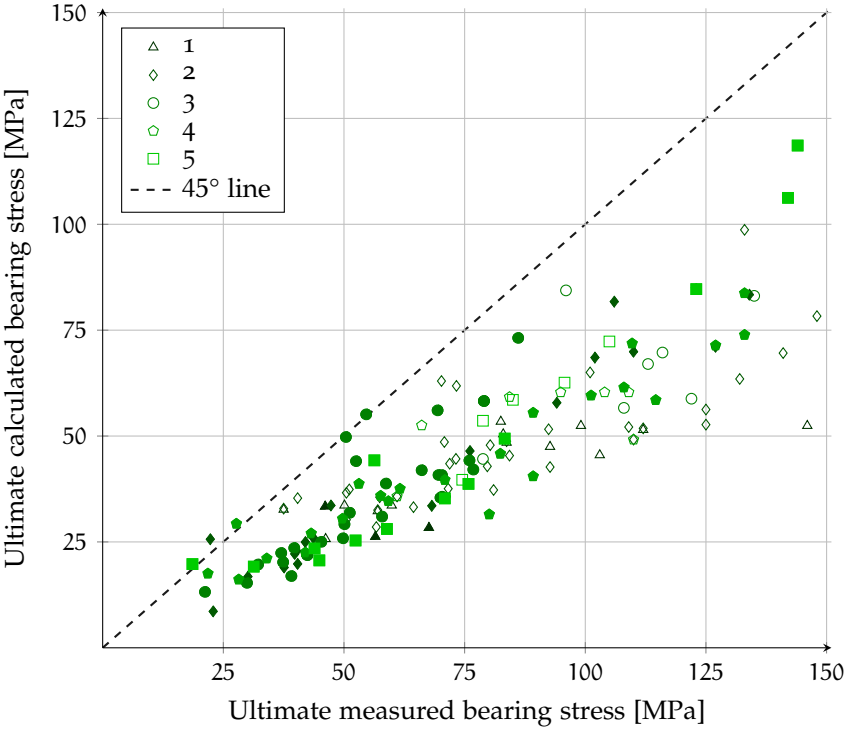

Figure 4.8: Zoom of the previous figure. Filled markers denote that the predicted failure mode is by compression criterion

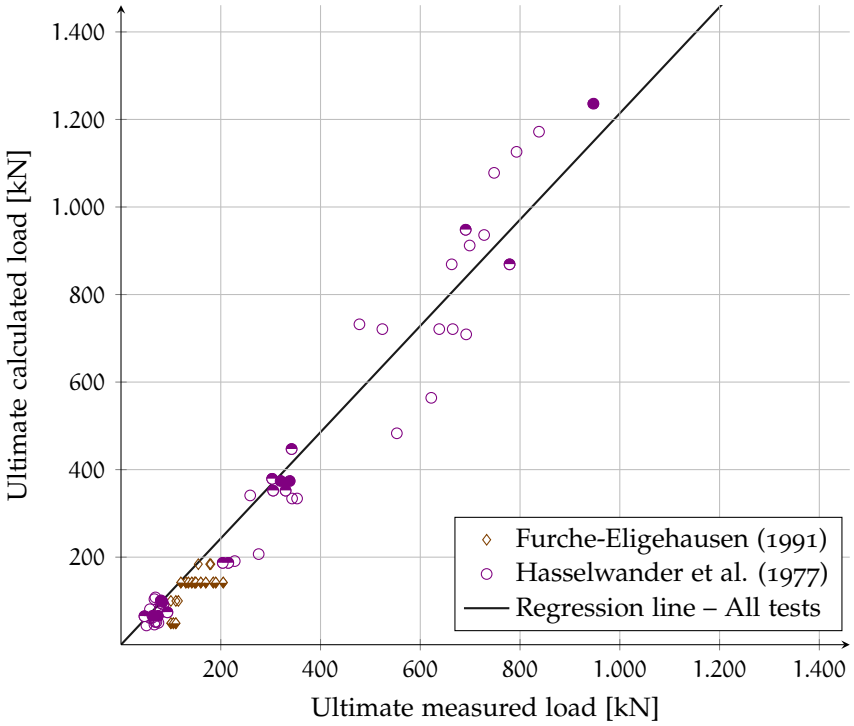

Figure 4.9: Tests by Furche and Eligehausen: comparison of predicted ultimate values and measured ultimate values. Filled markers denote that the predicted failure mode is by uniaxial compression. Half-filled markers denote a failure by triaxial compression

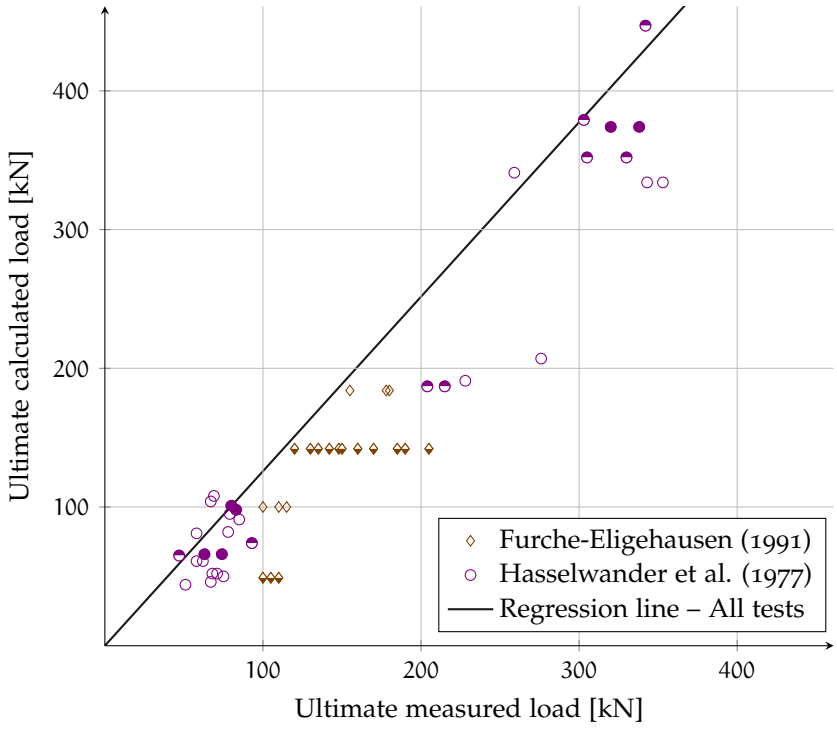

Figure 4.10: Zoom of the previous figure

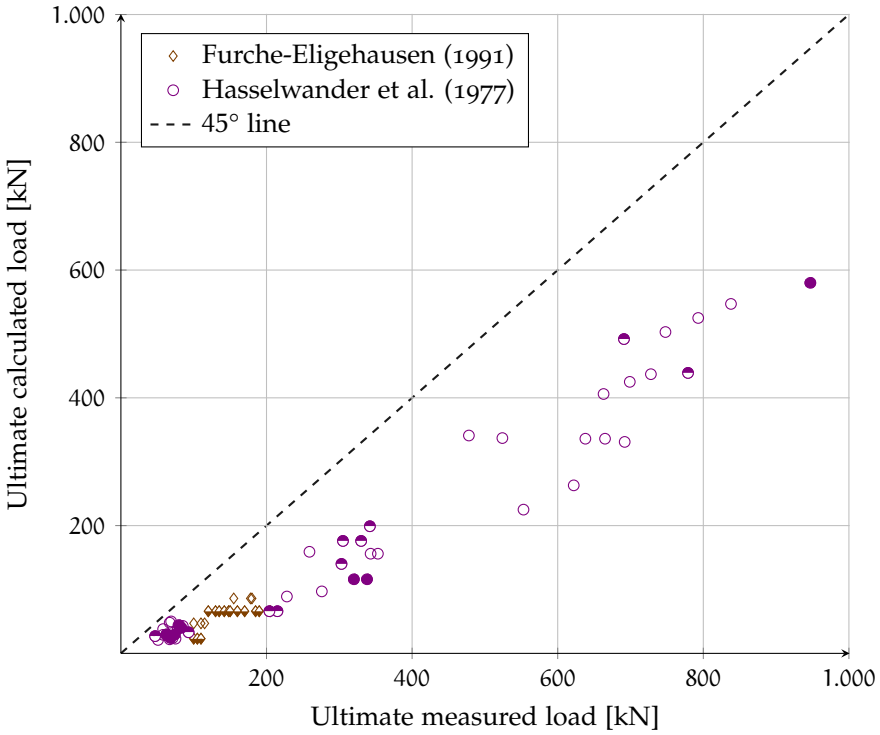

Figure 4.11: Comparison of factored model capacity to tests by Furche-Eligehausen on deep embedded headed bolt. Filled markers: failure by uniaxial compression; half-filled markers: failure by triaxial compression

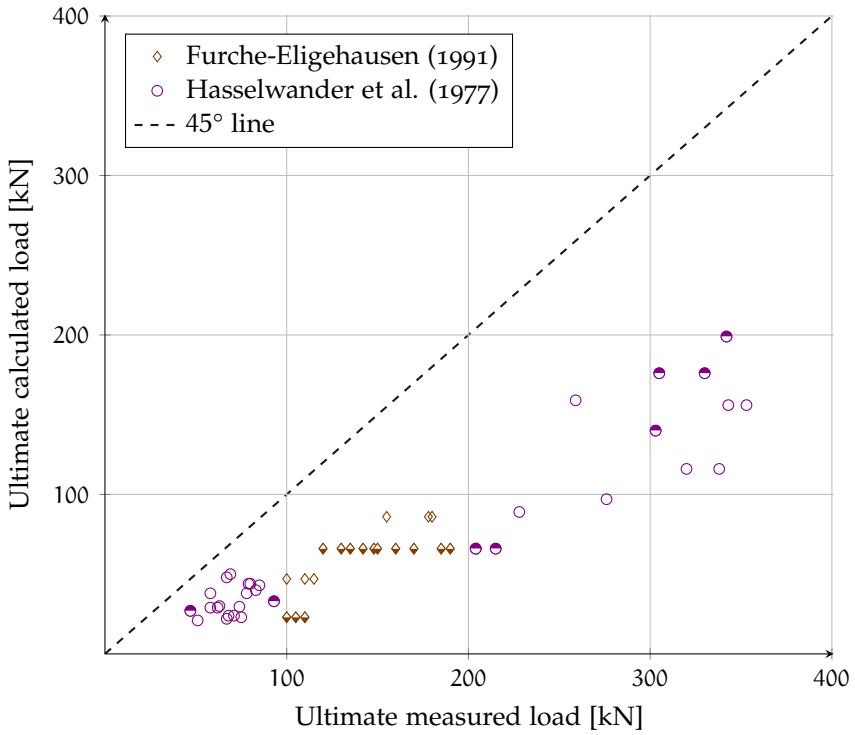

Figure 4.12: Zoom of the previous figure

4.4 BEHAVIOR OF THE PROPOSED FORMULATION

In this section the behavior of the proposed formulation is studied varying the concrete strength and the position of the anchor with respect to the concrete block. The anchor capacity predicted by the proposed formula is calculated and plotted as a function of the plate area and positioning. A square block of side 120 mm with a square loaded area is considered in this section: for each plate dimension ($a_1 \leqslant a$) the ultimate load has been calculated for four different concrete classes and four different positions[4].

The position considered varies from the side to the center, (Figure 4.16), from the corner to the center (Figure 4.17) or from the corner to the side (Figure 4.18).

Let c be the clear cover[5]: the maximum allowable cover for a centered plate is computed as $(a - a_1)/2$ and the value c/c_{max} changes gradually[6] between the two extreme positions: when c/c_{max} is equal to 0 there is no space between the edge of the plate and the edge of the block, while a value of c/c_{max} equal to 1 means a centered positioning.

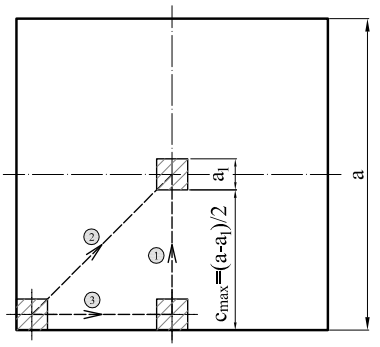

Figure 4.13: Variations of anchor positioning considered: from side to center (1), from corner to center (2), from corner to side (3)

From Figures 4.16 to 4.18 it is apparent that the anchorage capacity grows with increase in concrete strength, as is to be expected.

The blowout criterion is usually the governing criterion for plate dimensions of about half the block size, as shown in Figure 4.14. The range of a/a_1 values which result in blowout failure is larger in centered plates, as can be seen, for instance, by comparing the first and the last graphs of Figure 4.16. This behavior can be explained by considering the state of stress acting on the body: due to the diffusion of the load into the block, in a centered positioning the state of stress acting on the concrete block resembles that of a uniaxial compression plus a biaxial tension, therefore more demanding than a side or corner positioning, in which the state of stress is essentially a uniaxial compression or a uniaxial compression plus a uniaxial tension, as shown in Figure 4.15.

[4] Concrete tensile and compressive design strengths are used for the comparison.
[5] Distance from the concrete edge to the plate edge
[6] Four different calculations are performed

However, this would not necessarily mean that a centered plate has a lower capacity than a plate with a side or corner positioning, because the other criterion considered in order to determine the anchor capacity (failure due to compression), is the governing failure mode in case of a corner or a side plate, therefore the anchor capacity in this case is lower than that of a centered plate, as expected.

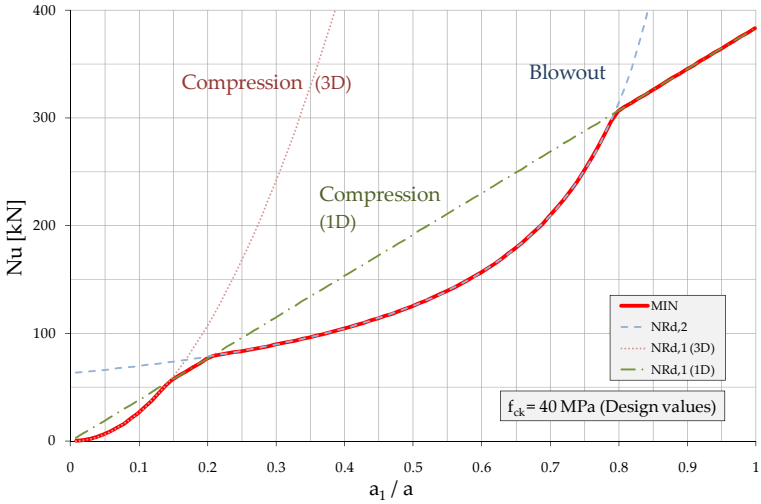

Figure 4.14: The anchor capacity, in red, plotted as a funcion of the plate dimension, with the three failure modes considered highlighted. Values calculated for a block with a 120 mm side, a centered plate and design strengths of concrete

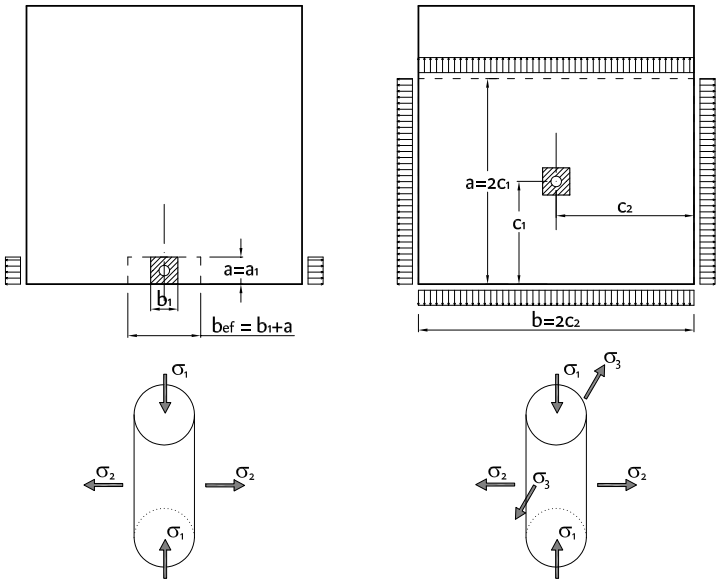

Figure 4.15: The state of stress on the concrete block for different positions

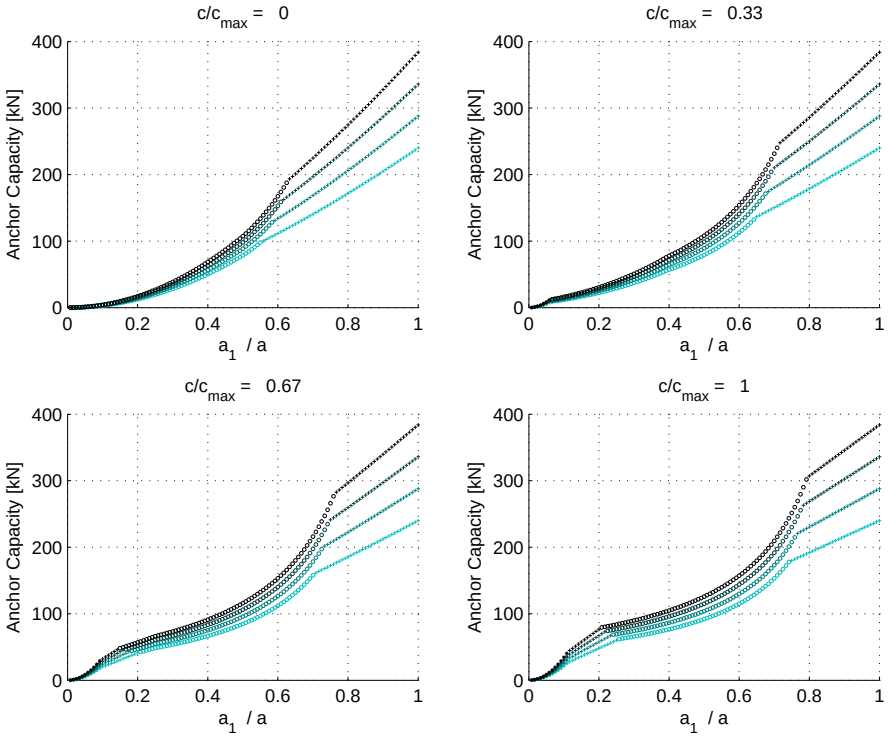

Figure 4.16: Position ranging from side to center. f_{ck} ranging from 25 to 40 MPa (darker line). $\circ$ is used in case of a blowout failure, while $\star, +$ are used if a compression failure (respectively, triaxial or uniaxial) is the governing criterion

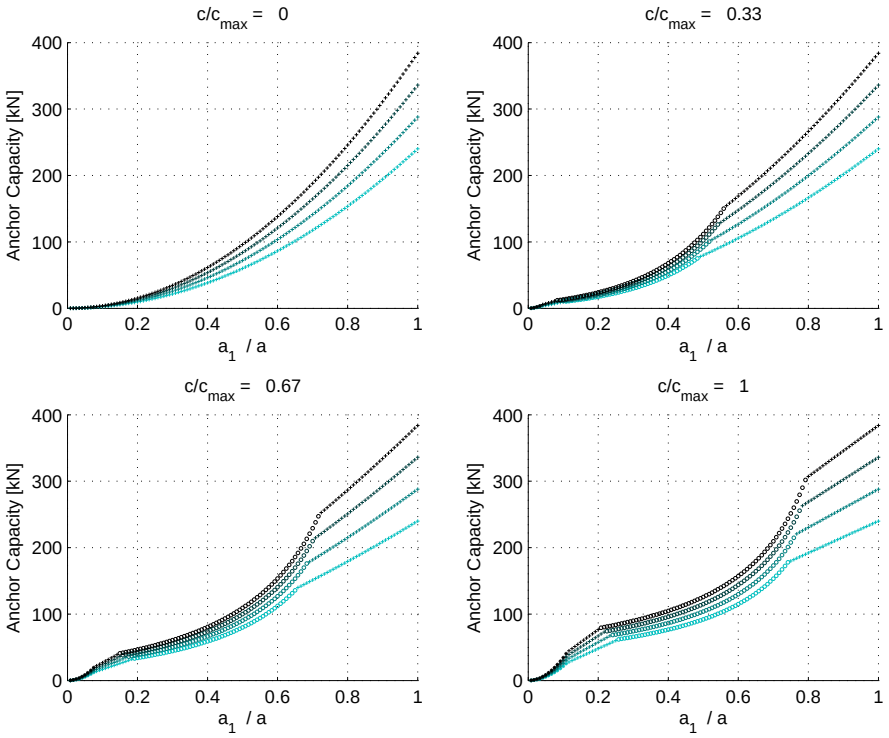

Figure 4.17: Position ranging from corner to center

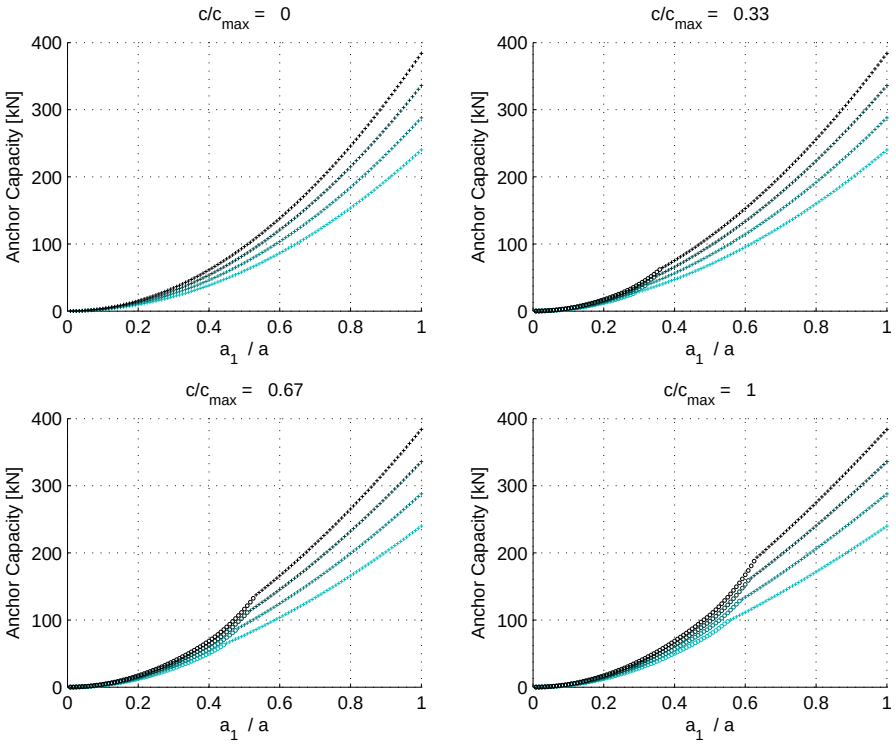

Figure 4.18: Position ranging from corner to side

4.5 ON BOND AND BEARING INTERACTION

Many authors claim that development length increases the anchorage capacity. However, the measure of the contribution is still debated.

DeVries [35] claims (see Section 1.2.4.1) that the contribution from bond is predictable by standard provisions, being at failure approximately 33% of the total load. However, given the uncertainty of the results he proposed to ignore the bond, thus calculating the anchorage considering only the contribution of the plate.

Bashandy [14] observed that the total capacity of the anchorage grows with the embedment length, but concluded that this was accompanied by a reduction of the part of the load carried by the head.

Thompson [117] formulated Bashandy's idea suggesting that the bond contributes to the total capacity by, at least, 30%, although this proposal is based on only one test with a relative head area[7] greater than 5,0, a test in which this ratio was 10,4. He proposed a *head size reduction factor* which depends on the net area to bar area ratio:

$$\chi = 1{,}0 - 0{,}7\left(\frac{A_n/A_b}{5{,}0}\right) \geqslant 0{,}3 \tag{4.1}$$

According to this formula, plates with a net area to bar area ratio less than 5,0 are prone to provide a contribution lower than 70% of the total load.

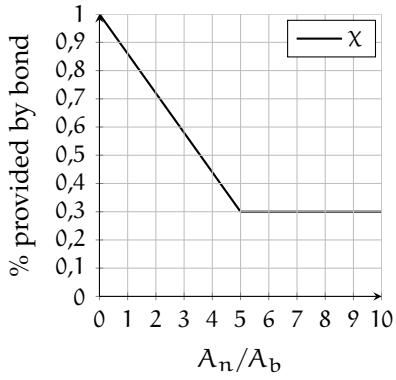

Figure 4.19: Thompson's χ factor

Therefore, in case of small plate dimensions there is the need of a greater development length, in order to compensate the loss of head capacity due to the reduced head size. Chun and Kim [29] consider reduced head sizes within $3{,}0 \leqslant A_n/A_b \leqslant 4{,}0$ as adequate to obtain an effective anchor, confirming indirectly the equation plotted in Figure 4.19. In fact, they claim that the bond along the bar and the bearing of the head contribute in these cases approximately by 50% each. Wright and McCabe [122] proposed a minimum development length of 60% of that needed with hooked bars, not dependent on head size. There are no other references to this problem of which the author is aware.

---

7 $$\frac{A_n}{A_b} = \frac{A_1 - A_b}{A_b} = \frac{a_1 b_1 - \frac{\pi {d_b}^2}{4}}{\frac{\pi {d_b}^2}{4}}$$

4.5.1 Code provisions

Code provisions are quite general (see Section 1.1.3) about reduced head size, reflecting the low amount of research done on this topic. Like some authors, they generally propose only a minimum development length associated with minimum plate dimensions:

ACI 318-08 limits plate dimensions to a value $A_n/A_b \geqslant 4{,}0$ and recommends a minimum development length — not dependent on head size — of 80% of the one needed for hooked bars, or 40% of the one needed for straight bars (for a ϕ 25 bar);

ACI 352-02 recommends a development length for a headed bar, l_{dh}, in non-seismic joints, of about 75% of that corresponding to hooked bars, l_{dh};

ACI 349-01 bases its recommendations on the Concrete Capacity Design (CCD) method, very conservative when the failure mechanism is different from the expected one, for example when a deep embedment is provided;

MODEL CODE 2010 requires a sufficient embedment to avoid a premature concrete cone-type failure, but does not provide guidance on when the anchorage can rely on the bond along the bar, referring to a generic determination by laboratory tests that would determine it.

In order to investigate whether or not the total anchorage capacity can be calculated as the sum of the contribution of bond and plate alone, a numerical study has been performed with a finite element model developed with the commercial software ATENA, a nonlinear finite element analysis program suitable for modeling of reinforced concrete structures.

The underlying theory and a summary review of the most common failure criteria are introduced in Appendix C in order to better understand the constitutive models adopted by ATENA. A more detailed review of this topic can be found, for instance, in Chen and Han [24], Fung and Tong [43] or Jirasek and Bazant [57].

4.5.1.1 *Model description*

For this thesis, a few models have been developed in ATENA representing a 35 mm diameter headed bar placed in the side of a concrete block and with variable development length. The anchor plate is $90 \times 90 \times 20$ mm, the total height of the block is 1400 mm and the thickness of the concrete underneath the plate is 60 mm. Block dimensions are 914×914 mm, as in DeVries' campaign. In order to reduce computational time only a half of the structure has been modeled, taking advantage of the problem symmetry.

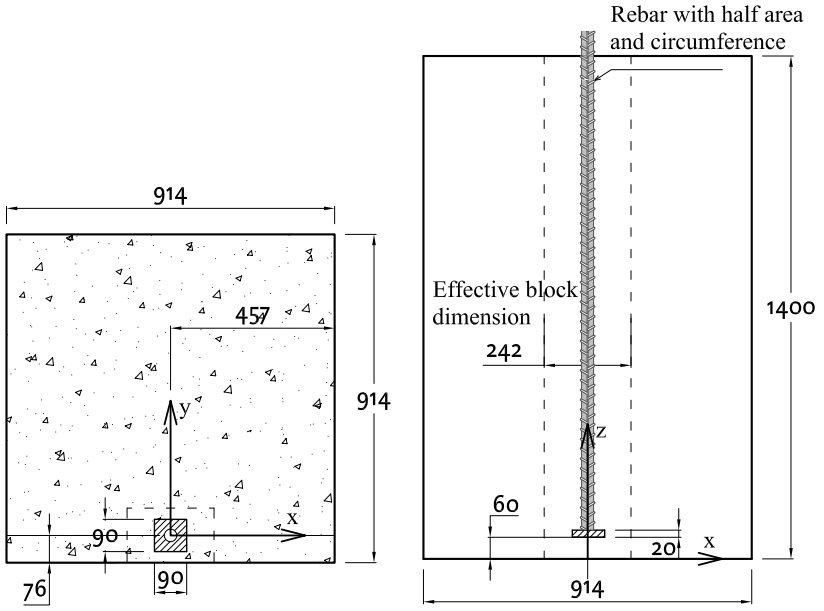

(a) *Plan view* **(b)** *Elevation view*

Figure 4.20: Model description

ATENA uses macroelements in order to define the geometry of solid blocks: each macro-element is defined separately, composed of joints, lines and surfaces and has its own mesh parameters. The FE mesh tool generates a solid 3D elements mesh in the whole structure at once. Compatibility of meshes on contact planes does not need to be enforced, since ATENA creates special master/slave conditions that ensure the compatibility of displacements. In order to take advantage of this special feature and obtain a less time-consuming model, a coarse mesh was used for the macroelements farthest from the bar.

Regarding the materials used, in this example a concrete *C12/15 mean value* has been used whereas a *3D Bilinear Steel Von Mises* with no hardening and very high yield limit was used for both the anchor plate and a little macroelement in which the bar is embedded and where the force is applied. In this location, a *monitor* records applied displacements and resulting forces throughout the analysis.

The reinforcements can be introduced by a series of segments conforming a polyline. If embedded in a macroelement the connection to the surrounding material can be set as a *perfect connection* or, like in this case, a bond model can be chosen. The material consitutive law is linear, and the bond model was calculated by ATENA[8] on the basis of the concrete strength. Also, the flag *no slip* was marked at the beginning and at the end of the rebar. The upper surface of the block

[8] *CEB-FIP Model Code 1990* for ribbed reinforcement, confined concrete and good bond quality.

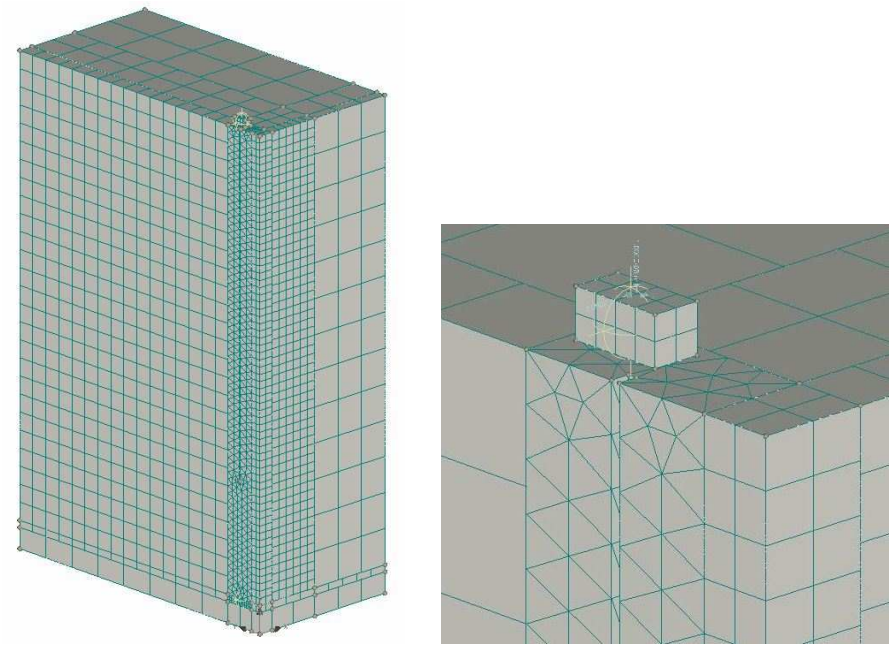

Figure 4.21: On the left, the whole model.
On the right, are visible the carving and the loading plate.
Axis:

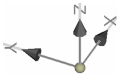

is restrained along z-direction, whereas the middle part is restrained along x-direction due to the simmetry of the problem.

In order to allow the calculation of a series of models with different development lengths, a small cavity has been left in the concrete macroelement around the bar axis, as shown in Figure 4.21.

In this way, the part of the bar not in contact with the macroelement cannot transfer stresses. Four different development lengths were chosen: 20, 33, 70 and 100 cm. The entire model has approximately 10 000 elements. The contact at the interface between concrete and the upper surface of the plate is set as *perfect connection*, while the other ones are set as *no connection*.

DEVELOPMENT LENGTH AND ANCHORAGE CAPACITY The development length needed has been estimated using the EC2 formulation, with the hypotesis of a good casting position ($\eta_1 = 1$), in presence of a straight bar ($\alpha_1 = 1$) with no active confinement nor transverse pressure acting on it ($\alpha_3 = \alpha_5 = 1$) and no welded transverse bar ($\alpha_4 = 1$). The cover was taken as 58,5 mm (76,0 if measured from the bar axis) and no safety factors were used.

$$
\begin{aligned}
\eta_2 &= (132 - \phi)/100 = 0{,}97 \\
f_{ctd} &= f_{ctm} = 0{,}3\, f_{ck}^{2/3} = 1{,}57 \text{ MPa} \\
f_{bd} &= 2{,}25\, \eta_1 \eta_2 f_{ctd} = 3{,}43 \text{ MPa} \\
l_{b,rdq} &= \frac{\phi \sigma_{sd}}{4\, f_{bd}} = \frac{35 \cdot 500}{4 \cdot 3{,}43} = 1275 \text{ mm} \\
c_{min} &= c_d = 58{,}5 \text{ mm} \\
\alpha_2 &= 1 - 0{,}15(c_d - \phi)/\phi \simeq 0{,}9 \\
l_{bd} &= \alpha_1 \alpha_2 \alpha_3 \alpha_4 \alpha_5 l_{b,rdq} \geqslant l_{b,min} \\
&= 1146 \text{ mm} \simeq 33\phi \ (> 0{,}3\ l_{b,rdq})
\end{aligned}
$$

The development length chosen for the numerical tests corresponds approximately to 15%, 30%, 60%, 90% of the calculated development length. For what concerns the capacity of the anchorage:

$$
\begin{aligned}
c_1 &= 76 \text{ mm} \\
a &= 2c_1 = 152 \text{ mm} \\
b &= 914 \text{ mm} \\
a_1 = b_1 &= 90 \text{ mm} \\
b_{ef} &= b_1 + a \leqslant b = 152 + 90 = 242 \text{ mm} \\
N_{Rd,2} &= \frac{8}{3} f_{ctm} \frac{a b_{ef}}{\left(1 - \sqrt{\frac{a_1 b_1}{a b_{ef}}}\right)} = \\
&= \frac{8}{3} \cdot 2{,}21 \cdot \frac{152 \cdot 242}{\left(1 - \sqrt{\frac{8100}{152 \cdot 242}}\right)} \simeq 408500 \text{ N} \qquad (4.2) \\
A_s &= 962 \text{ mm}^2 \\
\sigma_{head} &= 408\,500/962 = 425 \text{ MPa}
\end{aligned}
$$

RESULTS In this paragraph the results of the numerical tests are summaryzed. The total stresses are shown in Figure 4.23, while the percentage of the total stress provided by the head and by the bond along the bar is reported in Figure 4.24 and 4.25.

Some observations can be made about the behavior of the numerical model:

- The development length increases the anchorage capacity. With more development length provided, the peak stress is slightly shifted towards greater displacements (5 to 6 mm);
- The plate contribution to the anchorage is almost constant and approaches very well the theoretical value. Plates which can count on a smaller development length reach the expected resistance value earlier, with the maximum values in correspondence with a slip between 6 and 7 mm. Plates in the two specimens with a large development length (60% and 90% curves in Figure 4.24) behave almost equivalently;
- Initially, the force carried by the plate is very low and all the applied force is resisted by bond. The plate gathers force slowly, until the bond starts degradating (4 to 5,5 mm). After this moment, the force carried by the plate increases, assuming gradually the major part of the force until the blowout failure occurs. This mode of failure is due to the outward force exherted by the plate, which is prone to deform around the x-axis given the unbalanced amount of concrete on each side of the half-plate. This behavior is corroborated by Thompson' observation about bond deterioration [117]. Furthermore, ATENA correctly reproduces the failure mode, as shown in Figure 4.22.
- The smaller the development length provided, the more the percentage of the total load provided by the head at failure, as shown in Figure 4.26. Again, there is little difference between the 60% and 90% development length curves.
- At failure, approximately 40% of the total load was carried by bond, in both 60% and 90% curves, and with lower values when a lower percentage of development length was provided. This seems slighlty above the value proposed by Thompson in Equation 4.1 (30% for a plate with $A_n/A_b = 8{,}4$) and observed value reported by DeVries (33%). However, this test represents only a point of the curve.

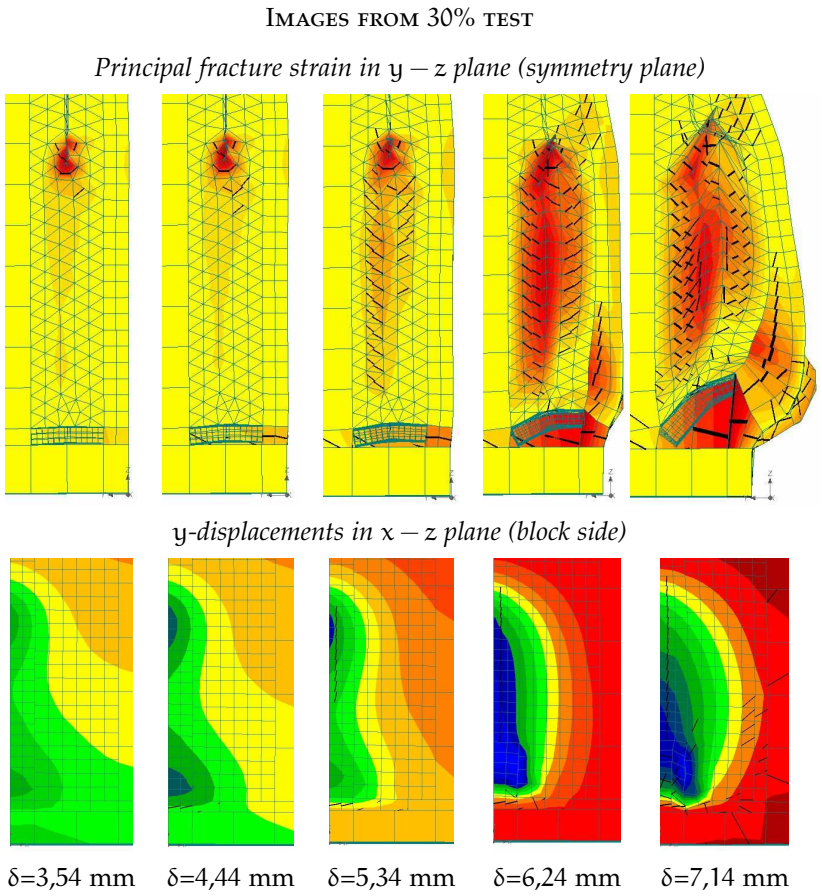

Figure 4.22: Magnified displacements ($\times 20$). Only cracks wider than 0,1 mm are shown. Regarding the second series, cold colours are used for negative displacements, allowing the identification of the blowout area: larger displacements occur in the proximity of the plate and the simmetry axis.

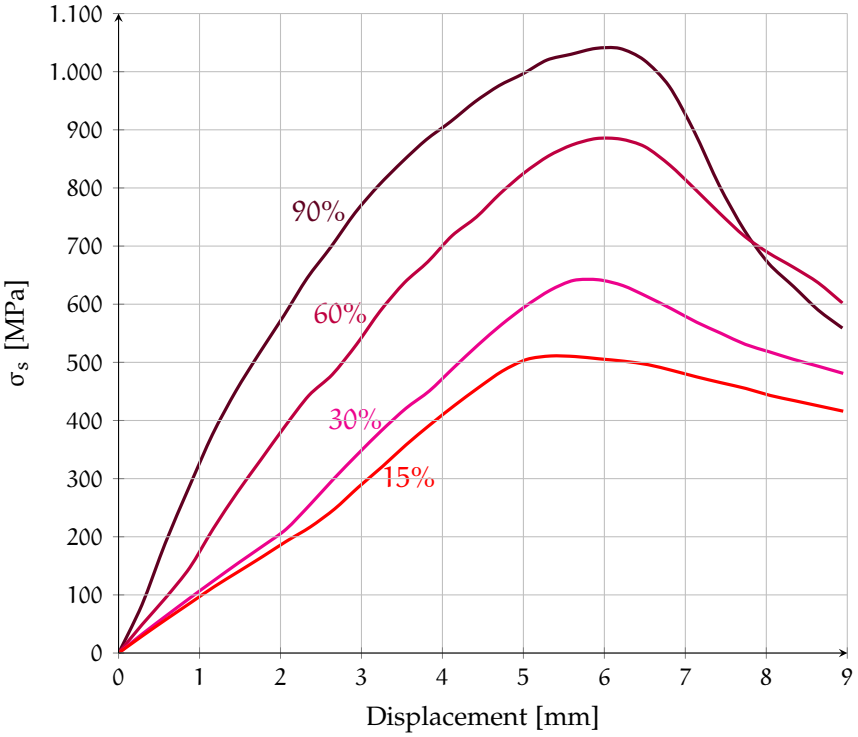

Figure 4.23: Total stress in the bar, measured at point of load application

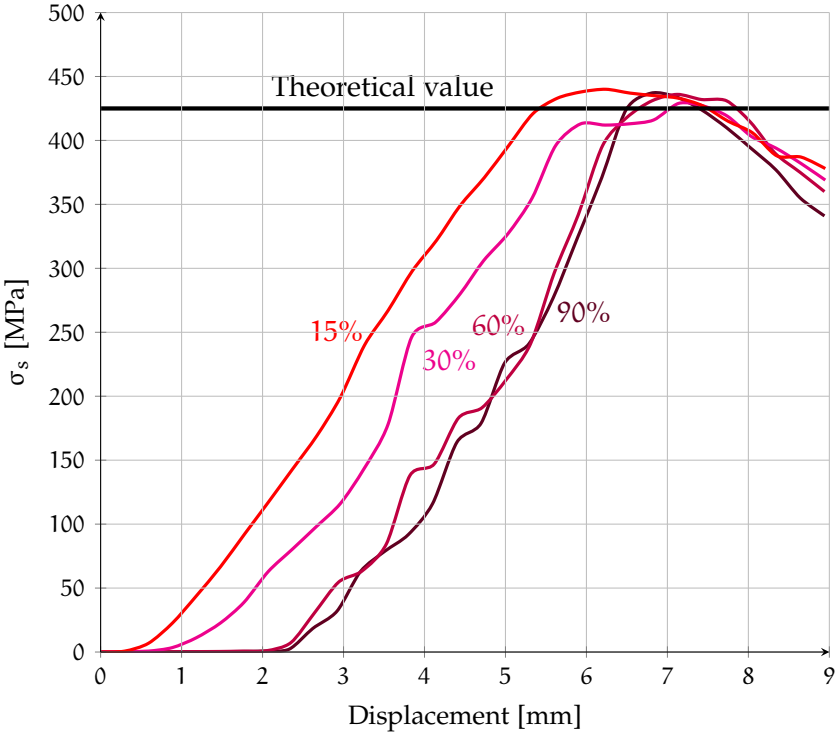

Figure 4.24: Stress in the bar at the rebar-plate intersection. Theoretical value refers to the plate capacity, according to Equation 4.2

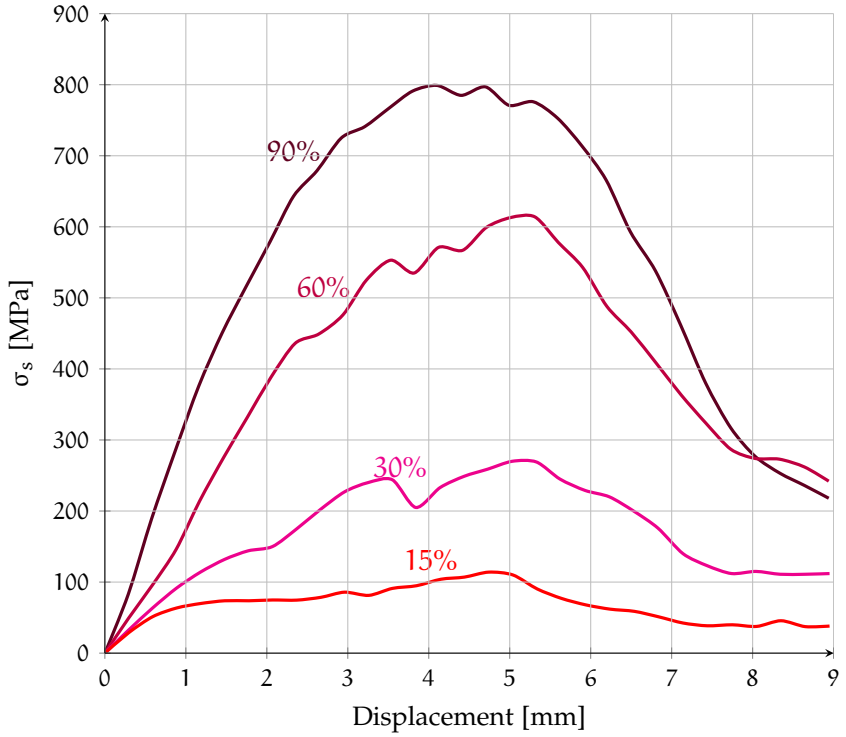

Figure 4.25: Contribution of bond to rebar stress calculated as the difference between the previous curves

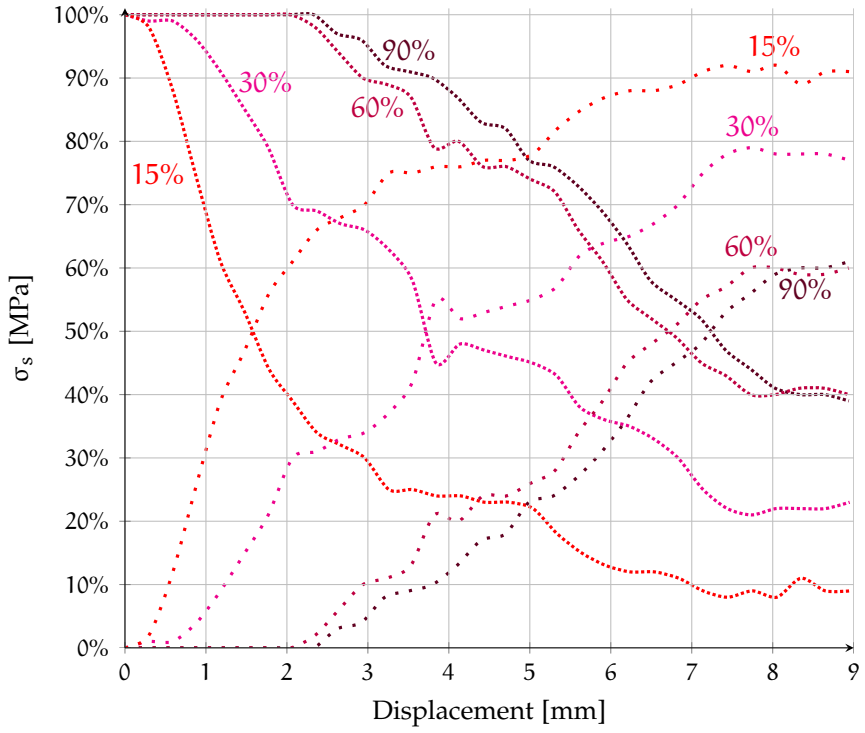

Figure 4.26: Comparison between stress due to the bond (densely dotted lines) and stress due to the anchor plate (loosely dotted lines)

4.6 SUMMARY

Other well-known studies on bearing strength and anchor bolts have been incorporated to the database for comparison with the theoretical proposal, joining the Niyogi's tests introduced in the previous chapter.

The design formula has been analyzed representing the anchorage capacity as a function of plate dimensions and positioning. According to the plots, the dominant criterion for medium plates with a center positioning is usually the blowout failure, while its importance is reduced in case of a side or corner positioning.

Finally, the availability of a certain development length is shown to be effective in increasing the anchorage capacity, in accordance with the finite element program ATENA and to other authors' experimental observations. The plate contribution is almost constant and very similar to the predicted value: its relative contribution rises soon after the first signs of bond deterioration.

Part III

TEST DESIGN, PREPARATION, AND DATA ANALYSIS

5 SPECIMEN FABRICATION AND TESTING PROCEDURE

Some laboratory tests have been performed on a knee joint, a structural element in which headed bars are suitable for a large scale application, as previously discussed in Section 2.1.3.

The structure which inspires the design of the test campaign and from which the corner of the frame is extracted, is shown in Figure 5.1: the length of the specimens, 2,50 m, corresponds approximately to the point in which no moment is acting (0,2L = 2,40). The section depth is taken as 0,85 m in order to perform a 1:1 scale tests and to avoid size effect considerations: the size of the element to be tested is almost the biggest possible considering the available facilities.

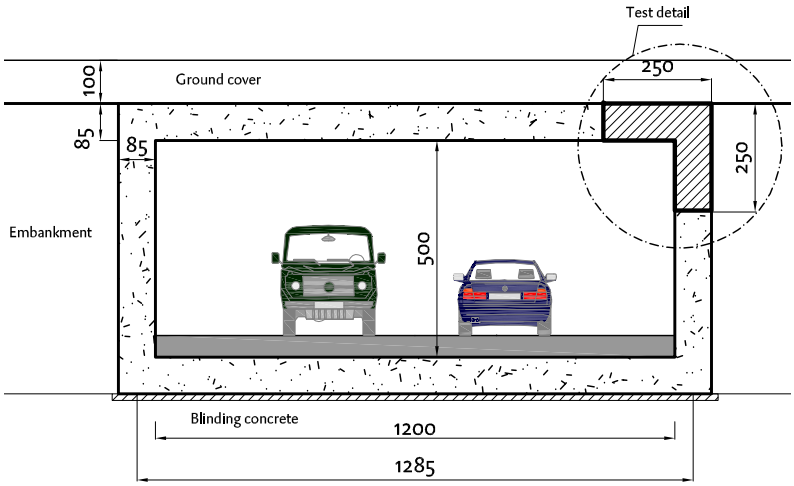

Figure 5.1: A knee joint of a 5 m height underpass

In this chapter the materials used, as well as the test preparation and setup, will be described, afterwards the results will be presented and the influence of the primary variables will be discussed.

5.1 SCOPE AND OBJECTIVES

Among the potential applications of mechanical anchorages discussed in Chapter 2, perhaps one of those with the greatest potential is the elimination of the lap splice in a corner of a structure by using two facing headed bars, as shown in Figure 5.2b.

In knee joints, the maximum moment localizes in the corner and for this reason the full development of the bar capacity is absolutely needed and must be provided by the anchor plate only. No contribution of the development length can be accounted for, simplifying the computation of the total anchorage capacity.

The primary objective of the present work consists in verifying the behavior of a plate-anchored reinforcement detail in which plate dimensions have been calculated with the proposed model, showing its adequacy with respect to a conventional detailing in which standard hooks are used.

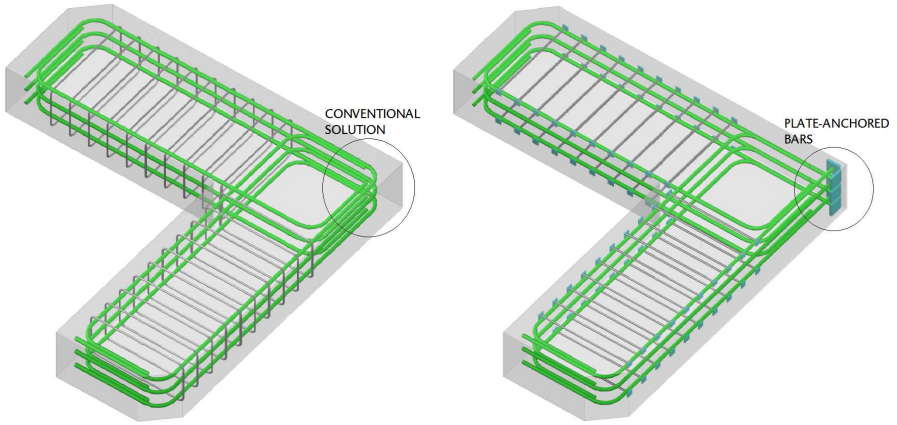

(a) *Conventional reinforcement* **(b)** *Alternative plate-anchored reinforcement*

Figure 5.2: Conventional and mechanical reinforcement details (ϕ25 specimens)

Eigth full-scale tests were performed considering three parameters as primary variables:

- The strength of concrete: 25 or 45 MPa;
- The detailing: Plate-anchored or Conventional;
- The size of the reinforcement bars: 25 or 16 mm.

Plate dimensions have been chosen assuming that the total force would be provided uniquely by the plate. The results do not depend on the development length, thus increasing the value of the research and making easier the interpretation of the test results. However, the strain profile of the tensile reinforcement bars will be monitored by means of strain gauges in order to verify the previous assumptions.

5.2 TEST PREPARATION

5.2.1 Materials

5.2.1.1 *Reinforcement bars*

The plate-anchored reinforcement bars, made of standard B500SD steel, were provided by GRUPO ARMATEK, who was also responsible for the welding process. Bar and plates have nominal yield strength of 500 MPa.

The connection between parts was realized with a friction-welding machine equipped with a programmable logic controller (PLC) that manages an automated welding cycle and ensures the consistency with the established quality parameters: rotational speed, axial force and time.

The component to be welded is held in a hydraulic mandrel, in the axis of rotation of the machine, brought up to a predefined rotational speed. The reinforcement bar is positioned in a stationary clamp, supported by a frame. The entire process — illustrated in Figure 5.3 — lasts approximately 20 seconds and the resultant welding is characterized by a homogenous microstructure.

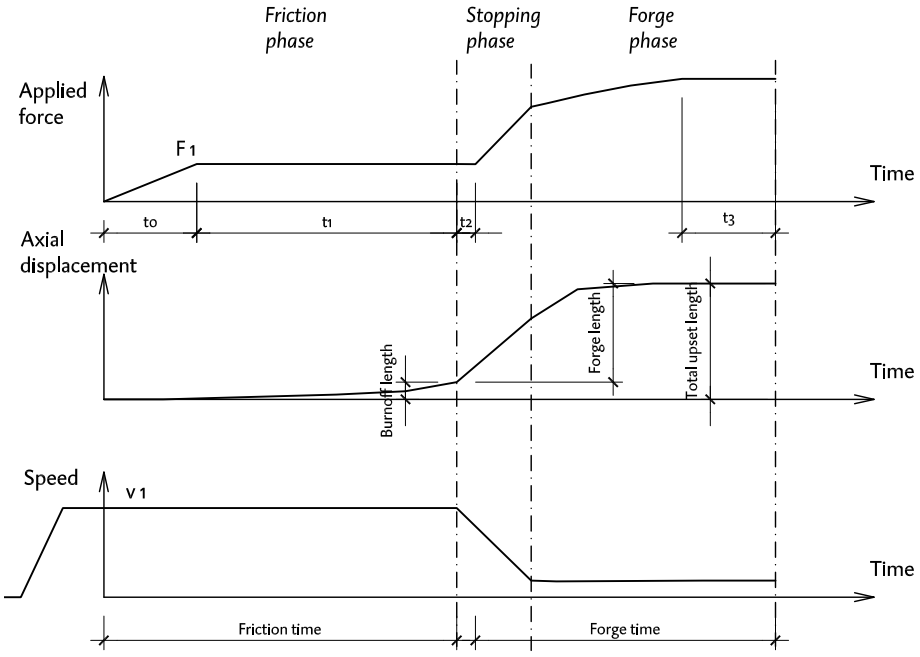

Figure 5.3: The friction-welding process

The three stages are described below:

1. While the axis is rotating at the established speed (v_1) the plate meets the rebar. After a short time delay (t_0), the axial force is increased up to a predetermined value (F_1);

Table 5.1: Plates dimensions [mm]

#	a_1	b_1	e_1
PL1	30	30	12
PL2	55	55	12
PL3	100	50	25
PL4	100	100	25

2. The previous conditions are maintained for a predetermined time (t_1), at the end of which the two materials become malleable. The axial displacements due to the applied force is measured continuosly: after a certain *burnoff length* is reached, the rotational speed is decreased rapidly while the applied force is increased a short time (t_2) afterwards;

3. The increased axial force is maintained for another predetermined time (t_3) during which the forge phase takes place, completing the weld. The total upset length is equal to the sum of the burnoff length and the forge length. The material displaced during the process forms a flashing — a ring of upset material created principally in the friction phase — which surrounds the welding zone.

Within the framework of this project four different plates have been welded to reinforcement bars, as shown in Figure 5.4 and detailed in Table 5.1. PL1 and PL2 have been welded to 16 mm rebars, while the bigger ones, PL3 and PL4, have been welded to 25 mm rebars. PL1 were also used for the 12 mm double-headed bars.

Although the process should be designed to ensure a connection which exceeds the tensile strength of the reinforcement bars, tests conducted on larger bars did not show the same ductility as the smaller ones. Measured yielding stress and ultimate stress are shown in Table 5.2.

(a) *PL3*

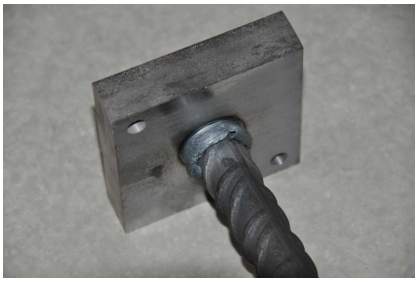

(b) *PL4*

(c) *From left to right, PL1 to PL4. On the background, the double-headead bar*

Figure 5.4: The plate-anchored rebars, with the ring of upset material and the two small holes made to facilitate the welding process.

#	ϕ [mm]	f_y [MPa]	f_u [MPa]
1	25	547	660
2	25	554	634
3	25	–	563
4	25	574	684
5	16	531	634
6	16	533	636
7	16	532	637
8	25	558	657
9	25	560	636
10	12	533	661
11	16	546	642

Table 5.2: Results of some tensile tests on headed bars.
One bar (#3) broke before reaching the yielding stress.

5.2.1.2 *Concrete*

The concrete was provided by Hympsa, part of group GCPV[1], one of the major Spanish cement groups, founded in 1903 and since 2002 a subsidiary of the construction company FCC. The concrete pouring was conducted by the laboratory technicians, the author, and other PhD students (Figure 5.5b) in two sessions, pouring four specimens each time. The two concrete classes considered in this campaign have a cylinder compressive strength of 25 and 45 MPa respectively.

(a) *The Abrams Cone. A slump of 70 mm means a soft concrete*

(b) *Men at work*

Figure 5.5: Concrete pouring

The first concrete batch was received on May 13th 2014. The slump test gives a S2 class consistency (see Figure 5.5a). From this batch, 20 cylindrical specimens have been manufactured in order to monitor the evolution of the concrete compressive strength over time, while two specimens were lost due to technical problems. The second batch was received on November 4th 2014. The slump was 95-100 mm, a S2-S3 class consistency. From this batch, 21 cylindrical specimens have been manufactured for concrete compression tests.

The complete results are presented in Table 5.3 and in Figure 5.6. The provider was warned about not exceeding the Eurocode mean compressive strength so that it would not affect the outcome of the tests.

5.2.2 Specimen drawings

The drawing details of the eight specimens are shown in Figure 5.7–5.9. All specimens have a rectangular cross section of 42,5 $\times$ 85 cm: at the corners, 45° chamfers provide flat surfaces for support and load introduction.

[1]Grupo Cementos Portland Valderrivas

			Compressive strength [MPa]				
Batch	Day	Tests	#1	#2	#3	Mean	Notes
1	7	3	17,6	18,6	17,5	17,9	
	14	3	18,1	20,4	19,7	19,4	
	21	3	20,1	20,2	18,9	19,7	
	37	1	23,8	-	-	23,8	25-TH-16
	52	2	19,5	21,1	-	20,3	25-TH-25
	59	3	23,6	22,7	21,8	22,7	25-CV-16
	66	3	23,1	25,3	25,0	24,4	25-CV-25
2	3	2	34,3	34,7	-	34,5	
	7	3	19,0	37,2	36,9	37,1	
	14	2	39,1	45,0	-	42,1	
	21	2	47,3	47,6	-	47,5	
	28	3	49,3	43,9	47,1	46,8	45-TH-16
	36	3	49,0	50,8	53,6	51,1	45-CV-16
	43	3	41,5	51,0	48,8	49,9	45-TH-25—45-CV-25
	76	3	49,6	48,3	50,7	49,5	

Table 5.3: Concrete batches: data highlighted in light gray are considered misleading and excluded from the mean value calculation

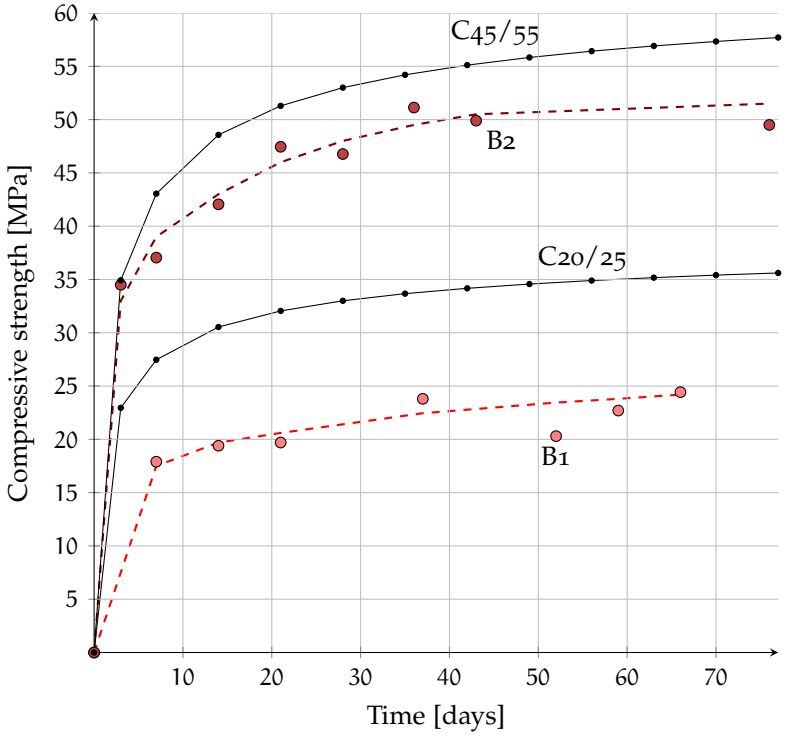

Figure 5.6: Batch B1-B2 compared to the Eurocode f_{cm} curves (solid line)

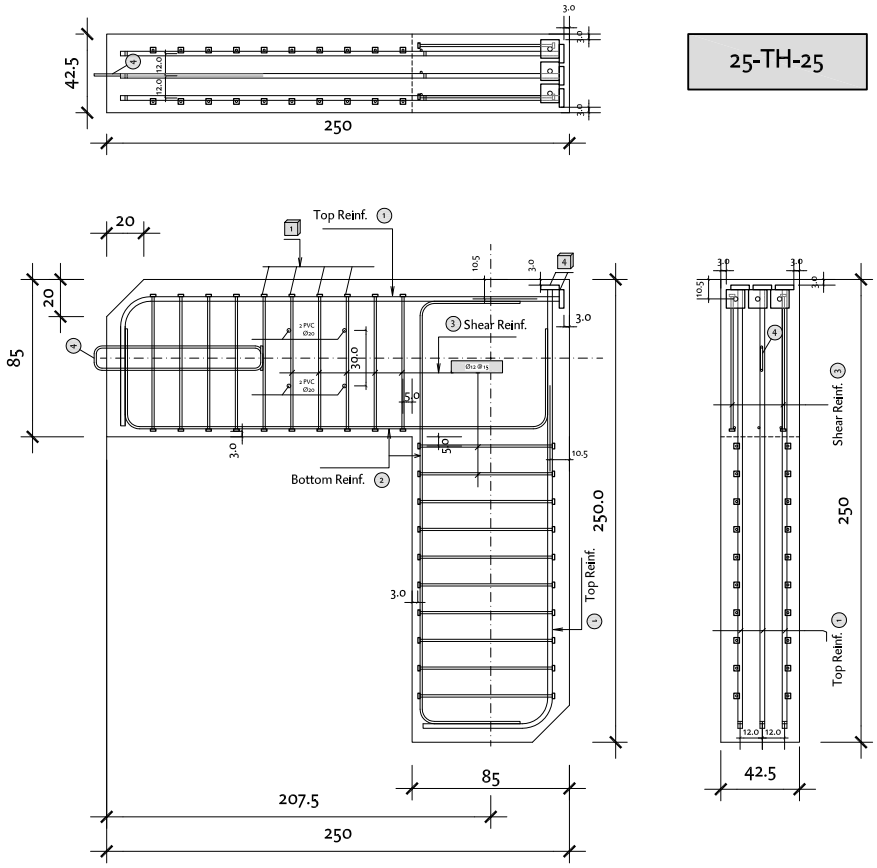

(a) *Specimen 25-TH-25*

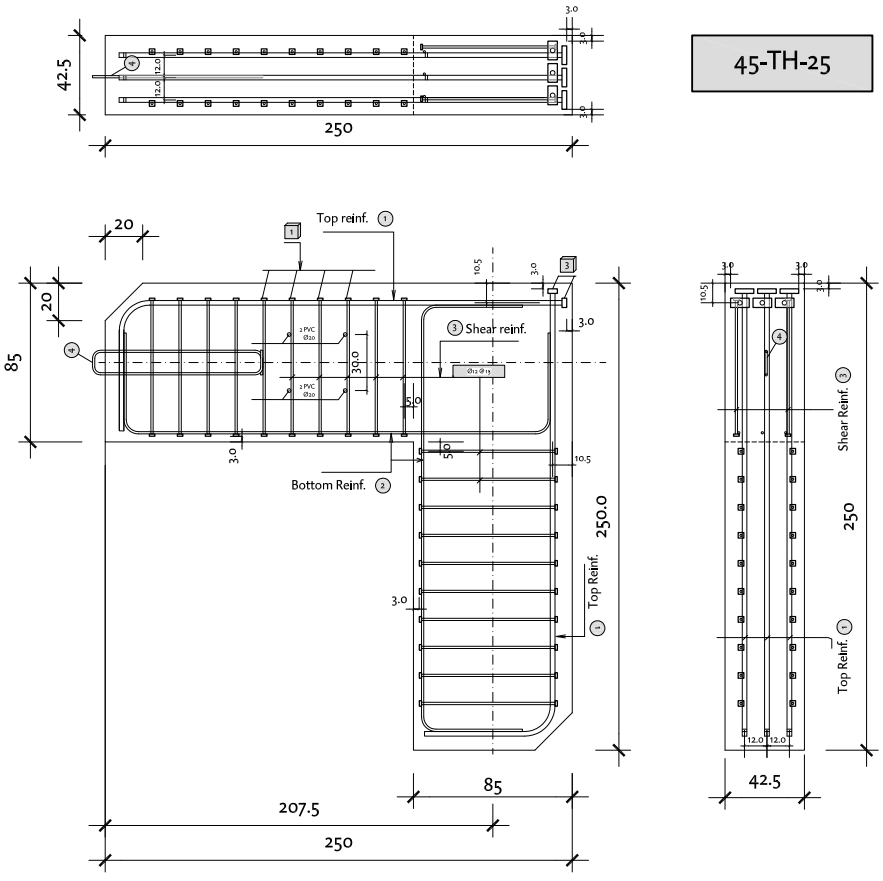

(b) *Specimen 45-TH-25*

Figure 5.7: Drawing details of the headed bar specimens with 25 mm rebars

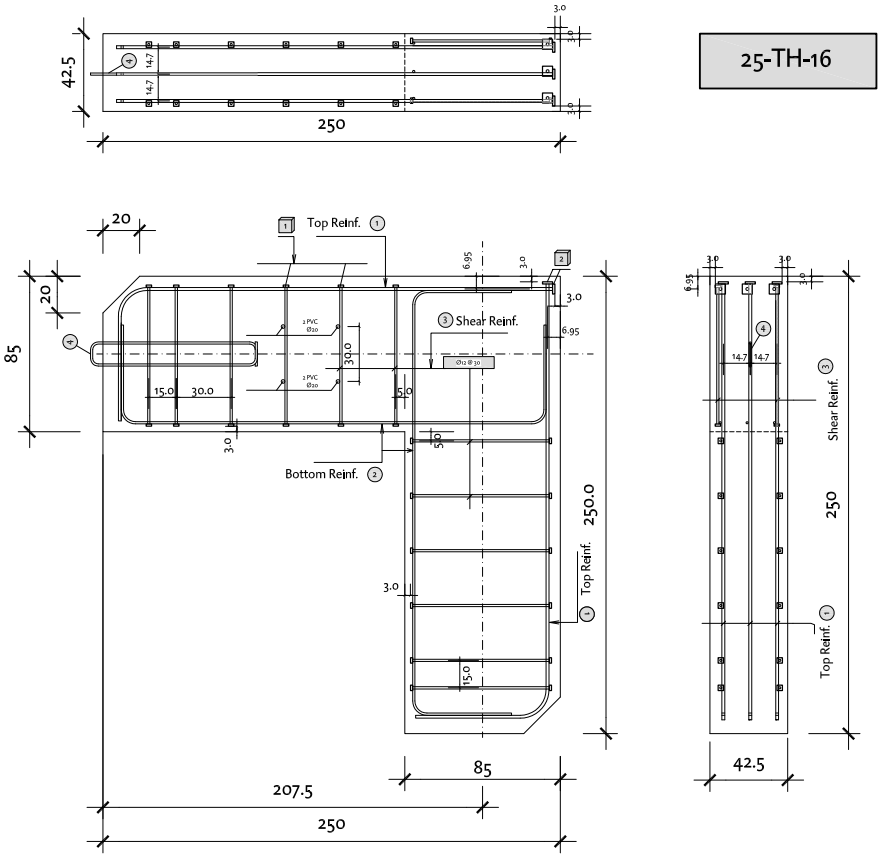

(a) *Specimen 25-TH-16*

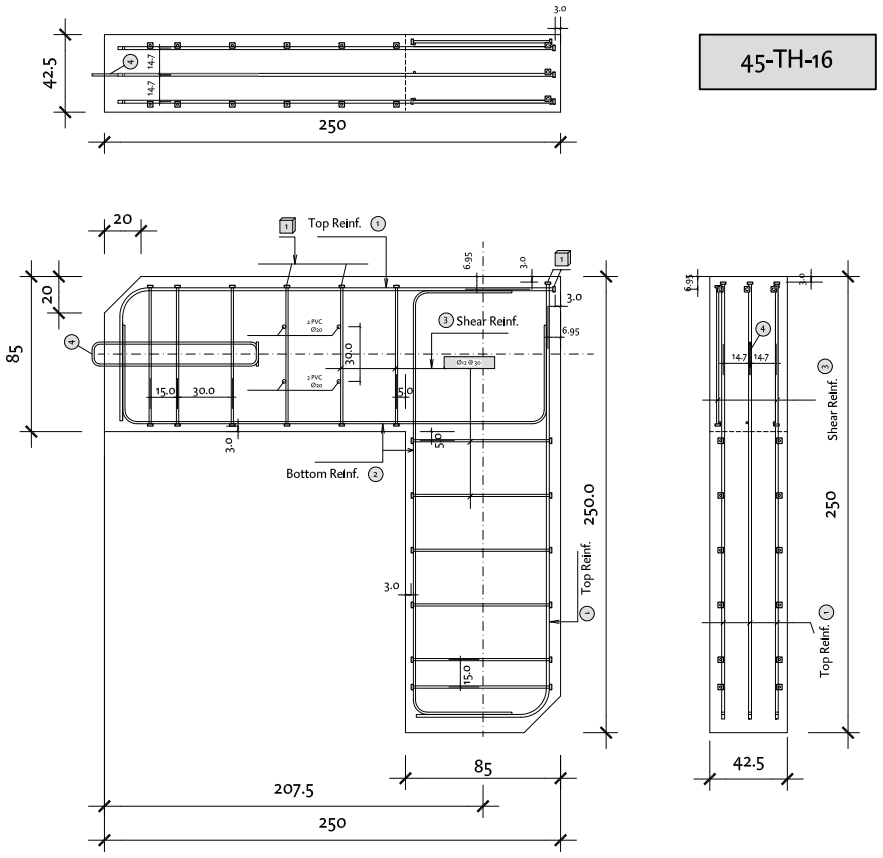

(b) *Specimen 45-TH-16*

Figure 5.8: Drawing details of the headed bar specimens with 16 mm rebars

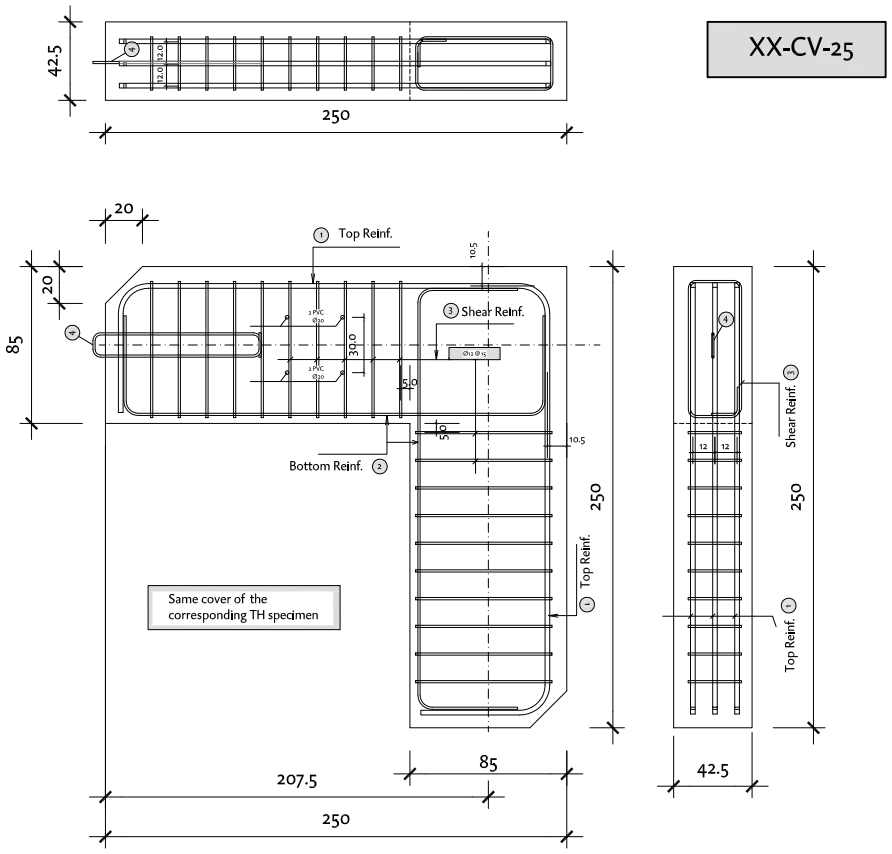

(a) *Specimen XX-CV-25*

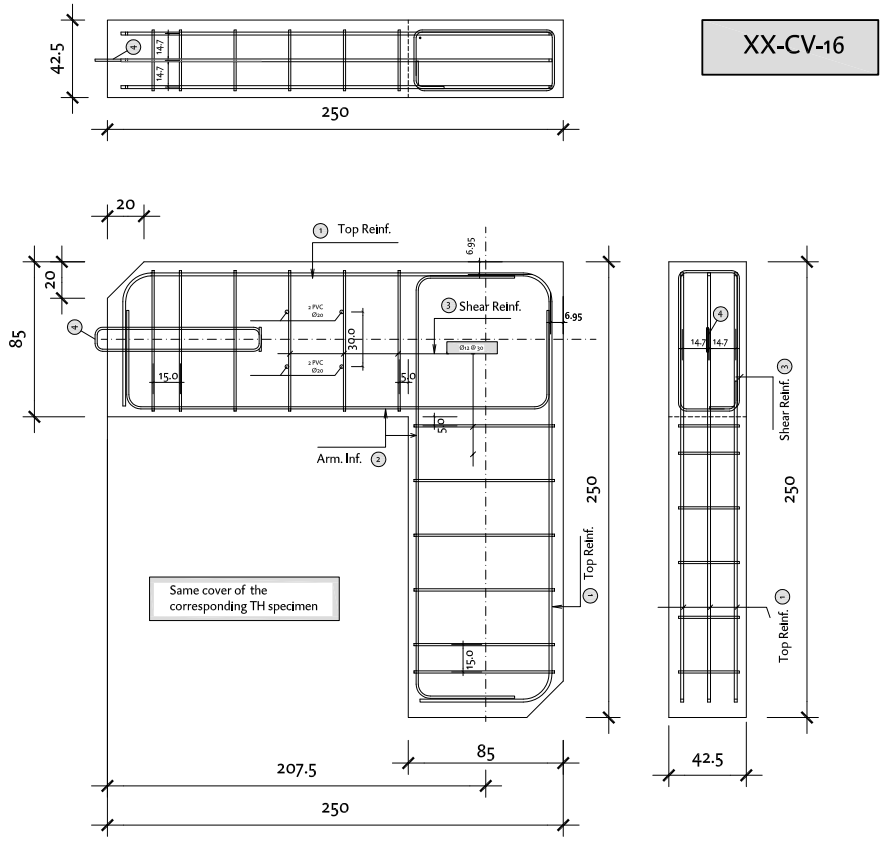

(b) *Specimen XX-CV-16*

Figure 5.9: Drawing details of the CV specimens

5.2.3 Specimen instrumentation

5.2.3.1 *Internal instrumentation*

The installation of strain gauges was regarded as an approriate and simple procedure to determine the stress in steel reinforcement during the tests, effective even if the gauge is placed very close to the plate, where the recorded data are prone to be used to determine the anchorage force provided uniquely by the plate.

Before starting the construction of the reinforcement cages, strain gauges[2] provided by Tokyo Sokky Kenkyujo Co. Ltd were installed on the middle bar of each specimen, as represented in Figure 5.10d. The dashed lines mark the position of the rebars in the conventional specimens, which do not have the strain gauge number 1, but only the gauges from 2b to 6. Gauges situated in the upper and lower part of the specimen are designated respectively as U and D series.

The gauges have a pre-attached vinyl lead wire and an entire coating with epoxy resin (see Figure 5.10a), which is transparent and flexible, thus ensuring an easy installation of the gauge. Furthermore, the coating provides in some degree a physical/mechanical protection during the pouring and vibration of concrete.

A preliminary preparation of the surface is needed: the main rib is smoothed with a circular saw and carefully cleaned from any debris. Perfect waterproofing is achieved by merely bonding the gauge with CN (Cyanoacrylate) adhesive, obtaining a final configuration as shown in Figure 5.10b.

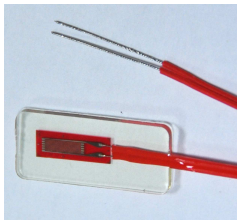

(a) *Strain gauges*

(b) *Gauge* #1 *after positioning*

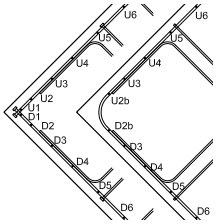

(c) *Gauges Location: U and D series*

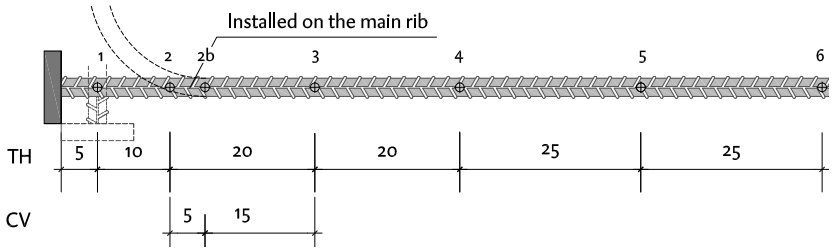

(d) *Gauges Location: TH – #1 to #6; CV – #2b to #6*

Figure 5.10: Strain Gauges

[2]WFLA-6-11-1L gauges, a waterproof series for mild steel, with 6 mm gauge length and 1 m long wire.

5.2.3.2 *External instrumentation*

Once the pouring took place, further instrumentation was provided in order to supply a more complete information, as described below and schematically plotted in Figure 5.13:

- A pattern of mechanical strain gauges[3] was attached to the concrete in order to record concrete surface strains at each load stage by means of a mechanical extensometer which measures the relative movement between the targets:
  - Two lines of targets (segments 1–10; 11–20 in Figure 5.13a), bonded on the outer (S) and the inner (I) portion of each side of the specimen, are meant to provide the strain plane thanks to the Navier's hypothesis that plane sections remain plane after deformation;
  - Some segments (see Figure 5.13b) record the strains along the compression strut on each side of the specimen (H and V series).
- A probe indicator monitors the horizontal displacement of the corner at its middle eight;
- Two LVDTs[4] measure the relative displacement (slip) between the plate of the middle bar and the side of the specimen. The access to the head is granted by means of a small hollow tubes cast into each specimen, as shown in Figure 5.11;

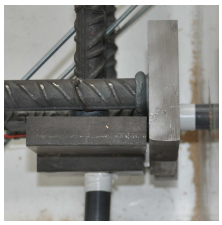

Figure 5.11: Slip measurement of anchorage plates

- TH specimens are equipped with six vibrating wire gauges. The idea behind their placement on the concrete surface is to intercept a lateral strain originated by the presence of bursting forces acting along the bar axis;
- A linear position transducer monitors the vertical displacement of the load application point;
- Finally, two clinometers are placed on the tension sides of the specimen near the load application point;
- The progression of cracks was recorded manually by markers and photos were taken during the tests.

[3] Small stainless steel locating discs
[4] Linear Variable Displacement Transducers

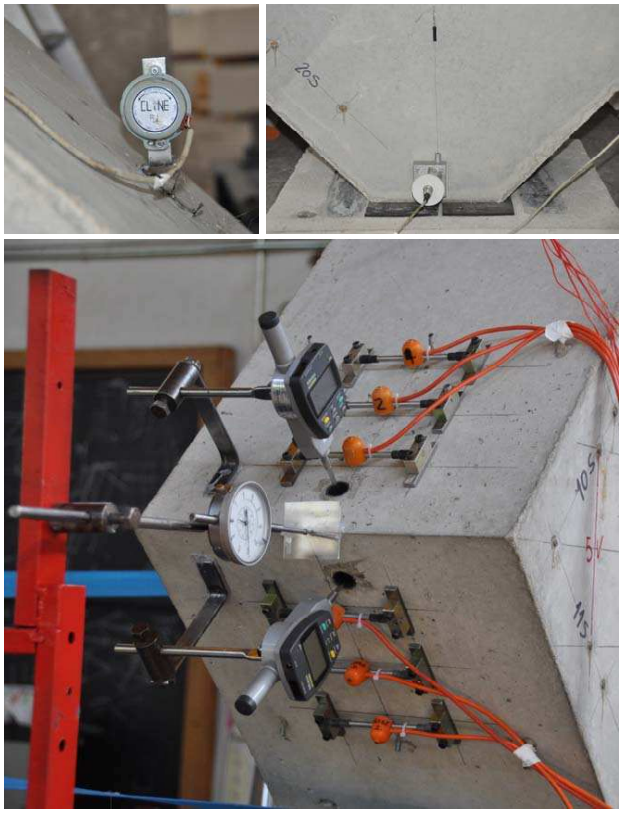

(a) *Photo*

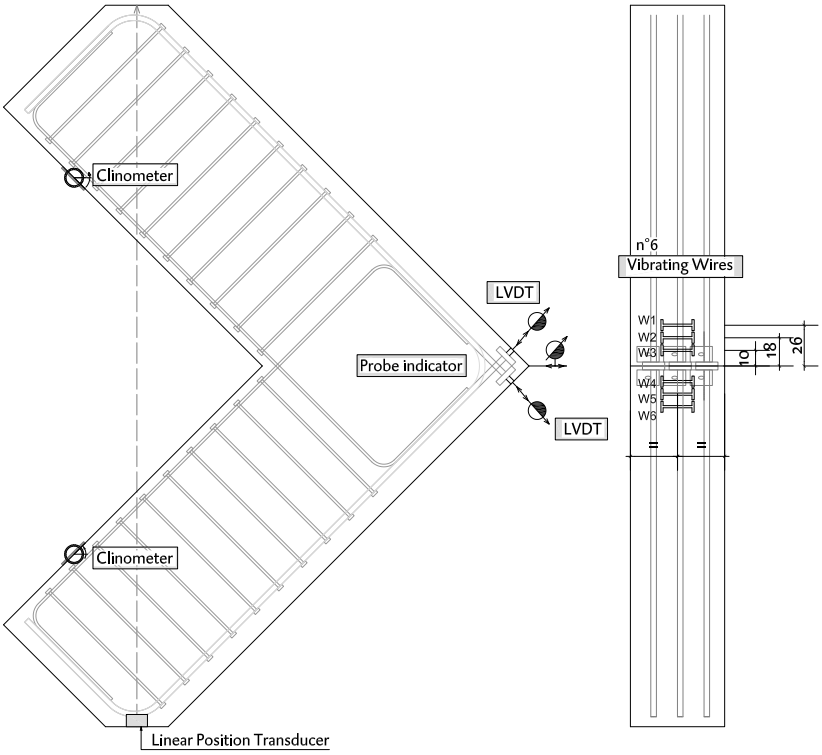

(b) *Drawing*

Figure 5.12: Specimen Instrumentation

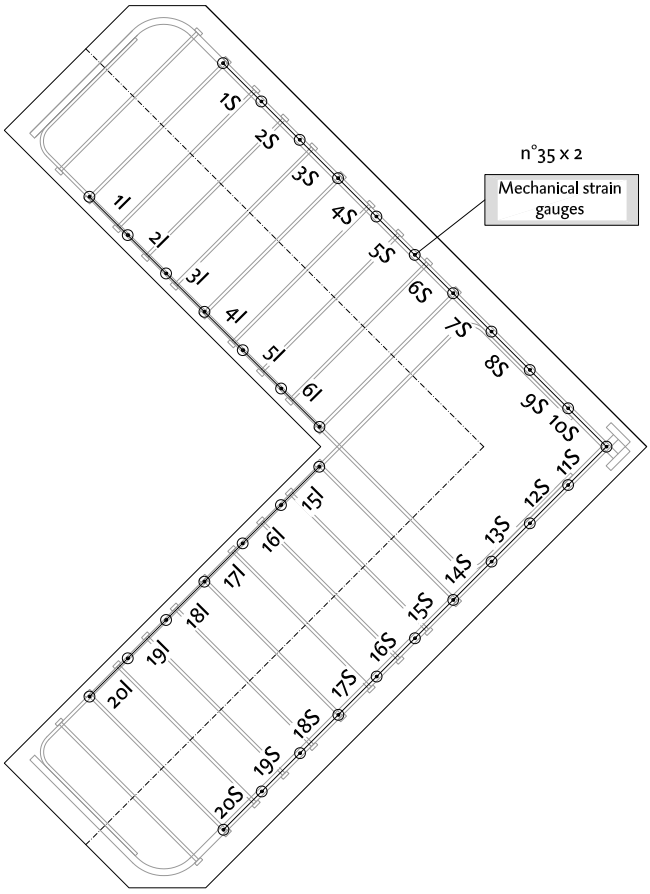

(a) *Targets on reinforcement axis*

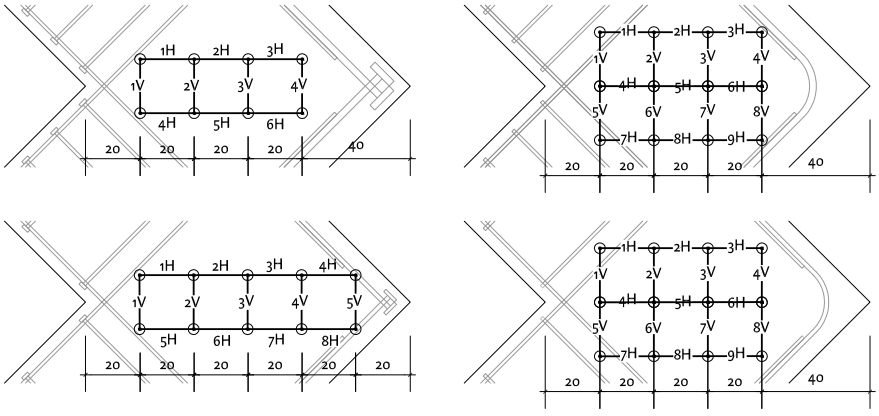

(b) *Targets on compression struts: TH specimens (left), CV specimens (right), 25 mm rebars (up) and 16 mm (down)*

Figure 5.13: Mechanical strain gauges on concrete surface

5.2.4 Fabrication

Since the plate-anchored reinforcement were only about 80 cm long, the rest of the top reinforcement (bar number 1 in Figures 5.7–5.8 were conventional reinforcement bars ending with a thread, which made possible the connection with the short headed rebars. These were provided by ANCON, who also provides *Bar X-L* couplers (Figure 5.14) in order to connect the two parts.

Figure 5.14: A bar coupler being tested on a rebar at the moment of reception

Each bar to be joined was cut and the ends were marginally enlarged by a cold forging process in order to increase the cross sectional area of the bar: through this procedure, the thread is cut into the enlarged ends of the bar avoiding a section reduction and consequently assuring the strength of the connection is at least equal to the characteristic yield strength of the bar.

The rest of the process was not particularly difficult: once built, the reinforcement cage is placed in the formwork, where it is supported by a bed of small rods positioned at a determined distance from the bottom. Special attention was paid to control the inclination of chamfers during the manufacture of test specimens (see Figure 5.15a–5.15b). The laboratory technicians stated that TH and CV specimens were very similar with regards to the effort required to build the specimens. After the fabrication, measurements were taken

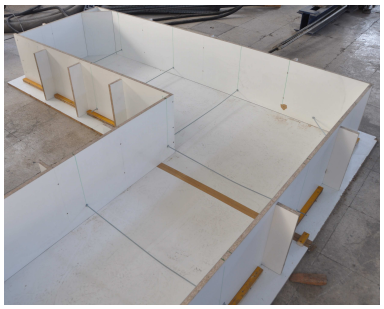

(a) *The formwork*

(b) *The 45° chamfer*

Figure 5.15: Two details of the manufacturing

in order to ensure that steel rebars were placed according to the initial drawings. Some of them have been reported in Figure 5.17–5.22.

(a) *Specimen*

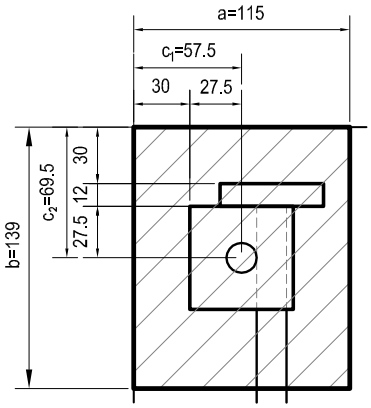

(b) *Block dimensions to be considered*

(c) *Side Cover (1)*

(d) *Side Cover (2)*

(e) *Top cover*

(f) *Bottom cover*

(g) *Plan view*

(h) *Elevation view*

Figure 5.16: Specimen 25-TH-16

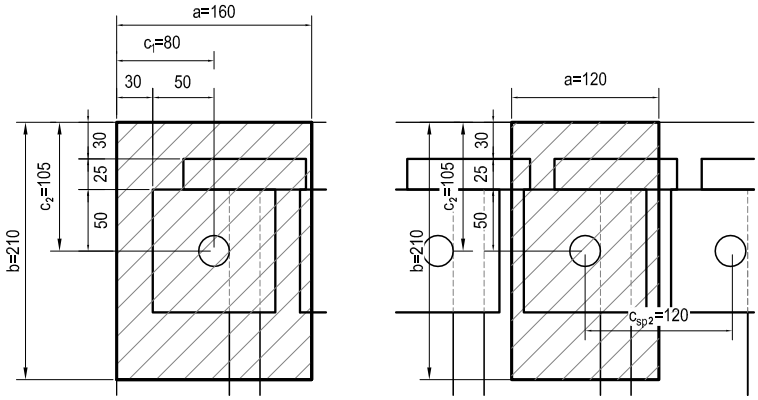

(a) *Block dimensions to be considered for side bar (left) and central bar (right)*

(b) *Specimen*

(c) *Side Cover (1)*

(d) *Side Cover (2)*

(e) *Top cover*

(f) *Bottom cover*

(g) *Plan view*

(h) *Elevation view*

Figure 5.17: Specimen 25-TH-25

(a) *Specimen*

(b) *Side Cover (1)*

(c) *Side Cover (2)*

(d) *Top cover*

(e) *Bottom cover*

Figure 5.18: Specimen 25-CV-16

(a) *Specimen*

(b) *Side Cover (1)*

(c) *Side Cover (2)*

(d) *Top cover*

(e) *Bottom cover*

Figure 5.19: Specimen 25-CV-25

(a) *Specimen*

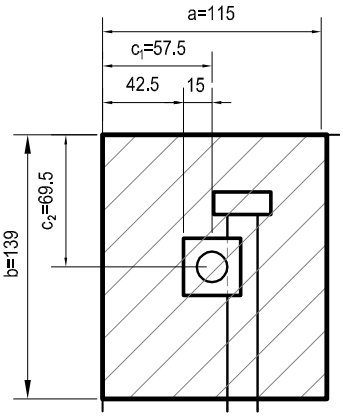

(b) *Block dimensions to be considered*

(c) *Side Cover (1)*

(d) *Side Cover (2)*

(e) *Top cover*

(f) *Bottom cover*

(g) *Plan view*

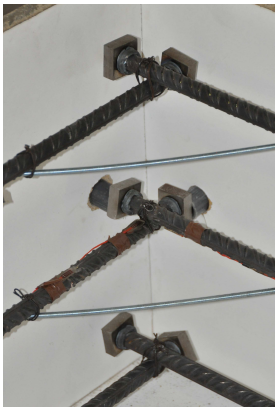

(h) *Elevation view*

Figure 5.20: Specimen 45-TH-16

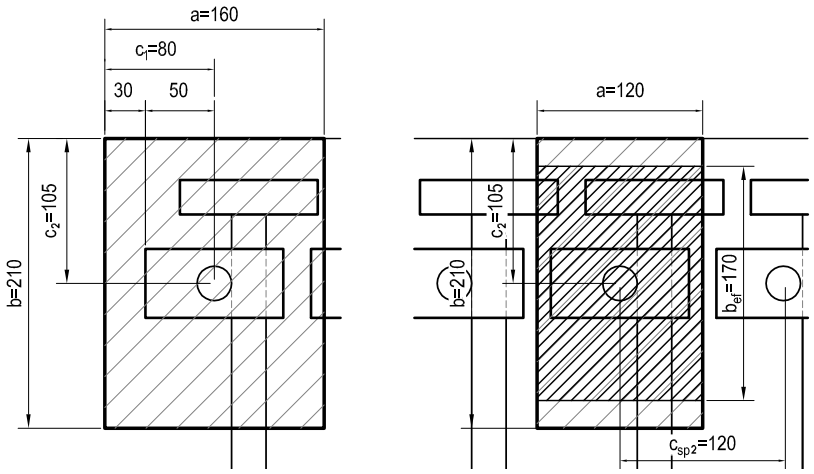

(a) *Block dimensions to be considered for side bar (left) and central bar (right)*

(b) *Specimen*

(c) *Side Cover (1)*

(d) *Side Cover (2)*

(e) *Top cover*

(f) *Bottom cover*

(g) *Plan view*

(h) *Elevation view*

Figure 5.21: Specimen 45-TH-25

(a) *Specimen*

(b) *Side Cover (1)*

(c) *Side Cover (2)*

(d) *Top cover*

(e) *Bottom cover*

Figure 5.22: Specimen 45-CV-16

(a) *Specimen*

(b) *Side Cover (1)*

(c) *Side Cover (2)*

(d) *Top cover*

(e) *Bottom cover*

Figure 5.23: Specimen 45-CV-25

5.2.5 Test Setup

The test setup is shown in Figures 5.24–5.25: the elements of interest are described in Table 5.4.

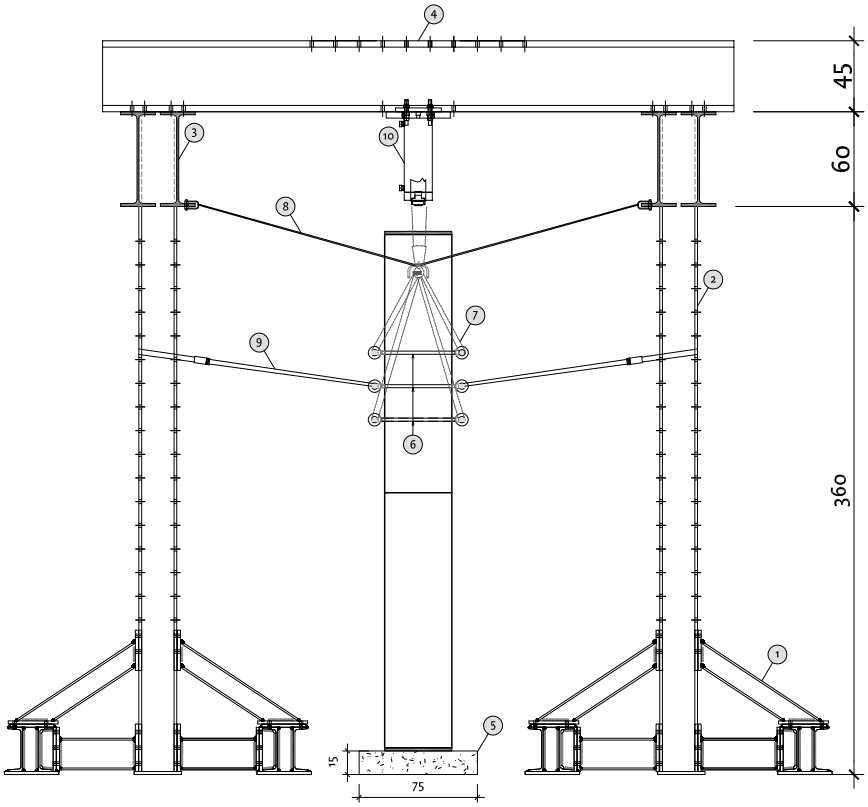

Figure 5.24: Test Setup: side view

#	Object	Notes
1	Frame base	Four anchorages for each column
2	Frame column	HEB 240
3	Frame beam	IPE 600
4	Welded profile	$(b; h; t_f; t_w) = (300; 450; 40; 30)$ [mm]
5	Support plate	$750 \times 750 \times 150$ mm
6	Passing bars	$\phi 20$ mm
7	Primary safety straps	Passive connection to the crane: equilibrium would not be lost in case of a sudden rupture
8	Secundary safety straps	Passive connection to the frame beam
9	Active hanging straps	Used to set the initial position, they are loosened when the applied load reaches 100 kN.
10	Static jack system	Maximum load: 1000 kN

Table 5.4: Legend

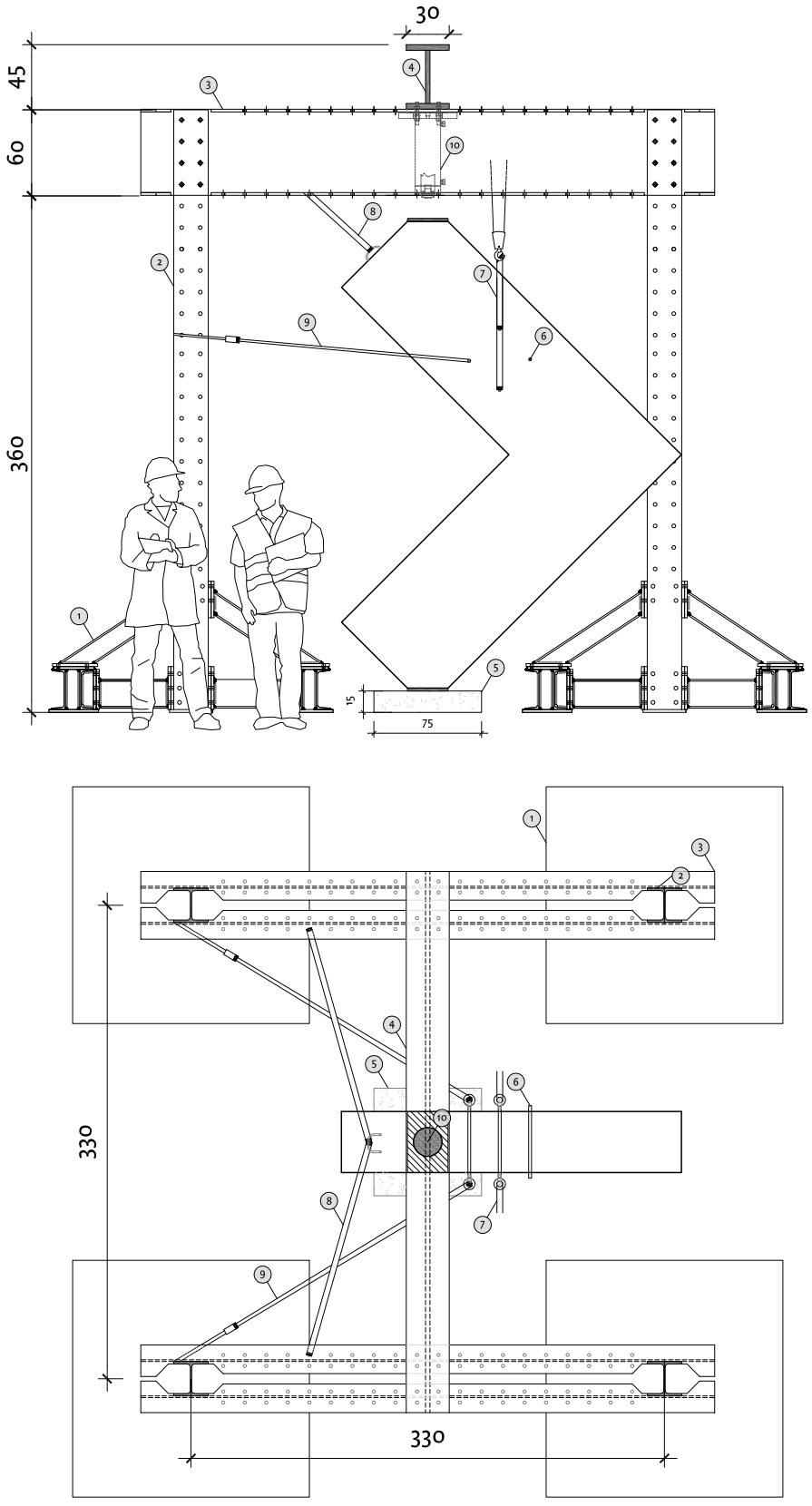

Figure 5.25: Test Setup: front and plan view

5.3 STRUCTURAL ANALYSIS

A three-level analysis has been performed: the first level is a sectional analysis. At a second level, each specimen has been analyzed with a structural analysis in which material nonlinearity has been taken into account: as the structure is isostatic, the moment diagram is fully determined and the procedure has a fast convergence. Each model provides information about displacements and rotations expected at each stage of the test and monotonic curves useful for comparison during the test execution. Finally, a more sofisticated analysis with a combined fracture-plastic model have been performed with the finite element software ATENA.

5.3.1 Expected behavior and failure mode

The mechanical reinforcement ratio ω is low for all the specimens tested, as shown in Table 5.5. According to Stroband and Kolpa [114] (see Section 1.3.5.1) the crushing of the diagonal strut is likely to be avoided, i. e. the joint is expected to be stronger than the members adjoining in: therefore, failure is expected to occur due to bending, with yielding of the reinforcement in the proximity of the corner.

The transverse reinforcement has been designed in order to avoid a shear failure of the adjoining members, ensuring a flexural-type failure.

Specimen	A_s [mm^2]	f_{cd} [MPa]	c [mm][5]	d [mm]	ω
25-XX-25	1473	25	105,0	745,0	0,093
45-XX-25	1473	45	105,0	745,0	0,052
25-XX-16	603	25	69,5	780,5	0,036
45-XX-16	603	45	69,5	780,5	0,020

Table 5.5: Mechanical reinforcement ratio for tested specimens. XX=Values for both TH and CV specimens

5.3.2 Sectional analysis

According to the test setup, the applied vertical force is decomposed into its axial (N) and shear (V) components, generating a bending moment M=1,225 N at the critical section, as shown in Figure 5.26. The presence of the axial component has no consequences on the failure mode, though its presence enhances the strength of the section against flexure.

[5] Unless otherwise specified, in this chapter the word cover means the *distance from the bar axis to the nearest exposed surface.*

Concrete cover for bars in tension is specified in Table 5.5 while bars in compression have a concrete cover of 66 mm in all specimens.

An interaction diagram is provided for each specimen in Figure 5.28, while the M–χ diagrams, calculated for a constant eccentricity (M/N=1,225 m), are provided in Figure 5.29. Table 5.6 gathers, for each specimen, the failure loads and other magnitudes of interest.

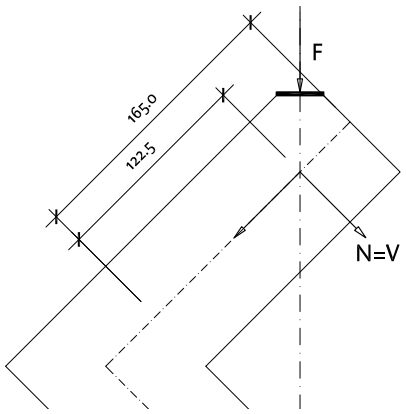

Figure 5.26: Decomposition of the applied force into its components

5.3.2.1 *Materials*

Concrete has been modeled using a general Sargin equation with no tensile strength (EN 1992-1-1–§3.1.5, Equation 3.14 – plotted in Figure 5.27), with $f_{cm} = (22; 24; 49; 51)$ MPa[6].

Steel has been modeled using a bilinear law with $f_y = 550; f_u = 660$; E=200 000; $\epsilon_u = 67{,}5$ ‰.

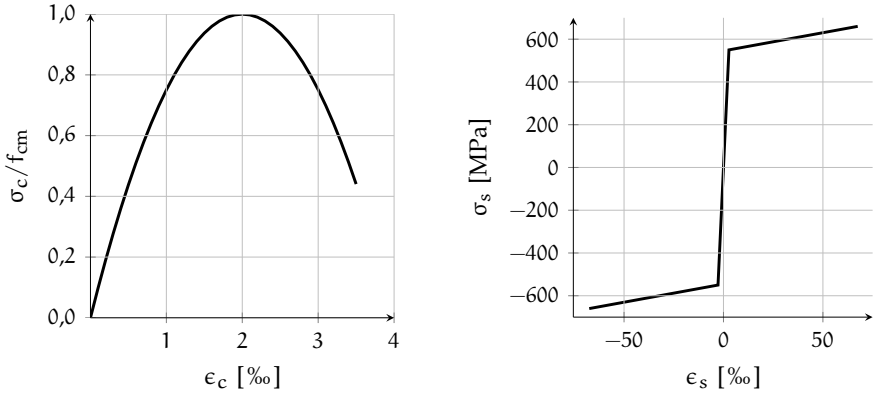

Figure 5.27: Stress-strain relations for concrete and steel

[6]The value 22 MPa refers to the first two specimens tested, while following values refer to remaining tests, ordered by the moment in which they were tested (see also Table 5.3).

5.3.2.2 *25-TH-25*

Specimen 25-TH-25, shown in Figure 5.7a, has a cover of 105 mm. Sectional analysis indicates a failure due to the excessive strain in steel, larger than 20 ‰at the ultimate load ($N_u M_u$) = (−638 kN, −781 kNm) , which, with the proposed setup, provides a jack load of $638 \cdot \sqrt{2} = 902$ kN. Axial load increases the strength of the section. However, it does not affect the capacity of the headed bar, since failure is due to excessive steel strains.

5.3.2.3 *45-TH-25*

The concrete used for this specimen (Figure 5.7b) has a mean compressive strength of 51 MPa. The expected ultimate load is (N_u, M_u) = (−725, −888), the jack load being 1025 kN. Again, a ductile behavior is expected, with a steel strain at failure equal to 27‰.

5.3.2.4 *25-TH-16*

A cover of 69,5 mm has been used for this specimen (Figure 5.8a). The ultimate flexural strength implies a jack load of 444 kN, with (N_u, M_u) = (−314, −385). Steel is expected to reach a strain of 30‰.

5.3.2.5 *45-TH-16*

A cover of 69,5 mm has been used for this specimen (Figure 5.8b). Failure is expected with a jack load of 499 kN, with (N_u, M_u) = (−357, −432). Steel strains larger than 52‰are expected at failure.

Specimen	N_{Rd} [kN]	M_{Rd} [kNm]	F_{Jack} [kN]	$\frac{1}{r_u}$ [km^{-1}]	ϵ_{su} [‰]	x [mm]
25-XX-25	−638	−781	902	−20,4	13,9	679
45-XX-25	−725	−888	1025	−36,1	27,2	753
25-XX-16	−314	−385	444	−40,4	30,8	764
45-XX-16	−353	−432	499	−66,3	52,9	797

Table 5.6: Expected faliure load for tested specimens.
XX=Values for both TH and CV specimens

Most likely it will not be possible to reach the failure load for specimens with larger bars, since the jack can apply a maximum nominal force of 1000 kN; however, it should be sufficient to reach a situation of extensive cracking with full yielding of the tensile reinforcement, thus serving the purpose.

5.3.3 Transverse reinforcement

In this section the needed amount of transverse reinforcement which ensures a flexural-type failure is calculated, avoiding a shear-related

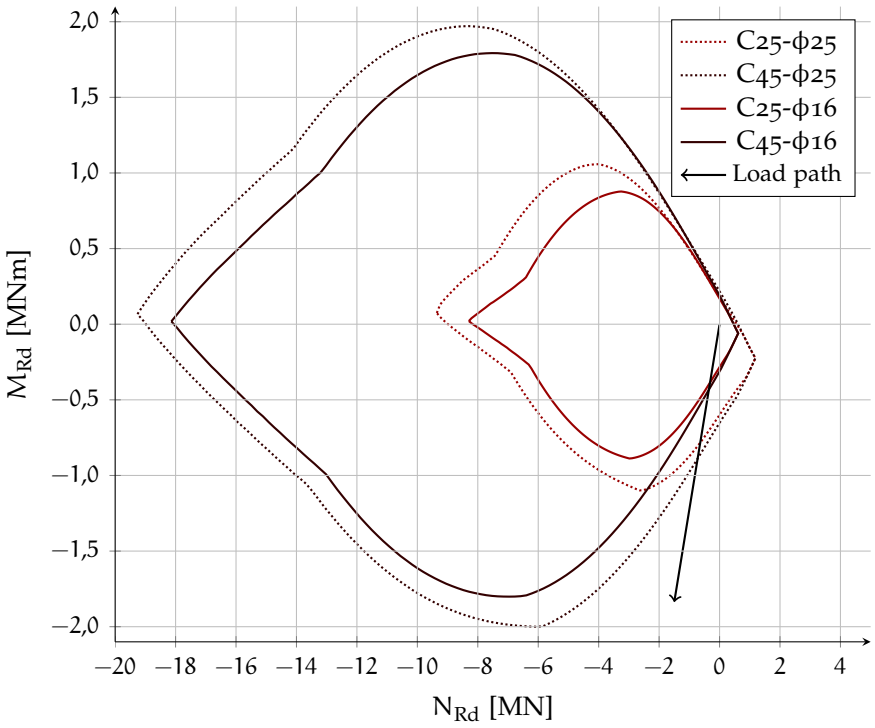

Figure 5.28: Interaction diagrams for the four specimens tested: the load path is shown in black

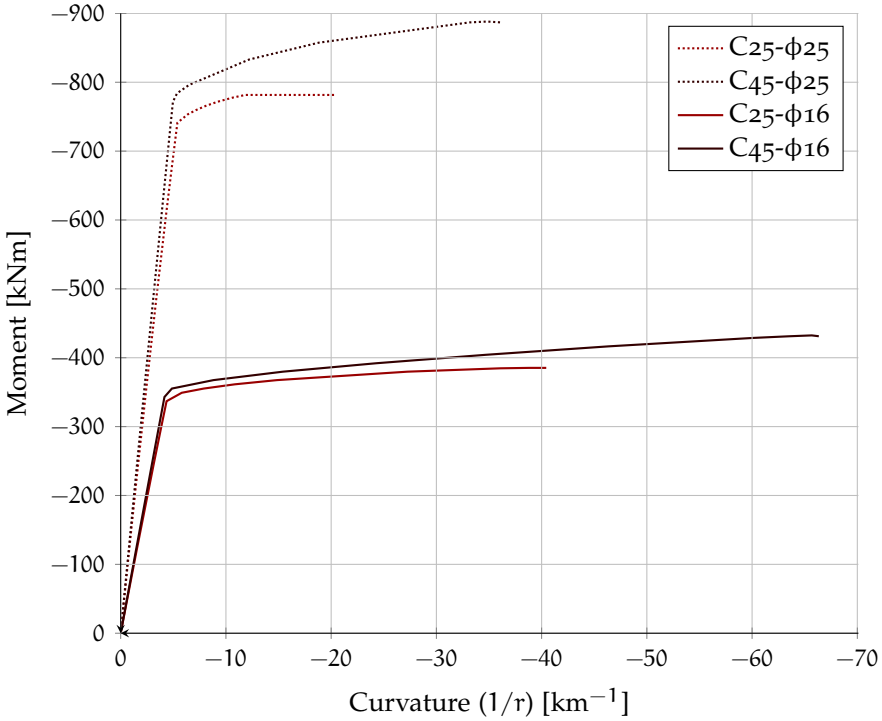

Figure 5.29: $M - 1/r$ diagrams for the four specimens tested, each one calculated for $N_{Rd} = M_{Rd}/1{,}225$

failure which could imply a premature, fragile, rupture of the specimen. The transverse reinforcement, in form of 12 mm rebars, is also made by plate-anchored bars, aiming to check the adequacy of mechanical anchorages for shear reinforcement.

The shear force V_{Sd} acting at failure in flexure on specimens with 25 or 16 mm rebars is, respectively:

$$V_{Sd} = (729; 357)\ \text{kN}$$

For members requiring shear reinforcement, the Eurocode 2–Part 1.1–§6.2.3 assumes the shear resistance, V_{Rd}, as:

$$\begin{aligned} V_{Rd} &= \min\left(V_{Rd,s}; V_{Rd,max}\right) = \\ &= \min\left(\frac{A_{sw}}{s} z f_{ywd} \cot\theta; \frac{\alpha_{cw} b_w z \nu_1 f_{cd})}{\cot\theta + \tan\theta}\right) > V_{Sd} \end{aligned}$$

The design value of the maximum shear force which can be sustained by the member limited by crushing of the compression struts, is sufficient if compared to the expected level of loads. For specimens with 25 mm rebars:

$$\begin{aligned} V_{Rd,max,C25} &= \frac{1 \cdot 425 \cdot 0{,}9 \cdot 745 \cdot 0{,}6 \cdot 16{,}67}{1000 \cdot (2{,}5 + 0{,}4)} = 983\ \text{kN} \\ V_{Rd,max,C45} &= V_{Rd,max,C25} \cdot 30/16{,}67 = 1769\ \text{kN} \end{aligned}$$

The amount of transverse reinforcement needed is:

$$\frac{A_{sw}}{s} \geqslant \frac{V_{Sd}}{z f_{ywd} \cot\theta}$$

which gives, for specimens with 25 and 16 mm rebars, respectively 1000 mm^2/m and 468 mm^2/m. The chosen detailing, with 12 mm diameter 2-legged stirrups and a spacing of 150 and 300 mm, corresponds respectively to 1,5 and 1,6 times the needed area.

5.3.4 Plate calculations

The experimental campaign is conducted in order to verify the structural design by means of demonstration tests: plate sizes have been designed as it would in practice, ensuring that is guaranteed the full yielding of the reinforcement using material design strengths, that is, $N_{Rd} \geqslant N_{Sd}$.

In a first approach, a tentative size for square plates was approximated supposing that the worst conditions in normal practice would be that of a 30 mm cover and a mininum clear space between plates of 20 mm, correspondent to the maximum dimension of the aggregates. Also, the minimum spacing between rebars (c_{sp2}) was supposed to be 100 mm (see Figure 5.30).

Regarding the shape of the anchorage plates, it was decided to use square shapes for concrete classes C25/30 and rectangular shapes for concrete classes C45/55. In such conditions, the problem is to find a plate size ($a_1 \times b_1$ with $a_1 = b_1$) such that:

$$
\begin{aligned}
a &= 2c_1 = \max(a_1 + 20; 100) \\
b &= 2c_2 = b_1 + 60 \\
N_{Sd} &= A_s f_{yd} \\
N_{Rd,1} &= \min\left(\sqrt{\frac{A_c}{A_n}}; 7{,}0\right) A_n f_{cd} \\
N_{Rd,2} &= \frac{8}{3} f_{ctd} \frac{A_c}{1 - \sqrt{\frac{A_1}{A_c}}} \\
N_{Rd} &= \min(N_{Rd,1}; N_{Rd,2}) \\
N_{Rd} &\geqslant N_{Sd}
\end{aligned}
$$

By means of the previous equations it can be figured out that the square plates must have a minimum size of 99, 62 and 37 mm for anchoring a rebar made of standard B500SD steel, for 25, 16 and 12 mm diameter respectively[7].

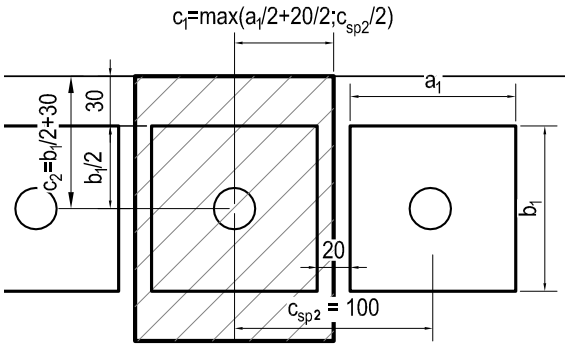

Figure 5.30: Calculation of minimum plate size

Given the presence of the two facing plates and a different spacing between rebars, plate sizes used for the experimental campaign are slightly different. Concrete cover is kept constant for specimens of each reinforcement bar diameter, thus rectangular plates have the same cover of square plates.

The block dimensions to be considered were identified as explained in Chapter 3 and are reported in Figure 5.16–5.17.

[7] In all cases the blowout failure is the governing criterion ($N_{Rd,2} < N_{Rd,1}$)

5.3.4.1 *25-TH-25*

The first calculation is referred to the side bar, while the second one refers to the middle plate (see Figure 5.17a). The ratio A_1/A_b is 20,4.

$$
\begin{aligned}
c_1 &= 30 + 100/2 = 80 \text{ mm} \\
c_2 &= 30 + 25 + 100/2 = 105 \text{ mm} \\
a &= 2c_1 = 2 \cdot 80 = 160 \text{ mm} \\
b &= 2c_2 = 2 \cdot 105 = 210 \text{ mm} \\
b_{ef} &= b_1 + \beta a \leqslant b \\
b_{ef} &= 100 + 1{,}00 \cdot 160 = 260 \leqslant 210 \\
A_n &= 100 \cdot 100 - 491 = 9509 \text{ mm}^2 \\
N_{Rd,1} &= \min\left(\sqrt{\frac{160 \cdot 210}{9509}}; 7{,}0\right) \cdot 9509 \cdot 16{,}67 = 298 \text{ kN} \\
N_{Rd,2} &= \frac{8}{3} \cdot 1{,}20 \frac{160 \cdot 210}{1 - \sqrt{\frac{100 \cdot 100}{160 \cdot 210}}} = 236 \text{ kN}
\end{aligned}
$$

The design minimum capacity is due to the blowout criterion, with a load 11% higher than the force needed to achieve yielding of the reinforcement (213 kN). The calculation is repeated for the middle plate:

$$
\begin{aligned}
c_2 &= 30 + 25 + 100/2 = 105 \text{ mm} \\
a &= c_{sp2} = 120 \text{ mm} \\
b &= 2c_2 = 2 \cdot 105 = 210 \text{ mm} \\
b_{ef} &= b_1 + \beta a \leqslant b \\
b_{ef} &= 100 + 1{,}00 \cdot 120 = 220 \leqslant 210 \\
N_{Rd,1} &= \min\left(\sqrt{\frac{120 \cdot 210}{9509}}; 7{,}0\right) \cdot 9509 \cdot 16{,}67 = 258 \text{ kN} \\
N_{Rd,2} &= \frac{8}{3} \cdot 1{,}20 \frac{120 \cdot 210}{1 - \sqrt{\frac{100 \cdot 100}{120 \cdot 210}}} = 217 \text{ kN}
\end{aligned}
$$

Again, the design minimum capacity is due to the blowout criterion, with a load only 2% higher than the force needed to achieve yielding of the reinforcement.

5.3.4.2 *25-TH-16*

$$
\begin{aligned}
c_1 &= 30 + 55/2 = 57{,}5 \text{ mm} \\
c_2 &= 30 + 12 + 55/2 = 69{,}5 \text{ mm} \\
a &= 2c_1 = 2 \times 57{,}5 = 115 \text{ mm} \\
b &= \min(2c_2; c_{sp2}) = \min(2 \cdot 69{,}5; 147) = 139 \text{ mm} \\
b_{ef} &= b_1 + \beta a \leqslant b \\
b_{ef} &= 55 + 1{,}00 \cdot 115 = 170 \leqslant 139 \\
A_n &= 55 \cdot 55 - 201 = 2824 \text{ mm}^2 \\
N_{Rd,1} &= \min\left(\sqrt{\frac{115 \cdot 139}{2824}}; 7{,}0\right) \cdot 2824 \cdot 16{,}67 = 112 \text{ kN} \\
N_{Rd,2} &= \frac{8}{3} \cdot 1{,}20 \cdot \frac{115 \cdot 139}{1 - \sqrt{\frac{55 \cdot 55}{115 \cdot 139}}} = 90 \text{ kN}
\end{aligned}
$$

The governing failure mode is the blowout criterion, with a load of 90 kN, a value slightly higher than the force needed to achieve yielding of the reinforcement (87 kN). The ratio A_1/A_b is 15,0.

5.3.4.3 *45-TH-25*

The first calculation is referred to the side bar, while the second one refers to the middle plate (see Figure 5.21a). The ratio A_1/A_b is 10,2.

$$
\begin{aligned}
c_1 &= 30 + 100/2 = 80 \text{ mm} \\
c_2 &= 105 \text{ mm} \\
a &= 2c_1 = 2 \cdot 80 = 160 \text{ mm} \\
b &= 2c_2 = 2 \cdot 105 = 210 \text{ mm} \\
b_{ef} &= b_1 + \beta a \leqslant b \\
b_{ef} &= 50 + 1{,}00 \cdot 160 = 210 \leqslant 210 \\
A_n &= 100 \cdot 50 - 491 = 4509 \text{ mm}^2 \\
N_{Rd,1} &= \min\left(\sqrt{\frac{160 \cdot 210}{4509}}; 7{,}0\right) \cdot 4509 \cdot 30 = 369 \text{ kN} \\
N_{Rd,2} &= \frac{8}{3} \cdot 1{,}77 \frac{160 \cdot 210}{1 - \sqrt{\frac{100 \cdot 50}{160 \cdot 210}}} = 258 \text{ kN}
\end{aligned}
$$

The design minimum capacity is due to the blowout criterion, with a load 21% higher than the force needed to achieve yielding of the

reinforcement (213 kN). The calculation is repeated for the middle plate:

$$
\begin{aligned}
c_2 &= 30 + 50/2 + 25 = 80 \text{ mm} \\
a &= c_{sp2} = 120 \text{ mm} \\
b &= 2c_2 = 2 \cdot 105 = 210 \text{ mm} \\
b_{ef} &= b_1 + \beta a \leqslant b \\
b_{ef} &= 50 + 1{,}00 \cdot 120 = 170 \leqslant 210 \\
N_{Rd,1} &= \min\left(\sqrt{\frac{120 \cdot 210}{4509}}; 7{,}0\right) \cdot 4509 \cdot 30 = 320 \text{ kN} \\
N_{Rd,2} &= \frac{8}{3} \cdot 1{,}77 \frac{120 \cdot 170}{1 - \sqrt{\frac{100 \cdot 50}{120 \cdot 210}}} = 191 \text{ kN}
\end{aligned}
$$

The design minimum capacity is due to the blowout criterion, in this case with 89% of the force needed to achieve yielding of the reinforcement. Despite the fact that this result is less than 1,0, it was decided to mantain the spacing between reinforcing bars equal to that of the previous tests.

5.3.4.4 *45-TH-16*

$$
\begin{aligned}
c_1 &= 30 + 55/2 = 57{,}5 \text{ mm} \\
c_2 &= 69{,}5 \text{ mm} \\
a &= 2c_1 = 2 \times 57{,}5 = 115 \text{ mm} \\
b &= \min(2c_2; c_{sp2}) = \min(2 \cdot 69{,}5; 147) = 139 \text{ mm} \\
b_{ef} &= b_1 + \beta a \leqslant b \\
b_{ef} &= 30 + 1{,}00 \cdot 115 = 145 \leqslant 139 \\
A_n &= 30 \cdot 30 - 201 = 699 \text{ mm}^2 \\
N_{Rd,1} &= \min\left(\sqrt{\frac{115 \cdot 139}{699}}; 7{,}0\right) \cdot 699 \cdot 30 = 100 \text{ kN} \\
N_{Rd,2} &= \frac{8}{3} \cdot 1{,}77 \cdot \frac{115 \cdot 139}{1 - \sqrt{\frac{30 \cdot 30}{115 \cdot 139}}} = 99 \text{ kN}
\end{aligned}
$$

The design minimum capacity is due to the blowout cricriterion, with a load of 99 kN, slightly higher than the force needed to achieve yielding of the reinforcement (87 kN). The ratio A_1/A_b is 4,5.

5.3.4.5 *Double-headed rebars*

Double-headed bars are tested in the four TH specimens, aiming to demostrate the adequacy of this type of detail for the anchorage of transverse reinforcement. For specimens with a concrete class C25/30,

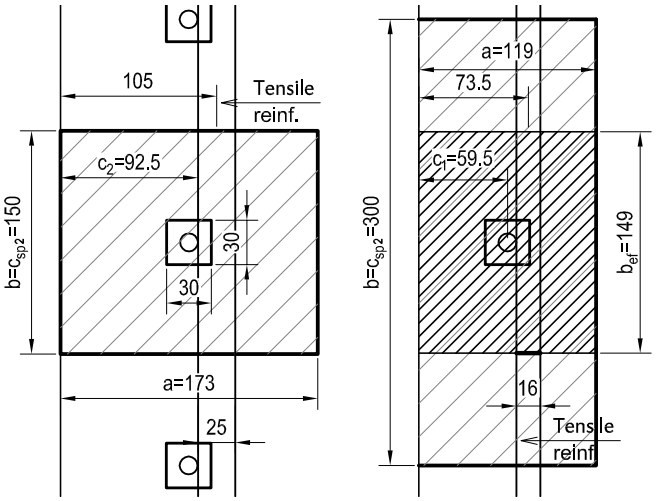

Figure 5.31: Block dimensions considered for the double headed rebars for specimens with 25 mm rebars (left) and 16 mm rebars (right)

the minimum anchor capacity is obtained with the following calculations, referred to the right side of Figure 5.31:

$$
\begin{aligned}
a &= 2c_1 = 119 \text{ mm} \\
b &= c_{sp2} = 300 \text{ mm} \\
b_{ef} &= b_1 + \beta a \leqslant b \\
b_{ef} &= 30 + 1{,}00 \cdot 119 = 149 \leqslant 300 \\
A_n &= 30 \cdot 30 - 113 = 787 \text{ mm}^2 \\
N_{Rd,1} &= \min\left(\sqrt{\frac{119 \cdot 300}{787}}; 9{,}0\right) \cdot 787 \cdot 16{,}67 = 88 \text{ kN} \\
N_{Rd,2} &= \frac{8}{3} \cdot 1{,}20 \cdot \frac{119 \cdot 149}{1 - \sqrt{\frac{30 \cdot 30}{119 \cdot 149}}} = 73 \text{ kN}
\end{aligned}
$$

The design mininum capacity is due to the blowout criterion, with a load of 73 kN, representing almost 150% of the force needed to achieve yielding of the reinforcement (49 kN). The ratio A_1/A_b is 8,0.

5.3.5 Nonlinear analysis

Nonlinear analyis provided some additional information regarding the configuration of the deformed structure during the test. The analysis consisted in a standard Newton-Raphson iterative procedure, in which the structure is modeled with beam elements[8] (see Figure 5.32): for each specimen the Load-Displacement and Load-Rotation curves were obtained and compared with the experimental results. Mate-

[8] Elements inside the core has been modeled with a linear moment-cutvature diagram, with a ratio $M/(1/r)$ approximately equal to the initial stiffness: 100 000 and 150 000 kNm^2, respectively, for specimens with 16 mm rebars or 25 mm rebars

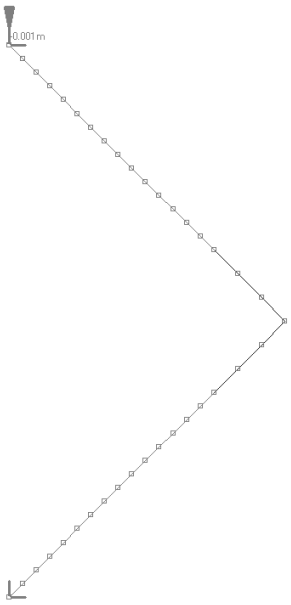

Figure 5.32: The structure as modeled, with eighteen elements on each side: the three elements inside the core has been modeled with a more rigid $M - 1/r$ diagram in order to locate the flexural plastic hinge at the intersection with the adjoining members

rial constitutive laws are taken from the section definition, as in Figure 5.27). Results from nonlinear analysis are provided in Figure 5.33.

5.3.6 Analysis by F.E. software ATENA

The description of the Finite Element Models used for the comparison with the experimental data is presented here, while the software used for the analysis has already been described in detail in Section C.3.

A total of four finite element models were prepared, the permutation of the two different reinforcement areas and the two different concrete classes being taken as primary variables. Some efforts were made to model the third primary variable, the presence of the anchorage plates, but finally this option was abandoned due to the following reasons:

- A plane (2D) analysis would not be a correct modeling of the plate elements, since the program could not represent the complex behavior of the anchorage area.
- In a 3D analysis, the reinforcement bars elements would be connected to steel macroelements needed to model the plates and the plates macroelements would be embedded into carved concrete macroelements. The tedious process requested to carve the concrete block and to establish all contacts between macroelements joined with the large computing time requested to perform the analysis led to abandon this option.

Furthermore, assuming that the plate anchorage does not fail prematurely, the same ultimate load has to be reached in both TH and

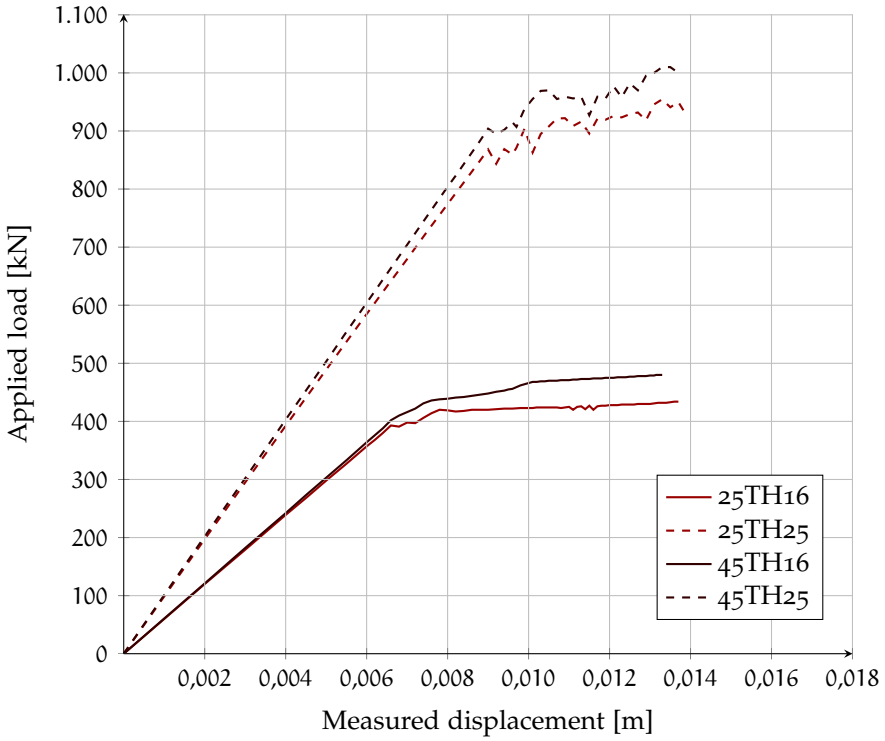

Figure 5.33: Applied load Vs displacement of the load application point. Theoretical estimations by nonlinear analysis

CV specimens, since they have the same cover. For the above reasons, only plane stress models with conventional detailing will be analyzed: the same curve will be used for the comparisons with both CV and TH experimental curves.

5.3.6.1 *Model description*

The models developed in ATENA are 2D models with conventional bar reinforcement. The two arms of the joint are 2500 mm long and the thickness assigned to all macroelements is 425 mm.

In order to reduce computational time a mesh size of 0,05 m for the steel elements and 0,10 m for concrete elements has been chosen. However, dozens of attempts were made in order to understand whether the mesh size would require refinement or not. Another parameter whose influence on the result has been assessed was the concrete tensile strength, which has been varied between 0,5 and 2,5 MPa: almost no influence were observed on the ultimate load[9].

The 25-CV-16 model is shown in Figure 5.34. Regarding the materials used, steel plates made of *Plane Stress Elastic Isotropic* material with $E = 200\,000$ MPa are positioned at both chamfers: its presence is

[9] As expected, the only influence observed was on the load at which the first crack formed: the difference tended to desappear with the grow of the applied force (tension stiffening effect).

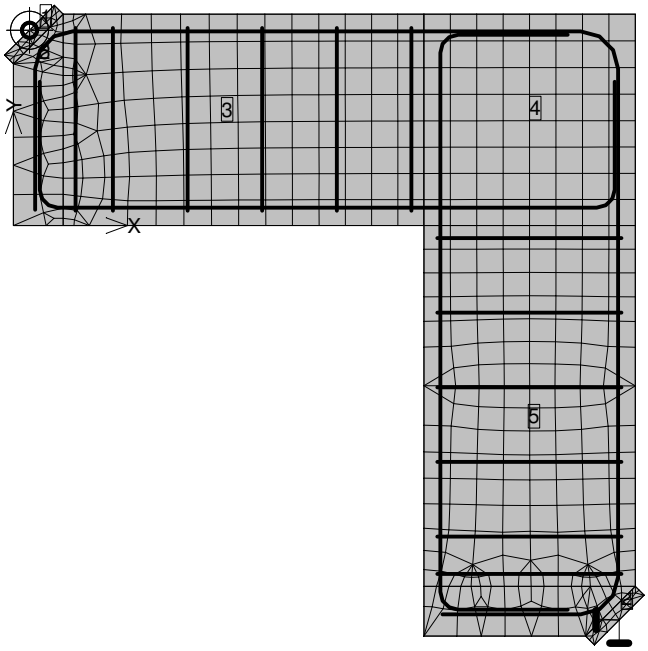

Figure 5.34: ATENA 25-XX-16 model. The monitors measuring the registered force and the imposed displacement can be seen in correspondence of the upper chamfer, while the bidirectional support is visible at the lower chamfer.

conceived to ensure a better distribution of the applied force on the concrete surface. Reinforcement bars are made of bilinear steel with $f_y = 550$ MPa, $f_u = 660$ MPa and $\varepsilon_{lim} = 67{,}5$ ‰set having a *perfect connection* with the surrounding concrete.

Finally, the concrete macroelements are made of a standard ATENA *3D Non Linear Cementitious 2* with default parameters[10] E=28480 MPa; $f_c = -22$ MPa. In tension, an exponential softening law is used, fully defined by the tensile strength f_t=2,10 MPa and the specific fracture energy $G_f = 52{,}5$ N/m. In compression, a linear softening is used: since the stress-strain curve in ATENA is based on uniaxial experiments, in a plane stress formulation the confinement effect cannot be modeled [22]. The governing parameter for the ultimate strain is the critical compressive displacement w_d: since the element size is 0,10 m, in all models has been set equal to ten times the default value ($w_d = -0{,}005$) m.

Results from ATENA analysis are provided in Figure 5.35.

5.4 TESTING PROCEDURE

The knee joint specimens are tested with a static jack capable of applying a maximum load of 1000 kN, which allow the execution of

[10] Value for specimen 25-CV-16

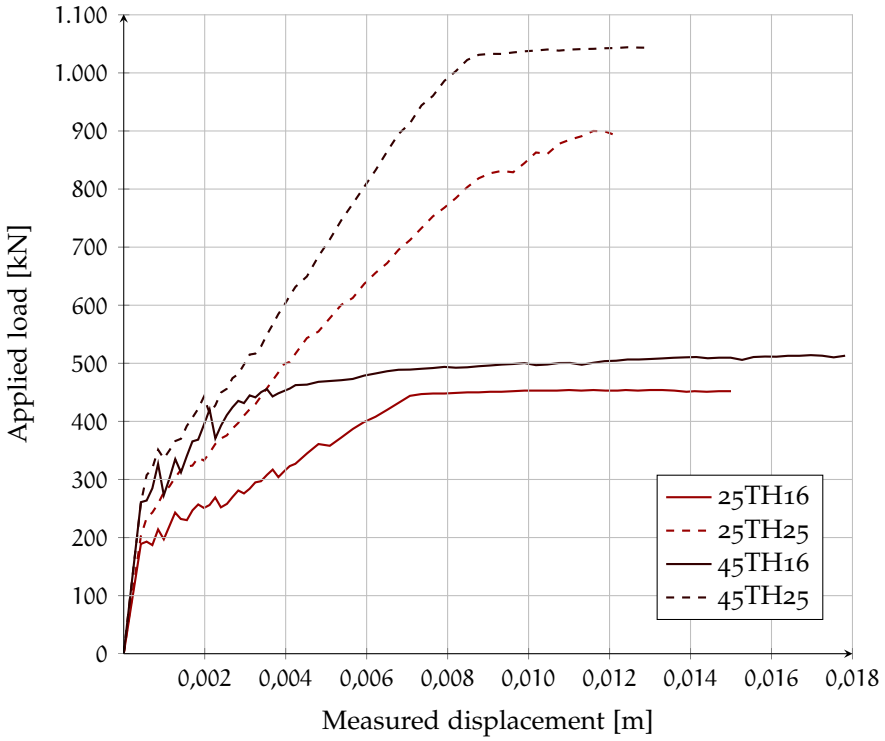

Figure 5.35: Applied load Vs displacement of the load application point. Theoretical estimations by ATENA

the tests up to the predicted level of maximum load: the specimens are placed in position, rotated 45 degrees respect to the directrix, as shown in Figure 5.25.

All instrumentation is connected to a data acquisition system and readings at each load increment were taken. At early load stages, the load was held constant while data such as crack widths and mechanical gauge readings were gathered; at final load stages only continuous measurements were taken. Complete tests data are reported in Appendix D.

5.5 SUMMARY

The test concept and preparation has been described in detail in this chapter together with the instrumentation used. Also, a series of theoretical predictions have been performed, along with the plates design and specimen fabrication.

A sectional analysis, a nonlinear analysis and a F.E. analysis have been performed in order to have different estimations of the ultimate load and the load-displacement curves: while sectional analysis provides information only about ultimate load and curvature, the ATENA analysis allows the study of the crack pattern.

6 TEST RESULTS

The relevant results and related considerations provided by the experimental campaign are presented in this chapter.

6.1 MODE OF FAILURE

The observed failure mode, when achieved, was due to bending of the section adjacent to the joint with full yielding of the tensile reinforcement, as predicted. The load-displacement and load-rotation graphs collected during the experimental campaign are very similar to the theoretical predictions. Strain data and crack patterns are consistent and provide an overall picture of the joint behavior. The behavior of specimens using plate-anchored bars or standard hooks was basically the same: no blowout failure was observed in any specimen and the ultimate load reached by both specimen was comparable.

A first flexural crack was observed initially, as expected. Subsequently, small load increments led to the formation of other flexural cracks close to the first one. As the load was further increased, some bond-related cracks developed just inside the corner, and two main cracks parallel to the central strut formed. Usually the last cracks observed were some inclined flexure-shear cracks located close to the point of application of loads. Failure, when achieved, consisted of the wide opening of one of the major cracks close to the face of the joint, with a rupture of the tensile reinforcement due to excessive strain.

Only the first flexural cracks and some bond-related cracks were observed in specimen 45-TH-16 (see Figure D.51). This led to a better understanding of the two-stage process which governs the behavior of a knee joint subjected to a closing moment: as can be seen in Figure 6.1, in a first phase the joint can develop tensile stresses, while the stress state differs noticeably after the cracking of the central strut, since such tensile stresses can no longer be developed.

The Strut-and-Tie models which correspond to the two phases descripted above are shown in Figure 6.2. It can be seen how the concrete tie excludes from the resistant mechanism the last part of the reinforcement. Strain gauge readings are consistent with this observation. In fact, no significant strains were recorded in the gauges nearest to the head face (gauges 1 and 2) in specimen 45-TH-16, while in other specimens the cracking of the central strut resulted in a sharp rise in strain of these gauges.

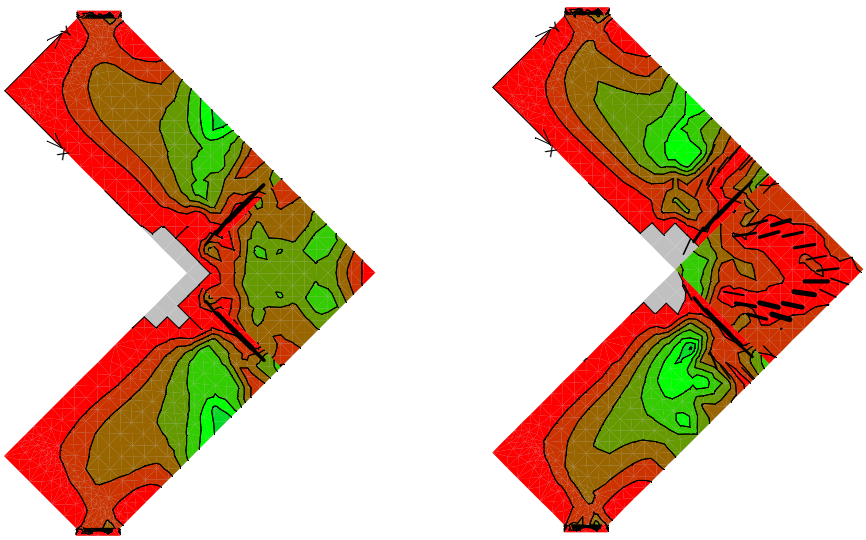

Figure 6.1: Principal maximum stresses (tensile stresses) according to an ATENA model before and after cracking of the central strut

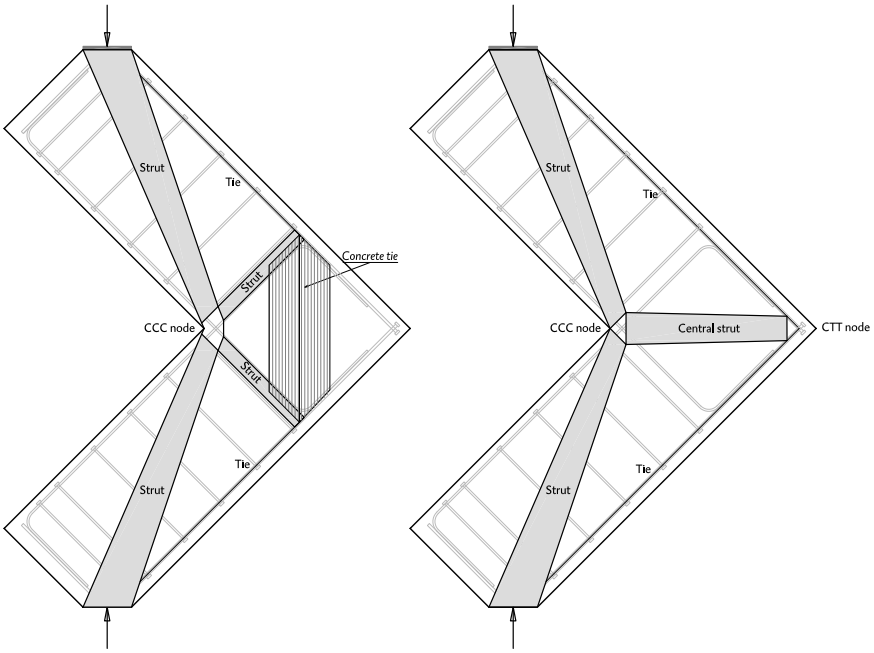

Figure 6.2: Strut-and-tie model before and after cracking of the central strut

Furthermore, comparing the crack pattern of specimen 45-TH-16 with the *sister-specimen* (45-CV-16), it can be noticed that cracks along the central strut formed at a load of 475 kN in the conventional specimen, a load very close to the ultimate load reached by specimen 45-TH-16 (490 kN). It can be concluded that in specimen 45-TH-16, the reinforcement reached the ultimate strain prior to the failure of the concrete tie.

A calculation of the width of the concrete tie ($w_{T'}$) is provided below in order to show that the previous conclusion is plausible:

$$T' = A_s f_{ym} \sqrt{2} = \frac{3 \cdot 201 \cdot 660 \cdot \sqrt{2}}{1000} = 563 \text{ kN}$$

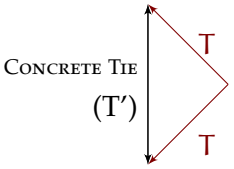

$$f_{ctm} = 0{,}30 \cdot {f_{ck}}^{2/3} = 0{,}30 \cdot 45^{2/3} = 3{,}80 \text{ MPa}$$
$$w_{T'} = 563000/(425 \cdot 3{,}80) \simeq 350 \text{ mm}$$

which is the width represented in Figure 6.2.

Thus, the difference between the crack pattern of the two specimens can be attributed to the normal scatter of concrete tensile strength. On the other hand, this implies that in specimen 45-TH-16 it has not been possible to study the effectiveness of the anchorage plate, since the stress in the reinforcement near the tip of the corner remained almost null during the test.

6.2 LOAD–DISPLACEMENT RESPONSE

The load-displacement curves are shown with the theoretical predictions by sectional analysis (in dashed lines) in Figures 6.3.

Specimens with plate-anchored reinforcement bars performed equivalently to specimens with a conventional detailing in terms of ultimate load. The ductility in terms of displacement, for specimens with 16 mm rebars, has been greater than the estimation by finite element analysis, but only due to convergence problems. Specimens with plate-anchored bars, reached an ultimate displacement respectively 50% and 30% greater of that reached by the correspondent conventional speciment, respectively for concrete class C25/30 and C45/55. However, the larger ductility achieved can be regarded as accidental, since the observed failure mode was the same in both cases.

Tests with 16 mm rebars showed a slight difference (15%) in terms of ultimate load. The difference can be partially attributed to different tensile strenght of steel, nonetheless, it is also worth noting that the bending moment which can be resisted by the section is very sensible to the concomitant axial load, given the low eccentricity of the test setup ($M = N \cdot 1{,}225$). Therefore, the ultimate load would vary

significantly in case of a different eccentricity, for instance in case of a different location of the critical crack.

Due to limitation regarding the loading capacity, tests with 25 mm rebars do not provide data on ultimate load or displacement, although it can be stated that TH and CV specimens performed equivalently in term of stiffness, with a greater stiffness for specimens with a concrete class C45/55, as expected. Yielding was however attained in all cases, so that a close approximation to ultimate load was obtained.

The six load cycles performed to increase damage have shown a small increase of the measured displacement of the control point.

6.3 CRACK PATTERN

In Appendix D the experimental crack width of segments closest to the face of the joint has been reported: the measured crack width has been compared to the theoretical steel stress, calculated at the middle of each measure segment. The same graphs are represented in Figure 6.4 for comparison, with a further average between the symmetrical segments S5-S16 and S6-S15[1].

The *crack width* depicted can be regarded as a simplification, i.e. no direct crack width measurement have been taken: furthermore, no cracks (or two cracks) developed in some segments. Still, each point is the average of four meaurement (two sections for each side of the specimen), thus, can be considered a good representation of the width of the flexural cracks.

From Figure 6.4, it can be concluded that plate-anchored detailing is comparable to conventional detailing in terms of crack control at service load levels and at ultimate load levels.
The following further observations can be made:

- No cracks have been observed on the side of the specimen near the anchorages as a consequence of forces spreading from the bearing plate. Although some significant strain has been recorded by the vibrating wires, no visual evidence of the presence of bursting cracks has been detected;
- The only difference between the crack pattern of CV and TH detailing is in the anchorage zone. Figure 6.5 reports the crack patterns of all specimens[2] within an area of 0,5 m from the tip of the corner. The following observations can be made:
  - In specimens with hooked rebar anchorages, cracks did not affect the hook zone and bond-related cracks stopped in correspondence with the beginning of the bend;

[1] See Figure 5.13a for the exact location of the measurement targets.

[2] Specimens 45-TH-16 and 45-CV-16 have been excluded from the comparison given the different failure mode of specimen 45-TH-16 (see Section 6.1)

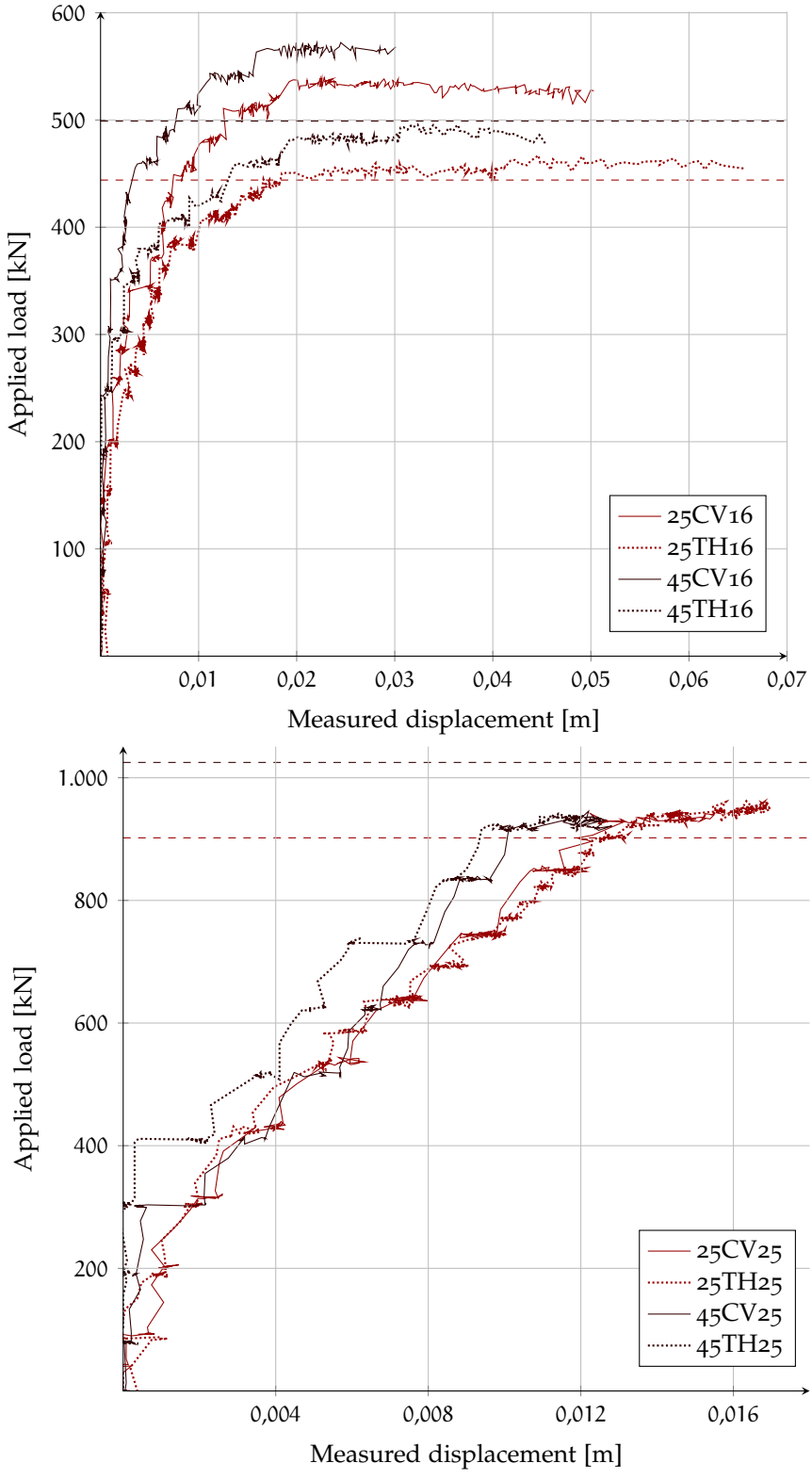

Figure 6.3: Load-displacement comparison for ϕ16 (top) and ϕ25 (bottom) specimens.
Load cycles have been hided for clearance

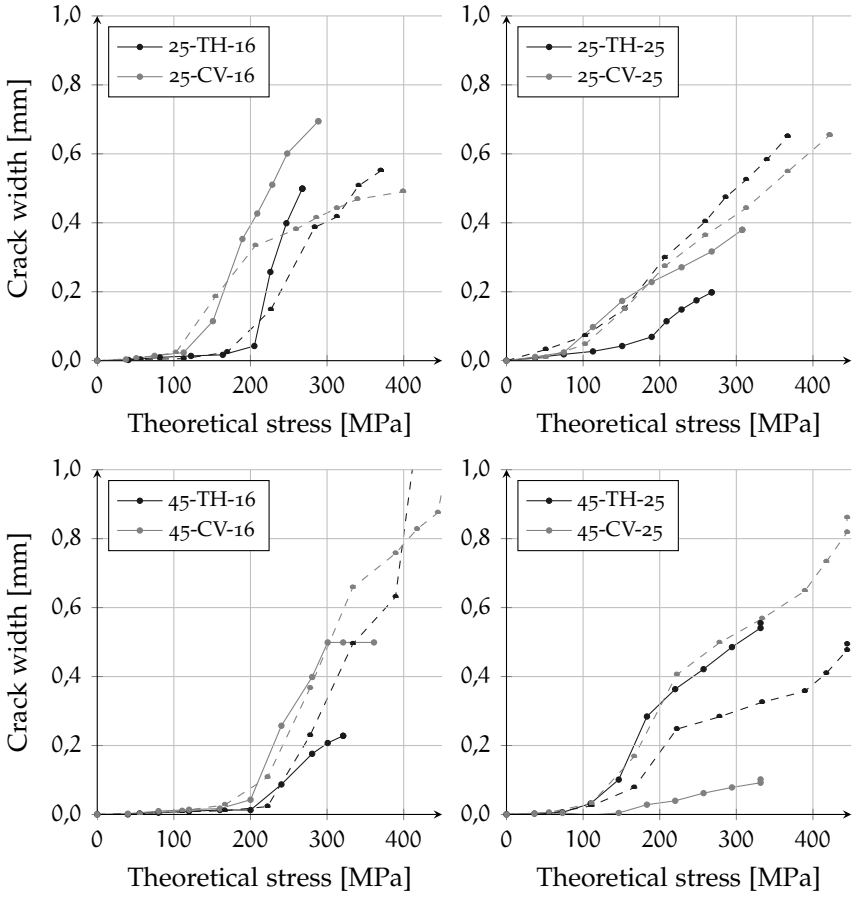

Figure 6.4: Crack width comparison. The average crack width of sections S5-S16 is represented in continuos lines, while dashed lines are used for the average crack width of section S6-S15.

– In specimens with plate-anchored reinforcement, cracks propagated towards the anchorage plates. This is regarded as a consequence of the plate contribution to the total anchorage capacity, since a certain slip is needed to mobilize the contribution of the head;
– Less slip is needed to mobilize the bearing strength of larger heads (see Section 6.3.1): in specimen 25-TH-25 fewer and shorter cracks have been observed in comparison with specimen 45-TH-25: for the same reason, in the former specimen, cracks did not reach the anchorage plate, although the rebars yielded (see for instance gauge U1 in Figure D.8).

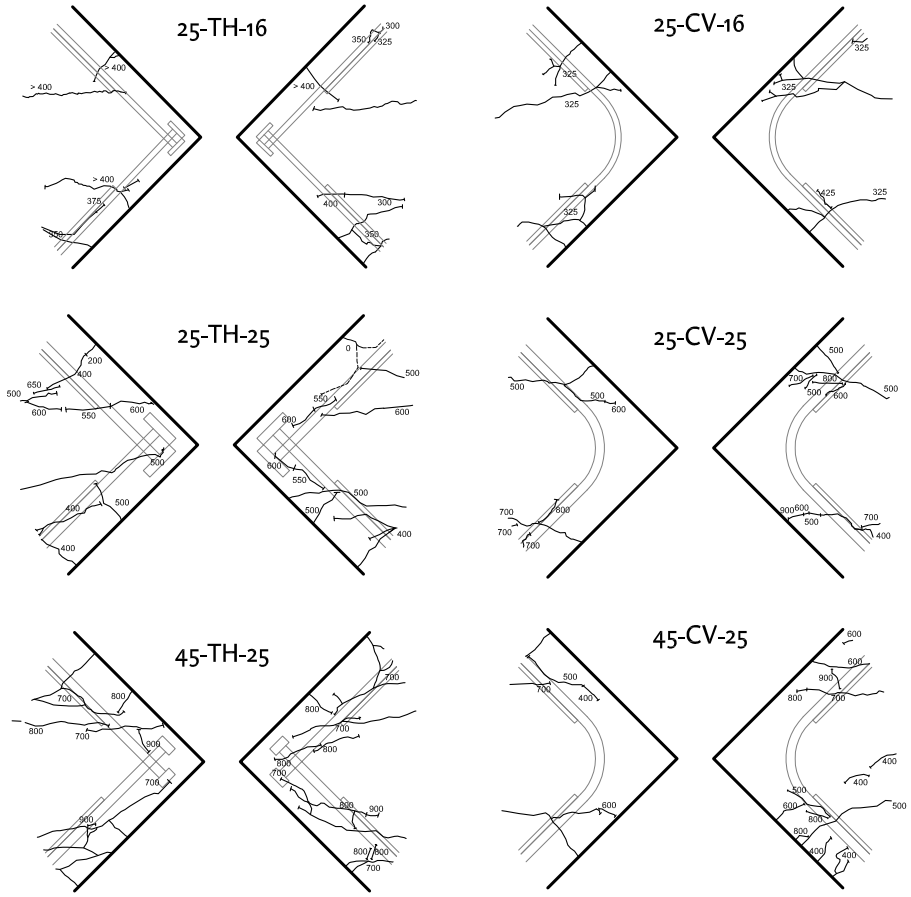

Figure 6.5: Comparison of cracks in anchorage zone

6.3.1 Head slip

Head slip measurements are consistent with strain gauge measurements and crack patterns: a graphical representation is provided in Figure 6.6 for specimen with 25 mm rebars. The following observations regarding measured head slip can be made:

- Only the upper fleximeter (LVDT 1) measured a displacement in specimen 25-TH-25, while LVDT 2 did not measure any slip at all;
- Only the upper fleximeter (LVDT 1) measured a displacement in specimen 45-TH-25 slip, while LVDT 2 meaured only white noise;
- Bars in specimen 25-TH-16 did not slip until failure was imminent, and even then, the slip measured with both LVDTs was less than 0,1 mm (see Section D.1.9);
- Only white noise was measured during the test by both LVDTs in specimen 45-TH-16.

6.4 DAMAGE IN PROXIMITY OF ANCHOR HEAD

Specimens anchored by smaller plates, which are also specimens with the larger measured slip (45-TH-16 and 45-TH-25) have been cut along the bar axis using a diamond saw (see Figure 6.7a) for a length of 90 cm.

The cut elements can be seen in Figure 6.7b–6.7c, in which some large cracks are visible, especially in the case of specimen with 16 mm rebars: there is no indication of concrete crushing close to heads, as can be seen in Figure 6.8a–6.8b.

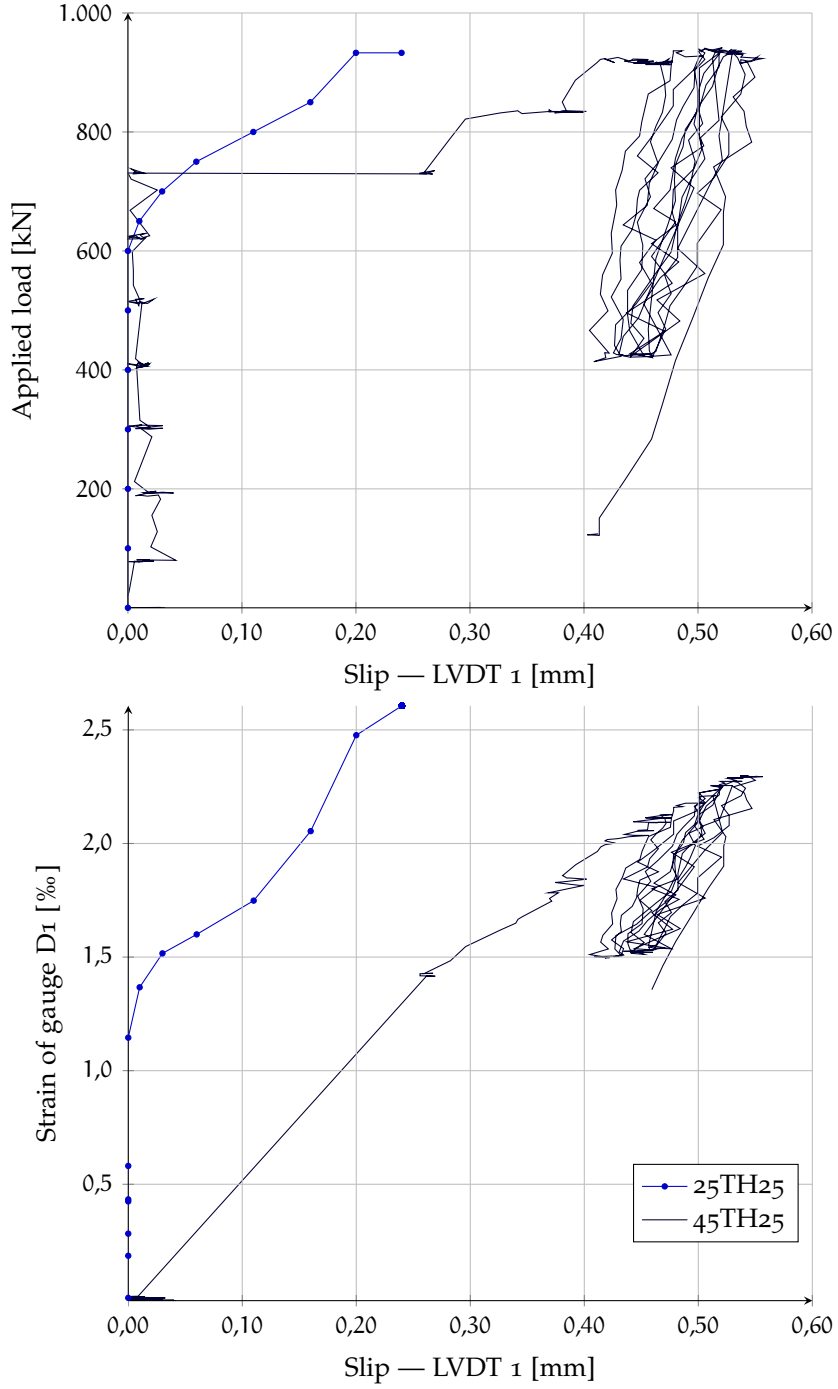

Figure 6.6: Head slip comparison: slip measured by LVDT 1 Vs applied load (top) or strain measured by gauge D1 (bottom)

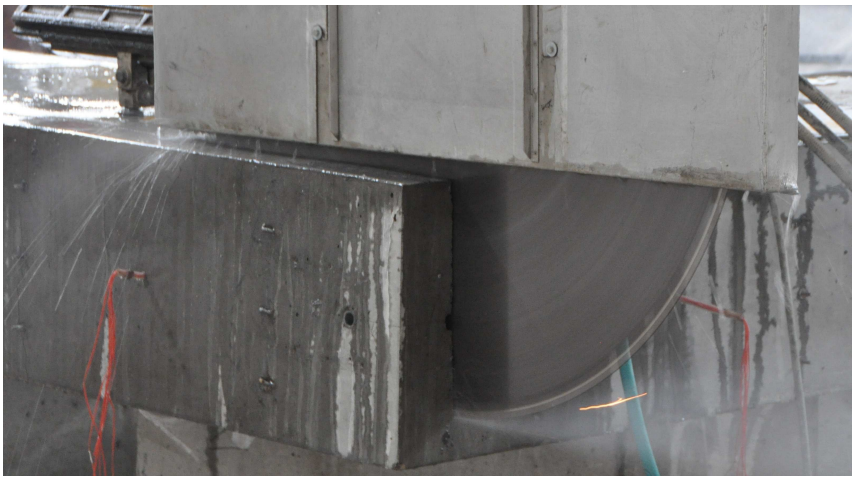

(a) *Saw cutting*

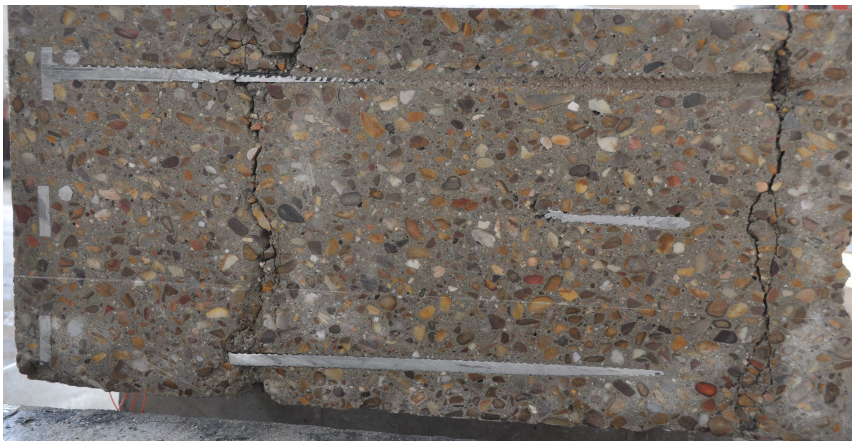

(b) *Specimen 45-TH-16*

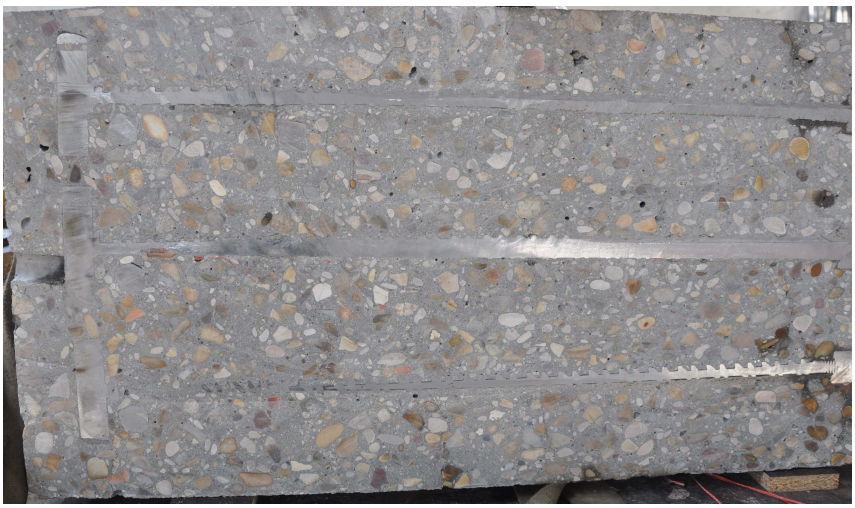

(c) *Specimen 45-TH-25*

Figure 6.7: Cut of elements

(a) *Detail of the edge plate - Specimen 45-TH-16*

(b) *Detail of the middle plate - Specimen 45-TH-25*

Figure 6.8: Absence of crushed concrete in the vicinity of anchor heads

Part IV

CONCLUSIONS

7 CONCLUSIONS AND FUTURE RESEARCH

7.1 SUMMARY

The state of the art on plate-anchored reinforcement bars used in reinforced concrete structures has been presented, with special regard to general and specific applications. This solution for anchorage of reinforcement bars has been extensively used in the recent past aiming to simplify the detailing of congested areas, showing good performances with respect to standard or L-shaped hooks in a wide range of applications. However, the use of such products is not yet widespread, no guidance is provided by the Eurocode and formulations provided by other codes suchs as ACI or Model Code 2010 are still based on an empirical or semi-empirical approach.

In order to face this undesirable situation, a new formulation based on a simple physical model has been proposed in this thesis: the formula, which can model the influence of all relevant parameters in the design of plate dimensions, addresses the problem of anchoring the tensile force in the bar exclusively by bearing on the head. It provides an excellent correlation with available experimental results and has shown significant improvement when compared with other existing models. Well-known studies on bearing strength and anchor bolts have been incorporated to the database for a further comparison.

The proposed design formulation is meant to be used when the maximum tensile force must be anchored by the plate. In cases when a certain development length is available, plate dimensions can be reduced, since the anchorage capacity can be regarded as the sum of bearing on the ribs of the bar and on the head. The bond-bearing interaction has been assessed via finite element analysis, confirming that the plate contribution to the total anchorage capacity is constant, independently from the development length assigned to the model. Initially, the force carried by the plate is almost null and all the applied force is resisted by bond; after a deterioration of the primary mechanism, the plate assumes gradually the major part of the force until the blowout failure occurs.

An experimental campaign on one of the most promising applications of mechanical anchorages, a CCT-node, has been carried out at the Structure Laboratory of the Technical University of Madrid. The effectiveness of a headed reinforcement detailing in a knee joint extracted from an underpass has been assessed through a comparison

between similar specimens: headed bars designed with the proposed formula have been shown to provide a feasable substitute for hooks in this specific application.

7.2 GENERAL CONCLUSIONS

The following general conclusions about the use of headed reinforcement bars in construction can be drawn from this thesis:

- Mechanical anchorages have been investigated and used in the recent past in a wide variety of concrete members, such as:
  - Beam primary and transverse reinforcement;
  - Beam-column or roof joints;
  - Pile-wharf and pile-to-foundation connections;
  - Transverse reinforcement in walls or slabs;
  - Lap splices and application in prefabrication industry.

  In the literature, the use of plate-anchored reinforcement bars is often declared to be as good as or better than conventional anchorages: they can potentially replace standard hooks, improving construction details and enabling a faster, more flexible, and therefore a more economical assembly. Among the potential uses of this product there are many common structures, such as underpasses, overpasses or buildings;

- Given the need for a general formulation allowing the design of anchor plates for specific conditions, a new and simple physical model has been proposed taking into account all relevant parameters.

  The classical formula for concentrated loads acting on a concrete block is reformulated so that the tensile force generated by the spreading out of the compression forces is taken by the tensile resistance of concrete. In addition, compression failure need to be checked: the proposed capacity equation is therefore:

$$N_{Rd} = \min N_{Rd,i} \Rightarrow \begin{cases} N_{Rd,1} = \min\left(\sqrt{\frac{A_c}{A_n}}; 7{,}0\right) A_n f_{cd} \\ N_{Rd,2} = \frac{8}{3} f_{ctd} \frac{a b_{ef}}{1 - \sqrt{\frac{a_1 b_1}{a b_{ef}}}} \end{cases}$$

- The comparison of the proposed model with experimental data is more than satisfactory, making the model a significant improvement when compared to other existing models. The proposed safety format is adequate and consistent with Eurocode;

- Other well-known studies on related topics, such as bearing strength and anchor bolts, have been incorporated to the database for comparison with the theoretical proposal, showing, again, good agreement;
- In line with the Model Code approach, the total anchor capacity should be taken as a combination of the capacity provided by bond along the bar with the capacity provided by bearing on the head. In this sense, the proposal of this thesis is to consider the plate contribution to the total capacity as constant: the total anchorage capacity is the sum of the contribution provided by bond, calculated with standard code provisions, and by bearing on the head.

7.3 SPECIFIC CONLUSIONS ON THE EXPERIMENTAL CAMPAIGN

The following specific conclusions about the behavior of corner joint subjected to a closing moment can be drawn from this thesis:

- A first flexural crack was observed at the face of the joint, after which other flexural cracks developed nearby;
- At first, the joint contributes to a Strut-and-Tie mechanism with a concrete tie. As the load further increased, some bond-related cracks developed inside the corner: when the effort required to crack the concrete tie is exceeded, two main cracks form parallel to the symmetry axis of the specimen. After this event, the terminal part of the ties become part of the resistant mechanism and the bond-related cracks eventually propagate towards the anchorage plates;
- The observed failure mode, when achieved, was due to bending of the section adjacent to the joint with full yielding of the tensile reinforcement. No blowout failure (or symptom thereof) was observed in any specimen;

From the comparison between a headed bar detailing and a conventional detailing, the following can be stated:

- A plate-anchored reinforcement detailing designed with the proposed formula performed equivalently to a conventional detailing in terms of ultimate load, load-deflection response and crack control;
- The strain gauges closest to the heads measured high strains, confirming the effectiveness of the anchorage since the first centimeters presented full yielding of reinforcement;

- No conclusions can be drawn on the very reduced plate dimensions used in the 45-TH-16 specimen, given the particular failure mode of this specimen which does not implied the failure of the concrete tie with the formation of a crack parallel to the central strut.

7.4 SUGGESTIONS FOR FUTURE RESEARCH

The following theoretical and experimental areas are suggested for future research:

- Additional research is needed to fully understand whether a rectangular loading plate differs from a square plate of the same area or not. It is difficult to find a solution on the basis of simple physical considerations, since the problem is complex: the state of stress in the concrete block not only depends on the plate dimensions but also on the concrete block dimensions and on the two cover dimensions, not mentioning the strength of materials.

  Work by Niyogi on the bearing strength of concrete provides some evidence that the proposed formula slightly overestimates the results of experimental tests for higher values of aspect ratio (defined as the large/width ratio of the loading plate) when the compression condition is the governing failure mode. However, this overestimation does not occur if the aspect ratio is limited to the range normally met by commercial plates. Furthermore, the experimental basis on headed bars is too limited to address this problem from a statistical point of view. From the DeVries' campaign, only nine corner tests with rectangular plates are governed by the compression condition, of which only five are overpredicted by the proposed formula, two of them with no concrete cover. Thus, an increase of the experimental basis appears desirable for a further refinement of the theoretical model.

- It is not clear whether friction-welded heads can be used on structures subjected to fatigue loads or not. The design fatigue curves for plate-anchored bars are available for welded and forged bars manufactured by HRC: the forged series, whose S-N curve is similar to that of a straigth bar, is presented as an improvement with respect to the welded series, whose performance is worst than that of bent bars when the number of stress cycles exceeds 5 millions.

  T-headed bars placed inside structural members have been tested limitedly: some tests on beam-column joints subjected to cyclic loading have shown good performances also when welded and threaded heads were used. However, the vast majority of them

are related to seismic loading: the only experimental campaign with a large number of cycles of which the author is aware was performed by Yoshitake et al. [124] with forged headed bars provided by the Dai-Ichi High Frequency Company and was related to shear reinforcement. Those particular rebars performed at least equal to bent bars, however, only six specimens were tested and only one specimen reached 2,5 million cycles.

The Eurocode provides the stress range which can withstand by straight bars, with a reduction factor for bent bars approximately equal to 0,5, but no references are made to headed bars. For the above reasons, a comprehensive study on fatigue loadings is needed for headed bars inside structural members.

- The use of plate-anchored reinforcement bars for lap splices or for cast-in-place closure strips of precast elements is promising, notwithstanding, the reference study of Thompson [117] is limited to rebars not exceeding a tensile strength of 420 MPa, and a more recent study by Chun and Lee [28] on high-strength headed bars is limited to a determined type of headed-bars with a net area of four times the bar area. Further experimental research is needed in this field.

Part V

APPENDICES

A STATISTICS

The fundamental statistics formulas and concepts used for this thesis are described in this appendix.

A.1 INTRODUCTION

In many situations, it is not possible to obtain data for the entire population, therefore it is necessary to estimate the statistics of a population from a sample. This process is known as statistical inference. The estimators may be referred to as *statistics*, these being any function of observations of a random sample.

A.1.1 Central tendency

The term *central tendency* relates to the way in which data tend to cluster around some value in statistical populations. The simplest measure of central tendency is the mean μ.

SAMPLE MEAN The sample mean is the arithmetic average of a set of values. It is a first central moment[1], and it is an unbiased estimator[2] for the population mean μ, i. e. this quantity is an estimator for the mean of the total population.

$$\bar{x} = \frac{1}{n} \sum_{i=1}^{n} x_i \tag{A.1}$$

A.1.2 Statistical dispersion

The term *statistical dispersion* relates to the variability or spread in a variable. Measures of statistical dispersion are listed below:

VARIANCE The variance is a measure of how far the numbers lie from the mean, spreading out from the central value. It is a second central moment. With x being a random variable, the variance of a

[1] A central moment of a sample with size n is defined as: $m_r = \frac{1}{n} \sum_{i=1}^{n} (x_i - \bar{x})^r$

[2] Using the Central Limit Theorem, the mean will be approximately normally distributed.

function with known mean having a probability density function p(x) is:

$$\sigma^2 = \int P(x)(x_i - \mu)^2 dx \tag{A.2}$$

SAMPLE VARIANCE The sample variance is the second sample central moment. It is used when the underlying distribution is unknown, because the whole set of discrete values is not available. In this case, a sample of n observations allows the estimation ($\bar{x}$) of the mean population (μ). Is defined by:

$$s_N^2 = \frac{1}{n}\sum_{i=1}^{n}(x_i - \bar{x})^2 \tag{A.3}$$

However, the sample variance calculated using this relation when applied to a small or moderately sized sample, tends to be lower than the true population variance and therefore it is called the biased sample variance. For this reason, some authors prefer the definition given in equation A.4, which makes the sample variance an unbiased estimator for the population variance. This correction is known as Bessel's correction and is a common source of confusion:

$$s^2 = s_{N-1}^2 = \frac{1}{n-1}\sum_{i=1}^{n}(x_i - \bar{x})^2 = \left(\frac{n}{n-1}\right) s_N^2 \tag{A.4}$$

For high values of n, the difference is negligible.

STANDARD DEVIATION The variance, as the sample variance, has units that are the square of the units of the variable itself; for this reason the use of other descriptive measures is generally preferred. The standard deviation is defined as:

$$\sigma = \sqrt{\sigma^2} \tag{A.5}$$

SAMPLE STANDARD DEVIATION The sample standard deviation, sometimes also known as the standard deviation, is the square root of the bias–corrected sample variance:

$$s = \sqrt{s^2} \tag{A.6}$$

CONFIDENCE INTERVAL For a normal distribution, the probability that a measurement falls within k standard deviations ($k\sigma = x_k$) of the mean , $P(\mu - x_k < x < \mu + x_k)$, is summarized in Table A.1:

SAMPLE COVARIANCE Covariance is a measure of how much two variables change together. A positive value of covariance implies similar behavior of the two variables. The sample covariance is defined as:

$$s_{XY} = \frac{1}{n-1}\sum_{i=1}^{n}(x_i - \bar{x})(y_i - \bar{y}) = \frac{1}{n-1}\sum_{i=1}^{n} x_i y_i - \bar{x}\bar{y} \tag{A.7}$$

x_k	$P(x_k)$
1,0000 σ	0,6827
1,2815 σ	0,9000
1,6448 σ	0,9500
2,0000 σ	0,9545
3,0000 σ	0,9973
4,0000 σ	0,9999

Table A.1: Confidence intervals

As done for the sample variance, the $n-1$ dividing factor has been used.

COEFFICIENT OF VARIATION (COV) The Coefficient of variation is a normalized measure of dispersion of a distribution. It is defined as the ratio of the standard deviation to the mean. When only a sample of data is available, the population CoV can be estimated using the following formula:

$$\text{CoV} = \frac{s}{\bar{x}} \tag{A.8}$$

SAMPLE CORRELATION COEFFICIENT The normalized version of the covariance is the correlation coefficient, sometimes also denoted as r. Covariance and correlation have the same sign. It is widely used as a measure of linear dependence between variables.

$$R = \frac{s_{XY}}{\sqrt{s_{XX}s_{YY}}} = \frac{\sum_{i=1}^{n}(x_i-\bar{x})(y_i-\bar{y})}{\sqrt{\sum_{i=1}^{n}(x_i-\bar{x})^2(y_i-\bar{y})^2}} \tag{A.9}$$

The correlation coefficient takes a value between 1 and -1 inclusive. With an estimated intercept term, it is also known as the Pearson's product–moment correlation coefficient.

In some cases a regression through the origin (RTO) is appropriate or even necessary. R-squared values for models with and without an intercept are not comparable and this can originate controversies due to the fact that R is not univocally defined, and the use of different softwares can result in outputs depending on the package used.

COEFFICIENT OF DETERMINATION An R^2 value can be calculated as the square of the correlation coefficient R. Throughout this dissertation the value provided by Excel chart trend lines has been used.

B COMPLETE DATA TABLES

The data taken from the pubblications cited in Section 4.2 are reported here. In all tables SI units (mm, MPa, kN) are used. Minimum calculated values are in red whereas the data which have not been taken into account in the comparison are highlighted in gray.

	Plate		Block		Concrete		Specimen				$N_{u,Model}$		
#	a_1	b_1	a	b	f_{cm}	f_{ctm}	n°	A_c/A_1	f_{cb}	$N_{u,exp}$	$N_{Rd,1}$	$N_{Rd,2}$	$N_{u,Model}/N_{u,Exp}$
1	12,7	203,2	203,2	203,2	32,1	2,0	3	16,0	81,3	210	332	293	1,39
2	17,0	203,2	203,2	203,2	30,5	2,0	3	11,9	66,4	230	365	310	1,35
3	25,4	203,2	203,2	203,2	31,3	2,0	3	8,0	58,6	302	457	348	1,15
4	33,8	203,2	203,2	203,2	26,9	1,7	4	6,0	44,2	303	453	317	1,04
5	50,8	203,2	203,2	203,2	28,6	1,8	3	4,0	39,6	409	590	396	0,97
6	63,5	203,2	203,2	203,2	31,1	2,0	3	3,2	40,7	525	718	511	0,97
7	67,8	203,2	203,2	203,2	31,3	2,0	3	3,0	39,4	542	747	532	0,98
8	101,6	203,2	203,2	203,2	31,6	2,0	4	2,0	34,8	718	921	747	1,04
9	203,2	203,2	203,2	203,2	28,8	1,8	4	1,0	27,9	1152	1191	-	1,03

Table B.1: Niyogi – Table 1. Strip loading on 8 inches cube specimens

	Plate		Block		Concrete		Specimen				$N_{u,Model}$		
#	a_1	b_1	a	b	f_{cm}	f_{ctm}	n°	A_c/A_1	f_{cb}	$N_{u,exp}$	$N_{Rd,1}$	$N_{Rd,2}$	$N_{u,Model}/N_{u,Exp}$
1	12,7	203,2	101,6	203,2	24,8	1,9	2	8,0	49,4	128	181	159	1,24
2	12,7	203,2	152,4	203,2	26,3	1,7	2	12,0	61,4	158	235	196	1,24
3	17,0	203,2	101,6	203,2	27,1	1,8	2	6,0	45,6	158	229	164	1,04
4	25,4	203,2	101,6	203,2	25,4	1,6	2	4,0	30,8	159	262	181	1,14
5	25,4	203,2	152,4	203,2	28,6	1,8	2	6,0	47,1	243	362	250	1,03
6	203,2	25,4	203,2	304,8	25,4	1,7	2	12,0	52,4	271	455	319	1,18
7	203,2	25,4	203,2	406,4	26,2	1,7	2	16,0	54,6	282	540	308	1,09
8	203,2	25,4	203,2	609,6	29,3	1,9	2	24,0	58,9	304	740	351	1,15
9	33,8	203,2	101,6	203,2	25,1	1,7	2	3,0	28,5	196	299	226	1,16
10	203,2	33,8	203,2	304,8	30,3	1,7	2	9,0	56,6	389	625	360	0,93
11	203,2	33,8	203,2	406,4	26,9	1,8	2	12,0	51,6	354	642	367	1,04
12	203,2	38,1	203,2	304,8	27,9	1,8	2	8,0	51,0	395	612	392	0,99
13	203,2	38,1	203,2	609,6	27,7	1,7	2	16,0	52,2	404	857	376	0,93
14	50,8	203,2	101,6	203,2	23,3	1,5	2	2,0	22,5	232	340	285	1,23
15	50,8	203,2	152,4	203,2	23,3	1,5	2	3,0	28,3	292	417	296	1,01
16	203,2	50,8	203,2	304,8	25,4	1,7	2	6,0	42,8	441	643	428	0,97
17	203,2	50,8	203,2	406,4	26,2	1,6	2	8,0	44,9	463	764	410	0,89
18	203,2	50,8	203,2	609,6	25,7	1,7	2	12,0	41,8	432	918	431	1,00
19	76,2	203,2	152,4	203,2	30,9	1,9	3	2,0	34,6	536	677	541	1,01
20	203,2	76,2	203,2	304,8	27,3	1,8	2	4,0	42,4	657	846	555	0,84
21	203,2	76,2	203,2	609,6	26,6	1,8	2	8,0	42,3	655	1166	562	0,86
22	203,2	101,6	203,2	304,8	29,1	1,8	2	3,0	39,7	820	1042	703	0,86
23	203,2	101,6	203,2	406,4	27,6	1,7	2	4,0	42,6	879	1141	671	0,76
24	203,2	101,6	203,2	609,6	31,5	1,8	2	6,0	47,0	970	1593	709	0,73
25	203,2	152,4	203,2	304,8	31,2	1,9	2	2,0	39,9	1235	1365	1069	0,87
26	203,2	152,4	203,2	609,6	31,4	1,9	2	4,0	44,7	1383	1943	1081	0,78
27	203,2	203,2	203,2	406,4	33,2	1,9	2	2,0	41,3	1704	1938	1426	0,84
28	203,2	304,8	203,2	609,6	29,1	1,8	2	2,0	36,7	2276	2552	2207	0,97

Table B.2: Niyogi – Table 2.
Strip loading on rectangular specimens with a height of 8 inches

	Plate		Block			Concrete		Specimen				$N_{u,Model}$		
#	a_1	b_1	a	b	h	f_{cm}	f_{ctm}	n°	A_c/A_1	f_{cb}	$N_{u,exp}$	$N_{Rd,1}$	$N_{Rd,2}$	$N_{u,Model}/N_{u,Exp}$
1	12,7	203,2	203,2	203,2	101,6	23,1	1,5	2	16,0	54,2	140	238	196	1,40
2	25,4	203,2	203,2	203,2	101,6	27,9	1,7	2	8,0	56,1	289	407	257	0,89
3	33,8	203,2	203,2	203,2	101,6	29,4	1,9	2	6,0	56,3	386	494	301	0,78
4	50,8	203,2	203,2	203,2	101,6	26,0	1,7	2	4,0	46,8	483	536	331	0,69
5	76,2	203,2	203,2	203,2	101,6	25,8	1,8	2	2,7	43,1	667	651	444	0,67
6	101,6	203,2	203,2	203,2	101,6	27,2	1,8	2	2,0	41,3	852	794	597	0,70
7	12,7	203,2	203,2	203,2	152,4	26,7	1,8	2	16,0	68,4	177	276	223	1,26
8	25,4	203,2	203,2	203,2	152,4	25,9	1,7	2	8,0	52,7	272	379	246	0,90
9	33,8	203,2	203,2	203,2	152,4	29,7	1,9	2	6,0	53,8	369	500	301	0,81
10	50,8	203,2	203,2	203,2	152,4	25,0	1,8	2	4,0	39,7	409	517	343	0,84
11	76,2	203,2	203,2	203,2	152,4	25,1	1,6	2	2,7	34,7	537	634	397	0,74
12	101,6	203,2	203,2	203,2	152,4	25,9	1,8	2	2,0	34,4	710	757	577	0,81
13	12,7	203,2	203,2	203,2	304,8	29,6	1,9	2	16,0	73,0	188	305	244	1,29
14	25,4	203,2	203,2	203,2	304,8	31,9	2,0	2	8,0	55,6	287	465	294	1,02
15	33,8	203,2	203,2	203,2	304,8	31,1	1,9	2	6,0	50,2	345	524	313	0,91
16	50,8	203,2	203,2	203,2	304,8	25,1	1,7	2	4,0	31,1	321	518	333	1,04
17	101,6	203,2	203,2	203,2	304,8	34,2	2,1	2	2,0	36,7	759	999	689	0,91
18	12,7	203,2	203,2	203,2	406,4	32,7	2,0	2	16,0	83,7	216	337	257	1,19
19	25,4	203,2	203,2	203,2	406,4	31,1	2,0	2	8,0	53,2	275	455	290	1,06
20	33,8	203,2	203,2	203,2	406,4	27,8	1,8	2	6,0	41,7	286	468	294	1,03
21	50,8	203,2	203,2	203,2	406,4	31,2	2,0	2	4,0	35,7	369	645	377	1,02
22	101,6	203,2	203,2	203,2	406,4	29,9	1,9	2	2,0	25,7	530	874	631	1,19
23	12,7	203,2	203,2	203,2	609,6	31,0	1,9	2	16,0	81,4	210	320	241	1,15
24	25,4	203,2	203,2	203,2	609,6	28,4	1,8	2	8,0	45,6	235	415	273	1,16
25	33,8	203,2	203,2	203,2	609,6	27,7	1,8	2	6,0	36,0	247	466	295	1,20
26	50,8	203,2	203,2	203,2	609,6	28,2	1,9	2	4,0	29,7	307	582	358	1,17
27	101,6	203,2	203,2	203,2	609,6	10,0	1,9	2	2,0	22,7	469	291	622	0,62

Table B.3: Niyogi – Table 3. Strip loading on square prism specimens

	Plate		Block		Concrete		Specimen				$N_{u,Model}$		
#	a_1	b_1	a	b	f_{cm}	f_{ctm}	n°	A_c/A_1	f_{cb}	$N_{u,exp}$	$N_{Rd,1}$	$N_{Rd,2}$	$N_{u,Model}/N_{u,Exp}$
1	12,7	50,8	203,2	203,2	29,6	1,9	3	64,0	193,5	125	134	233	1,07
2	12,7	76,2	203,2	203,2	29,5	1,9	4	42,7	158,1	153	186	249	1,22
3	12,7	101,6	203,2	203,2	31,8	2,0	3	32,0	133,3	172	232	274	1,35
4	12,7	152,4	203,2	203,2	29,8	1,7	3	21,3	102,0	197	267	237	1,20
5	25,4	50,8	203,2	203,2	29,6	1,8	3	32,0	123,7	160	216	240	1,35
6	25,4	76,2	203,2	203,2	26,0	1,7	3	21,3	87,1	169	232	241	1,38
7	25,4	101,6	203,2	203,2	29,6	1,9	3	16,0	79,6	205	305	276	1,35
8	25,4	152,4	203,2	203,2	29,6	1,8	3	10,7	65,4	253	374	285	1,12
9	33,8	50,8	203,2	203,2	28,5	1,8	3	24,1	104,5	179	240	253	1,34
10	33,8	76,2	203,2	203,2	29,7	1,9	3	16,0	80,8	208	306	275	1,32
11	33,8	101,6	203,2	203,2	29,7	1,9	3	12,0	72,4	248	354	290	1,17
12	33,8	152,4	203,2	203,2	29,7	1,9	3	8,0	54,3	279	433	319	1,14
13	50,8	76,2	203,2	203,2	27,0	1,6	3	10,7	66,3	257	342	258	1,01
14	50,8	101,6	203,2	203,2	24,8	1,6	3	8,0	51,0	263	363	280	1,06
15	50,8	127	203,2	203,2	27,6	1,7	3	6,4	48,7	314	451	309	0,98
16	50,8	152,4	203,2	203,2	28,1	1,8	3	5,3	43,5	337	503	344	1,02
17	76,2	101,6	203,2	203,2	31,5	1,9	3	5,3	51,3	397	563	378	0,95
18	101,6	152,4	203,2	203,2	30,2	1,8	3	2,7	34,8	537	765	509	0,94

Table B.4: Niyogi – Table 4.
Rectangular loading on 8 inches cube specimens

	Plate		Block			Concrete		Specimen				$N_{u,Model}$		
#	a_1	b_1	a	b	h	f_{cm}	f_{ctm}	n°	A_c/A_1	f_{cb}	$N_{u,exp}$	$N_{Rd,1}$	$N_{Rd,2}$	$N_{u,Model}/N_{u,Exp}$
1	50,8	76,2	203,2	203,2	101,6	26,2	1,6	2	10,7	41,7	161	331	246	1,53
2	50,8	101,6	203,2	203,2	101,6	26,8	1,8	2	8,0	54,6	282	392	301	1,07
3	50,8	152,4	203,2	203,2	101,6	26,2	1,6	2	5,3	48,1	373	468	301	0,81
4	50,8	101,6	203,2	203,2	152,4	29,8	1,6	2	8,0	58,9	304	434	270	0,89
5	50,8	152,4	203,2	203,2	152,4	34,2	2,1	2	5,3	59,5	461	611	411	0,89
6	50,8	101,6	203,2	203,2	304,8	25,4	1,7	2	8,0	49,9	257	371	296	1,15
7	50,8	152,4	203,2	203,2	304,8	26,3	1,8	2	5,3	39,9	309	470	340	1,10
8	50,8	101,6	203,2	203,2	406,4	31,4	2,1	2	8,0	60,8	314	458	351	1,12
9	50,8	152,4	203,2	203,2	406,4	32,0	2,0	2	5,3	46,5	360	571	380	1,06
10	50,8	101,6	203,2	203,2	609,6	29,0	1,9	2	8,0	52,3	270	424	322	1,19
11	50,8	152,4	203,2	203,2	609,6	31,6	2,0	2	5,3	41,2	319	565	379	1,19

Table B.5: Niyogi – Table 5. Rectangular loading on square prism specimens

	Plate		Block		Concrete		Specimen				$N_{u,Model}$			
#	a_1	b_1	a	b	f_{cm}	f_{ctm}	n°	A_c/A_1	f_{cb}	$N_{u,exp}$	$N_{Rd,1}$	$N_{Rd,2}$	$N_{u,Model}/N_{u,Exp}$	Reference
1	25,4	25,4	203,2	203,2	28,2	1,8	6	64,0	200	129	127	225	0,99	
2	35,8	35,8	203,2	203,2	29,7	1,9	6	32,2	141	181	216	255	1,19	
3	50,8	50,8	203,2	203,2	27,2	1,7	5	16,0	81,9	211	281	254	1,20	
4	71,9	71,9	203,2	203,2	27,7	1,8	6	8,0	57,2	296	405	309	1,05	
5	101,6	101,6	203,2	203,2	30,6	1,9	5	4,0	47,3	489	632	413	0,85	
6	152,4	152,4	203,2	203,2	31,4	2,0	4	1,8	34,2	795	972	881	1,11	
7	203,2	203,2	203,2	203,2	28,8	1,8	4	1,0	27,9	1152	1191	-	1,03	
8	25,4	25,4	203,2	203,2	19,3	1,5	3	64,0	142,4	92	87	184	0,95	[98] – Table 1
9	35,8	35,8	203,2	203,2	17,3	1,2	3	32,2	84,1	108	126	155	1,17	...
10	50,8	50,8	203,2	203,2	19,3	1,5	3	16,0	63,6	164	199	215	1,21	...
11	71,9	71,9	203,2	203,2	15,0	1,1	2	8,0	31,7	164	219	180	1,10	...
12	101,6	101,6	203,2	203,2	14,8	1,0	2	4,0	22,6	233	306	213	0,91	...
13	25,4	203,2	203,2	203,2	14,6	1,1	2	8,0	30,6	158	213	180	1,14	[98] – Table 2
14	50,8	203,2	203,2	203,2	14,6	1,1	2	4,0	23,5	243	302	232	0,96	...
15	101,6	203,2	203,2	203,2	14,6	1,1	2	2,0	16,4	339	427	397	1,17	...

Table B.6: Niyogi – Table 6. Concentric loading on 8 inches cube specimens

	Plate		Block			Concrete		Specimen				$N_{u,Model}$		
#	a_1	b_1	a	b	h	f_{cm}	f_{ctm}	n°	A_c/A_1	f_{cb}	$N_{u,exp}$	$N_{Rd,1}$	$N_{Rd,2}$	$N_{u,Model}/N_{u,Exp}$
1	25,4	25,4	203,2	203,2	101,6	28,3	1,8	4	64,0	120,1	77	128	228	1,65
2	35,8	35,8	203,2	203,2	101,6	30,2	2,0	4	32,2	91,4	117	220	263	1,87
3	50,8	50,8	203,2	203,2	101,6	29,8	1,9	4	16,0	76,9	198	308	280	1,41
4	71,9	71,9	203,2	203,2	101,6	28,5	1,8	4	8,0	60,6	313	416	311	0,99
5	101,6	101,6	203,2	203,2	101,6	25,5	1,7	4	4,0	48,9	505	526	369	0,73
6	25,4	25,4	203,2	203,2	152,4	27,2	1,8	3	64,0	166,2	107	123	228	1,15
7	35,8	35,8	203,2	203,2	152,4	29,6	1,8	3	32,2	118,1	151	216	236	1,42
8	50,8	50,8	203,2	203,2	152,4	27,2	1,8	3	16,0	72,3	187	281	268	1,44
9	71,9	71,9	203,2	203,2	152,4	29,6	1,8	3	8,0	58,6	303	433	301	0,99
10	101,6	101,6	203,2	203,2	152,4	30,1	1,9	3	4,0	45,6	471	621	427	0,91
11	25,4	25,4	203,2	203,2	304,8	28,3	1,8	2	64,0	205,1	132	128	230	0,96
12	35,8	35,8	203,2	203,2	304,8	25,2	1,8	2	32,2	123,2	158	183	238	1,16
13	50,8	50,8	203,2	203,2	304,8	28,5	1,9	2	16,0	88,4	228	294	278	1,22
14	71,9	71,9	203,2	203,2	304,8	27,2	1,8	2	8,0	51,3	265	397	300	1,13
15	101,6	101,6	203,2	203,2	304,8	28,1	2,0	2	4,0	40,4	417	580	436	1,05
16	25,4	25,4	203,2	203,2	406,4	27,8	1,8	3	64,0	200,7	129	126	231	0,97
17	35,8	35,8	203,2	203,2	406,4	28,5	1,9	3	32,2	141,9	182	208	252	1,14
18	50,8	50,8	203,2	203,2	406,4	29,2	1,9	3	16,0	92,2	238	302	277	1,17
19	71,9	71,9	203,2	203,2	406,4	31,5	2,0	2	8,0	58,9	304	460	347	1,14
20	101,6	101,6	203,2	203,2	406,4	32,1	2,0	2	4,0	42,8	441	662	445	1,01
21	25,4	25,4	203,2	203,2	609,6	25,2	1,8	2	64,0	177,8	115	114	220	0,99
22	35,8	35,8	203,2	203,2	609,6	28,7	2,0	2	32,2	131,5	169	209	261	1,24
23	50,8	50,8	203,2	203,2	609,6	30,9	1,9	2	16,0	98,8	255	319	280	1,10
24	71,9	71,9	203,2	203,2	609,6	29,2	1,9	2	8,0	55,6	287	427	320	1,11
25	101,6	101,6	203,2	203,2	609,6	29,2	1,9	2	4,0	38	392	603	421	1,07

Table B.7: Niyogi – Table 7. Concentric loading on square prism specimens

	Plate		Block			Concrete		Specimen				$N_{u,Model}$		
#	a_1	b_1	a	b	e_a	f_{cm}	f_{ctm}	n°	A_c/A_1	f_{cb}	$N_{u,exp}$	$N_{Rd,1}$	$N_{Rd,2}$	$N_{u,Model}/N_{u,Exp}$
1	25,4	25,4	152,4	203,2	25,4	30,1	1,9	3	48,0	187,5	121	134	160	1,11
2	25,4	25,4	101,6	203,2	50,8	30,1	1,9	3	32,0	135,3	87	110	83	0,95
3	25,4	25,4	50,8	203,2	76,2	30,1	1,9	3	16,0	98,5	64	78	33	0,51
4	35,8	35,8	177,6	203,2	12,8	29,2	1,7	3	28,1	122,9	158	199	197	1,25
5	35,8	35,8	152,4	203,2	25,4	28,8	1,8	3	24,1	113,6	146	182	179	1,23
6	35,8	35,8	126,8	203,2	38,2	29,2	1,7	3	20,1	108,7	139	168	122	0,87
7	35,8	35,8	101,6	203,2	50,8	29,2	1,8	3	16,1	93,7	120	151	97	0,80
8	35,8	35,8	50,8	203,2	76,2	29,2	1,8	3	8,0	66,9	86	106	46	0,54
9	50,8	50,8	177,6	203,2	12,8	33,0	2,1	3	14,0	92,7	239	318	272	1,14
10	50,8	50,8	152,4	203,2	25,4	29,2	2,0	3	12,0	75,0	194	261	229	1,18
11	50,8	50,8	126,8	203,2	38,2	28,8	1,9	3	10,0	72,1	186	235	169	0,91
12	50,8	50,8	101,6	203,2	50,8	29,2	2,0	3	8,0	63,6	164	213	138	0,84
13	50,8	50,8	50,8	203,2	76,2	26,2	1,7	3	4,0	42,3	109	135	81	0,74
14	101,6	101,6	177,6	203,2	12,8	27,0	1,9	3	3,5	39,7	410	521	398	0,97
15	101,6	101,6	152,4	203,2	25,4	30,9	2,0	4	3,0	41,8	432	552	381	0,88
16	101,6	101,6	126,8	203,2	38,2	29,2	1,7	3	2,5	37,7	389	476	311	0,80
17	101,6	101,6	101,6	203,2	50,8	26,6	1,8	4	2,0	27,0	278	389	338	1,22

Table B.8: Niyogi – Table 8. Uniaxial eccentric loading on 8 inches cube specimens

	Plate		Block				Concrete		Specimen				$N_{u,Model}$		
#	a_1	b_1	a	b	e_a	e_b	f_{cm}	f_{ctm}	n°	A_c/A_1	f_{cb}	$N_{u,exp}$	$N_{Rd,1}$	$N_{Rd,2}$	$N_{u,Model}/N_{u,Exp}$
1	25,4	25,4	152,4	152,4	25,4	25,4	30,2	1,8	3	36,0	165,7	107	117	136	1,09
2	25,4	25,4	101,6	101,6	50,8	50,8	30,2	1,8	3	16,0	115,5	75	78	67	0,90
3	25,4	25,4	50,8	50,8	76,2	76,2	30,2	1,8	3	4,0	60,8	39	39	25	0,64
4	35,8	35,8	177,6	177,6	12,8	12,8	27,9	1,8	3	24,6	113,8	146	177	192	1,21
5	35,8	35,8	152,4	152,4	25,4	25,4	29,6	1,9	3	18,1	113,7	146	161	152	1,04
6	35,8	35,8	126,8	126,8	38,2	38,2	27,9	1,9	3	12,5	85,9	110	127	112	1,02
7	35,8	35,8	101,6	101,6	50,8	50,8	29,6	1,9	3	8,0	78,5	101	108	80	0,79
8	35,8	35,8	50,8	50,8	76,2	76,2	29,2	1,9	3	2,0	46,1	59	53	44	0,74
9	50,8	50,8	177,6	177,6	12,8	12,8	26,2	1,8	3	12,2	69,9	180	236	217	1,20
10	50,8	50,8	152,4	152,4	25,4	25,4	32,8	2,1	3	9,0	78,3	202	254	195	0,96
11	50,8	50,8	126,8	126,8	38,2	38,2	26,5	1,7	3	6,2	54,7	141	170	122	0,87
12	50,8	50,8	101,6	101,6	50,8	50,8	31,3	2,0	3	4,0	56,1	145	162	107	0,74
13	50,8	50,8	76,0	76,0	63,6	63,6	29,0	2,0	3	2,2	40,9	106	112	91	0,86
14	50,8	50,8	50,8	50,8	76,2	76,2	31,6	2,0	4	1,0	36,5	94	82	-	0,87
15	101,6	101,6	177,6	177,6	12,8	12,8	26,6	1,9	3	3,1	38,0	392	481	367	0,94
16	101,6	101,6	152,4	152,4	25,4	25,4	28,0	1,8	3	2,3	34,7	358	433	337	0,94
17	101,6	101,6	126,8	126,8	38,2	38,2	26,4	1,8	3	1,6	30,2	312	341	388	1,09
18	101,6	101,6	101,6	101,6	50,8	50,8	27,9	1,8	4	1,0	23,9	246	288	-	1,17
19	50,8	50,8	177,6	152,4	12,8	25,4	27,8	1,8	2	10,5	68,8	178	232	193	1,09
20	50,8	50,8	177,6	101,6	12,8	50,8	27,8	1,8	2	7,0	56,3	145	190	143	0,98
21	50,8	50,8	177,6	50,8	12,8	76,2	29,0	1,8	2	3,5	46,0	119	140	91	0,76
22	50,8	50,8	152,4	101,6	25,4	50,8	31,7	2,0	2	6,0	63,1	163	200	138	0,85
23	50,8	50,8	152,4	50,8	25,4	76,2	31,7	2,0	2	3,0	50,5	130	142	96	0,74
24	50,8	50,8	101,6	50,8	50,8	76,2	30,4	1,9	3	2,0	39,0	101	111	91	0,90

Table B.9: Niyogi – Table 9. Biaxial eccentric loading on 8 inches cube specimens

	Plate		Block		Concrete		Specimen				$N_{u,Model}$		
#	a_1	b_1	a	b	f_{cm}	f_{ctm}	n°	A_c/A_1	f_{cb}	$N_{u,exp}$	$N_{Rd,1}$	$N_{Rd,2}$	$N_{u,Model}/N_{u,Exp}$
1	44,5	44,5	152,4	152,4	21,9	2,4	3	11,8	62,5	123	149	206	1,20
2	50,8	50,8	152,4	152,4	21,9	2,4	3	9,0	58,3	150	170	218	1,13
3	63,5	63,5	152,4	152,4	21,9	2,4	3	5,8	49,4	199	212	250	1,07
4	76,2	76,2	152,4	152,4	21,9	2,4	3	4,0	41,5	241	255	291	1,06
5	101,6	101,6	152,4	152,4	21,9	2,4	3	2,3	32,5	335	339	437	1,01
6	63,5	63,5	228,6	228,6	26,1	2,6	2	13,0	82,5	333	378	509	1,14
7	76,2	76,2	228,6	228,6	26,1	2,6	2	9,0	71,3	414	454	551	1,10
8	101,6	101,6	228,6	228,6	26,1	2,6	2	5,1	53,9	557	605	662	1,09
9	44,5	44,5	152,4	152,4	52,5	4,2	3	11,8	114,2	226	355	368	1,57
10	50,8	50,8	152,4	152,4	52,5	4,2	2	9,0	105,8	273	406	391	1,43
11	63,5	63,5	152,4	152,4	52,5	4,2	3	5,8	91,7	370	508	447	1,21
12	76,2	76,2	152,4	152,4	52,5	4,2	3	4,0	77,8	452	609	521	1,15
13	101,6	101,6	152,4	152,4	52,5	4,2	3	2,3	63,9	660	812	781	1,18
14	50,8	50,8	152,4	152,4	26,5	2,7	3	9,0	80,7	208	205	248	0,98
15	76,2	76,2	152,4	152,4	26,5	2,7	3	4,0	55,3	321	307	330	0,96
16	152,4	152,4	152,4	152,4	26,5	2,7	3	1,0	25,4	589	615	-	1,04
17	50,8	50,8	152,4	152,4	35,0	3,2	3	9,0	90,8	234	271	298	1,15
18	76,2	76,2	152,4	152,4	35,0	3,2	3	4,0	55,8	324	406	397	1,23
19	152,4	152,4	152,4	152,4	35,0	3,2	3	1,0	30,1	700	812	-	1,16
20	22,5	22,5	90,04	90,04	11,9	1,6	4	16,0	67,2	34	24	45	0,71
21	33,8	33,8	90,04	90,04	11,9	1,6	3	7,1	37,7	43	36	54	0,84
22	45,0	45,0	90,04	90,04	11,9	1,6	3	4,0	24,7	50	48	67	0,96
23	67,5	67,5	90,04	90,04	11,9	1,6	4	1,8	18,5	85	72	135	0,85
24	25,4	25,4	152,4	152,4	40,8	3,6	3	36,0	221,3	143	158	264	1,11
25	31,0	31,0	152,4	152,4	40,8	3,6	2	24,2	179,3	172	193	277	1,12
26	35,8	35,8	152,4	152,4	40,8	3,6	3	18,1	157,2	202	223	288	1,10
27	50,8	50,8	152,4	152,4	40,8	3,6	2	9,0	106,9	276	316	330	1,15
28	76,2	76,2	152,4	152,4	40,8	3,6	2	4,0	82,7	480	474	441	0,92
29	35,8	35,8	152,4	152,4	33,5	3,1	3	18,1	114,0	146	183	253	1,25
30	76,2	76,2	152,4	152,4	33,5	3,1	3	4,0	58,7	341	389	386	1,13
31	22,5	22,5	135,06	135,06	33,5	3,1	3	36,0	155,1	79	102	182	1,30
32	45,0	45,0	135,06	135,06	33,5	3,1	3	9,0	81,5	165	204	228	1,23
33	25,4	38,1	152,4	152,4	45,6	3,8	2	24,0	203,4	197	216	298	1,10
34	25,4	50,8	152,4	152,4	45,6	3,8	2	18,0	185,5	239	250	311	1,04
35	25,4	76,2	152,4	152,4	45,6	3,8	2	12,0	146,9	284	306	334	1,08
36	25,4	101,6	152,4	152,4	45,6	3,8	2	9,0	125,5	324	353	356	1,09
37	50,8	76,2	152,4	152,4	45,6	3,8	2	6,0	93,2	361	433	401	1,11
38	50,8	101,6	152,4	152,4	45,6	3,8	2	4,5	66,5	343	500	449	1,31

Table B.10: Hawkins – Concentric loading

	Plate		Block				Concrete		Specimen				$N_{u,Model}$		
#	a_1	b_1	a	b	e_a	e_b	f_{cm}	f_{ctm}	n°	A_c/A_1	f_{cb}	$N_{u,exp}$	$N_{Rd,1}$	$N_{Rd,2}$	$N_{u,Model}/N_{u,Exp}$
1	25,4	25,4	152,4	152,4	63,5	63,5	21,0	2,3	4	1,0	30,4	20	14	-	0,69
2	25,4	25,4	152,4	152,4	63,5	63,5	21,0	2,3	4	1,0	46,8	30	14	-	0,45
3	36,1	36,1	152,4	152,4	58,2	58,2	21,0	2,3	8	1,0	30,3	39	27	-	0,69
4	50,8	50,8	152,4	152,4	50,8	50,8	21,0	2,3	5	1,0	32,4	84	54	-	0,65
5	62,2	62,2	152,4	152,4	45,1	45,1	21,0	2,3	4	1,0	29,6	115	81	-	0,71
6	76,2	76,2	152,4	152,4	38,1	38,1	21,0	2,3	4	1,0	31,7	184	122	-	0,66
7	25,4	25,4	152,4	152,4	-	63,5	41,4	3,6	3	6,0	106,9	69	65	42	0,61
8	29,7	29,7	152,4	152,4	-	61,5	41,4	3,6	3	5,1	97,9	86	82	58	0,67
9	36,1	36,1	152,4	152,4	-	58,2	41,4	3,6	4	4,2	95,1	124	111	85	0,69
10	43,7	43,7	152,4	152,4	-	54,4	41,4	3,6	3	3,5	88,0	168	147	125	0,74
11	61,5	61,5	152,4	152,4	-	45,5	41,4	3,6	3	2,5	82,7	312	246	247	0,79
12	76,2	76,2	152,4	152,4	-	37,8	41,4	3,6	3	2,0	53,6	311	341	379	1,10
13	43,7	43,7	152,4	152,4	-	54,4	41,4	3,6	4	3,5	58,8	112	147	125	1,11
14	36,1	36,1	152,4	152,4	-	58,2	41,4	3,6	2	4,2	101,1	132	111	85	0,65
15	50,8	50,8	152,4	152,4	-	50,8	41,4	3,6	2	3,0	84,8	219	185	169	0,77
16	76,2	76,2	152,4	152,4	-	38,1	41,4	3,6	2	2,0	72,5	421	340	379	0,81
17	50,8	50,8	152,4	152,4	-	50,8	26,5	2,7	3	3,0	50,5	130	118	125	0,91
18	76,2	76,2	152,4	152,4	-	38,1	26,5	2,7	3	2,0	45,2	263	217	282	0,83
19	50,8	50,8	152,4	152,4	-	50,8	35,0	3,2	3	3,0	58,5	151	156	151	1,00
20	76,2	76,2	152,4	152,4	-	38,1	35,0	3,2	3	2,0	48,1	279	287	339	1,03
21	25,4	25,4	152,4	152,4	48,0	48,0	30,5	2,9	3	4,9	60	93,1	44	45	0,73
22	25,4	25,4	152,4	152,4	24,1	24,1	30,5	2,9	3	16,8	85	131,5	81	112	0,95
23	25,4	25,4	152,4	152,4	-	-	30,5	2,9	3	36,0	166,9	108	118	218	1,10
24	25,4	25,4	152,4	152,4	-	63,5	33,8	3,1	3	6,0	69,0	45	53	37	0,83
25	25,4	25,4	152,4	152,4	-	42,4	33,8	3,1	3	16,0	123,4	80	87	77	0,97
26	25,4	25,4	152,4	152,4	-	21,1	33,8	3,1	3	26,0	166,9	108	111	158	1,03
27	36,1	36,1	152,4	152,4	38,1	38,1	34,8	3,2	3	4,5	87,0	113	96	94	0,83
28	43,9	43,9	152,4	152,4	38,1	38,1	34,8	3,2	3	3,0	59,2	114	117	117	1,02
29	50,8	50,8	152,4	152,4	38,1	38,1	34,8	3,2	3	2,3	55,7	144	135	149	0,94
30	36,1	36,1	152,4	152,4	38,1	38,1	34,8	3,2	3	4,5	66,2	86	96	94	1,09
31	29,2	57,2	152,4	152,4	-	47,5	46,6	3,9	3	5,2	102,7	171	178	137	0,80
32	27,9	71,1	152,4	152,4	-	40,4	46,6	3,9	3	5,5	104,1	207	217	190	0,92
33	25,4	76,2	152,4	152,4	-	38,1	46,6	3,9	3	6,0	97,6	189	221	203	1,08
34	25,4	101,6	152,4	152,4	-	25,4	46,6	3,9	3	6,0	96,5	249	295	271	1,09
35	25,4	127,0	152,4	152,4	-	12,7	46,6	3,9	3	6,0	77,6	250	368	339	1,35
36	25,4	152,4	152,4	152,4	-	-	46,6	3,9	3	6,0	84,1	326	442	407	1,25
37	50,8	72,4	152,4	152,4	-	39,9	46,6	3,9	3	3,0	86,9	319	297	267	0,84
38	25,4	38,1	152,4	152,4	-	63,5	34,1	3,2	3	4,0	72,4	70	66	60	0,86
39	25,4	50,8	152,4	152,4	-	63,5	34,1	3,2	3	3,0	65,2	84	76	89	0,91
40	25,4	76,2	152,4	152,4	-	63,5	34,1	3,2	3	2,0	53,4	103	93	162	0,90
41	50,8	76,2	152,4	152,4	-	38,1	34,1	3,2	3	3,0	58,1	225	228	231	1,02
42	50,8	76,2	152,4	152,4	-	50,8	34,1	3,2	3	2,0	50,2	194	186	241	0,96

Table B.11: Hawkins – Eccentric loading

	Plate		Block			Concrete		Specimen			$N_{u,Model}$		
#	a_1	b_1	a	b	h	f_{cm}	f_{ctm}	A_c/A_1	f_{cb}	$N_{u,exp}$	$N_{Rd,1}$	$N_{Rd,2}$	$N_{u,Model}/N_{u,Exp}$
1	76	75	150	150	25	29,4	3,5	3,9	125,0	713	333	423	0,47
2	76	75	150	150	50	34,5	3,8	3,9	70,9	404	391	459	0,97
3	76	75	150	150	75	29,4	3,5	3,9	67,6	385	333	423	0,86
4	76	75	150	150	90	37,2	3,4	3,9	59,9	341	421	411	1,20
5	76	75	150	150	120	27,8	3,5	3,9	56,5	322	315	423	0,98
6	76	75	153	153	153	33,4	3,2	4,1	57,0	325	386	394	1,19
7	76	75	150	150	217	33,2	3,9	3,9	46,1	263	376	471	1,43
8	76	75	150	150	300	35,2	3,4	3,9	50,1	286	399	411	1,40
9	76	75	150	150	350	34,3	3,3	3,9	37,5	214	388	399	1,82
10	76	75	150	150	400	32,2	2,6	3,9	46,2	263	365	314	1,19
11	76	75	150	150	25	70,6	5,3	3,9	164,0	935	800	640	0,69
12	76	75	150	150	38	78,9	4,7	3,9	180,0	1026	894	568	0,55
13	76	75	150	150	50	69,2	4,6	3,9	136,0	775	784	556	0,72
14	76	75	150	150	63	69,2	4,6	3,9	98,0	559	784	556	1,00
15	76	75	150	150	75	70,6	5,3	3,9	146,0	832	800	640	0,77
16	76	75	150	150	90	70,6	5,3	3,9	99,1	565	800	640	1,13
17	76	75	150	150	120	68,0	4,6	3,9	103,0	587	770	556	0,95
18	76	75	153	153	153	70,9	5,1	4,1	112,0	638	819	629	0,98
19	76	75	150	150	217	69,2	4,8	3,9	92,7	528	784	580	1,10
20	76	75	150	150	300	74,1	5,4	3,9	82,5	470	839	652	1,39
21	76	75	150	150	350	67,7	4,9	3,9	83,7	477	767	592	1,24
22	76	75	150	150	400	66,1	5,1	3,9	83,0	473	749	616	1,30

Table B.12: Williams – Table A40

	Plate		Block			Concrete		Specimen			$N_{u,Model}$		
#	a_1	b_1	a	b	h	f_{cm}	f_{ctm}	A_c/A_1	f_{cb}	$N_{u,exp}$	$N_{Rd,1}$	$N_{Rd,2}$	$N_{u,Model}/N_{u,Exp}$
1	10	10	102	102	102	34,8	2,8	104,0	277,0	28	31	86	1,13
2	20	20	102	102	102	33,2	3,9	26,0	129,0	52	68	135	1,31
3	25	25	102	102	102	33,2	3,9	16,6	102,0	64	85	143	1,33
4	32	32	102	102	102	34,8	2,8	10,2	92,4	95	114	113	1,20
5	51	51	102	102	102	33,2	3,9	4,0	47,3	123	173	216	1,40
6	75	75	102	102	102	33,2	3,9	1,8	40,2	226	254	409	1,12
7	92	92	102	102	102	34,8	2,8	1,2	40,4	342	327	793	0,96
8	102	102	102	102	102	33,2	3,9	1,0	30,1	313	345	-	1,10
9	102	102	102	102	102	20,9	2,6	1,0	22,9	238	217	-	0,91
10	102	102	102	102	102	58,3	4,4	1,0	68,2	710	607	-	0,85
11	32	32	153	153	153	30,3	3,0	22,9	127,0	130	148	237	1,14
12	75	75	153	153	153	33,4	3,2	4,2	57,0	321	383	392	1,20
13	120	120	153	153	153	30,3	3,0	1,6	37,6	541	556	868	1,03
14	20	20	153	153	153	70,9	5,1	58,5	377,0	151	217	366	1,44
15	32	32	153	153	153	78,9	4,7	22,9	251,0	257	386	371	1,44
16	75	75	153	153	153	70,9	5,1	4,2	112,0	630	814	625	0,99
17	120	120	153	153	153	70,9	5,1	1,6	80,3	1156	1302	1476	1,13
18	75	75	150	150	350	34,3	3,3	4,0	37,5	211	386	396	1,83
19	75	75	150	150	350	67,7	4,9	4,0	83,7	471	762	588	1,25

Table B.13: Williams (2) – Table A41 (1/2)

	Plate		Block			Concrete		Specimen			$N_{u,Model}$		
#	a_1	b_1	a	b	h	f_{cm}	f_{ctm}	A_c/A_1	f_{cb}	$N_{u,exp}$	$N_{Rd,1}$	$N_{Rd,2}$	$N_{u,Model}/N_{u,Exp}$
20	50	25	102	102	102	31,0	3,2	8,3	76,0	95	112	136	1,18
21	50	25	102	102	102	69,2	4,6	8,3	154,0	193	250	195	1,01
22	153	10	153	153	153	35,2	3,2	15,3	104,0	159	211	268	1,32
23	153	25	153	153	153	37,2	3,4	6,1	71,9	275	352	356	1,28
24	153	31	153	153	153	35,2	3,2	4,9	61,0	289	371	363	1,26
25	153	50	153	153	153	37,2	3,4	3,1	50,5	386	498	496	1,28
26	153	75	153	153	153	35,2	3,2	2,0	43,7	501	577	666	1,15
27	153	93	153	153	153	37,2	3,4	1,6	42,0	598	679	963	1,14
28	153	118	153	153	153	37,2	3,4	1,3	39,8	719	765	1743	1,06
29	153	10	153	153	153	69,2	4,8	15,3	170,0	260	414	403	1,55
30	153	25	153	153	153	68,3	4,4	6,1	125,0	478	646	461	0,96
31	153	31	153	153	153	68,3	4,4	4,9	110,0	522	720	500	0,96
32	153	50	153	153	153	69,2	4,8	3,1	92,7	709	926	700	0,99
33	153	75	153	153	153	68,3	4,4	2,0	81,0	929	1119	916	0,99
34	153	93	153	153	153	69,2	4,8	1,6	73,2	1042	1263	1360	1,21
35	153	118	153	153	153	69,2	4,8	1,3	76,1	1374	1423	2461	1,04
36	120	25	153	153	153	36,9	3,0	7,8	84,3	253	309	292	1,15
37	92	25	153	153	153	35,2	3,4	10,2	94,1	216	258	309	1,19
38	75	25	153	153	153	36,9	3,0	12,5	101,0	189	244	261	1,29
39	63	25	153	153	153	35,2	3,4	14,9	110,0	173	214	287	1,23
40	50	25	153	153	153	36,9	3,0	18,7	134,0	168	200	244	1,19
41	37	25	153	153	153	36,2	2,9	25,3	154,0	142	168	226	1,18
42	120	25	153	153	153	68,0	4,6	7,8	141,0	423	570	447	1,06
43	92	25	153	153	153	68,0	4,6	10,2	159,0	366	499	418	1,14
44	75	25	153	153	153	69,2	4,6	12,5	193,0	362	458	401	1,11
45	63	25	153	153	153	68,0	4,6	14,9	189,0	298	413	388	1,30
46	50	25	153	153	153	69,2	4,6	18,7	198,0	248	374	374	1,51
47	37	25	153	153	153	68,0	4,6	25,3	249,0	230	316	358	1,37
48	120	50	153	153	153	36,2	2,9	3,9	56,7	340	429	367	1,08
49	91	50	153	153	153	36,2	2,9	5,1	64,4	293	374	324	1,11
50	75	50	153	153	153	34,4	2,9	6,2	71,6	269	322	302	1,12
51	62	50	153	153	153	36,2	2,9	7,6	79,7	247	308	285	1,15
52	120	50	153	153	153	70,6	5,3	3,9	109,0	654	837	670	1,02
53	91	50	153	153	153	69,2	4,6	5,1	125,0	569	714	514	0,90
54	75	50	153	153	153	67,7	4,9	6,2	132,0	495	634	510	1,03
55	62	50	153	153	153	70,6	5,3	7,6	148,0	459	601	520	1,13
56	75	75	153	153	153	36,5	3,5	4,2	57,4	323	419	429	1,30
57	150	31	150	150	350	35,2	3,2	4,8	40,4	188	360	352	1,87
58	150	75	150	150	350	35,2	3,2	2,0	22,3	251	560	656	2,23
59	150	31	150	150	350	68,3	4,4	4,8	70,8	329	699	484	1,47
60	150	75	150	150	350	68,3	4,4	2,0	51,1	575	1087	902	1,57
61	75	25	150	150	350	36,9	3,0	12,0	70,2	132	240	253	1,82
62	50	25	150	150	350	36,9	3,0	18,0	106,0	133	196	236	1,48
63	75	25	150	150	350	70,9	4,7	12,0	133,0	249	461	397	1,59
64	50	25	150	150	350	70,9	4,7	18,0	182,0	228	376	369	1,62
65	75	50	150	150	350	34,4	2,9	6,0	50,5	189	316	294	1,55
66	75	50	150	150	350	67,7	4,9	6,0	73,3	275	622	497	1,81

Table B.14: Williams (2) – Table A41 (2/2)

	Plate		Block					Concrete		Specimen			$N_{u,Model}$		
#	a_1	b_1	a	b	h	e_a	e_b	f_{cm}	f_{ctm}	A_c/A_1	f_{cb}	$N_{u,exp}$	$N_{Rd,1}$	$N_{Rd,2}$	$N_{u,Model}/N_{u,Exp}$
1	50	25	102	102	102	0	0	31,0	3,2	8,3	76,0	95	112	136	1,18
2	50	25	102	102	102	0	38,5	31,0	3,2	8,3	42,4	53	55	87	1,04
3	25	50	102	102	102	0	26,0	31,0	3,2	8,3	57,9	72	78	76	1,05
4	50	25	102	102	102	26,0	38,5	31,0	3,2	8,3	29,9	37	39	-	1,04
5	50	25	102	102	102	0	0	69,2	4,6	8,3	154,0	193	250	195	1,01
6	50	25	102	102	102	0	38,5	69,2	4,6	8,3	79,0	99	124	125	1,25
7	25	50	102	102	102	0	26,0	69,2	4,6	8,3	122,0	153	175	109	0,71
8	50	25	102	102	102	26,0	38,5	69,2	4,6	8,3	69,6	87	87	-	0,99
9	25	25	102	102	102	0	38,5	36,8	0	16,6	58,7	37	46	-	1,27
10	37	25	102	102	102	0	38,5	36,8	0	11,2	51,2	47	57	-	1,19
11	50	25	102	102	102	0	38,5	31,0	3,2	8,3	42,4	53	55	87	1,04
12	63	25	102	102	102	0	38,5	37,5	0	6,6	45,3	71	75	-	1,05
13	75	25	102	102	102	0	38,5	36,8	0	5,5	37,0	69	80	-	1,16
14	92	25	102	102	102	0	38,5	36,8	0	4,5	37,4	86	89	-	1,04
15	102	25	102	102	102	0	38,5	37,5	0	4,1	32,2	82	96	-	1,16
16	12	25	102	102	102	0	38,5	35,2	2,9	34,7	57,8	17	31	17	0,96
17	20	25	102	102	102	0	38,5	35,2	2,9	20,8	64,7	32	40	26	0,81
18	25	25	102	102	102	0	38,5	74,1	5,4	16,6	96,0	60	94	61	1,02
19	37	25	102	102	102	0	38,5	74,1	5,4	11,2	86,1	80	114	98	1,23
20	50	25	102	102	102	0	38,5	69,2	4,6	8,3	79,0	99	124	125	1,25
21	63	25	102	102	102	0	38,5	74,1	5,4	6,6	69,4	109	149	206	1,36
22	75	25	102	102	102	0	38,5	78,9	4,7	5,5	54,6	102	173	234	1,69
23	92	25	102	102	102	0	38,5	78,9	4,7	4,5	50,4	116	191	636	1,65
24	102	25	102	102	102	0	38,5	74,1	5,4	4,1	52,5	134	189	-	1,41
25	12	25	102	102	102	0	38,5	78,9	4,7	34,7	184,0	55	69	27	0,49
26	20	25	102	102	102	0	38,5	78,9	4,7	20,8	105,0	53	89	42	0,81
27	32	32	102	102	102	0	0	27,8	3,5	10,2	76,8	79	91	142	1,15
28	32	32	102	102	102	0	35	27,8	3,5	10,2	39,7	41	51	65	1,25
29	32	32	102	102	102	35,0	35	27,8	3,5	10,2	21,2	22	28	-	1,31
30	32	32	102	102	102	0	0	70,9	5,1	10,2	188,0	193	231	206	1,07
31	32	32	102	102	102	0	35	70,9	5,1	10,2	113,0	116	130	95	0,82
32	32	32	102	102	102	35,0	35	70,9	5,1	10,2	66,1	68	73	-	1,07
33	32	32	102	102	102	0	10,0	29,4	3,5	10,2	70,3	72	86	120	1,20
34	32	32	102	102	102	0	20,0	29,4	3,5	10,2	70,0	72	75	94	1,04
35	32	32	102	102	102	0	30,0	29,4	3,5	10,2	50,1	51	62	68	1,20
36	32	32	102	102	102	11,0	11,0	29,4	3,5	10,2	70,3	72	75	100	1,05
37	32	32	102	102	102	22,0	22,0	29,4	3,5	10,2	49,8	51	55	70	1,07
38	32	32	102	102	102	32,0	32,0	29,4	3,5	10,2	39,1	40	36	85	0,89
39	32	32	102	102	102	0	10,0	69,2	4,8	10,2	165,0	169	203	165	0,97
40	32	32	102	102	102	0	20,0	69,2	4,8	10,2	135,0	138	176	128	0,93
41	32	32	102	102	102	0	30,0	69,2	4,8	10,2	116,0	119	145	93	0,79
42	32	32	102	102	102	11,0	11,0	69,2	4,8	10,2	153,0	157	177	137	0,87
43	32	32	102	102	102	22,0	22,0	68,0	4,6	10,2	108,0	111	126	92	0,83
44	32	32	102	102	102	32,0	32,0	68,0	4,6	10,2	78,8	81	83	112	1,02

Table B.15: Williams (3) – Table A42

	Plate		Block					Concrete		Specimen			$N_{u,Model}$		
#	a_1	b_1	a	b	h	e_a	e_b	f_{cm}	f_{ctm}	A_c/A_1	f_{cb}	$N_{u,exp}$	$N_{Rd,1}$	$N_{Rd,2}$	$N_{u,Model}/N_{u,Exp}$
1	153	31	153	153	153	0	10	35,2	3,4	4,9	61,6	292	346	357	1,18
2	153	31	153	153	153	0	20	35,2	3,4	4,9	59,2	281	319	329	1,14
3	153	31	153	153	153	0	30	34,4	2,9	4,9	49,7	236	283	260	1,10
4	153	31	153	153	153	0	40	34,4	2,9	4,9	43,2	205	250	248	1,21
5	153	31	153	153	153	0	50	32,2	2,6	4,9	34	161	200	239	1,24
6	153	31	153	153	153	0	61	32,2	2,6	4,9	28,2	134	153	-	1,14
7	153	31	153	153	153	0	10	74,1	5,4	4,9	104	493	728	567	1,15
8	153	31	153	153	153	0	20	74,1	5,4	4,9	109	517	671	523	1,01
9	153	31	153	153	153	0	30	74,1	5,4	4,9	94,9	450	609	485	1,08
10	153	31	153	153	153	0	40	70,6	5,3	4,9	84,3	400	514	453	1,13
11	153	31	153	153	153	0	50	78,9	4,7	4,9	66,1	314	489	432	1,38
12	153	31	153	153	153	0	61	66,1	5,1	4,9	53,1	252	314	-	1,24
13	153	31	153	153	153	0	0	35,2	3,2	4,9	61,0	289	371	363	1,26
14	153	31	153	153	153	0	0	68,3	4,4	4,9	110,0	522	720	500	0,96
15	32	32	153	153	153	0	60,5	35,2	2,6	22,9	70,9	73	79	48	0,67
16	32	32	153	153	153	0	60,5	66,1	5,1	22,9	123,0	126	148	95	0,76
17	32	32	153	153	153	0	0	30,4	2,9	22,9	127,0	130	149	229	1,14
18	32	32	150	150	150	0	10	33,4	3,6	22,0	133,0	136	149	243	1,10
19	32	32	150	150	150	0	30	33,4	3,6	22,0	108,0	111	124	152	1,12
20	32	32	150	150	150	0	40	34,0	3,3	22,0	89,2	91	111	101	1,11
21	32	32	150	150	150	0	50	33,4	3,6	22,0	82,4	84	93	79	0,93
22	32	32	153	153	153	0	60,5	32,3	2,6	22,9	71,0	73	72	48	0,67
23	32	11	150	150	150	0	69,5	33,4	3,6	63,9	5,1	2	25	33	14,18
24	32	32	150	150	150	10	10	29,6	2,5	22,0	114,6	117	123	149	1,05
25	32	32	150	150	150	20	20	34	3,3	22,0	101,2	104	120	150	1,15
26	32	32	150	150	150	30	30	29,6	2,5	22,0	89,2	91	85	84	0,92
27	32	32	150	150	150	40	40	29,6	2,5	22,0	80,1	82	66	60	0,73
28	32	32	150	150	150	50	50	29,6	2,5	22,0	42,0	43	47	46	1,08
29	32	32	150	150	150	59	59	34,3	3,3	22,0	21,8	22	35	-	1,57
30	21	21	150	150	150	55	55	29,6	2,5	51,0	6,9	3	25	22	7,38
31	11	11	150	150	150	69,5	69,5	29,6	2,5	186,0	8,3	1	4	-	3,57
32	32	32	150	150	150	35	59	35,8	3,4	22,0	27,7	28	58	63	2,04
33	32	32	150	150	150	5	20	35,8	3,4	22,0	109,7	112	142	188	1,27
34	32	32	150	150	150	15	59	35,8	3,4	22,0	57,6	59	71	63	1,08
35	32	11	150	150	150	20	69,5	44,1	3,4	63,9	11,4	4	29	31	7,17
36	32	32	150	150	150	0	0	77,6	4,6	22,0	251,0	257	372	351	1,37
37	32	32	150	150	150	0	59	66,0	5,0	22,0	133,0	136	146	93	0,68

Table B.16: Williams (4) – Table A43

	Plate		Block				Concrete		Specimen			$N_{u,Model}$		
#	a_1	b_1	a	b	h	e_b	f_{cm}	f_{ctm}	A_c/A_1	f_{cb}	$N_{u,exp}$	$N_{Rd,1}$	$N_{Rd,2}$	$N_{u,Model}/N_{u,Exp}$
1	32	32	38	150	150	59	35,2	2,9	5,6	18,6	19	39	114	2,06
2	32	32	50	150	150	59	31,0	3,2	7,3	31,3	32	40	68	1,24
3	32	32	58	150	150	59	31,0	3,2	8,5	44,9	46	43	62	0,93
4	32	32	75	150	150	59	31,0	3,2	11,0	43,9	45	49	60	1,08
5	32	32	93	150	150	59	30,3	3,0	13,6	52,4	54	53	56	0,99
6	32	32	114	150	150	59	30,3	3,0	16,7	58,9	60	59	56	0,93
7	32	32	153	153	153	60,5	32,2	2,6	22,9	70,9	73	72	48	0,67
8	32	32	217	150	150	59	30,3	3,0	31,8	75,8	78	81	56	0,72
9	32	32	300	150	150	59	32,2	2,6	43,9	83,3	85	101	48	0,57
10	32	32	36	150	150	59	70,6	5,3	5,3	56,3	58	77	285	1,33
11	32	32	50	150	150	59	78,9	4,7	7,3	74,5	76	101	100	1,31
12	32	32	66	150	150	59	70,6	5,3	9,7	78,8	81	104	99	1,22
13	32	32	75	150	150	59	74,1	5,4	11,0	85,0	87	116	101	1,16
14	32	32	92	150	150	59	66,1	5,1	13,5	95,7	98	115	95	0,97
15	32	32	114	150	150	59	66,1	5,1	16,7	105,0	108	128	95	0,88
16	32	32	153	153	153	60,5	66,1	5,1	22,9	123,0	126	148	95	0,76
17	32	32	217	150	150	59	69,2	4,6	31,8	142,0	145	185	86	0,59
18	32	32	300	150	150	59	66,1	5,1	43,9	144,0	147	207	95	0,65

Table B.17: Williams (5) – Table A44

	Headed bolt				Block			Concrete		Specimen		$N_{u,Model}$		
#	d_b	d_{ext}	A_1	$a_1 = b_1$	c_1	c_2	h_d	$f_{cc,200}$	f_{ctm}	A_1/A_b	P_u	$N_{Rd,1}$	$N_{Rd,2}$	$N_{u,Model}/N_{u,Exp}$
1	25	40	1257	35,4	40	600	400	26,4	2,5	2,6	100	142	100	1,00
2	25	40	1257	35,4	40	600	400	26,4	2,5	2,6	110	142	100	0,91
3	25	40	1257	35,4	40	600	400	26,4	2,5	2,6	115	142	100	0,87
4	25	40	1257	35,4	60	600	400	26,4	2,5	2,6	130	142	172	1,09
5	25	40	1257	35,4	60	600	400	26,4	2,5	2,6	135	142	172	1,05
6	25	40	1257	35,4	60	600	400	26,4	2,5	2,6	142	142	172	1,00
7	25	40	1257	35,4	60	600	400	26,4	2,5	2,6	148	142	172	0,96
8	25	40	1257	35,4	60	600	400	26,4	2,5	2,6	150	142	172	0,94
9	25	40	1257	35,4	60	600	500	26,4	2,5	2,6	120	142	172	1,18
10	25	40	1257	35,4	60	600	500	26,4	2,5	2,6	160	142	172	0,88
11	25	40	1257	35,4	60	600	500	26,4	2,5	2,6	170	142	172	0,83
12	25	40	1257	35,4	80	600	400	26,4	2,5	2,6	185	142	266	0,76
13	25	40	1257	35,4	80	600	400	26,4	2,5	2,6	190	142	266	0,74
14	25	40	1257	35,4	80	600	400	26,4	2,5	2,6	205	142	266	0,69
15	25	31	755	27,5	60	600	400	26,4	2,5	1,5	100	49	152	0,49
16	25	31	755	27,5	60	600	400	26,4	2,5	1,5	105	49	152	0,46
17	25	31	755	27,5	60	600	400	26,4	2,5	1,5	110	49	152	0,44
18	25	45	1590	39,9	60	600	400	26,4	2,5	3,2	155	257	184	1,19
19	25	45	1590	39,9	60	600	400	26,4	2,5	3,2	178	257	184	1,04
20	25	45	1590	39,9	60	600	400	26,4	2,5	3,2	180	257	184	1,02

Table B.18: Furche and Eligehausen's tests

	Headed bolt				Block		Concrete		Specimen		$N_{u,Model}$		
#	d_b	d_{ext}	A_1	$a_1 = b_1$	c_1	c_2	f'_c	f_{ctm}	A_1/A_b	P_u	$N_{Rd,1}$	$N_{Rd,2}$	$N_{u,Model}/N_{u,Exp}$
1	25	63	3167	56,3	38	457	38	3,4	6,2	276	517	207	0,75
2	25	63	3167	56,3	76	457	27	2,7	6,2	346	503	334	0,97
3	25	63	3167	56,3	102	457	24	2,5	6,2	342	447	468	1,31
4	25	63	3167	56,3	76	457	27	2,7	6,2	353	503	334	0,95
5	44	102	8108	90,0	86	457	27	2,7	5,2	622	867	564	0,91
6	44	102	8108	90,0	111	457	25	2,6	5,2	665	912	721	1,08
7	44	102	8108	90,0	137	457	32	3,0	5,2	793	1297	1126	1,42
8	44	102	8108	90,0	137	457	30	2,9	5,2	748	1216	1078	1,44
9	44	102	8108	90,0	175	457	27	2,7	5,2	947	1236	1440	1,31
10	44	102	8108	90,0	111	457	25	2,6	5,2	638	912	721	1,13
11	44	102	8108	90,0	137	457	34	3,1	5,2	838	1378	1172	1,40
12	44	76	4561	67,5	111	457	18	2,1	2,9	303	379	482	1,25
13	44	83	5352	73,2	111	457	30	2,9	3,4	692	798	709	1,02
14	44	89	6207	78,8	111	457	38	3,4	4,0	663	1168	869	1,31
15	44	127	12 668	112,6	111	457	19	2,1	8,2	524	902	721	1,38
16	44	102	8108	90,0	111	457	37	3,3	5,2	728	1349	936	1,29
17	44	127	12 668	112,6	111	457	27	2,7	8,2	699	1282	912	1,30
18	32	55	2364	48,6	48	305	32	3,0	3,0	228	307	191	0,84
19	32	55	2364	48,6	76	305	32	3,0	3,0	259	352	341	1,32
20	32	55	2364	48,6	111	305	32	3,0	3,0	330	352	605	1,07
21	32	55	2364	48,6	143	305	32	3,0	3,0	305	352	916	1,15
22	32	55	2364	48,6	76	305	17	2,0	3,0	215	187	224	0,87
23	32	55	2364	48,6	76	305	17	2,0	3,0	204	187	224	0,92
24	51	86	5789	76,1	76	406	33	3,1	2,9	553	711	483	0,87
25	51	86	5789	76,1	102	406	36	3,3	2,9	478	899	732	1,53
26	51	86	5789	76,1	152	406	36	3,3	2,9	691	948	1299	1,37
27	51	86	5789	76,1	203	406	33	3,1	2,9	779	869	1947	1,12
28	51	86	5789	76,1	102	406	15	1,8	2,9	320	374	408	1,17
29	51	86	5789	76,1	102	406	15	1,8	2,9	338	374	408	1,11
30	13	35	958	30,9	19	114	24	2,5	7,6	51	64	44	0,87
31	13	35	958	30,9	25	114	24	2,5	7,6	71	74	52	0,74
32	13	35	958	30,9	25	114	22	2,4	7,6	75	68	50	0,66
33	13	35	958	30,9	32	114	38	3,4	7,6	85	132	91	1,07
34	13	35	958	30,9	32	114	21	2,3	7,6	58	73	61	1,06
35	13	27	570	23,9	32	114	22	2,4	4,5	68	56	52	0,76
36	13	44	1552	39,4	32	114	22	2,4	12,2	58	100	81	1,39
37	13	44	1552	39,4	38	114	25	2,6	12,2	67	124	104	1,55
38	13	27	570	23,9	38	114	24	2,5	4,5	63	66	70	1,06
39	13	44	1552	39,4	38	114	22	2,4	12,2	79	109	95	1,20
40	13	35	958	30,9	44	114	27	2,7	7,6	69	110	108	1,57
41	13	35	958	30,9	51	114	23	2,4	7,6	80	101	120	1,26
42	13	27	570	23,9	51	114	21	2,3	4,5	47	65	99	1,39
43	13	35	958	30,9	57	114	21	2,3	7,6	83	98	133	1,18
44	13	27	570	23,9	64	114	24	2,5	4,5	93	74	156	0,80
45	13	35	958	30,9	25	114	20	2,2	7,6	67	62	46	0,69
46	13	35	958	30,9	32	114	21	2,3	7,6	62	73	61	0,99
47	13	35	958	30,9	38	114	24	2,5	7,6	78	91	82	1,06
48	13	27	570	23,9	38	114	24	2,5	4,5	74	66	70	0,90

Table B.19: Tests by Hasselwander et al.

C YIELD AND FAILURE CRITERIA

C.1 STRESS TENSORS AND INVARIANTS

The three-dimensional stress state of a material is traditionally defined by the Cauchy stress tensor σ_{ij} at the point under consideration, whose components depend on the orientation of the coordinate system in present (deformed) configuration, but whose invariants are independent of the coordinate system chosen to represent it. The eigenvectors of the matrix constitute the principal directions in which the principal stresses (i.e. the matrix eigenvalues, being $\sigma_I \geqslant \sigma_{II} \geqslant \sigma_{III}$) are acting. The homogenous system is:

$$\left(\sigma_{ij} - \sigma\delta_{ij}\right)\vec{n_j} = 0 \tag{C.1}$$

whose solution is:

$$\det\left(\sigma_{ij} - \sigma\delta_{ij}\right) = 0 \tag{C.2}$$

where σ are the unknown eigenvalues, δ_{ij} is the Kronecker delta and $\vec{n_j}$ are the unknown eigenvectors. The characteristic equation has three real roots:

$$\begin{aligned}\sigma^3 &- \left(\sigma_{xx} + \sigma_{yy} + \sigma_{zz}\right)\sigma^2 + \\ &\left(\sigma_{xx}\sigma_{yy} + \sigma_{xx}\sigma_{zz} + \sigma_{yy}\sigma_{zz} - \tau_{xy}^2 - \tau_{xz}^2 - \tau_{yz}^2\right)\sigma \\ &- \tau_{xz}^2\sigma_{yy} - \tau_{yz}^2\sigma_{xx} - \tau_{xy}^2\sigma_{zz} + 2\tau_{xy}\tau_{xz}\tau_{yz} + \\ &+ \sigma_{xx}\sigma_{yy}\sigma_{zz} = 0\end{aligned} \tag{C.3}$$

The stress invariants are defined as follows:

$$I_1 = \text{trace}\left(\sigma_{ij}\right) \tag{C.4}$$

$$I_2 = \frac{1}{2}\left[\text{trace}\left(\sigma_{ij}\right)^2 - \text{trace}\left(\sigma_{ij}^2\right)\right] \tag{C.5}$$

$$I_3 = \det\left(\sigma_{ij}\right) \tag{C.6}$$

With this notation, equation C.3 can be rewrite as:

$$\sigma^3 - I_1\sigma^2 + I_2\sigma - I_3 = 0 \tag{C.7}$$

The stress tensor is often decomposed into two parts, the hydrostatic pressure and the deviatoric tensor.

$$p = I_1/3 \tag{C.8}$$

$$s_{ij} = \sigma_{ij} - p\delta_{ij} \tag{C.9}$$

The homogeneous system and the characteristic equation can be obtained also for the deviatoric tensor:

$$\det\left(s_{ij} - s\delta_{ij}\right) = 0 \tag{C.10}$$

$$s^3 - J_1 s^2 - J_2 s - J_3 = 0 \tag{C.11}$$

Is thus possible to calculate another set of invariants, which are:

$$J_1 = \text{trace}\left(s_{ij}\right) = 0 \qquad \text{(due to the state of pure shear)} \tag{C.12}$$

$$\begin{aligned} J_2 &= \frac{1}{6}\left[(\sigma_{xx} - \sigma_{yy})^2 + (\sigma_{yy} - \sigma_{zz})^2 + (\sigma_{zz} - \sigma_{xx})^2\right] + \\ &+ \sigma_{xy}^2 + \sigma_{yz}^2 + \sigma_{zx}^2 = \\ &= \frac{1}{6}\left[(\sigma_I - \sigma_{II})^2 + (\sigma_{II} - \sigma_{III})^2 + (\sigma_{III} - \sigma_I)^2\right] \end{aligned} \tag{C.13}$$

$$J_3 = \det\left(s_{ij}\right) \tag{C.14}$$

A different measure of J_2 is often used, known as the equivalent or Von Mises stress, defined as:

$$\begin{aligned} \sigma_{VM} &= \sqrt{3J_2} = \\ &= \sqrt{\frac{1}{2}\left[(\sigma_I - \sigma_{II})^2 + (\sigma_{II} - \sigma_{III})^2 + (\sigma_{III} - \sigma_I)^2\right]} = \\ &= \sqrt{\frac{1}{2}\left[(\sigma_{xx} - \sigma_{yy})^2 + (\sigma_{yy} - \sigma_{zz})^2 + (\sigma_{zz} - \sigma_{xx})^2\right]} + \\ &+ \sqrt{\left[3\sigma_{xy}^2 + 3\sigma_{yz}^2 + 3\sigma_{zx}^2\right]} \end{aligned} \tag{C.15}$$

It can be inferred that the J_2 invariant is a measure of how much the stress state deviates from a state of pure hydrostatic stress.

C.1.1 Haigh-Westergaard coordinates

A general shape of the failure surface for an isotropic material can be illustrated in terms of the Haigh-Westergaard coodinates (ξ, ρ, θ), cylindrical coordinates which are functions of the three stress invariants.

$$\xi = \frac{1}{\sqrt{3}} I_1 = \sqrt{3}p \tag{C.16}$$

$$\rho = \sqrt{2J_2} \tag{C.17}$$

$$\cos(3\theta) = \frac{3\sqrt{3}}{2}\frac{J_3}{J_2^{3/2}} \tag{C.18}$$

In the Haigh-Westergaard space (see Figure C.1a), ξ measures the hydrostatic pressure or mean stress, while the deviatoric plane, also called π plane, is the plane normal to the hidrostatic axis. ρ gives the measure of the distance with respect to the hydrostatic axis. The $(\xi - \rho)$ plane is called meridian plane or *Rendulic plane* (Figure C.1b) and

describes how the deviatoric stress can be supported with a varying hydrostatic stress, a very common representation under a state of plain stress or plain strain[1]. A projection of the failure surface on this plane is called meridian and is identified by its *Lode angle* θ [73], which varies between 0° and 60°[2].

The principal stresses are related to the Haigh-Westergaard coordinates by:

$$\begin{bmatrix} \sigma_1 \\ \sigma_2 \\ \sigma_3 \end{bmatrix} = \frac{1}{\sqrt{3}} \begin{bmatrix} \xi \\ \xi \\ \xi \end{bmatrix} + \sqrt{\frac{2}{3}}\rho \begin{bmatrix} \cos(\theta) \\ \cos(\theta - 2\pi/3) \\ \cos(\theta + 2\pi/3) \end{bmatrix} \tag{C.19}$$

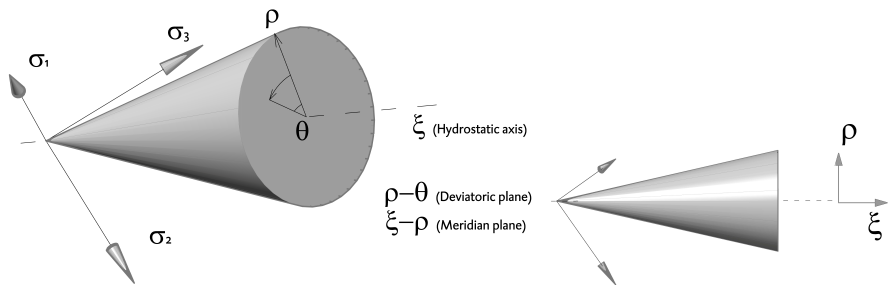

(a) *The Haigh-Westergaard stress space* **(b)** *The meridian plane*

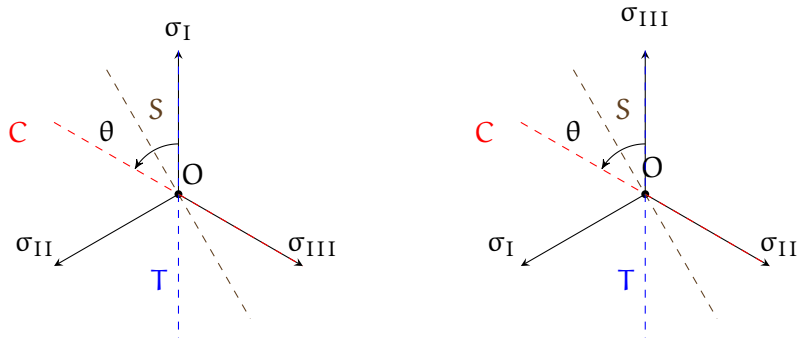

(c) σ_1 *is equal to the maximum compressive stress* **(d)** σ_1 *is equal to the maximum tensile stress*

Figure C.1: A generic failure surface in the Haigh-Westergaard stress space with different definitions of the Lode Angle

The Lode angle is controlled by the relationship of the intermediate principal stress to the major and minor principal stresses (Figure C.1c). When two equal principal stresses are smaller than the third one θ is equal to 60° (compressive meridian). On the other hand when two equal principal stresses are larger than the third one θ is equal to 0° (tensile meridian)[3]. Therefore, the Lode angle mea-

[1] For instance, the Mohr-Coulomb criterion $\tau = c + \sigma \tan \phi$, used in soil mechanics, is represented in the meridian plane

[2] The function $\cos(3\theta)$ is periodic with period 60°.

[3] Changing the definition of the Lode angle using $(-\sin)$ instead of (cos) gives the opposite result, as shown in Figure C.1d.

sures the magnitude of the intermediate principal stress in relation to the others. For this reason, the meridian determined by θ=30° is sometimes called the shear meridian (see Figure C.2b).

C.2 YIELD AND FAILURE CRITERIA

A failure criterion can be generally expressed as a function of the stress invariants and a certain number of material parameters (k_i):

$$f(\xi, \rho, \theta, k_i) = 0 \tag{C.20}$$

In most ductile metals, the influence of the hydrostatic pressure p is not relevant, while is very relevant in many nonmetallic materials such as soils or concrete. For this reason, generally, under the definition *failure criteria* there is is a nomenclature distinction between yield criteria, intented for ductile materials whose behavior is little or not dependent on hydrostatic pressure, and failure criteria for brittle materials, which in turn depends strongly on it.

C.2.1 Independence of hydrostatic pressure

Tresca proposed the first yield criterion for a material under a combined state of stress in 1864, when he selected as the key variable the maximum shear stress $\tau_{max} = \max\left(\frac{1}{2}(\sigma_{ii} - \sigma_{jj})\right)$ and identified the maximum allowable shear stress as half the yield stress measured in a uniaxial tensile test ($\sigma_0/2$). The failure surface has the hydrostatic axis as generator: since the possible permutations of the principal stresses are six, a regular hexagon defines the failure surface in the deviatoric plane, and the yield surface is therefore conformed by an hexagonal prism.

A more complex criterion, which takes into account the influence of the intermediate principal stress, is the 1913 Von Mises or maximum distorsion energy criterion. Although the general expression of the failure surface is the same, he considered as the key variable the octahedral shearing stress. As in the previous case, the yield surface is completely determined by its cross section (the π plane), but in this case[4] the geometry on the deviatoric plane is a circular cylinder with radius $\rho = \sqrt{\frac{2}{3}}\sigma_0$, σ_0 being again the yield stress measured in a uniaxial tensile test.

The two surfaces agree only in some points: if the maximum allowable stress is the one reached in a uniaxial tensile test, the Von Mises failure surface cirumscribes the hexagon (this is the usual representation) and σ_{VM} is at most 1,15 times σ_{TR}.

[4] In case of a biaxial stress state, the intersection of the failure surface with the plane $\sigma_{III} = 0$ is an eccentrically-located ellipse.

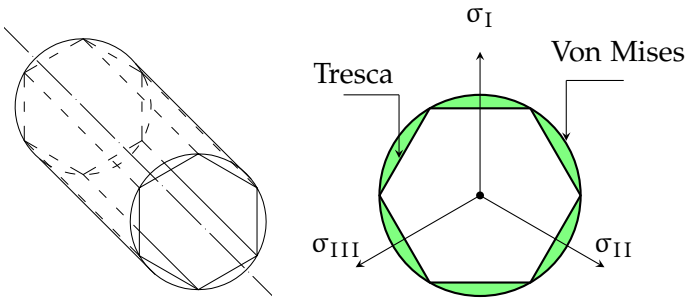

(a) *Yield surfaces*

(b) *Deviatoric (π) plane:* $\rho = \sqrt{\frac{2}{3}}\sigma_Y$

Figure C.2: Tresca and Von Mises criteria. On the right are indicated the Lode angle and the principal meridians

Both criteria are represented in Figure C.2, with some of the geometrical entities described above.

C.2.2 Dependence of hydrostatic pressure

For materials with a strong dependence of hydrostatic pressure the general failure surface assumes its general form, as in Equation C.20.

The maximum principal stress criterion, also known as Rankine criterion, dates back to 1876 and is the simplest way to assess the failure of fragile materials: for each direction i, at any point the stress has to be lower than the ultimate strength. This criterion, for materials having different tensile and compressive strengths, corresponds to an eccentrically-located cube in the coordinate system with axis σ_1, σ_2, σ_3 and to a pyramid in the Haigh-Westergaard stress space.

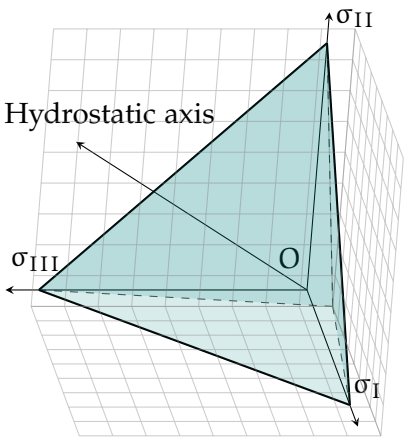

Figure C.3: Rankine failure surface

As cohesive materials have normally higher compressive strengths, a normal procedure uses different models to assess tensile or compressive failure of the material. As models which deal with tension only need one parameter, the maximum tensile stress allowable, these criteria are also called *tension cut-off criteria*. If the Rankine criterion is used only to assess a tensile failure, the failure surface will be an infinite pyramid, with a triangular cross section by the deviatoric plane (Figure C.3).

For the compressive part of the model the Mohr-Coulomb criterion (1900) can be used, which can be regarded as a generalized Tresca

model accounting for the hydrostatic pressure effect. As a generalized Tresca model, it has the same disadvantage: it does not take into account the effect of the intermediate principal stress and its failure surface is a cone with an hexagonal cross-section.

The Druker-Prager criterion (1952) tackles this problem with a generalized version of the Von Mises model accounting for the hydrostatic pressure effect, providing a smooth conical surface as in Figure C.4. However, this model does not show variation with θ in the deviatoric plane. For this reason, another model has been developed, the Modified Mohr-Coulomb criterion, which has a smoothed surface with a cross-section somewhere between a hexagon and a circle.

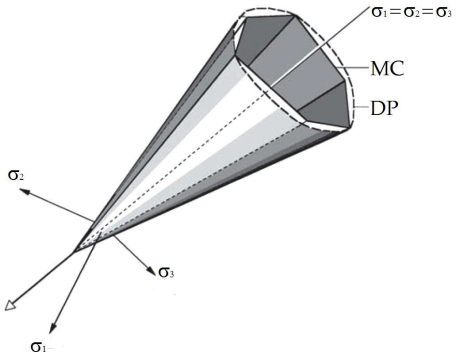

Figure C.4: Drucker-Prager and Mohr-Coulomb failure surfaces. Source: [16]

In some cases, usually when dealing with granular materials, a compression cap is also used to introduce an elastic limit in pure hydrostatic compression and to control plastic volumetric changes: as densification occurs, the yield surface expands and eventually reduces to the Drucker–Prager or Mohr-Coulomb yield function for fully dense bodies (Figure C.5). The three surfaces should conform a smooth surface in order to avoid numerical instabilities associated with corner points.

C.3 ATENA

The main application field of the Finite Element program, created by Ĉervenka Consulting, is the analysis of concrete and reinforced concrete structures, focused on non linear analysis. The software is currently used in a variety of real projects and international prediction competitions, for instance in 2005 the software helped the company in winning a competion whose target was to predict the shear strength of slabs with inclined reinforcement. Vladimir Ĉervenka, director of the company, was also the winner of the *International Competition to Predict the Response of Reinforced Concrete Panels*, held by University of Toronto in 1982, organized to compare analytical methods applied to elements subjected to any combination of shear and tension or compression, that is, a generic two dimensional stress-states [31].

Based on advanced constitutive models, it can be used for realistic simulation of structural behavior. Craking phenomena are modeled by a smeared crack approach, in which fixed or rotating cracks can

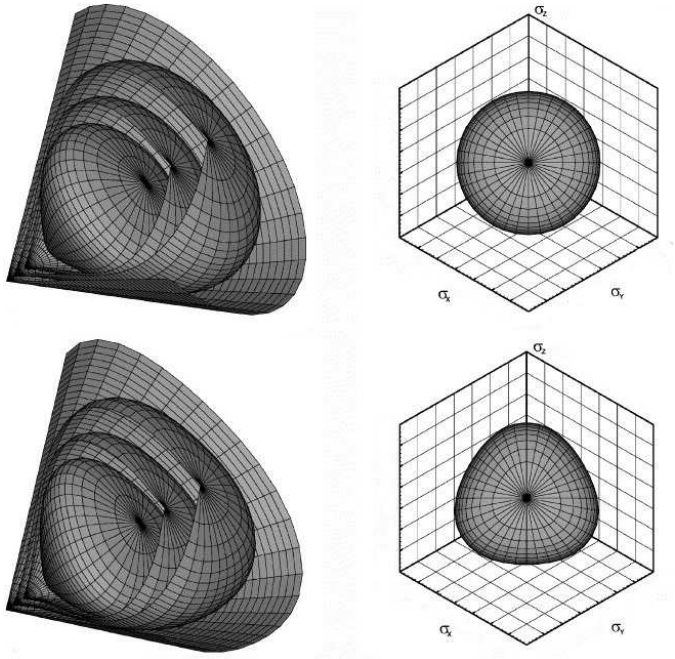

Figure C.5: General shape of a failure surface with a cone-cap, for different values of relative density. At the right the shape of the cross-section through the deviatoric plane is shown. At the top, a capped Drucker-Prager yield surface, at the bottom the same model based on the modified Mohr-Coulomb failure surface. Source: [12]

be considered. The reinforcements can be modeled as smeared or discrete. A few bond-slip laws are implemented but they can also be user-defined. Newton-Raphson, modified Newton Raphson or Arc Length methods are available as solving techniques.

C.3.1 Concrete constitutive laws

A concrete model is usually based on the current plasticity theory. Many constitutive laws are available in literature for concrete, most of them belonging to one of the following three main categories:

- Plastic models taking into account permanent deformations;
- Damage models considering the stiffness degradation;
- Combined models, more recent and capable of considering both phenomena.

ATENA uses a three dimensional combined fracture-plastic model for concrete described, among others, by Ĉervenka and Papanikolaou [21]. The model, based on the method of strain decomposition, was first introduced by De Borst [34]. Tension is handled by a fracture model that adopts the Rankine failure criterion with an exponential

softening, while the plasticity model is based on the Menétrey-Willam failure surface. A combined algorithm allows the two models to be formulated separately. In rate form[5],

$$\dot{\epsilon_{ij}} = \dot{\epsilon_{ij}}^{e} + \dot{\epsilon_{ij}}^{p} + \dot{\epsilon_{ij}}^{f} \tag{C.21}$$

$$\dot{\sigma_{ij}} = D_{ijkl} \cdot \left(\dot{\epsilon_{kl}}^{e} - \dot{\epsilon_{kl}}^{p} - \dot{\epsilon_{kl}}^{f}\right) \tag{C.22}$$

where D_{ijkl} is the fourth-order stiffness tensor, a 6×6 matrix which controls the relationship between stresses and strains.

FRACTURE MODEL FOR CONCRETE CRAKING At the crack tip the stress field can be separated into three components — usually called mode I, II and III — referring respectively to tension, in-plane shear and out-of-plane shear, as represented in Figure C.6. The model is capable of addressing the three modes of crack propagation.

The damage is fully described by the fracture energy density, G_f, needed for opening a crack, the tensile strength f_t and the stress crack opening law, i. e., the shape of stress softening function. The fracture energy is dissipated through smeared cracks, which localize within a crack band due to the softening nature of the crack opening law.

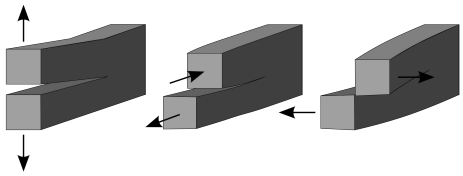

Figure C.6: Fracture modes

The Rankine criterion is formulated with the equation:

$$f_k^f = \sigma_{ij}^t - f_t \leqslant 0 \tag{C.23}$$

When f_k^f is positive, the increment of fracture strain in a direction normal to the failure surface is solved by iterations since the value of current tensile strength is a function of the crack opening w, which in turn depends on the Hordijk's material softening law [52].

The crack opening is then computed by multiplying the characteristic length[6] by the total fracture strain plus the current increment. For further details see ATENA program documentation [23].

PLASTICITY MODEL FOR CONCRETE CRUSHING The Menetrey-Willam three parameter yield surface is used for the modeling of concrete in compression [86]. This criterion "combines the traditional Rankine criterion of maximum tensile strength with the Mohr-Coulomb

[5] Strain rate is the rate of change in strain of a material with respect to time (to the last step). e=elastic, p=plastic, f=fracture.

[6] In the present model, the crack band size is calculated as a size of the element projected along the crack direction k. The crack band approach adopted ensures that the energy dissipation does not depend on the finite element size.

hypothesis of shear strength". It incorporates the effect of all three principal stresses and is expressed in terms of Haigh-Westergaard coordinates.

The three parameters that define the shape and size of the loading surface are the mean uniaxial compressive concrete strength, the mean uniaxial tensile concrete strength and the eccentricity parameter of out-of-roundness (e).

Parameter e defines the roundness of the failure surface in the deviatoric section, which is triangular at low confinement and circular at high confinement. It also influences the equibiaxial compressive strength (f_{bc}): the lower limit ($e = 0{,}5$) leads to f_{bc} equal to the uniaxial compressive strength, whereas the upper limit increases f_{bc} to more than 5 times the uniaxial strength. The author's recommended value is 0,52, which implies $f_{bc} = 1{,}14 f_c$, a value similar to the one obtained by Kupfer et al. [65] in their famous experimental work.

The position of the yield surface is not fixed but can move along the hydrostatic axis and expand or contract depending on the hardening/softening parameters. Concrete crushing in one direction implies in reality an effect on cracking in other directions: in the model it is assumed that after the plasticity criterion is violated the tensile strength in all directions gradually decreases to zero.

The model can handle distinct loading scenarios, and its accuracy has been assessed validating it [99] against several experimental results on uniaxial, biaxial and triaxial tests. The reasonable correlation obtained makes the model applicable to large scale finite element analysis. Future developments of the plasticity part of the model may include a cap surface in order to introduce an upper bound on hydrostatic compression.

D LABORATORY TESTS DATA

D.1 SPECIMEN 25-TH-16

The first test took place 37 days after concrete pouring. The day before the test a concrete cylinder was tested: the compressive strength was 23,8 MPa, although the mean compressive strength of the concrete batch was more likely 22 MPa (see Section 5.2.1.2).

D.1.1 General behavior

The test execution was fluid, without significant problems. The starting position was soon stabilized and the safety straps were loosened: the applied load was increased step by step (see Table D.1) and manual measurements were taken at each step. Once a load of 325 kN was reached, no manual measurements were taken for safety reasons.

The first flexural crack was observed between 150 and 200 kN. Two other cracks soon developed nearby around 250-275 kN, while the last ones developed at a higher load (375-400 kN). The last cracks formed were other flexural cracks and some bond-related cracks (parallel to the rebars) near the corner and a wide crack along the central strut. After the 400 kN load step some cracks began to be wider than others, anticipating the final failure due to the excessive strain in the reinforcement, which occurred at a load of 465 kN (see Figure D.1).

Double headed shear reinforcement and anchorage plates did not shown any sign of weakening during the test.

D.1.2 Load-displacement

The load-displacement graph presented in Figure D.2, represents the applied load and the measured displacement of the load application point during the test. Three different predictions are superposed in the graph, a simple sectional analysis, a non-linear analysis, and a more sofisticated non-linear finite element analysis performed with ATENA (previously described in Section 5.3.6).

Global ductility in terms of displacement of the control point was very high in comparison with both predictions: this fact is related to convergence problems of models, given the very small slope of the yield zone of the curve.

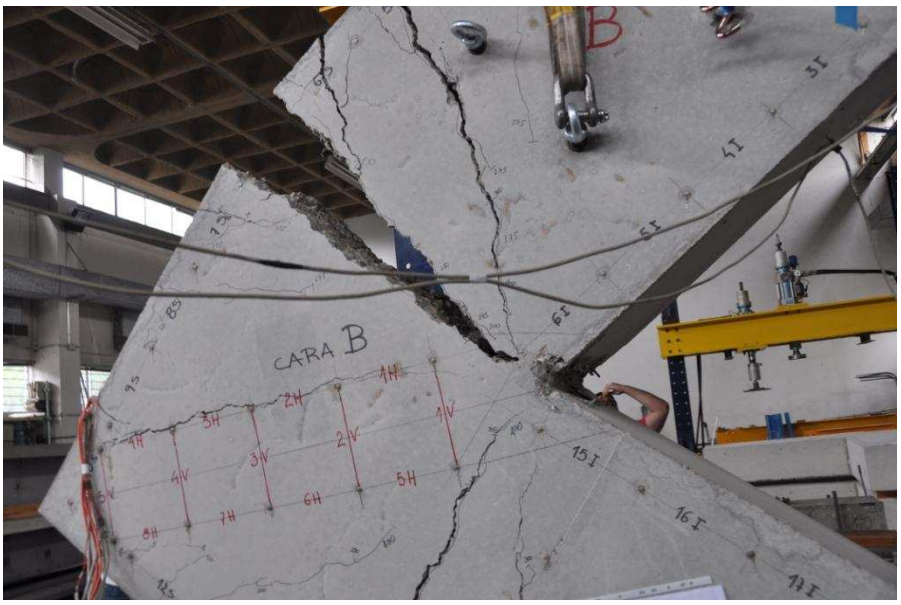

Figure D.1: The final configuration after failure: after the crushing of concrete in the compression corner[1] due to yielding of the flexural reinforcement, a sudden rupture of the tensile reinforcement was observed.
Note[1]: It is not meant here that failure is due to lack of capacity of concrete. After yielding of the flexural reinforcement the compressed fiber of concrete tries to absorb extra bending by absorbing moments as well as the compressive component of general flexure (see figure below). This leads to crushing of the most compressed fiber

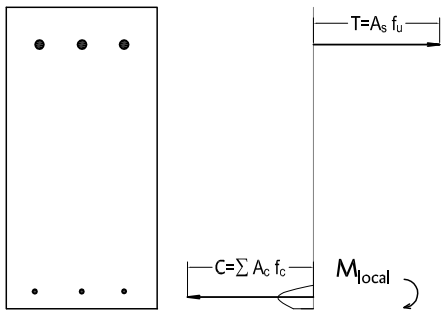

Step	Load [kN]	Notes
1	50	
2	100	
3	150	
4	200	First flexural crack
5	250	
6	275	Formation and growth of flexural cracks
7	300	
8	325	
9	350	
10	375	
11	400	
12	425	A large crack appears parallel to the compression strut
13	435	
14	445	
15	455	
16	465	

Table D.1: 25-TH-16. Load steps

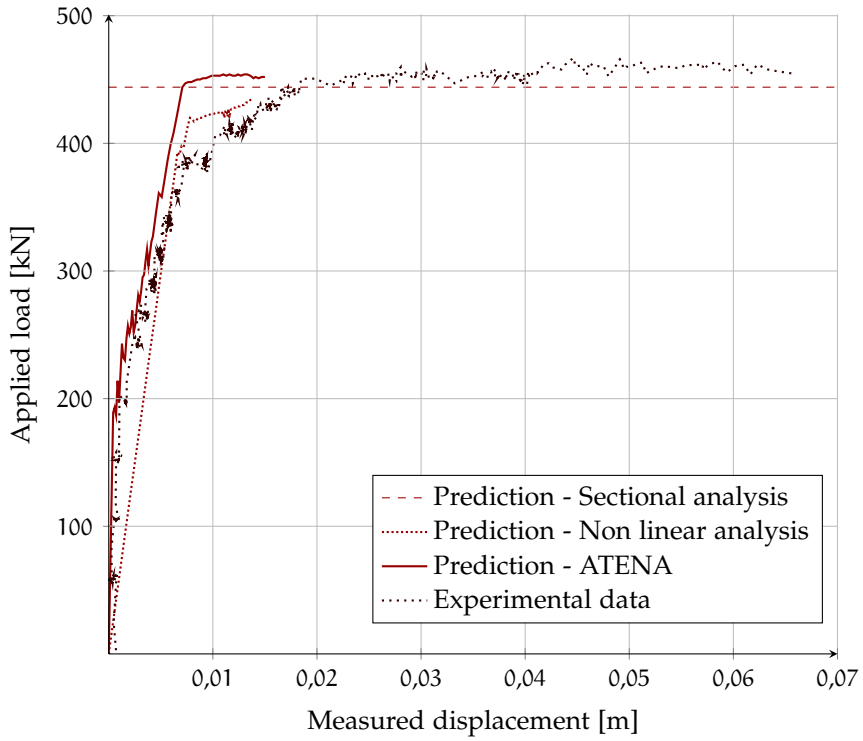

Figure D.2: Applied load vs. displacement of the load application point. In red lines the theoretical estimations. The prediciton by non-linear analysis is calculated without considering tension stiffening (concrete is modeled with no tensile strength)

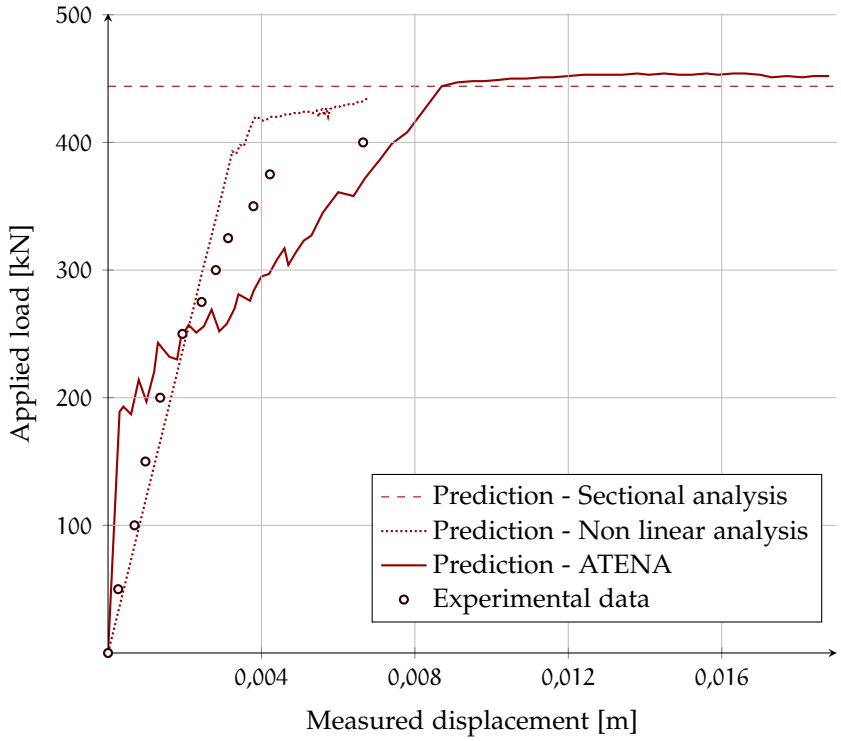

Figure D.3: Applied load vs. horizontal displacement (probe indicator). In red lines the theoretical estimations

A similar graph is provided in Figure D.3 for the horizontal displacement measured by the probe indicator, although in this case the experimental series stops earlier for safety reasons.

D.1.3 Load-rotation

A small rigid rotation of approximately 10^{-5} rad/kN was observed during the test. The results presented in Figure D.4 are compensated to take this rotation into account.

D.1.4 Moment-curvature

The experimental moment-curvature for some sections (see Figure 5.13) is shown in Figure D.5.

The experimental curvatures are calculated, for each section, as the substraction of strains measured by targets on the reinforcement axes in that section divided by the distance between the two lines[2]; the experimental moments are computed as the force perpendicular to the beam axis multiplied by the distance of the segment axis to the point of application of the load (1,075 m for sections 6-15 and 0,875 m of sections 5-16).

[2] $1/r = \frac{\varepsilon_s - \varepsilon_i}{d - 2d'}$

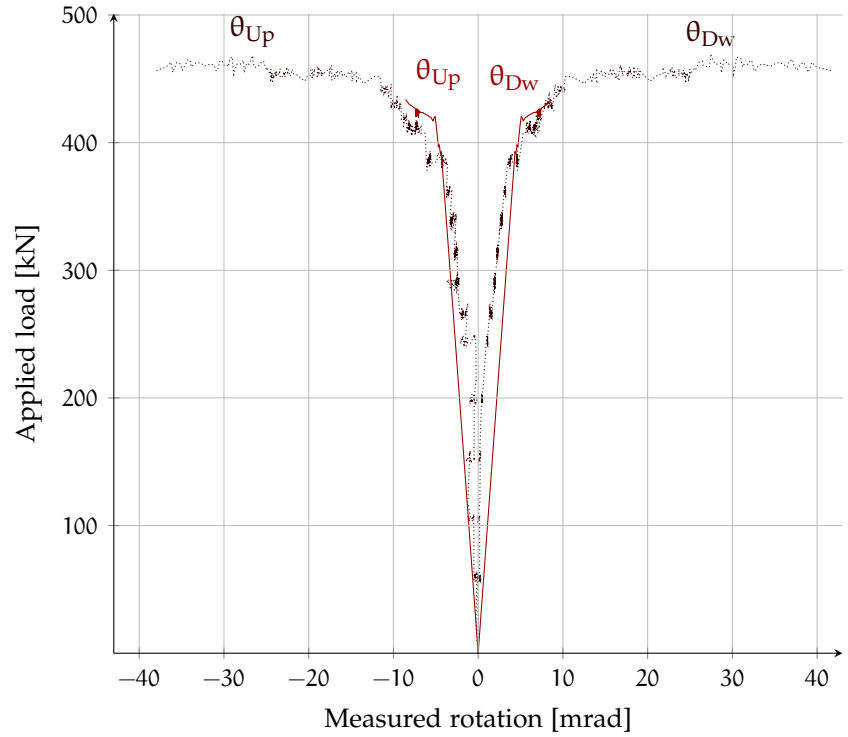

Figure D.4: Applied load vs. measured rotations.
In solid line, the non linear theoretical estimation

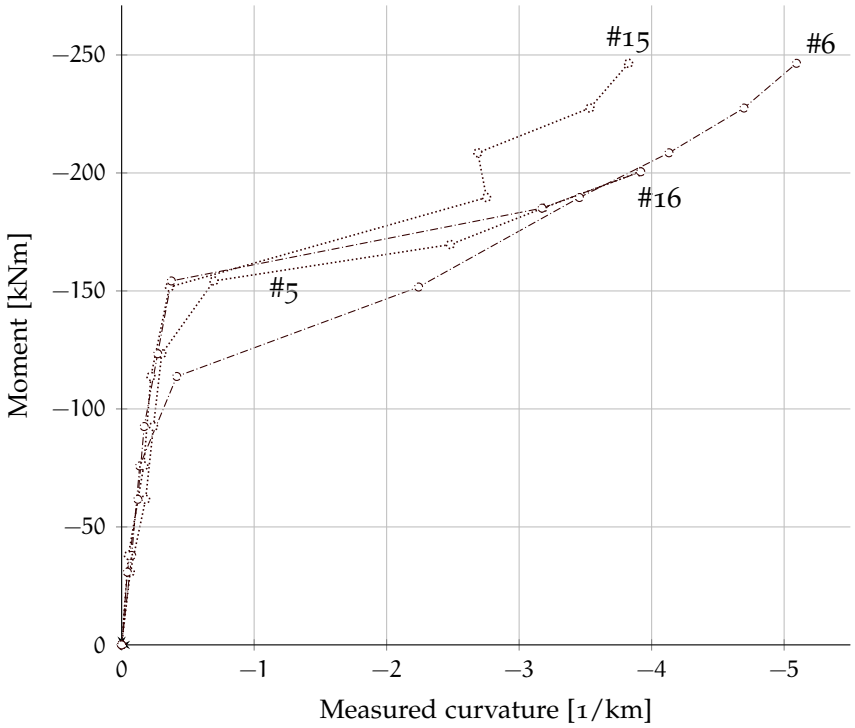

Figure D.5: 25-TH-16. Average (A and B sides) of measured M–χ diagram for some relevant sections

D.1.5 Crack pattern

Crack evolution described in Section D.1.1 is carefully reproduced in Figure D.7, where the position of the mechanical strain gauges is also represented.

The serviceability load can be estimated as a percentage of the ultimate load. If it is assumed $G_k = Q_k$:

$$F_{SLS} = \frac{(1{,}0 + 0{,}3)}{(1{,}35 + 1{,}5)} F_{ULS} \simeq 0{,}46\ F_{ULS} = 203\ \text{kN}$$

At the top of Figure D.6 is shown the measured crack width[3] compared to the applied load, while at the bottom is provided the measured crack width compared to the theoretical steel stress, calculated at the middle of each segment.

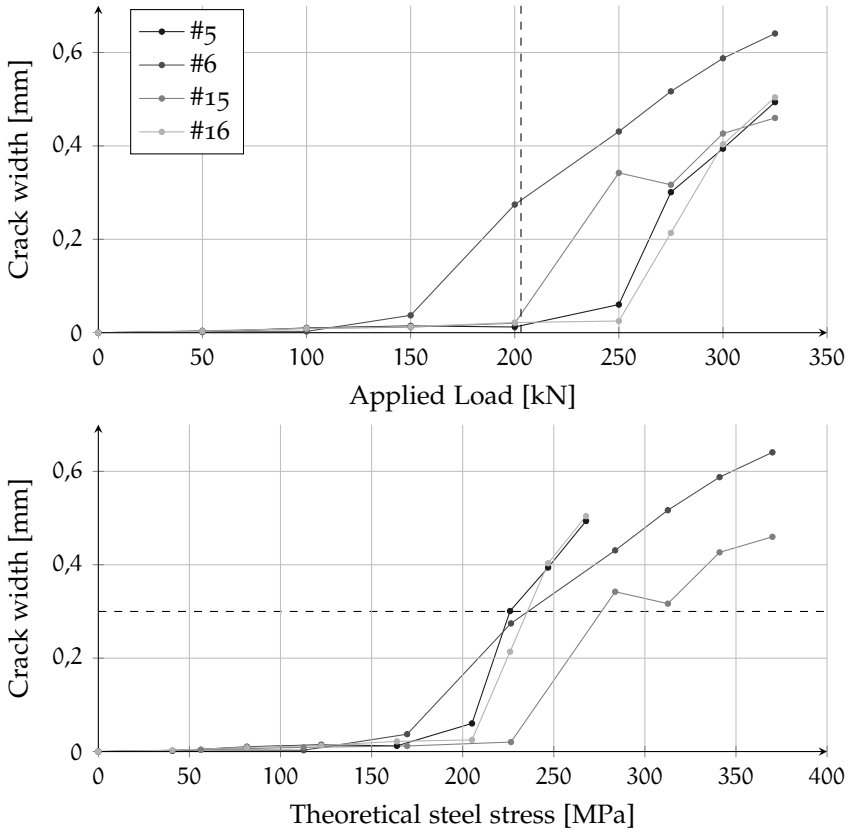

Figure D.6: 25-TH-16. Average (A and B sides) of measured crack width as a function of the applied load (top) and theoretical steel stress (bottom). The serviceability load and a crack width reference value of 0,3 mm are represented in dashed lines

[3]The experimental crack width has been calculated supposing that the measured strain is all due to fracture strain, since the elastic strain is very small and therefore it can be neglected. Elastic strain due to compression reached, at most, 0,07 mm for sections 6 and 15.

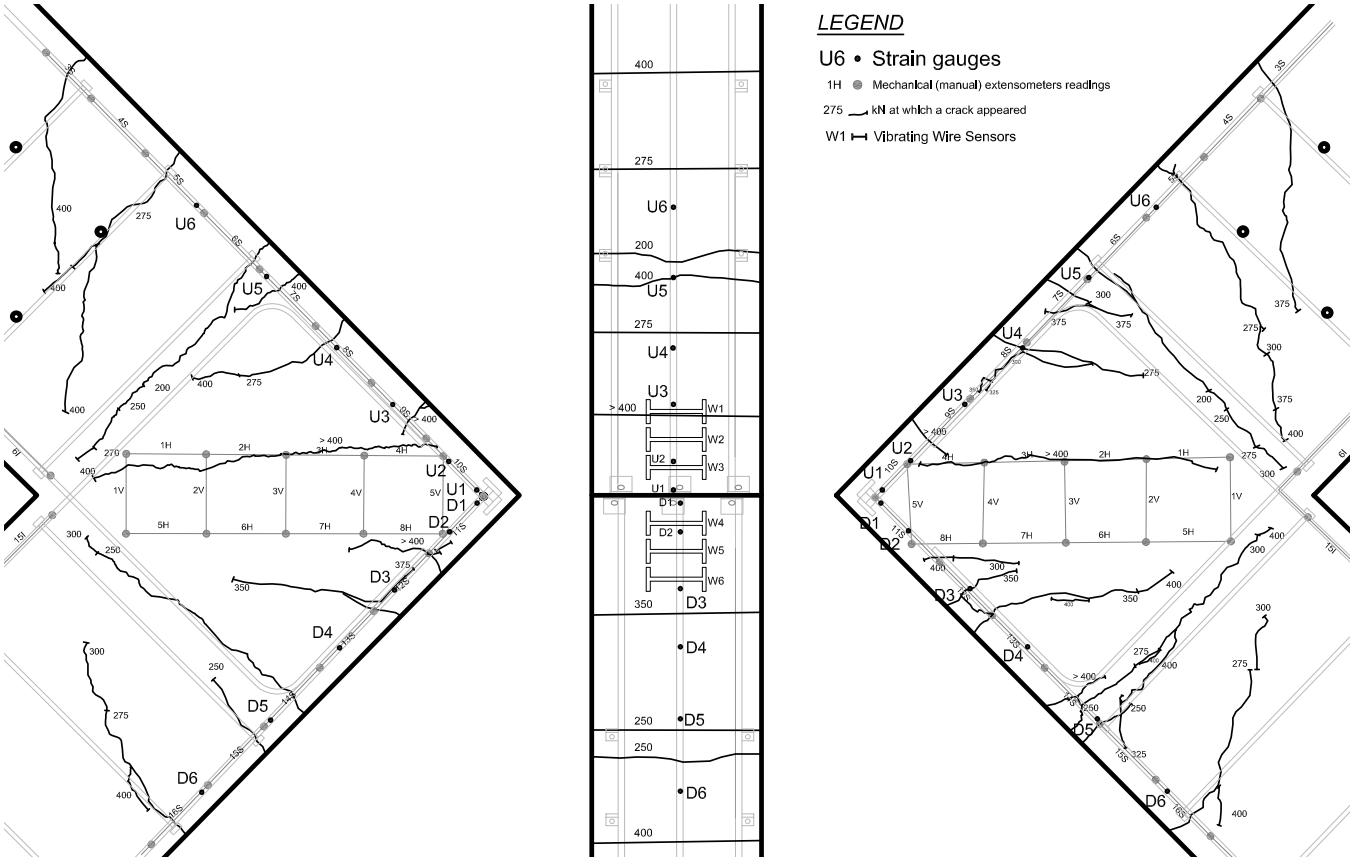

Figure D.7: 25-TH-16. Crack pattern before failure. From left to right: front view (A), side view, front view (B)

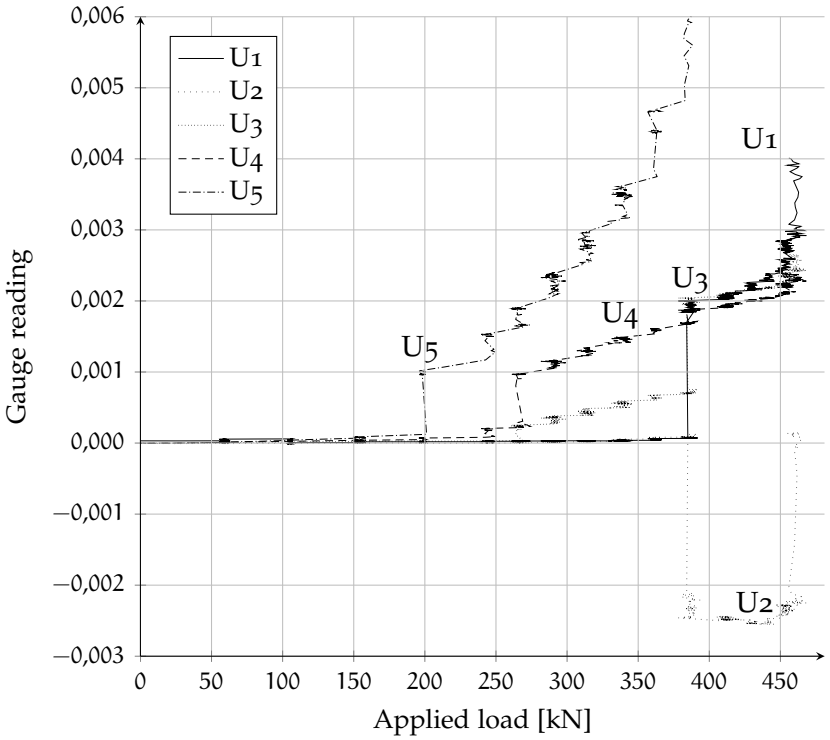

Figure D.8: 25-TH-16. Gauge readings (U)

D.1.6 Strain gauges

The first flexural crack was located in the adjoining members near to the core, while the last cracks developed within the joint. This sequence is corroborated, for instance, by the gauge reading number 5, which is the first that reaches a high strain, as can be observed in Figures D.8–D.9.

The appearance of a crack usually implies a sudden increase in the stress measured by the gauge, although on some occasions the stress in a given gauge may even be reduced by the growth of nearby cracks.

Signal from gauge U6 was lost at the beginning. Yielding of the bar occurred close to the head, since the first gage from the head face (Gauge U1) reached a maximum strain of 4‰.

D.1.7 Compression Strut

The positioning of the targets was found not to be satisfactory because they did not fully cover the zone where diagonal cracks can develop. In this specimen a crack developed partly outside of the measuring length. For this reason the measurement area was extended in the following tests by adding an extra line of measurement bases.

The recorded compressive strain should be maximum in the strut axis. Most measurements provide, as expected, tensile strains in the

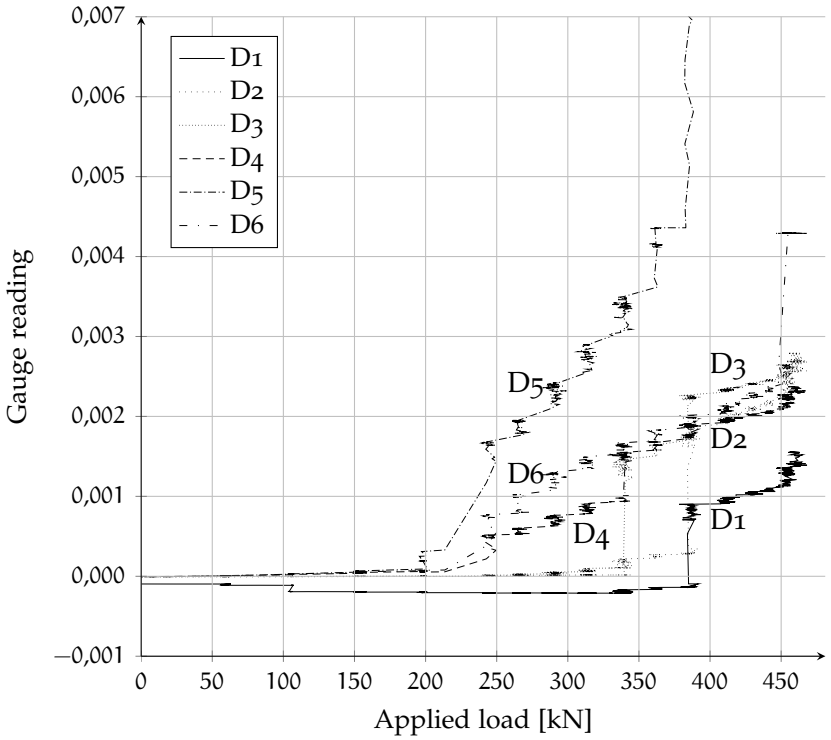

Figure D.9: 25-TH-16. Gauge readings (D)

V series and compressive strains in the H series (see Figure D.10), with a maximum compressive strain of −221 με in 1H (A side)[4].

D.1.8 Vibrating Wire Strain Gauges

The vibrating wire sensors are often used for embedded or surface strain measurements. The idea behind their placement was to measure a lateral strain originated by the presence of bursting forces acting along the bar axis.

Many wires recorded a null strain up to the failure: only the W2 wire reading was significant, however, only compressive strains were recorded (see Figure D.11). This can be attributed either to the greater influence of the two surrounding plates, or, more likely, to the presence of a crack that would have distorted the measurement (see Figure D.12).

D.1.9 Head slip

The measured slip of the central heads was almost null during the test, with the only exception consisting in a 0,04 mm slip of the lower

[4]All values reported here correspond to the last manual measurement taken, with an applied load of 325 kN

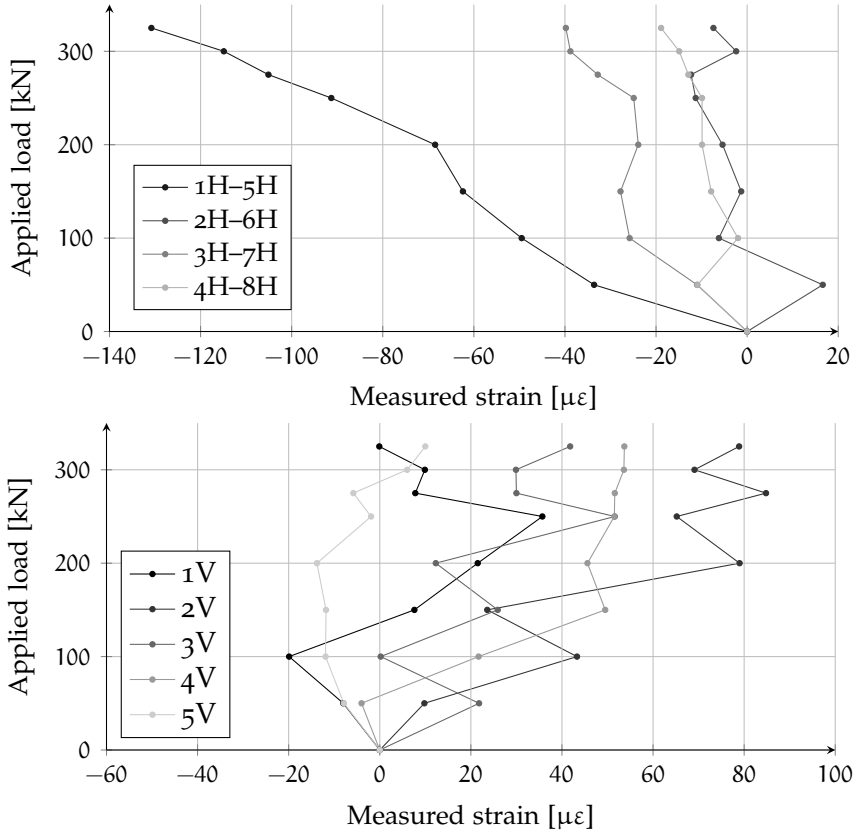

Figure D.10: 25-TH-16. Average (A and B sides) measured strains compared to the applied load. Horizontal symmetrical chords have been further averaged

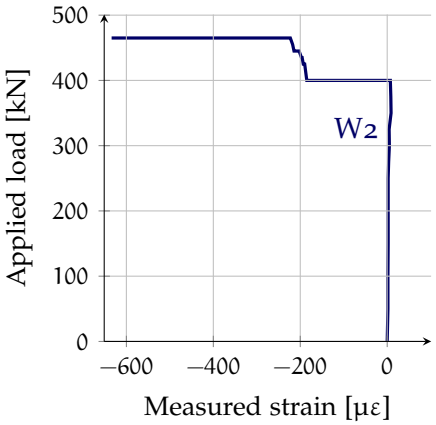

Figure D.11: 25-TH-16. Vibrating wire W2

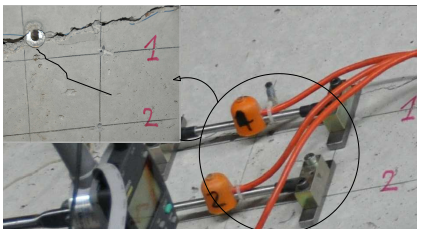

Figure D.12: Vibrating wires area

fleximeter in the last 30 seconds before failure. Readings were taken every 5 seconds.

This observation is in accordance with Figures D.8–D.9, since in proximity of the anchorage plate higher strains have been measured in the lower gauges (D series) only with high load levels.

As reported by Thompson "For the smaller head sizes [...] some bars [...] did not slip until failure was imminent". Thus, this cannot be considered as a questionable data. On the contrary, the absence of a relative slip can be regarded as the evidence of the good health of the anchorage.

D.2 SPECIMEN 25-TH-25

This specimen was the second to be tested. Since the concrete still had not reached the design compressive strength, it was agreed to wait one week more than the time strictly needed for the test preparation.

The day before the test — 52 days after concrete pouring — two concrete cylinders were tested: the mean compressive strength was 20.3 MPa, although the mean compressive strength of the concrete batch was more likely around 23,5 MPa (see Section 5.2.1.2).

D.2.1 General behavior

Some days before the test an incidence occurred during the handling of the specimen, which suffered an impact with the ground after falling from its intermediate position during the lifting, due to the rupture of the lifting reinforcement. All specimens have been lifted up from the ground by the following procedure:

- The specimen is first lifted from only one point, using the reinforcement left embedded in one arm of the corner.
- After a 90 degree rotation, the eye-bolts are connected to ϕ20 mm bars and the specimen is lifted: due to the position of the lifting point with respect to the center of gravity, the specimen rotates automatically in search for the equilibrium position, approaching itself to the position where it will be fixed for the execution of the test.

The specimen presented cracking of the bottom and both sides of one of the adjoining members. All cracks resulting from this event were marked as "0", as shown in Figure D.13.

Again, the test execution was regular: the applied load was incremented step by step (see Table D.2) and manual measurements were taken in each step. Once a load of 700 kN was reached no measurements were taken close to the specimen for safety reasons.

The state of cracking induced by the impact with the ground affected the crack development on the upper part of the specimen, which was confused especially on side B, where, instead of a *first crack*, a progressive widening and branching of pre-existing cracks was observed. On the lower part of the specimen, A and B sides were more similar, with the first crack observed at a load of 200 kN.

Bond-related cracks appeared at a load of 400 kN and progressed until 600 kN, while the crack parallel to the central strut developed at a load between 500 and 600 kN. The maximum available load was not sufficient to reach a complete rupture of the specimen, however, a state of extensive cracking was reached and the gauge closest to the plate measured a strain larger than 5‰. After the maximum available load was reached, four load cycles were applied to increase damage.

(a) *Left side* **(b)** *Right side*

Figure D.13: 25TH25. Cracking due to the impact on the ground

As for the previous specimen, double headed reinforcement and anchorage plates did not show any sign of weakening during the test.

Step	Load [kN]	Notes
1	100	
2	200	First flexural crack
3	300	
4	400	Formation of bond-related cracks
5	500	Formation of cracks parallel to the central strut
6	550	
7	600	
8	650	
9	700	
10	750	
11	800	
12	850	
13	900	
14	933	Capacity of loading system is reached
15	–	Four cycles 200-933 kN to increase damage

Table D.2: 25-TH-25. Load steps

D.2.2 Load-displacement

The load-displacement graphs in Figure D.14 represent the vertical displacement of the load application point during the test and the horizontal displacement measured by the probe indicator versus the applied load, although in the latter case the experimental series stops earlier for safety concerns. Unloading-loading cycles aimed at increasing damage once the maximum capacity of the jack was reached.

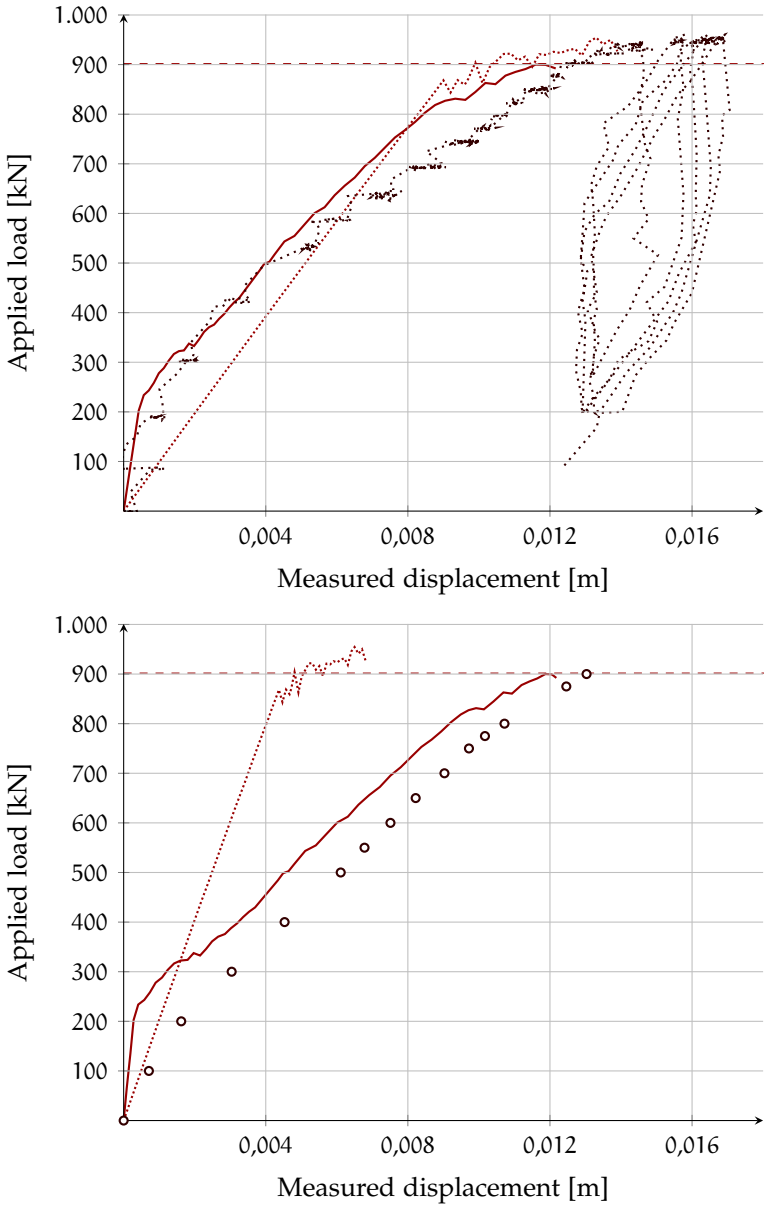

Figure D.14: Vertical displacement of the load application point (up) and horizontal displacement measured by the probe indicator (down). Experimental data (·····)(··) and predictions by sectional analysis (- - -), non–linear analysis (·····) and ATENA (——)

D.2.3 Load-rotation

A small rigid rotation of approximately $4{,}0 \cdot 10^{-6}$ rad/kN was observed during the test. The results presented in Figure D.15 are compensated to take this rotation into account. As can be seen, there is still some asymmetry in the graph, probably due to the lower stifness of the upper arm, consequence of the pre-existent state of cracking.

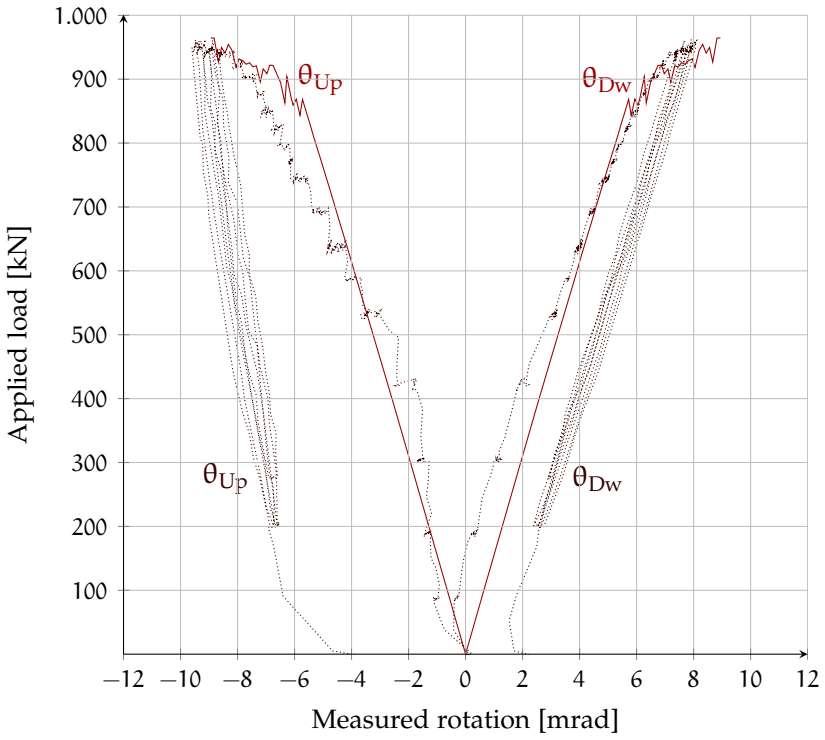

Figure D.15: Applied load Vs measured rotations.
In solid line, the non linear theoretical estimation

D.2.4 Moment-curvature

The experimental moment-curvature for some sections (see Figure 5.13) is shown in Figure D.16.

The experimental curvatures are calculated, for each section, as the substraction of strains measured by targets on the reinforcement axes in that section divided by the distance between the two lines[5]; the experimental moments are computed as the force perpendicular to the beam axis multiplied by the distance of the segment axis to the point of application of the load (1,075 m for sections 6-15 and 0,875 m for sections 5-16).

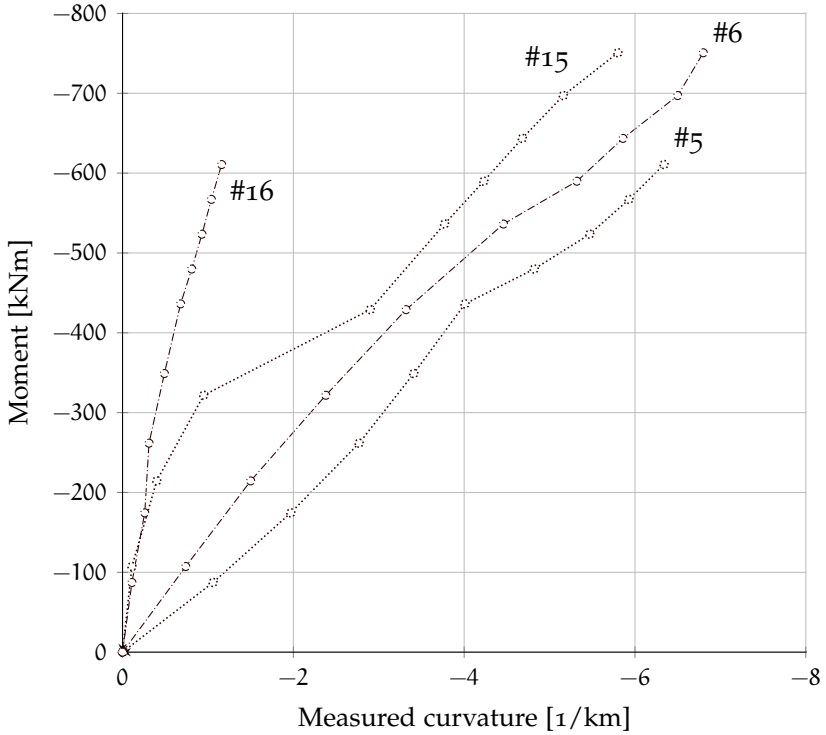

Figure D.16: 25-TH-25. Average (side A and B) measured M–χ diagram for some relevant sections compared to the theoretical prediction

D.2.5 Crack pattern

Crack evolution described in Section D.2.1 is carefully reproduced in Figure D.18, where the position of the mechanical strain gauges is also represented.

The serviceability load can be estimated as a percentage of the ultimate load. If it is assumed $G_k = Q_k$:

$$F_{SLS} = \frac{(1{,}0 + 0{,}3)}{(1{,}35 + 1{,}5)} F_{ULS} \simeq 0{,}46\ F_{ULS} = 411\ \text{kN}$$

[5] $1/r = \frac{\varepsilon_s - \varepsilon_i}{d - 2d'}$

At the top of Figure D.6 is shown the measured crack width compared to the applied load, while at the bottom is provided the measured crack width compared to the theoretical steel stress, calculated at the middle of each segment.

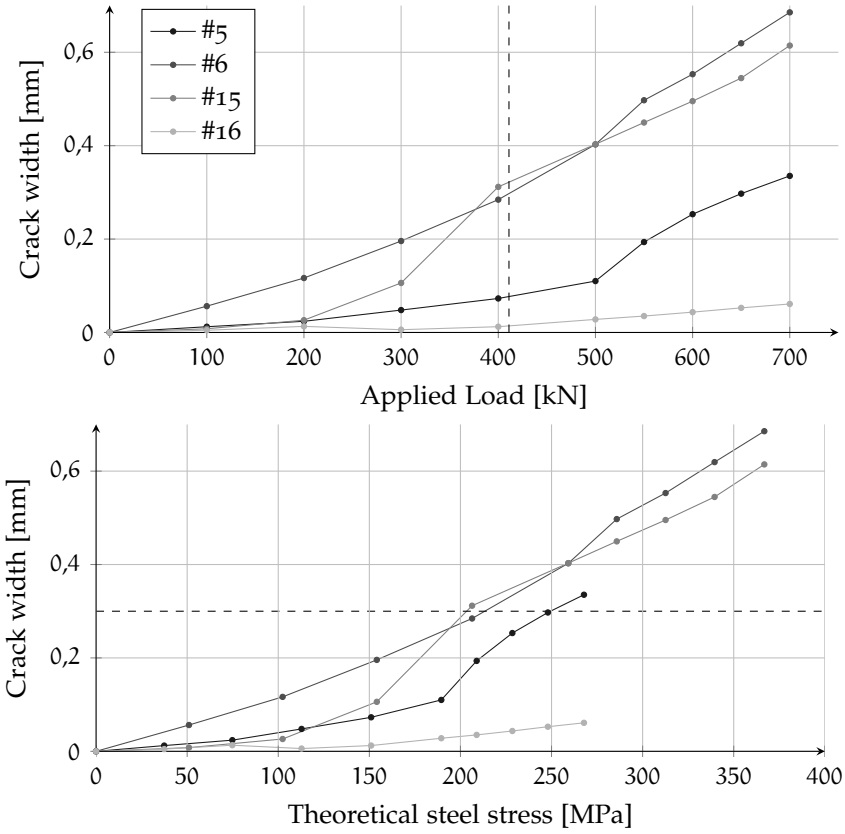

Figure D.17: 25-TH-25. Average (A and B sides) of measured crack width as a function of the applied load (top) and theoretical steel stress (bottom). The serviceability load and a crack width reference value of 0,3 mm are represented in dashed lines

D.2.6 Strain gauges

Crack opening occurred gradually in the upper part of the specimen, due to the handling incidence (see Section D.2.1). At a load of 500 kN, the stress rose in gauges U1-U2-U3 as a consequence of crack opening, while gauges U4-U5-U6 recorded a gradual increment throughout the test.

Again, the first flexural crack is located between the core and the adjoining members, while the last cracks developed within the joint.

At the ultimate load, the D2 gauge measured a strain of 1,5‰, while D1, U1 and U2 gauges recorded strains higher than 2,5‰.

Therefore, it can be stated the reinforcement yielded almost certainly in the first centimeters from the anchorage plate: the ultimate

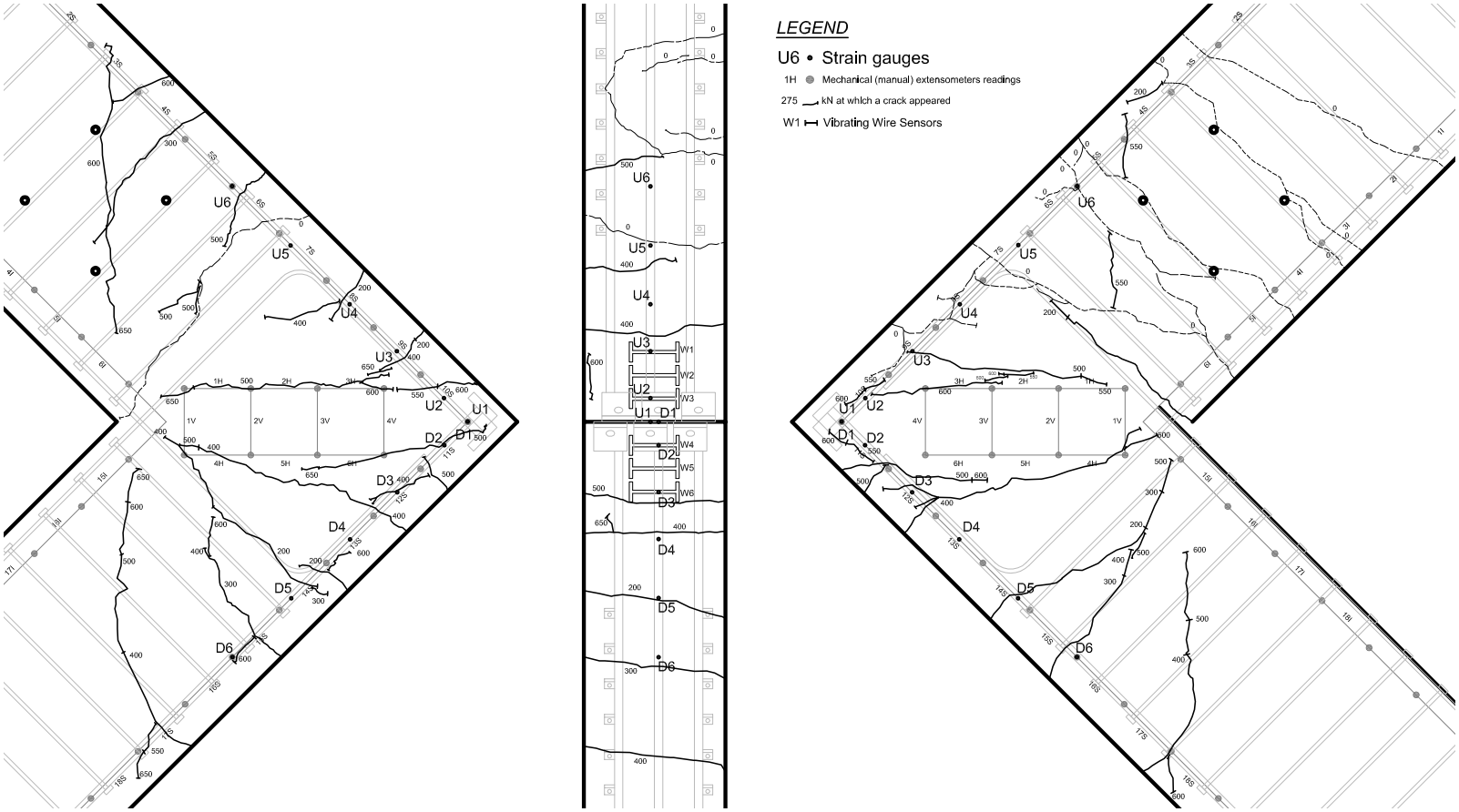

Figure D.18: 25-TH-25. Crack pattern at a load of 650 kN. From left to right: front view (A), side view, front view (B)

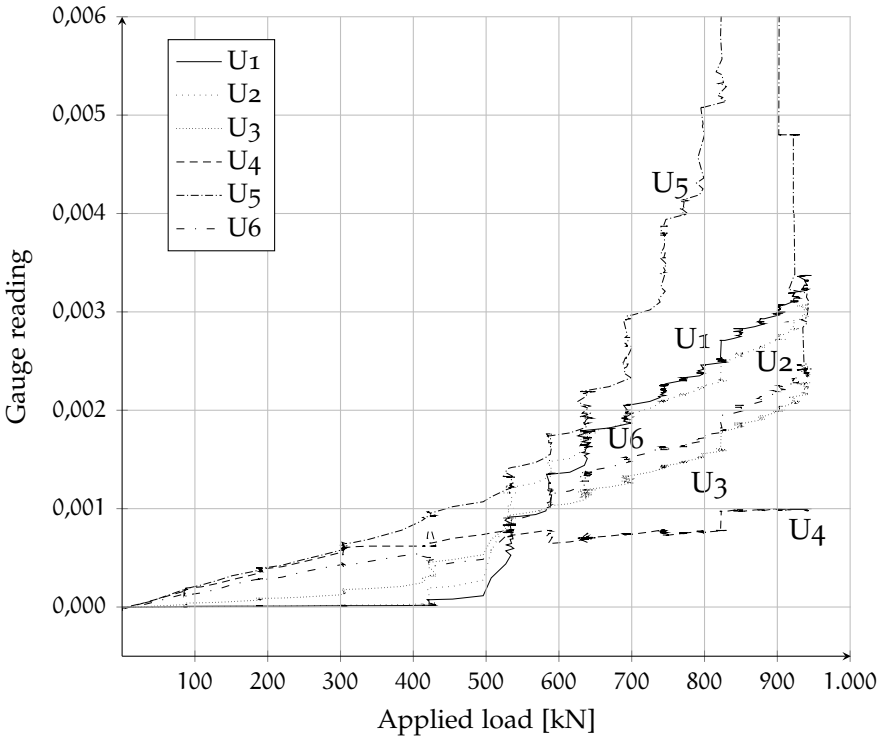

Figure D.19: 25-TH-25. Gauge readings (U)

limit states due to the loss of anchorage was not observed at this level of load.

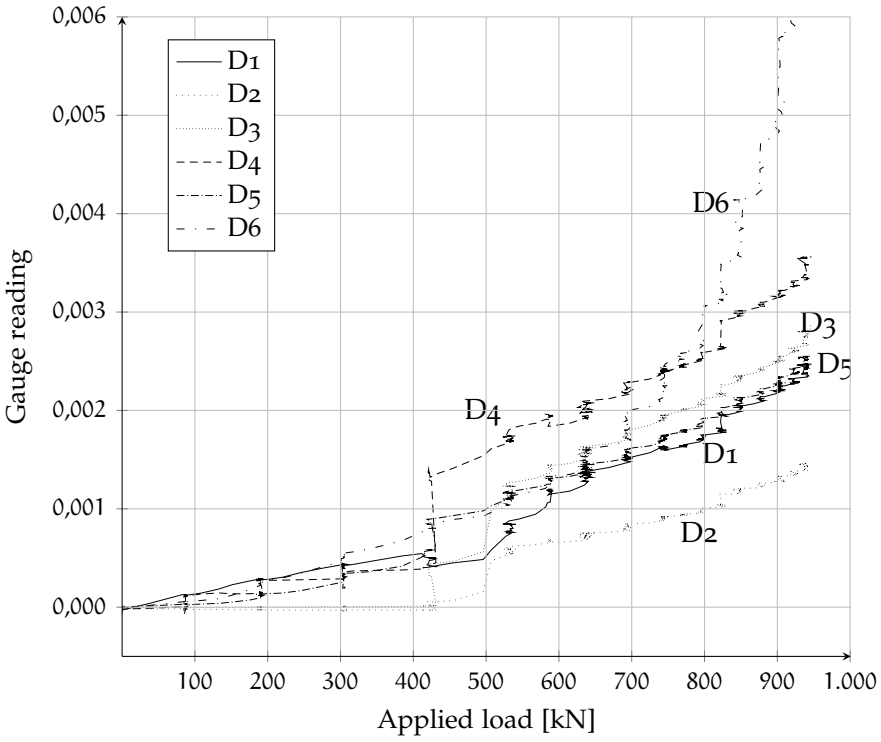

Figure D.20: 25-TH-25. Gauge readings (D)

D.2.6.1 *Hysteresis curves*

The same graph of the previous paragraph is reported in Figure D.21 for gauges 1 and 2 including the measurements during the cyclic loading[6]: gauge D1 measured a strain ranging between 1‰ and 2,5‰, while gauge U1 oscillated from 2‰ to 4‰.

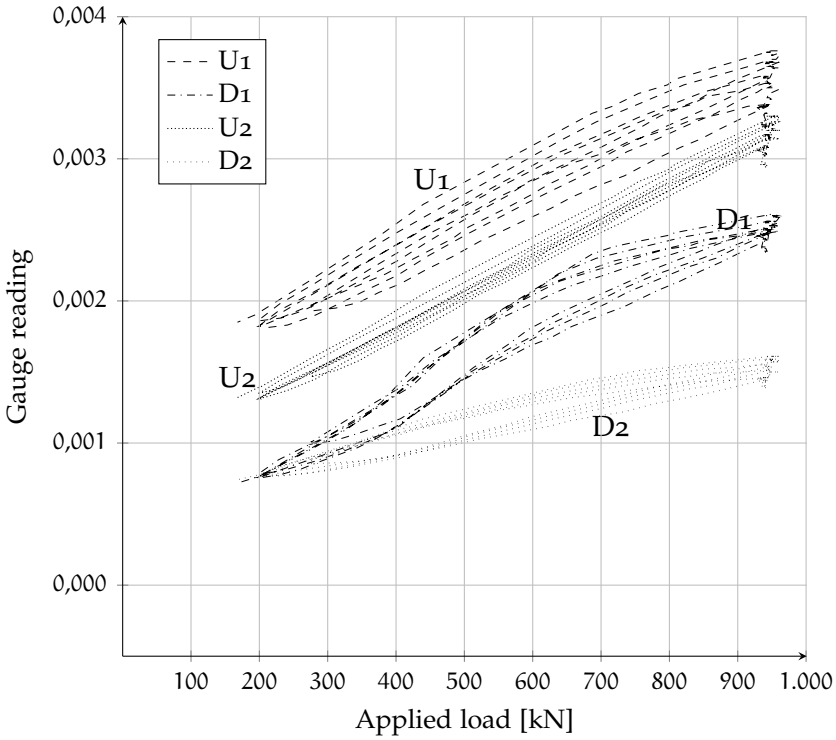

Figure D.21: 25-TH-25. Hysteresis curves for gauges 1 and 2

D.2.7 Compression Strut

The positioning of the targets was found not to be satisfactory because they did not fully cover the zone where diagonal cracks can develop. In this specimen a crack developed partly outside of the measuring length. For this reason the measurement area was extended in the following tests by adding an extra line of measurement bases.

The recorded compressive strain should be maximum in the strut axis. Most measurements provide, as expected, tensile strains in the V series and compressive strains in the H series (see Figure D.22), with a maximum compressive strain of -717 $\mu\varepsilon$ in 6H (A side)[7].

[6] Loading-unloading cycles aimed at increase damage once the maximum capacity of the jack was reached.

[7] All values reported here correspond to the last manual measurement taken, with an applied load of 700 kN

Large cracks opened on A side, with a crack wider than 0,7 mm intercepting segments V2 and V4.[8]

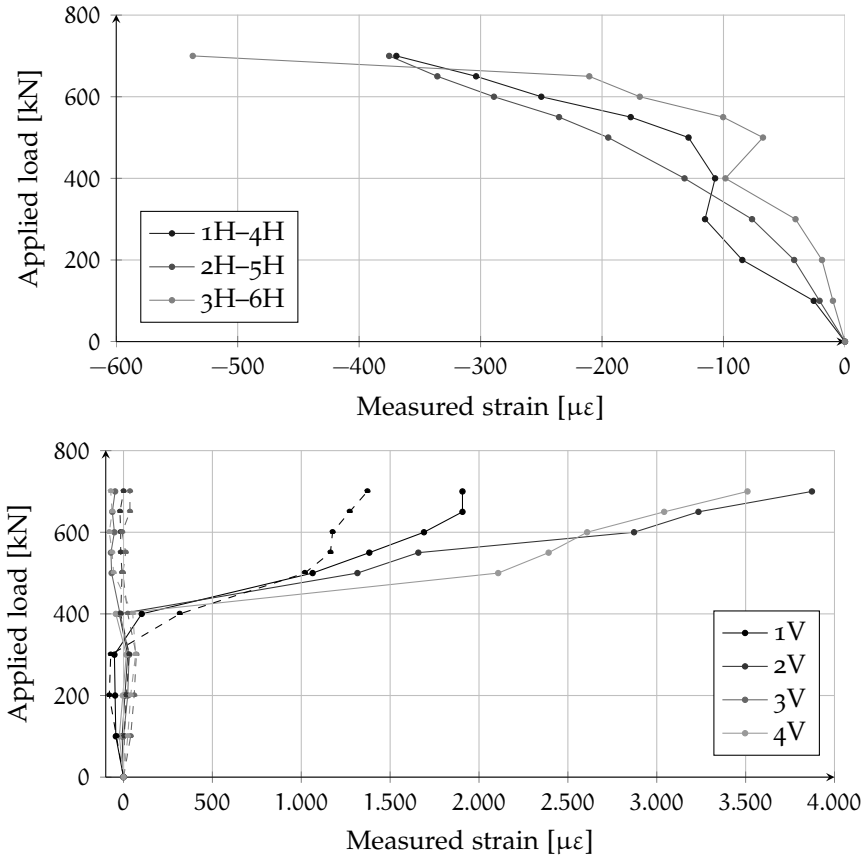

Figure D.22: 25-TH-25. Top: average (side A and B) measured strains compared to the applied load, symmetrical chords have been further averaged; Bottom: vertical measured strains compared to the applied load. In dashed lines values for B side

D.2.8 Vibrating wire strain gauges

In this specimen a lateral strain originated by the presence of bursting forces acting along the bar axis was observed.

All wires started to record a non-null strain from a load of 400 kN. The three wires placed on the lower side, the ones which measure the influence of the upper middle plate, recorded strains larger than 100 με (Figure D.23).

D.2.9 Head slip

The measured slip of the central head was null throughout the test in the upper fleximeter (LVDT 1), while the lower instrument (LVDT 2)

[8] The distance between measurement targets is 200 mm.

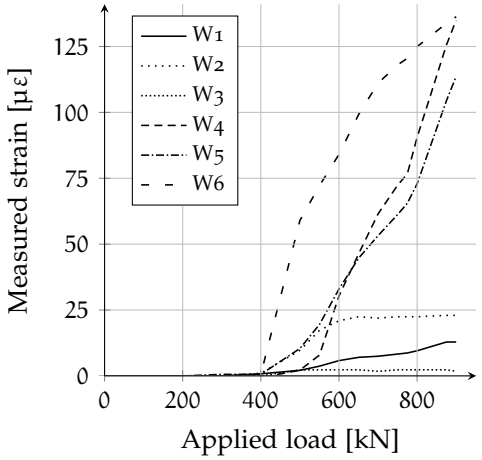

Figure D.23: 25-TH-25. Vibrating wires

recorded a maximum slip of 0,24 mm at the end of the 4th loading cycle, as shown in Figure D.24 .

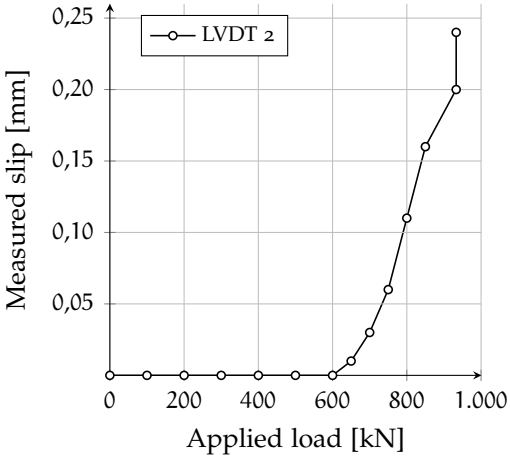

Figure D.24: 25-TH-25. Head slip

These measurements are in accordance with Figures D.19–D.20, since in proximity of the anchorage plate, higher stresses have been measured in the upper strain gauges (U series).

D.3 SPECIMEN 25-CV-16

The test took place 59 days after concrete pouring. The day before the test 3 concrete cylinders were tested: the mean compressive strength was 22,7 MPa, although the mean compressive strength of the concrete batch was at that time more likely around 23,7 MPa (see Section 5.2.1.2).

D.3.1 General behavior

The test execution was fluid, without significant problems. The starting position was soon stabilized and the safety straps were loosened: the applied load was incremented step by step (see Table D.3) and manual measurements were taken at each step. Once a load of 350 kN was reached no measurements were taken close to the specimen for safety reasons.

Step	Load [kN]	Notes
1	50	
2	100	
3	150	First flexural crack
4	200	Formation and growth of flexural cracks
5	250	
6	275	
7	300	
8	325	Formation of cracks parallel to the central strut
9	350	
10	375	
11	400	
12	425	
13	450	
14	475	
15	485	

Table D.3: 25-CV-16. Load steps

The first flexural crack was observed at the 150 kN load step. Other cracks soon developed nearby between 150 and 200 kN, while bond-related cracks (parallel to the rebars) started developing at 325 kN, the same load at which the first cracks along the central strut formed.

Subsequent increases in load resulted in cracks widening, anticipating the final failure due to the excessive strain in the reinforcement, which occurred at a load of 485 kN (see Figure D.25).

D.3.2 Load-displacement

The load-displacement graphs presented in Figure D.26 represent the vertical displacement of the load application point during the test

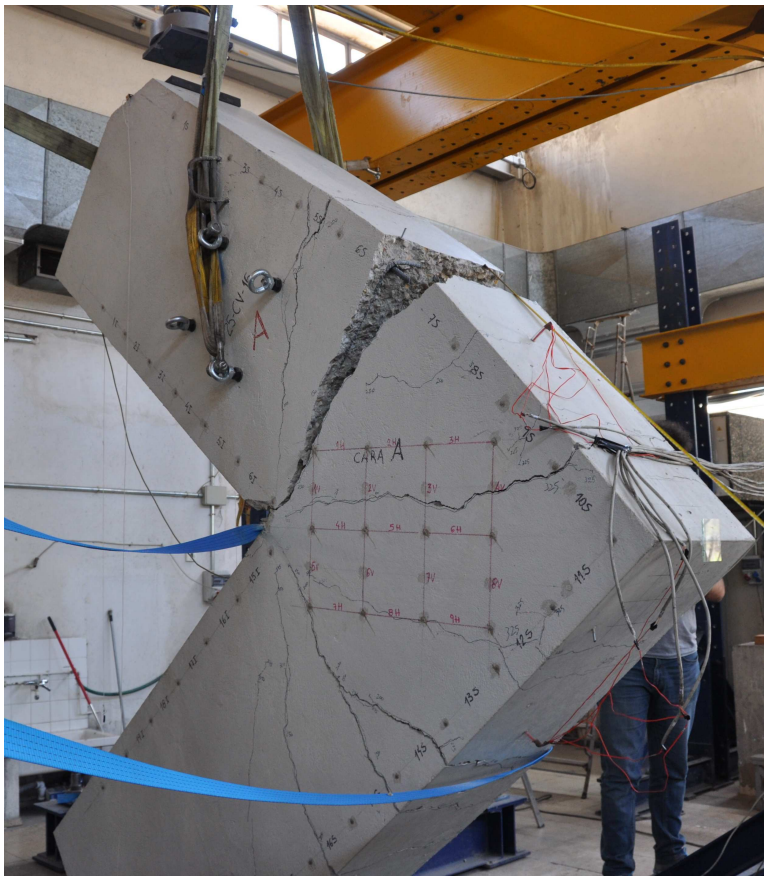

Figure D.25: The final configuration after failure: a rupture of the tensile reinforcement was observed (see also Figure D.1)

and the horizontal displacement measured by the probe indicator, although in this case the experimental series stops earlier for safety concerns.

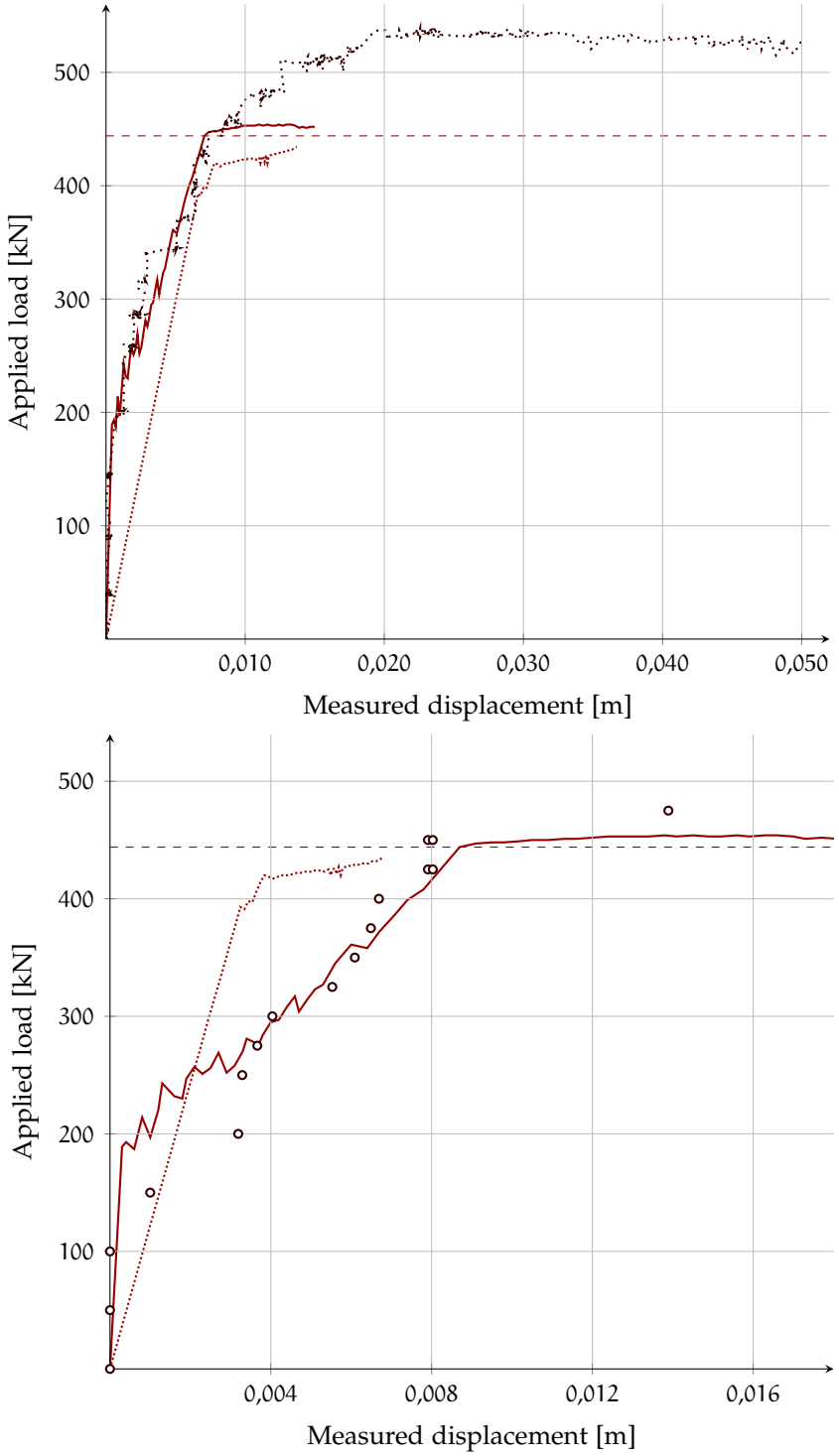

Figure D.26: Vertical displacement of the load application point (up) and horizontal displacement measured by the probe indicator (down). Experimental data (·····)(··) and predictions by sectional analysis (- - -), non–linear analysis (·····) and ATENA (——)

D.3.3 Load-rotation

No clear signs of rigid rotations were observed in this test. The measured results are reported in Figure D.27

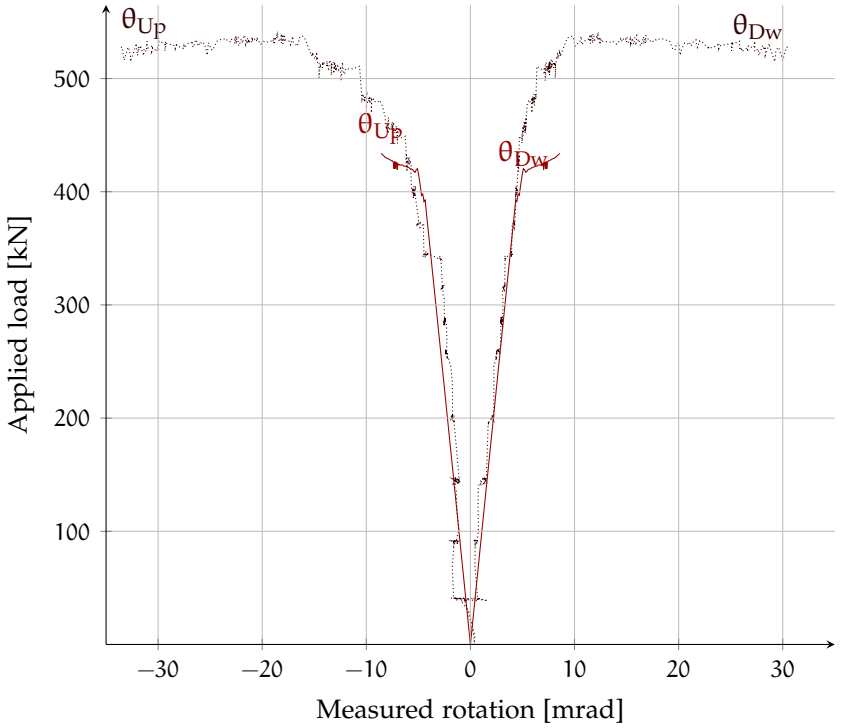

Figure D.27: Applied load Vs measured rotations.
In solid line, the non linear theoretical estimation

D.3.4 Moment-curvature

The experimental moment-curvature for some sections (see Figure 5.13) is shown in Figure D.28.

The experimental curvatures are calculated, for each section, as the substraction of strains measured by targets on the reinforcement axes in that section divided by the distance between the two lines[9]; the experimental moments are computed as the force perpendicular to the beam axis multiplied by the distance of the segment axis to the point of application of the load (1,075 m for sections 6-15 and 0,875 m for sections 5-16).

[9] $1/r = \frac{\varepsilon_s - \varepsilon_i}{d - 2d'}$

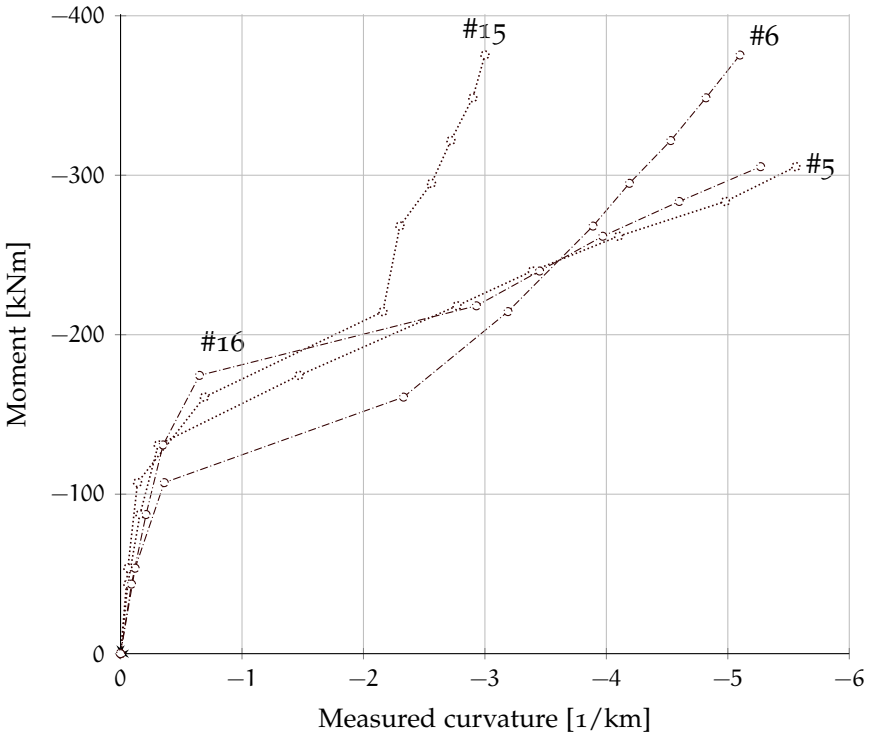

Figure D.28: 25-CV-16. Average (side A and B) measured M–χ diagram for some relevant sections compared to the theoretical prediction

D.3.5 Crack pattern

Crack evolution described in Section D.3.1 is carefully reproduced in Figure D.30, where the position of the mechanical strain gauges is also represented.

At the top of Figure D.29 is shown the measured crack width compared to the applied load, while at the bottom is provided the measured crack width compared to the theoretical steel stress, calculated at the middle of each segment.

D.3.6 Strain gauges

A very similar behavior was observed in both upper and lower part of the specimen. The first flexural crack is located between the core and the adjoining members, while the last cracks developed within the joint. This sequence is corroborated, for instance, by the U5 gauge reading, which is the first with a jump in strain, occurring at a load of 150 kN. Gauges U6 and U4 follow at a load of 200 kN, while the last two ones start recording significant strains at a load of 350 kN. Strains higher than 2,5‰were recorded in all gauges, as shown in Figures D.31–D.32.

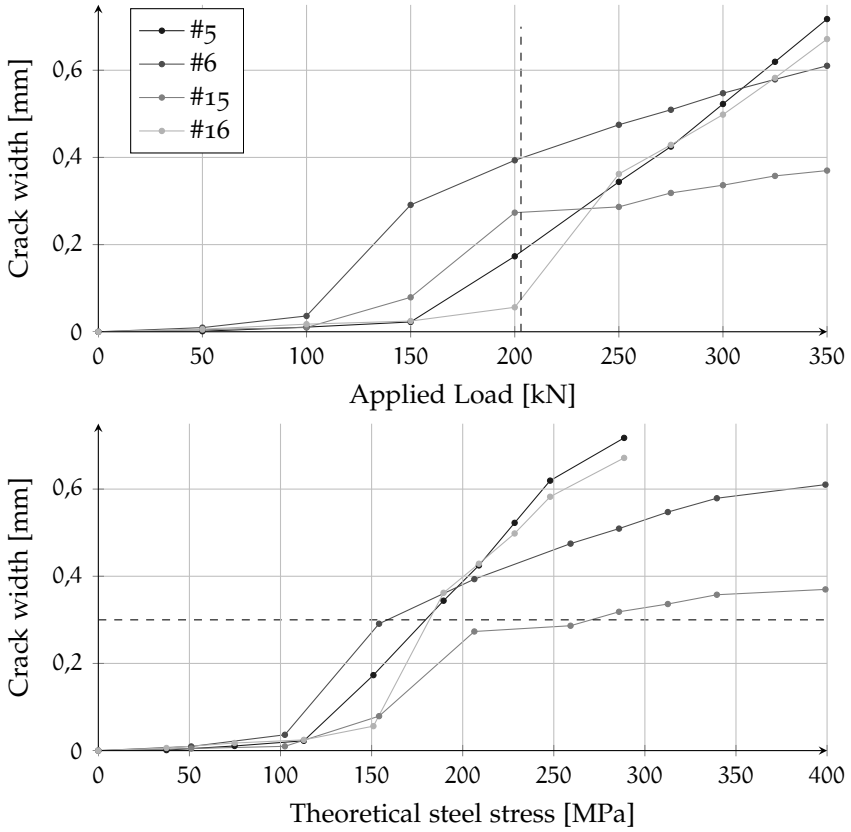

Figure D.29: 25-CV-16. Average (A and B sides) of measured crack width as a function of the applied load (top) and theoretical steel stress (bottom). The serviceability load and a crack width reference value of 0,3 mm are represented in dashed lines

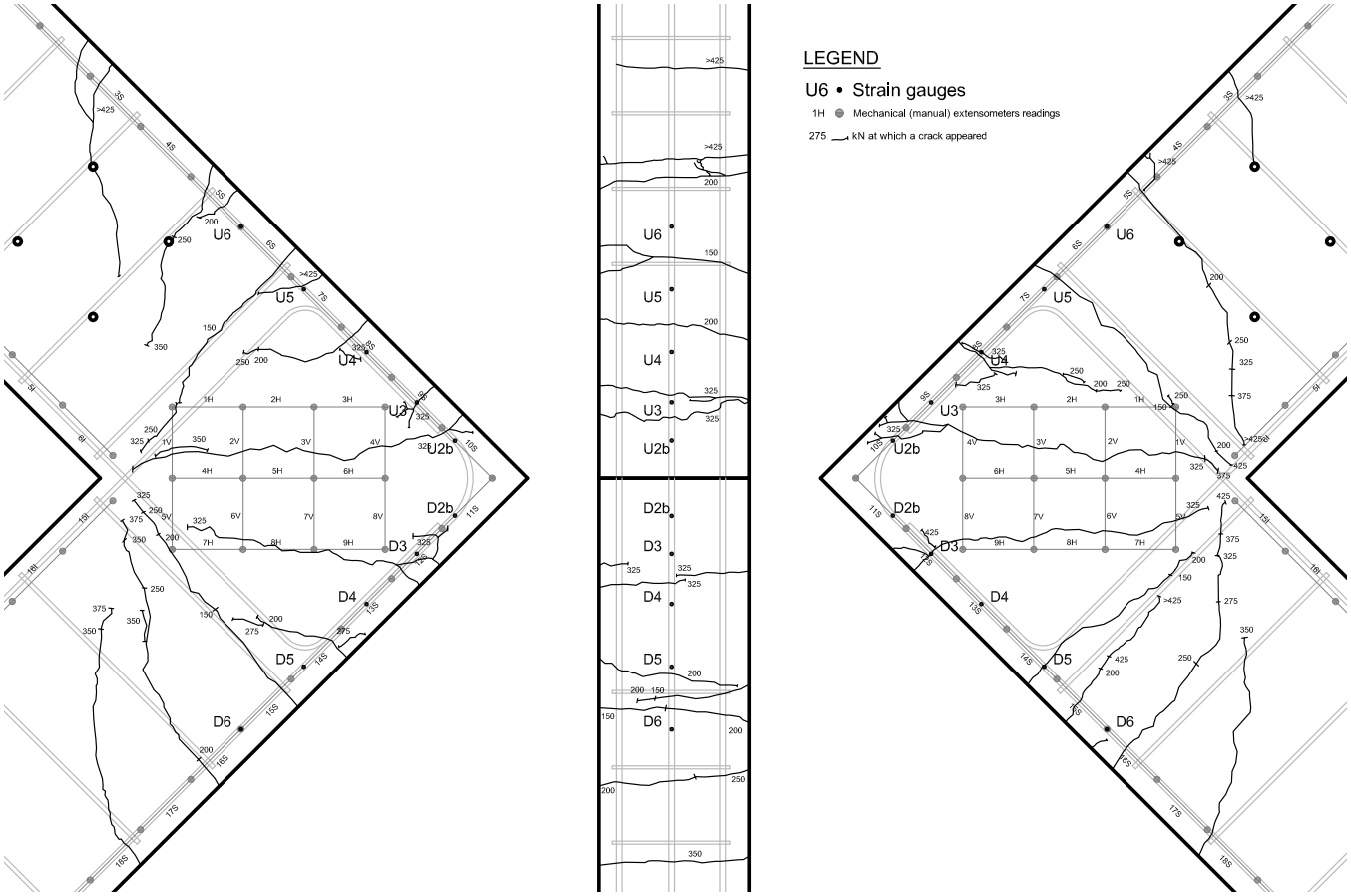

Figure D.30: 25-CV-16. Crack pattern before failure. From left to right: front view (A), side view, front view (B)

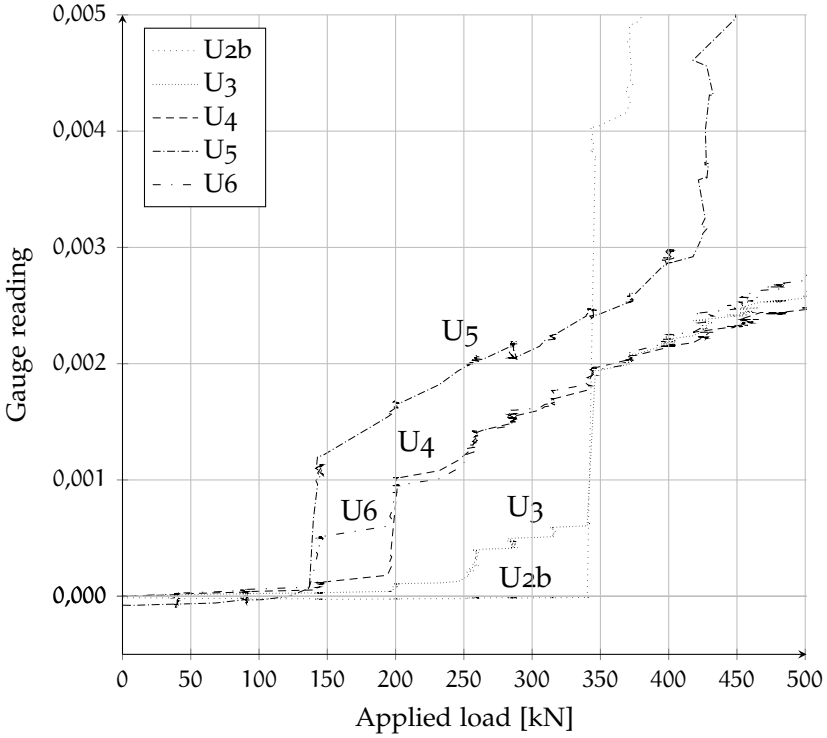

Figure D.31: 25-CV-16. Gauge readings (U)

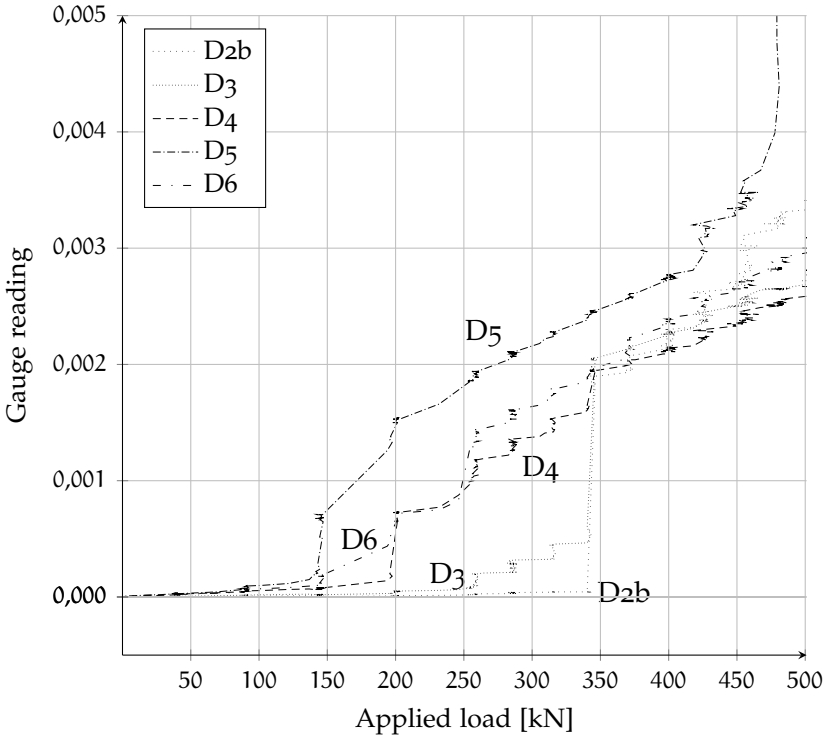

Figure D.32: 25-CV-16. Gauge readings (D)

D.3.7 Compression Strut

The positioning of the targets was changed with respect to previously tested specimens. However, measurements were not taken at segments 5V and 7H (B side) due to the presence of a safety straps.

The measured compressive strain was maximum in the strut axis (segments from 4H to 6H), where the mean compressive strain was around −300 με, with a maximum in segment H4 (−380 με; −330 με respectively on A side and B side). On the A side, a crack intercepts segments V1 to V4 and V6, while on B side two cracks intercept all segments. The wider cracks were measured on the outer edge (4V, 8V). Full data are reported in Figure D.33–D.34.

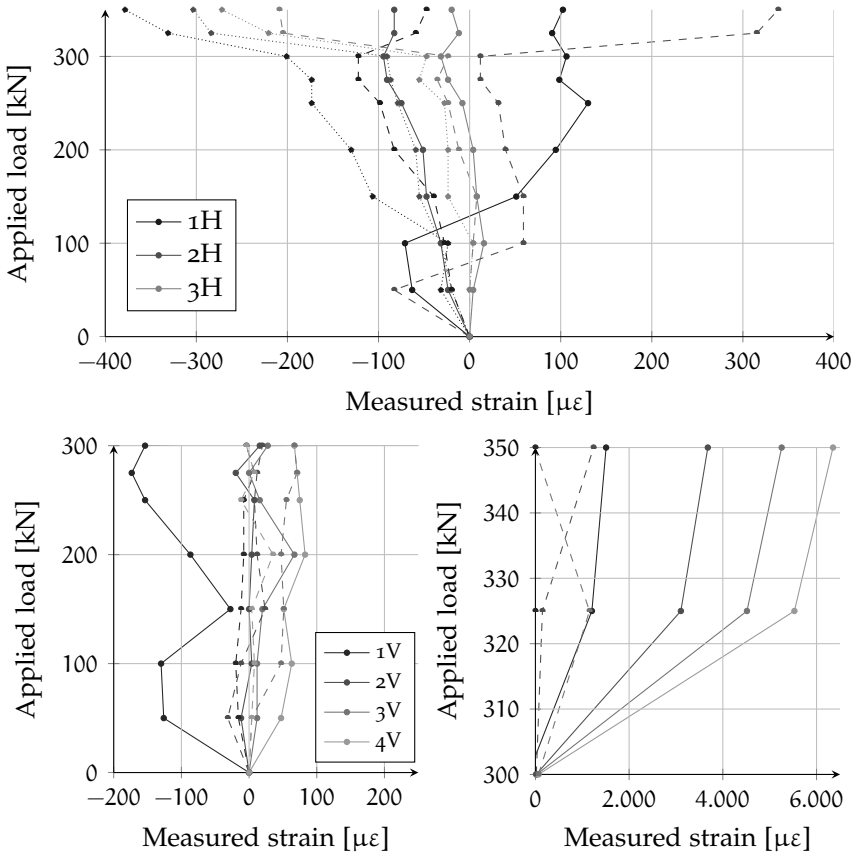

Figure D.33: 25-CV-16 – A side. Top: measured horizontal strains compared to the applied load. In dotted lines values for segments 4H to 6H, in dashed lines values for segments 7H to 9H; Bottom: vertical measured strains compared to the applied load. In dashed lines values for segments 5V to 8V

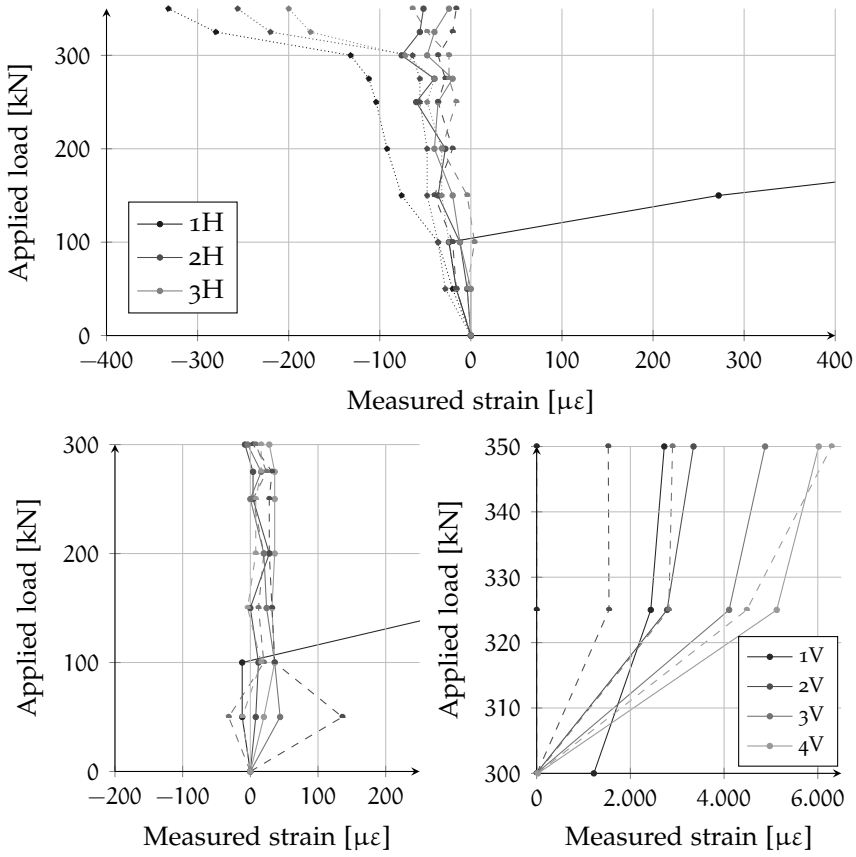

Figure D.34: 25-CV-16 – B side. Top: measured horizontal strains compared to the applied load. In dotted lines values for segments 4H to 6H, in dashed lines values for segments 7H to 9H; Bottom: vertical measured strains compared to the applied load. In dashed lines values for segments 5V to 8V

D.4 SPECIMEN 25-CV-25

The test took place 66 days after concrete pouring. The day before the test 3 concrete cylinders were tested: the mean compressive strength was 24,4 MPa (see Section 5.2.1.2 for complete data).

D.4.1 General behavior

The test execution was fluid, without incidents. The starting position was soon stabilized and the safety straps were loosened: the applied load was incremented step by step (see Table D.4) and manual measurements were taken on each step. Once a load of 800 kN was reached no measurements were taken close to the specimen for safety reasons.

The first flexural crack was observed at the 200 kN load step. Other flexural cracks soon developed nearby between 300 and 400 kN, while bond-related cracks (parallel to the rebars) started developing at 400 kN. The first cracks along the central strut formed at 500 kN. Subsequent increases in load resulted in cracks widening and branching.

The maximum available load was not sufficient to reach a complete rupture of the specimen, however, a state of extensive cracking of concrete and yielding of reinforcement was reached. After the maximum available load was reached, four load cycles were applied to increase damage. The gauge closest to the hook measured a strain larger than 5‰.

Step	Load [kN]	Notes
0	0	
1	100	
2	200	First flexural crack
3	300	
4	400	Formation of bond-related cracks
5	500	Formation of cracks parallel to the central strut
6	600	
7	700	
8	800	
9	850	
10	900	
11	933	Capacity of loading system is reached
12	–	Four cycles 400-933 kN to increase damage

Table D.4: 25-CV-25. Load steps

D.4.2 Load-displacement

The load-displacement graphs in Figure D.35 represent the vertical displacement of the load application point during the test and the horizontal displacement measured by the probe indicator versus the applied load, although in the latter case the experimental series stops earlier for safety concerns. Unloading-loading cycles aimed at increasing damage once the maximum capacity of the jack was reached.

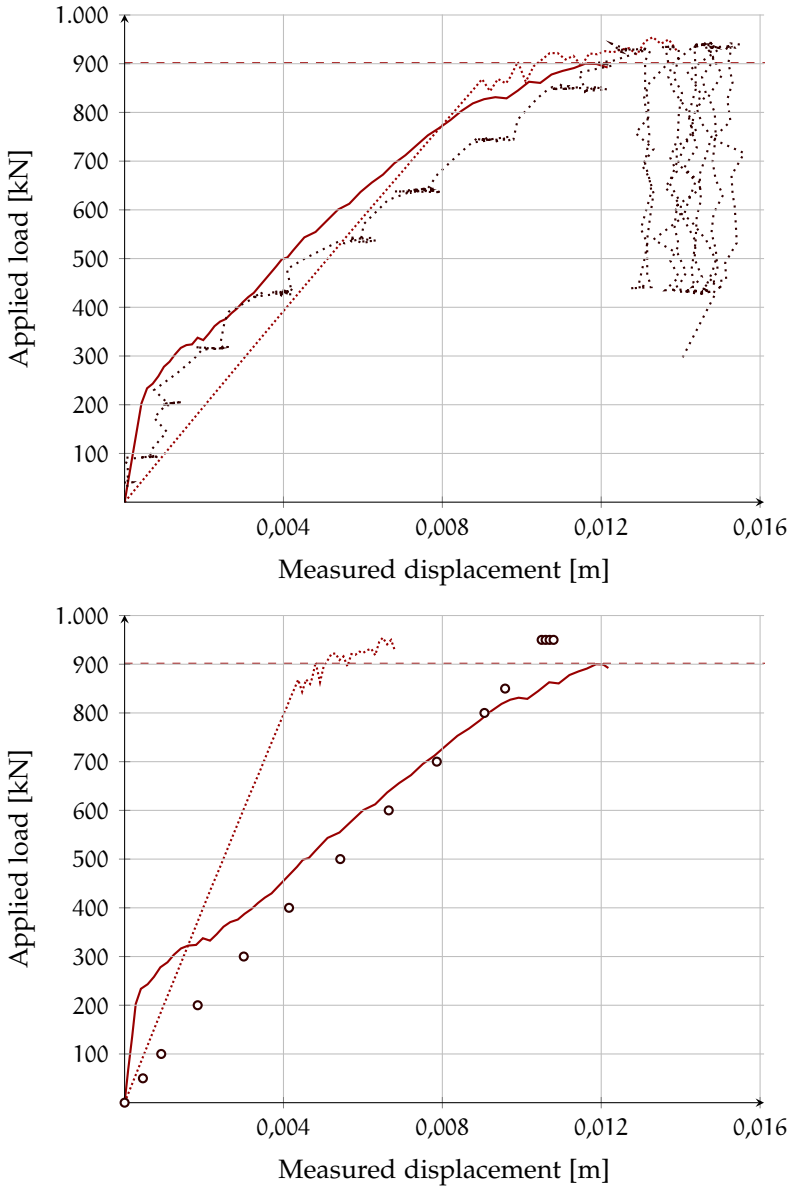

Figure D.35: Vertical displacement of the load application point (up) and horizontal displacement measured by the probe indicator (down). Experimental data (·····)(··) and predictions by sectional analysis (- - -), non–linear analysis (·····) and ATENA (——)

D.4.3 Load-rotation

The specimen experimented some movements in the first 100 kN. A small rigid rotation of 3,0 $\cdot 10^{-6}$ rad/kN was observed during the test. The results presented in Figure D.36 are compensated to take this rotation into account.

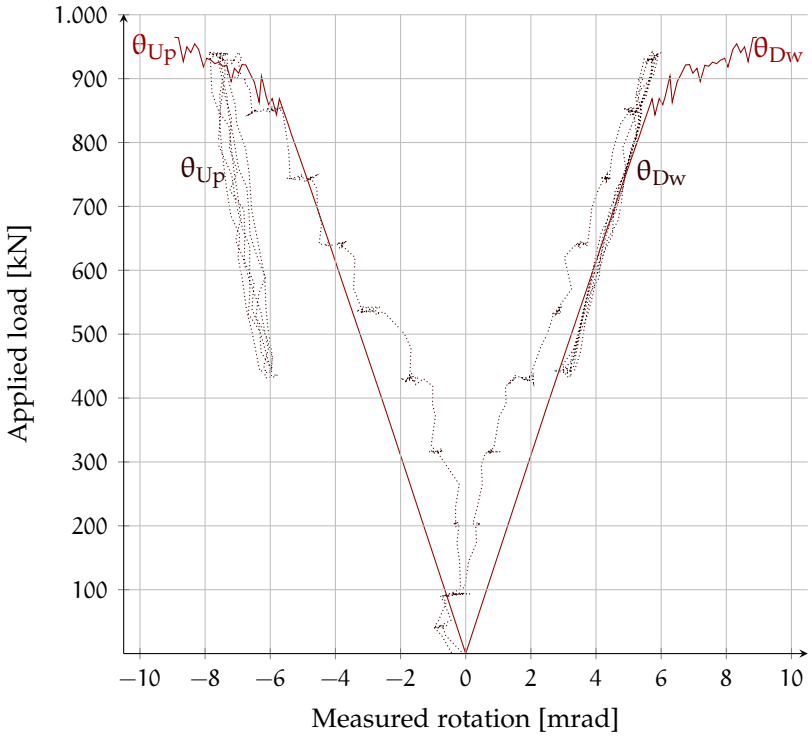

Figure D.36: Applied load Vs measured rotations.
In solid line, the non linear theoretical estimation

D.4.4 Moment-curvature

The experimental moment-curvature for some sections (see Figure 5.13) is shown in Figure D.37.

The experimental curvatures are calculated, for each section, as the substraction of strains measured by targets on the reinforcement axes in that section divided by the distance between the two lines[10]; the experimental moments are computed as the force perpendicular to the beam axis multiplied by the distance of the segment axis to the point of application of the load (1,075 m for sections 6-15 and 0,875 m for sections 5-16).

[10] $1/r = \frac{\varepsilon_s - \varepsilon_i}{d - 2d'}$

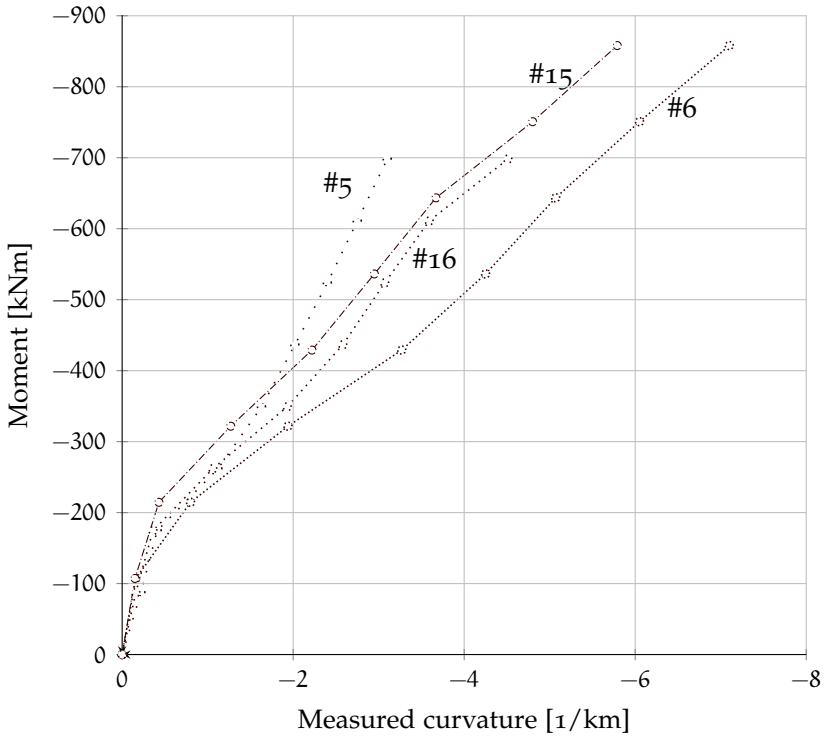

Figure D.37: 25-CV-25. Average (side A and B) measured M–χ diagram for some relevant sections compared to the theoretical prediction

D.4.5 Crack Pattern

Crack evolution described in Section D.4.1 is carefully reproduced in Figure D.39, where the position of the mechanical strain gauges is also represented.

At the top of Figure D.38 is shown the measured crack width compared to the applied load, while at the bottom is provided the measured crack width compared to the theoretical steel stress, calculated at the middle of each segment.

D.4.6 Strain gauges

The first flexural crack is located between the core and the adjoining members, while the last cracks developed within the joint. This sequence is corroborated, for instance, by the U5 gauge reading, which is the first that reaches a high strain: strains of up to 2‰were recorded in all gauges, as can be observed in Figures D.40–D.41.

A similar behavior was obserbed in both upper and lower part of the specimen. Gauge 5 is the one with the higher strain throughout the test, while gauges 4 and 6 start rising with a load between 200 and 300 kN. The last two gauges recorded a significant strain increase starting from 400 and 500 kN.

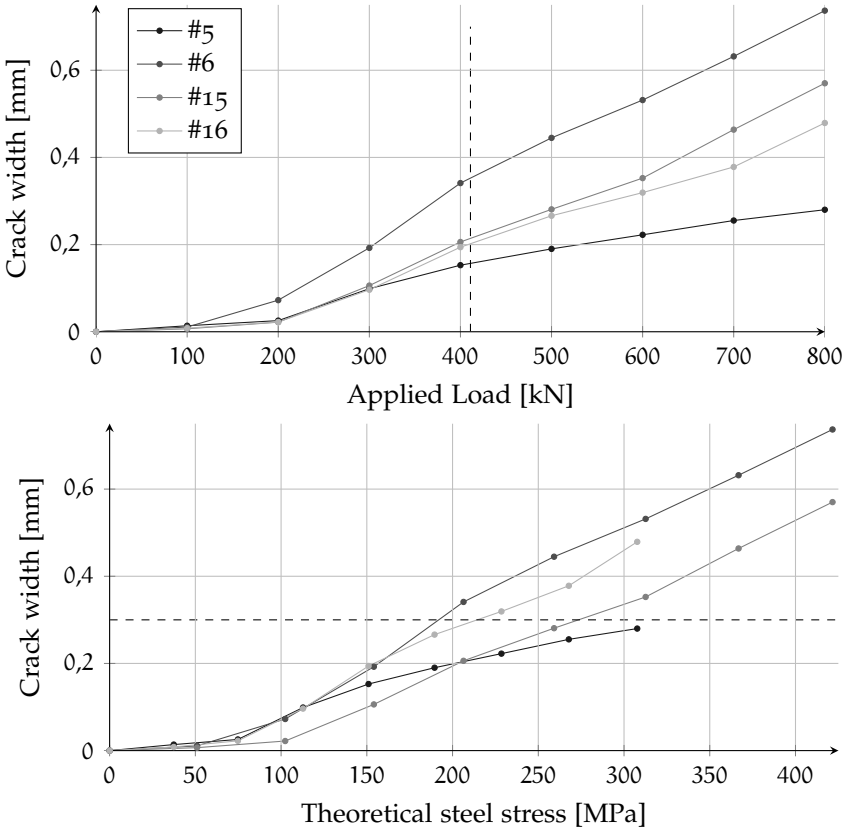

Figure D.38: 25-CV-25. Average (A and B sides) of measured crack width as a function of the applied load (top) and theoretical steel stress (bottom). The serviceability load and a crack width reference value of 0,3 mm are represented in dashed lines

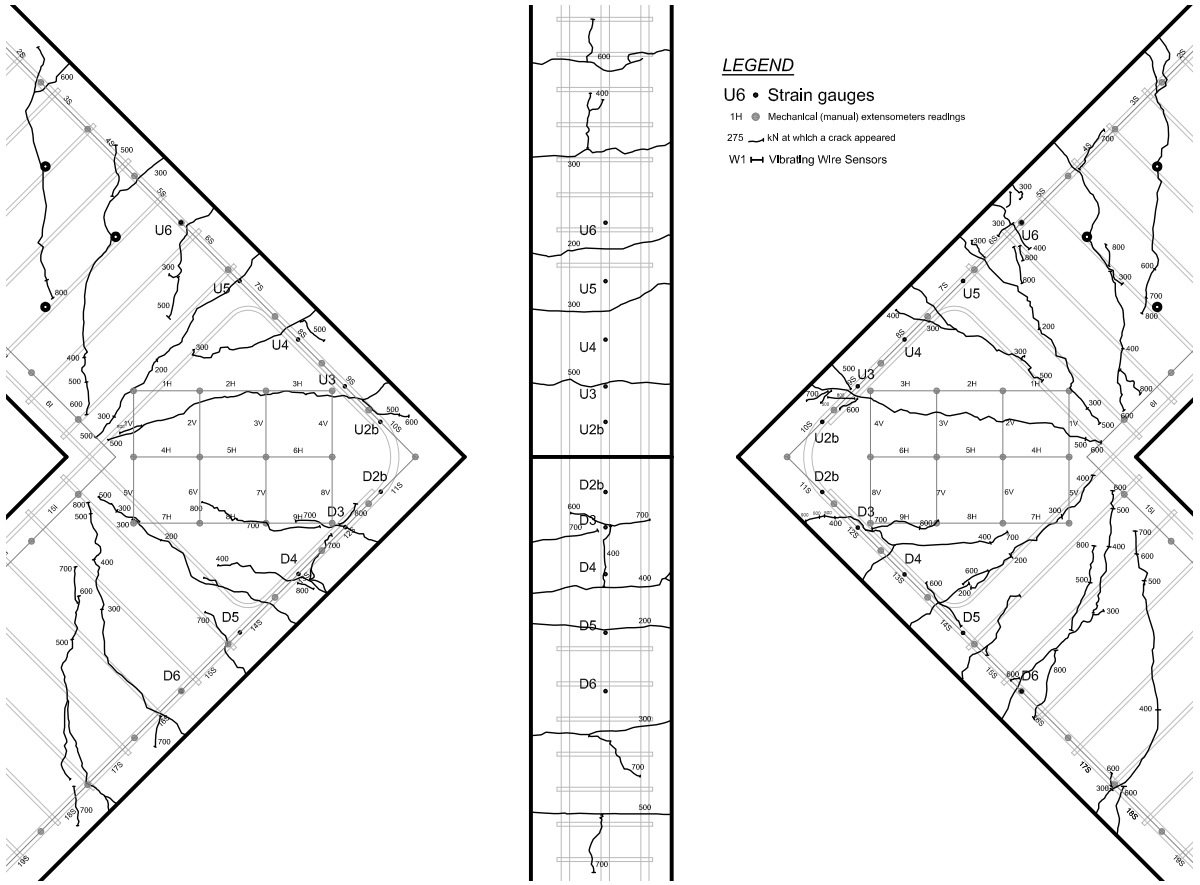

Figure D.39: 25-CV-25. Crack pattern at a load of 600 kN. From left to right: front view (A), side view, front view (B)

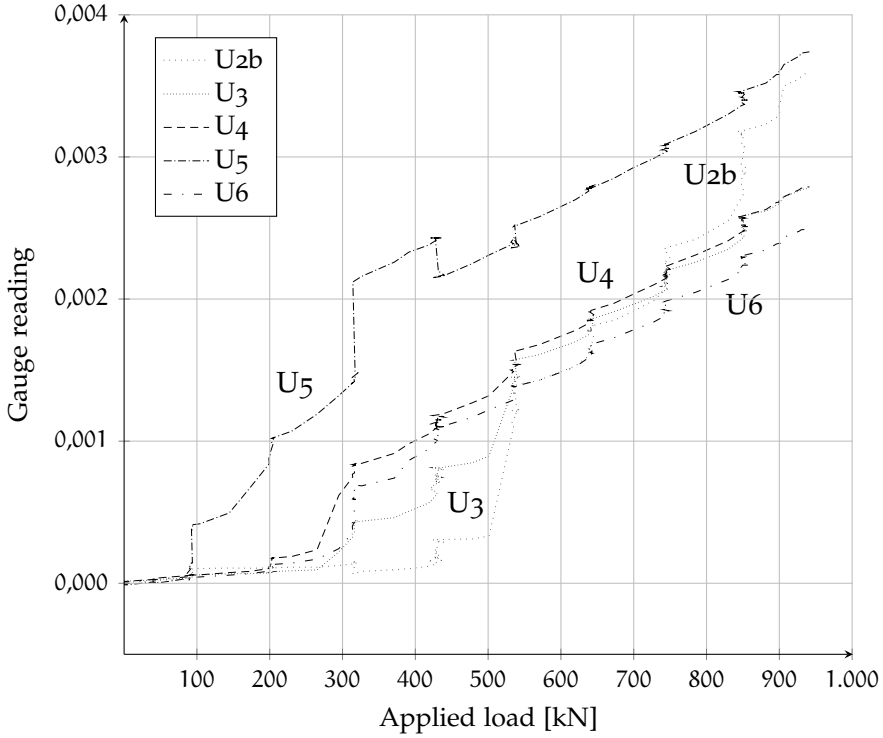

Figure D.40: 25-CV-25. Gauge readings (U)

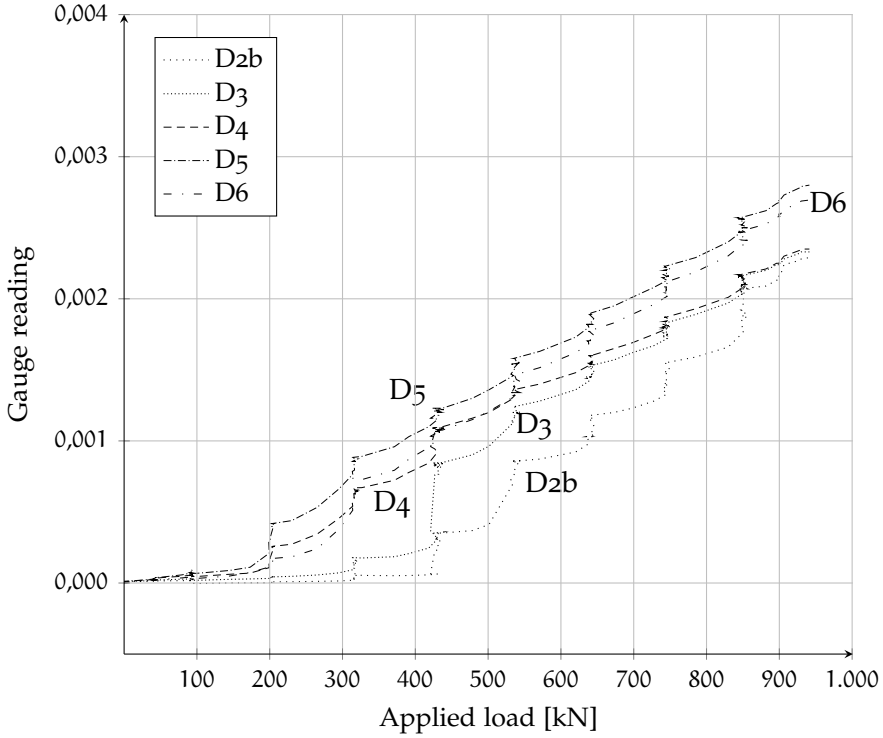

Figure D.41: 25-CV-25. Gauge readings (D)

D.4.6.1 *Hysteresis curves*

The same graph of the previous paragraph is reported in Figure D.42 for gauges 2b including the measurements during the cycling load[11].

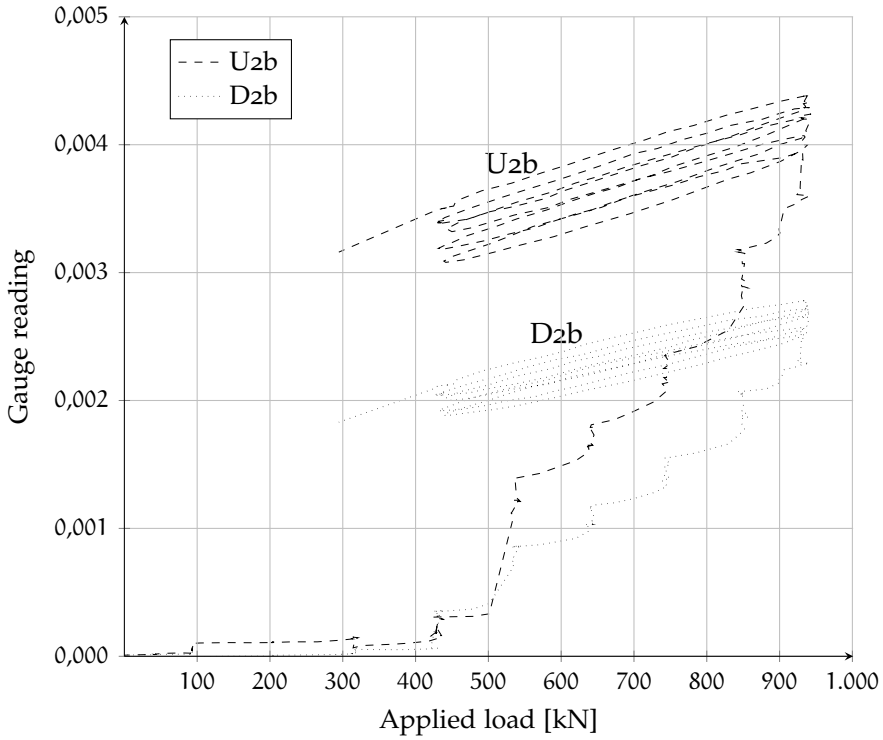

Figure D.42: 25-CV-25. Hysteresis curves for gauge 2b

D.4.7 Compression Strut

The recorded compressive strain was maximum in the strut axis: maximum strains were measured in segment 4H (−780 με; −900 με respectively in A side and B side). On A side, a crack intercepts segments 1V to 4V, 5V and 7V, while on B side two cracks intercept segments 1V to 5V. The wider cracks were measured on the outer edge (segment 4V). Full data are reported in Figure D.43–D.44.

[11] Loading-unloading cycles aimed at increase damage once the maximum capacity of the jack was reached.

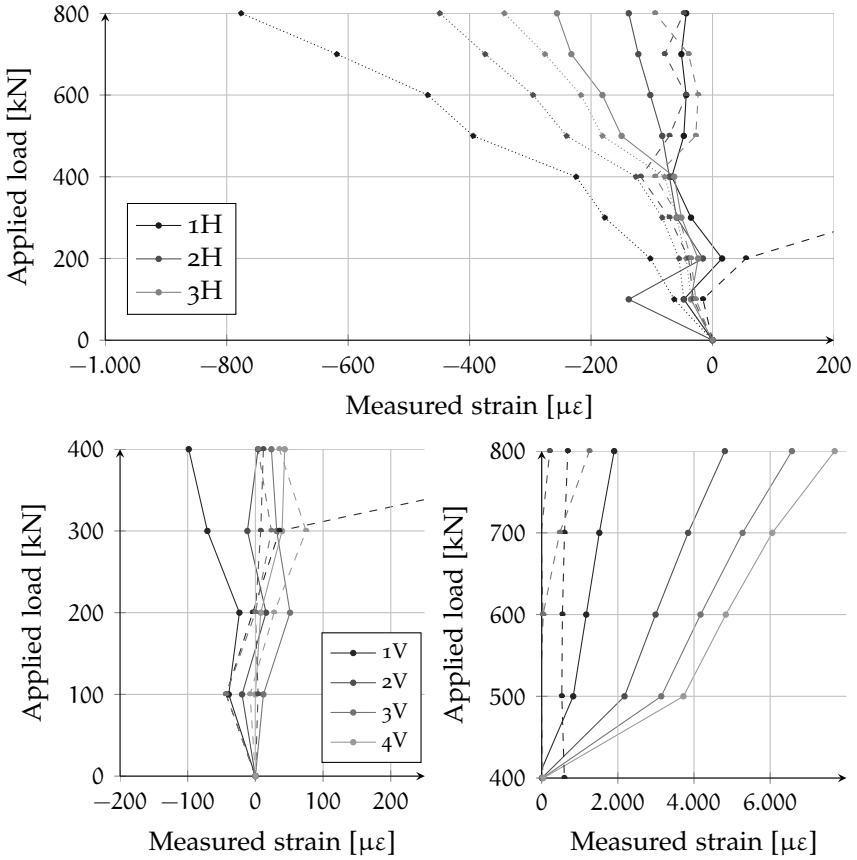

Figure D.43: 25-CV-25 – A side. Top: measured horizontal strains compared to the applied load. In dotted lines values for segments 4H to 6H, in dashed lines values for segments 7H to 9H; Bottom: vertical measured strains compared to the applied load. In dashed lines values for segments 5V to 8V

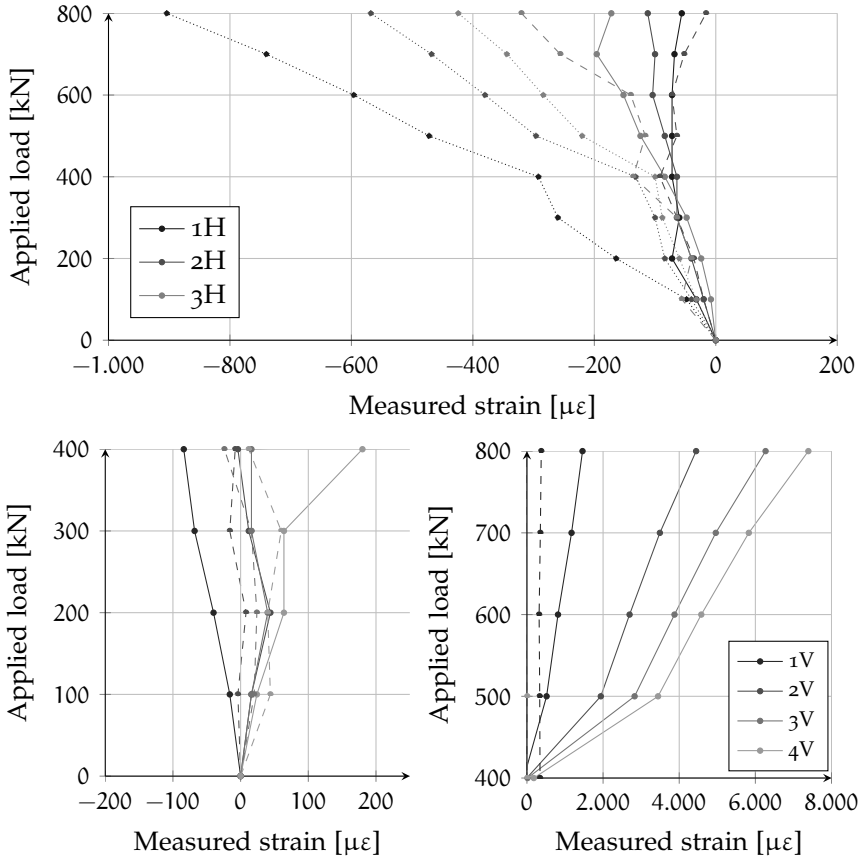

Figure D.44: 25-CV-25 – B side. Top: measured horizontal strains compared to the applied load. In dotted lines values for segments 4H to 6H, in dashed lines values for segments 7H to 9H; Bottom: vertical measured strains compared to the applied load. In dashed lines values for segments 5V to 8V

D.5 SPECIMEN 45-TH-16

The first test with the concrete class C45/55 took place 29 days after concrete pouring. The day before the test three concrete cylinders were tested: the mean compressive strength was 46,8 MPa, although the mean compressive strength of the concrete batch was more likely around 48 MPa (see Section 5.2.1.2).

D.5.1 General behavior

As for the previous described specimens, the applied load was increased step by step (see Table D.5) and manual measurements were taken at each step. Once a load of 400 kN was reached no manual measurements were taken for safety reasons.

The first flexural crack was observed between 200 and 250 kN. Two other cracks soon developed branching from the first one up to 300 kN, while subsequent level of loads only increased cracks opening. The last cracks formed were some bond-related cracks (parallel to the rebars) just inside the corner. Failure, which occurred at a load of 490 kN, was due to the excessive strain in the reinforcement (see Figure D.45).

Double headed shear reinforcement did not shown any sign of weakening during the test. No slip was measured during the test by both LVDTs and no significant strain was observed by means of the vibrating wire gauges.

D.5.2 Load-displacement

The load-displacement graph, presented in Figure D.46, represents the applied load and the measured displacement of the load application point during the test. Three different predictions are superposed on the graph, a simple sectional analysis, a non-linear analysis, and a more sofisticated non-linear finite element analysis performed with ATENA (as previously described in Section 5.3.6).

Again, a good correspondance between theoretical and experimental curves can be observed. Global ductility in terms of displacement of the control point was high in comparison with both predictions: this fact is related to convergence problems of models, given the very horizontal shape of the yield curve. A similar graph is provided in Figure D.47 for the horizontal displacement measured by the probe indicator[12], although in this case the experimental series stops earlier for safety reasons.

[12] As done for the previous specimens, the measured horizontal displacement has been corrected taking into account the rigid rotation estimated in Section D.5.3.

Figure D.45: The final configuration after failure: a rupture of the tensile reinforcement was observed (see also Figure D.1)

Step	Load [kN]	Notes
1	50	
2	100	
3	150	
4	200	
5	250	First flexural crack
6	300	Formation and growth of flexural cracks
7	350	Formation of bond-related cracks
8	375	
9	400	
10	425	
11	450	
12	475	
13	490	

Table D.5: 45-TH-16. Load steps

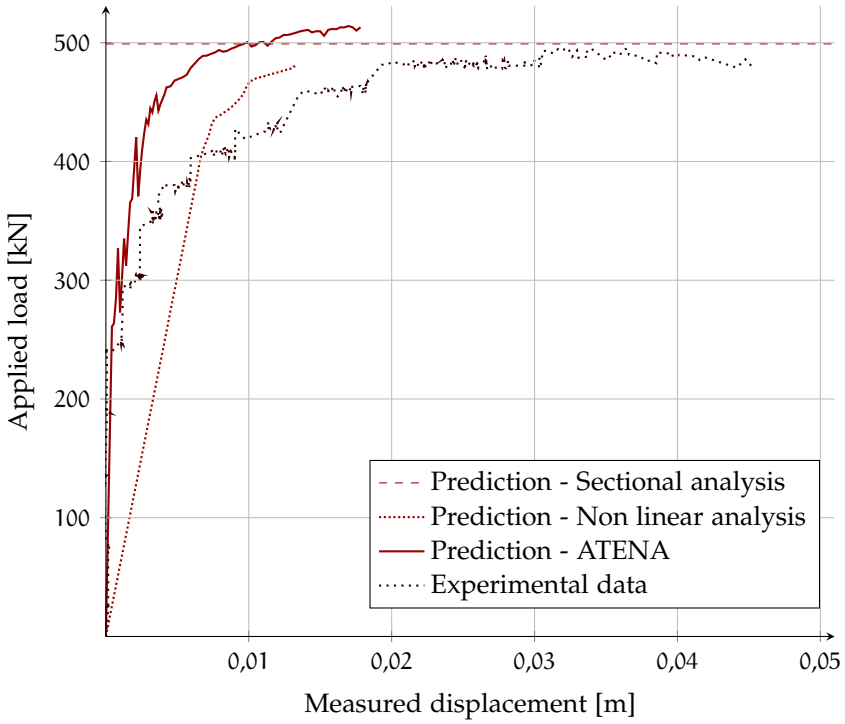

Figure D.46: Applied load Vs displacement of the load application point. In red lines the theoretical estimations

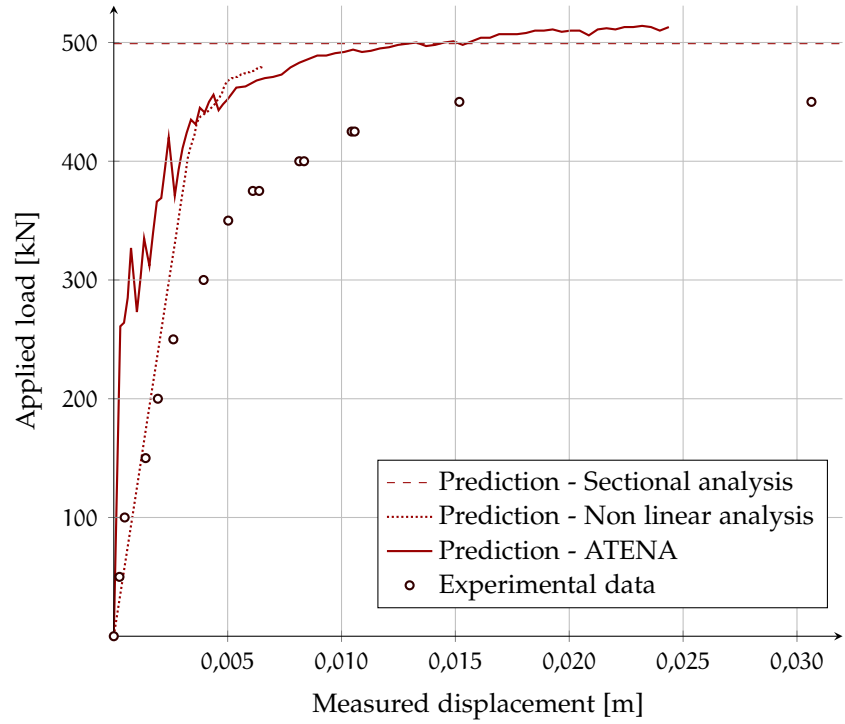

Figure D.47: Applied load Vs horizontal displacement (probe indicator). In red lines the theoretical estimations

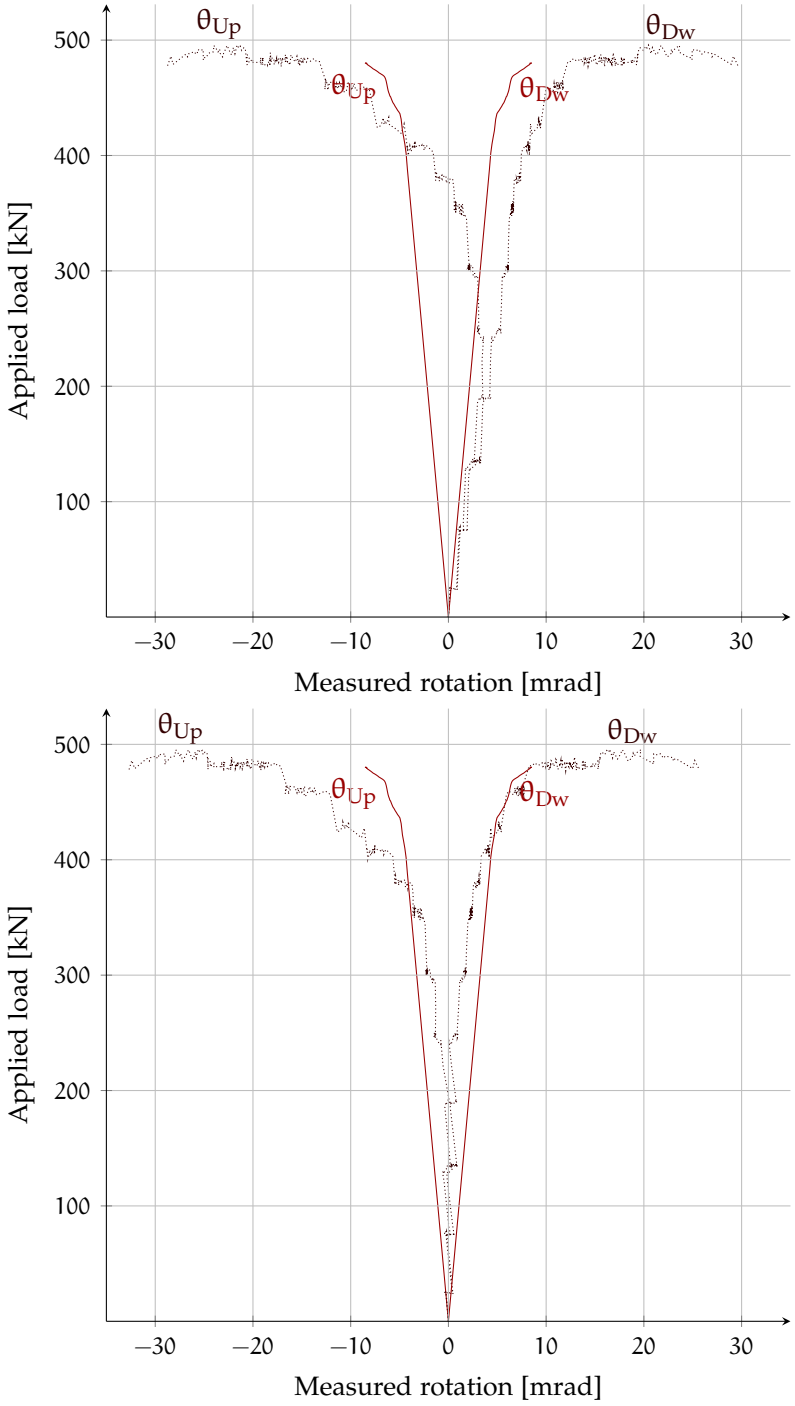

Figure D.48: Applied load Vs measured (up) and adjusted (down) rotations. In solid line, the non linear theoretical estimation

D.5.3 Load-rotation

A small rigid rotation of approximately $-1{,}8 \cdot 10^{-5}$ rad/kN was observed during the test. However, this rotation stabilized and even changed its sign after a load of 250 kN was reached. The second factor used for the correction is $2{,}0 \cdot 10^{-5}$ rad/kN

The raw data are presented in the upper graph of Figure D.48, while in the lower graph the same data are compensated to take into account the rigid rotation.

D.5.4 Moment-curvature

The experimental moment-curvature for some sections (see Figure 5.13) is shown in Figure D.49.

The experimental curvatures are calculated, for each section, as the substraction of strains measured by targets on the reinforcement axes in that section divided by the distance between the two lines[13]; the experimental moments are computed as the force perpendicular to the beam axis multiplied by the distance of the segment axis to the point of application of the load (1,075 m for sections 6-15 and 0,875 m of sections 5-16).

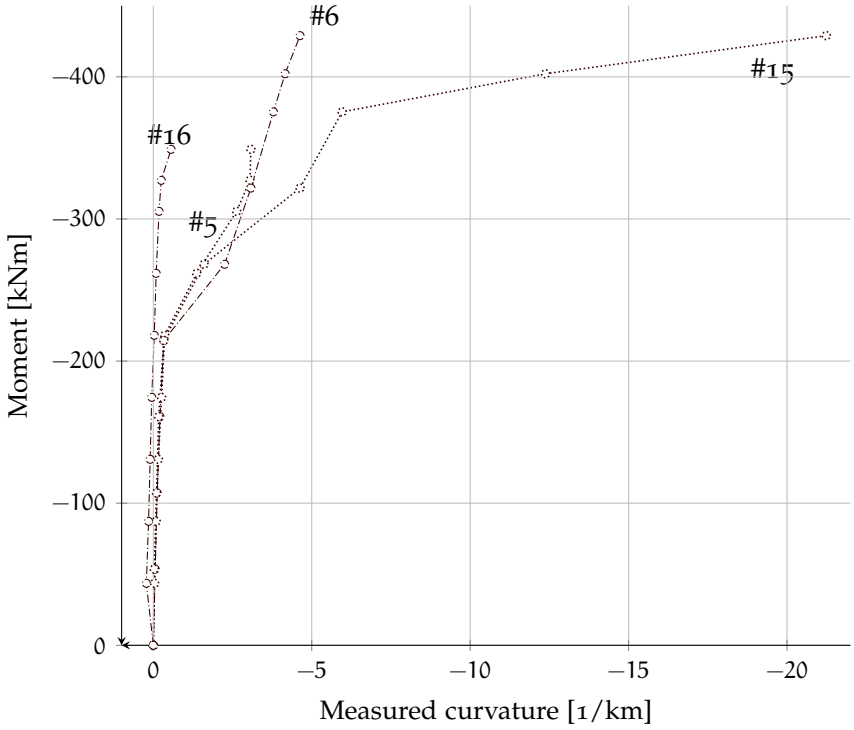

Figure D.49: 45-TH-16. Average (side A and B) measured M–χ diagram for some relevant sections

D.5.5 Crack pattern

Crack evolution described in Section D.5.1 is carefully reproduced in Figure D.51, where the position of the mechanical strain gauges is also represented.

[13] $1/r = \frac{\varepsilon_s - \varepsilon_i}{d - 2d'}$

The serviceability load can be estimated as a percentage of the ultimate load. If it is assumed $G_k = Q_k$:

$$F_{SLS} = \frac{(1{,}0 + 0{,}3)}{(1{,}35 + 1{,}5)} F_{ULS} \simeq 0{,}46\ F_{ULS} = 228\ \text{kN}$$

At the top of Figure D.50 is shown the measured crack width compared to the applied load, while at the bottom is provided the measured crack width compared to the theoretical steel stress, calculated at the middle of each segment.

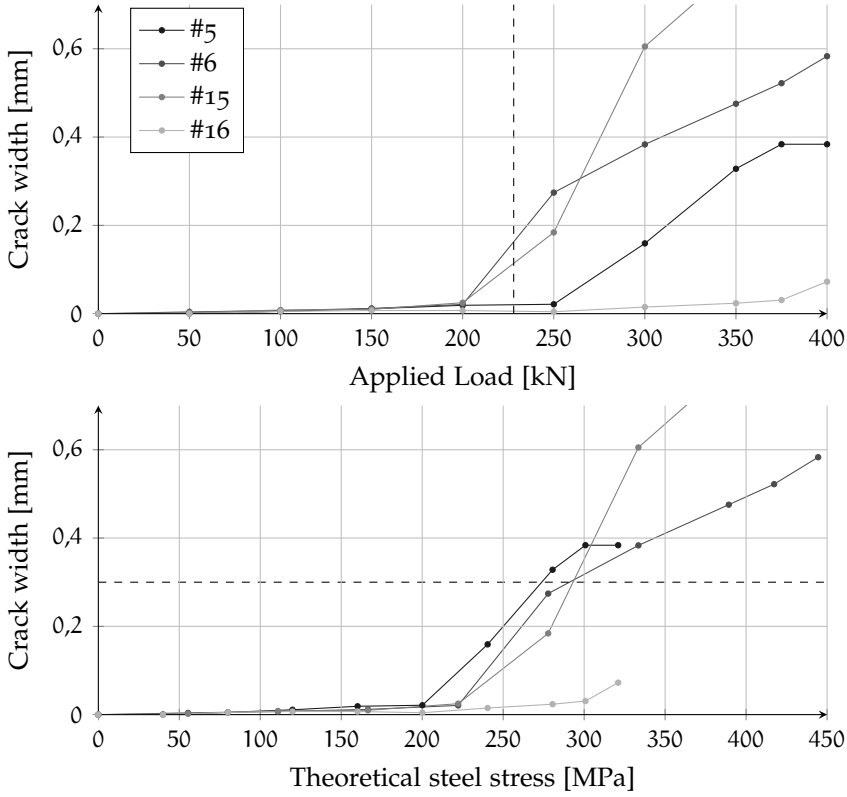

Figure D.50: 45-TH-16. Average (A and B sides) of measured crack width as a function of the applied load (top) and theoretical steel stress (bottom). The serviceability load and a crack width reference value of 0,3 mm are represented in dashed lines

D.5.6 Strain gauges

The first flexural crack was located in the adjoining members near to the core, while the last cracks were some bond-related cracks developed just inside the joint. No cracks developed inside the joint. Complete data are shown in Figures D.52–D.53. Gauge U5 broke unexpectedly at a load of 350 kN, while gauges U4 and U6 experienced a strain loss at a load greater than 450 kN. Gauges U1 and U2 did not reach significant strains, while gauge U3 reached a strain of 1,3‰.

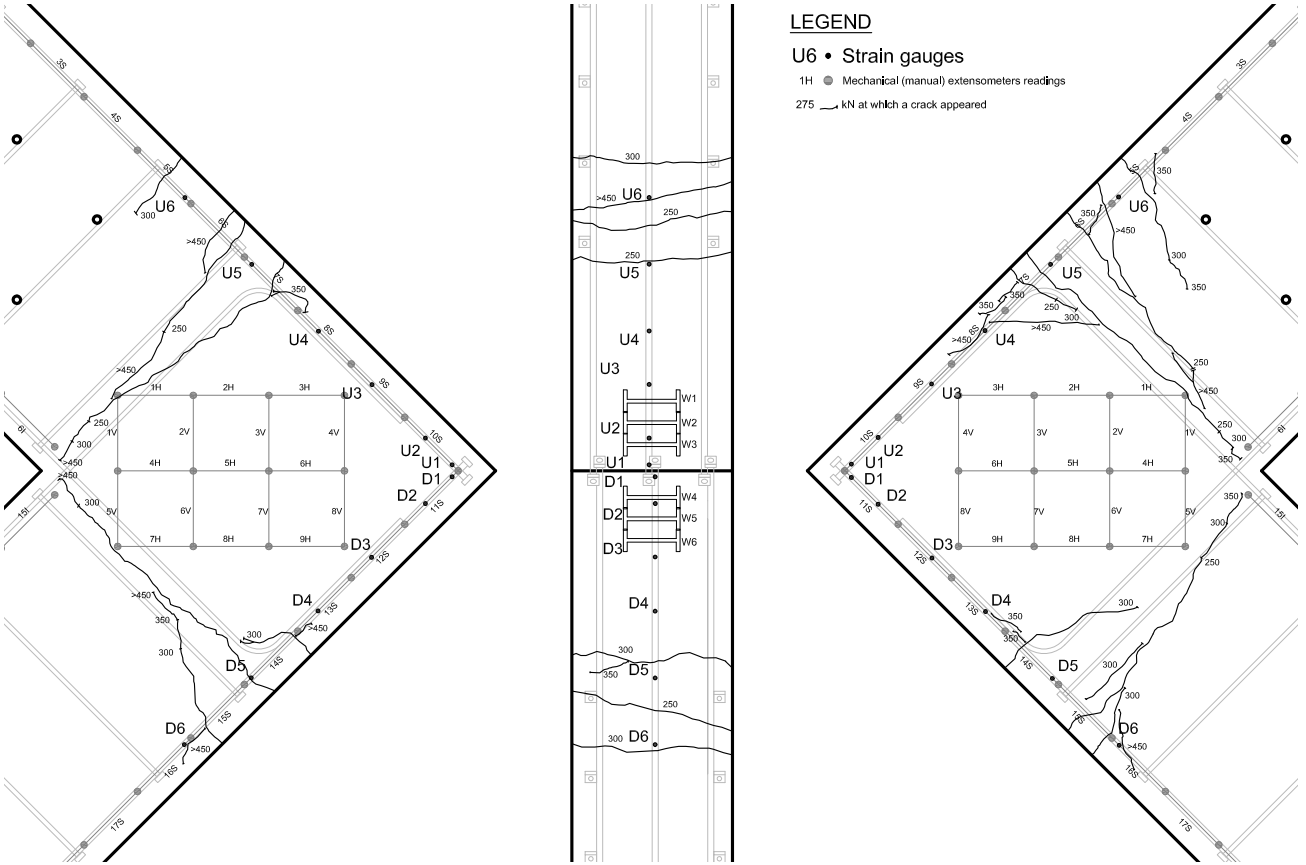

Figure D.51: 45-TH-16. Crack pattern before failure. From left to right: front view (A), side view, front view (B)

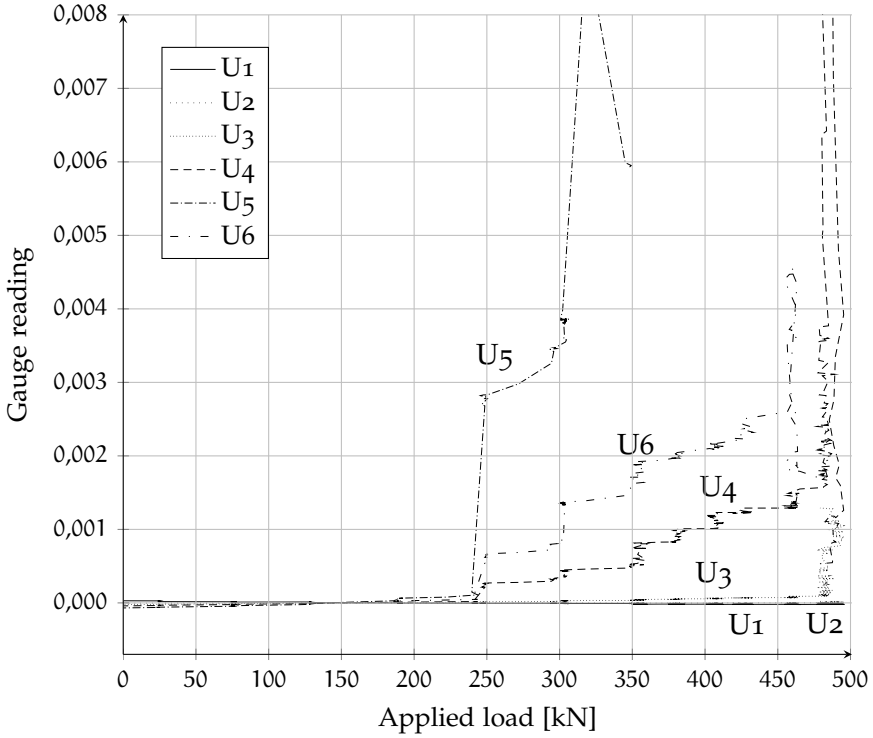

Figure D.52: 45-TH-16. Gauge readings (U)

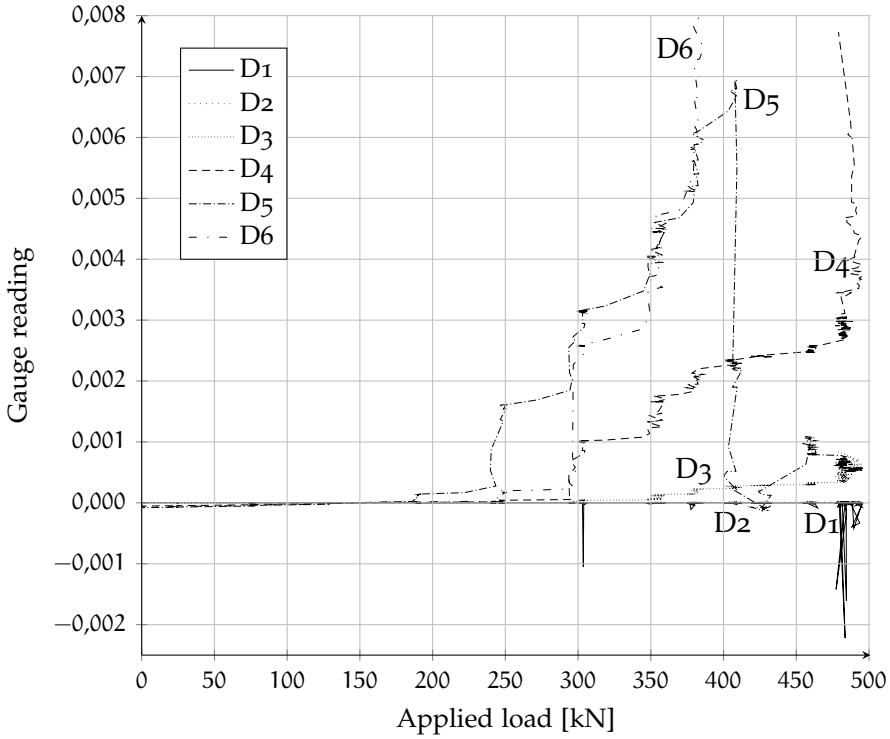

Figure D.53: 45-TH-16. Gauge readings (D)

Gauge D6 broke at a load of 400 kN due to excessive strain, while gauge D5 experienced a loss of strain at the same load. Gauge D4 reached a strain of almost 8‰before failure, while gauges U1, U2 and U3 did not reach significant strains.

D.5.7 Compression Strut

The recorded compressive strain was maximum in segments 2H (A side) and 1H (B side). Segments 1V (A side) and 5V (both sides) measured only compressive strains. No cracks were formed parallel to the central strut in this specimen. Full data are reported in Figure D.54–D.55.

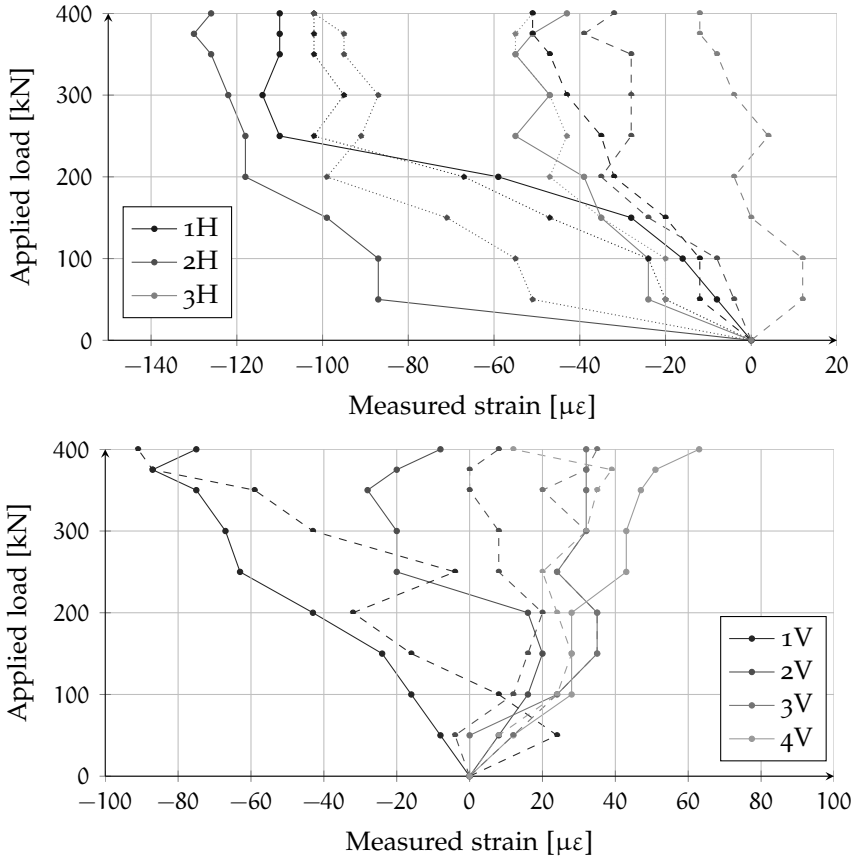

Figure D.54: 45-TH-16 – A side. Top: measured horizontal strains compared to the applied load. In dotted lines values for segments 4H to 6H, in dashed lines values for segments 7H to 9H; Bottom: vertical measured strains compared to the applied load. In dashed lines values for segments 5V to 8V

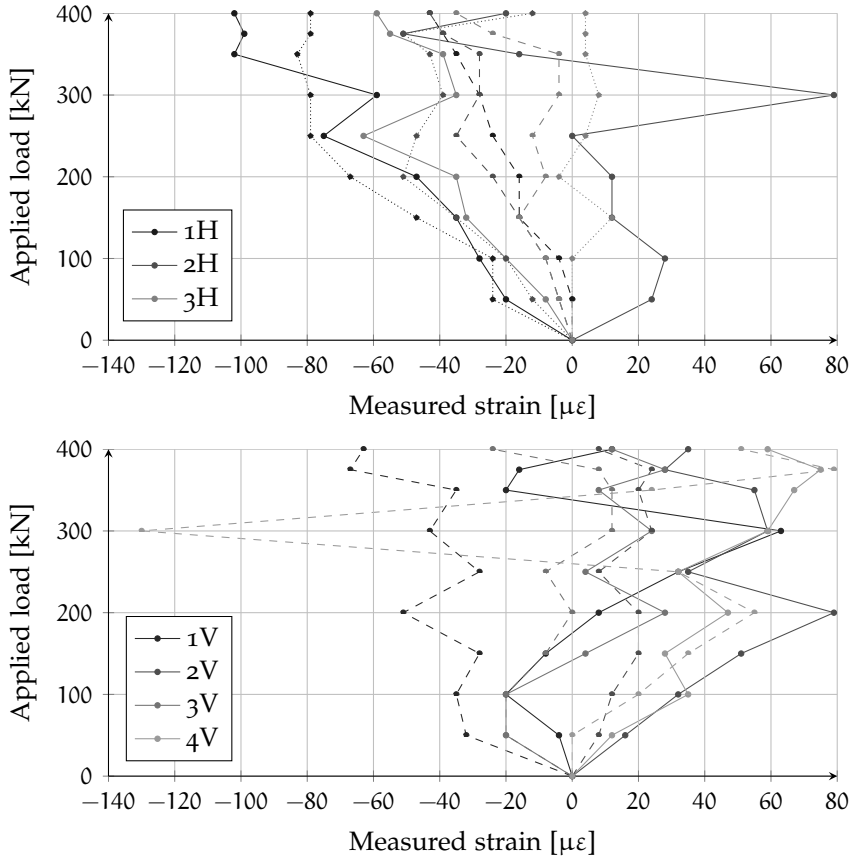

Figure D.55: 45-TH-16 – B side. Top: measured horizontal strains compared to the applied load. In dotted lines values for segments 4H to 6H, in dashed lines values for segments 7H to 9H; Bottom: vertical measured strains compared to the applied load. In dashed lines values for segments 5V to 8V

D.6 SPECIMEN 45-TH-25

The test took place 42 days after concrete pouring. The day after the test three concrete cylinders were tested: the mean compressive strength was 49,9 MPa, although the mean compressive strength of the concrete batch was more likely around 51 MPa (see Section 5.2.1.2).

D.6.1 General behavior

The applied load was increased step by step (see Table D.6) and manual measurements were taken at each step. As were no safety concerns, a final manual measurement was taken at the end of the test.

The first flexural crack was observed at a load of 300 kN. Other flexural cracks soon developed nearby between 400 and 600 kN, while bond-related cracks (parallel to the rebars) started developing at 500 kN.

Cracks along the central strut developed from a load of 700 kN. The maximum load available was not sufficient to reach a complete rupture of the specimen, however, a state of extensive cracking of concrete and yielding of reinforcement was reached and the gauge closest to the plate measured a strain larger than 2‰. After the maximum load was reached, six load cycles were applied to increase damage.

Double headed shear reinforcement did not shown any sign of weakening during the test. One of the anchorage plates experienced a slip, lower than 0,6 mm.

D.6.2 Load-displacement

The load-displacement graph, presented in Figure D.56, represents the applied load and the measured displacement of the load application point during the test. Three different predictions are superposed on the graph, a simple sectional analysis, a non-linear analysis, and

Step	Load [kN]	Notes
1	100	
2	200	
3	300	First flexural crack
4	400	
5	500	Formation of bond-related cracks
6	600	
7	700	Formation of cracks parallel to the central strut
8	800	
9	900	
10	933	Capacity of loading system is reached
11	–	Six cycles 400-933 kN to increase damage

Table D.6: 45-TH-25. Load steps

a more sofisticated non-linear finite element analysis performed with ATENA (as previously described in Section 5.3.6). In this case, the measured horizontal displacement has not been corrected taking into account a supposed rigid rotation of the specimen (see Section D.6.3).

Again, good correspondance between theoretical and experimental curves can be observed. Global ductility in terms of displacement of the control point was high in comparison with both predictions: this fact is related to convergence problems of models, given the very horizontal shape of the yield curve.

D.6.3 Load-rotation

Unclear data were obtained using the clinometers, making a compensation similar to that obtained for previous specimens hard to obtain. In this case, a corrected graph can be obtain performing an average of the two measurements. The original data are presented at the top of Figure D.57, while at the bottom is presented the average curve, which is represented symmetrically.

D.6.4 Moment-curvature

The experimental moment-curvature for some sections (see Figure 5.13) is shown in Figure D.58.

The experimental curvatures are calculated, for each section, as the substraction of strains measured by targets on the reinforcement axes in that section divided by the distance between the two lines[14]; the experimental moments are computed as the force perpendicular to the beam axis multiplied by the distance of the segment axis to the point of application of the load (1,075 m for sections 6-15 and 0,875 m of sections 5-16).

D.6.5 Crack pattern

Crack evolution described in Section D.6.1 is carefully reproduced in Figure D.60, where the position of the mechanical strain gauges is also represented.

The serviceability load can be estimated as a percentage of the ultimate load. If it is assumed $G_k = Q_k$:

$$F_{SLS} = \frac{(1{,}0 + 0{,}3)}{(1{,}35 + 1{,}5)} F_{ULS} \simeq 0{,}46\ F_{ULS} = 467\ \text{kN}$$

At the top of Figure D.59 is shown the measured crack width compared to the applied load, while at the bottom is provided the measured crack width compared to the theoretical steel stress, calculated at the middle of each segment.

[14] $1/r = \frac{\varepsilon_s - \varepsilon_i}{d - 2d'}$

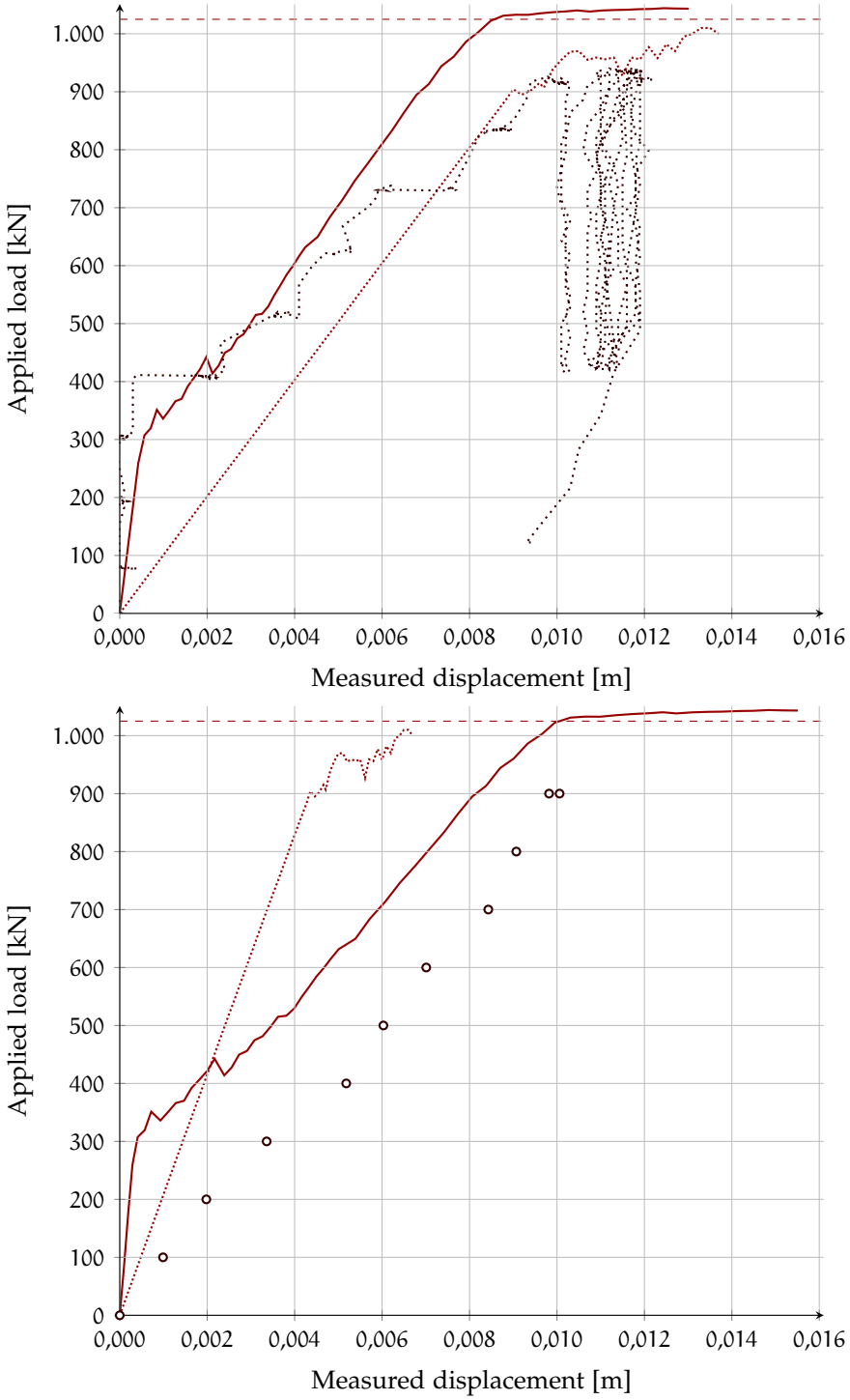

Figure D.56: Vertical displacement of the load application point (up) and horizontal displacement measured by the probe indicator (down). Experimental data (·····)(··) and predictions by sectional analysis (- - -), non–linear analysis (·····) and ATENA (——)

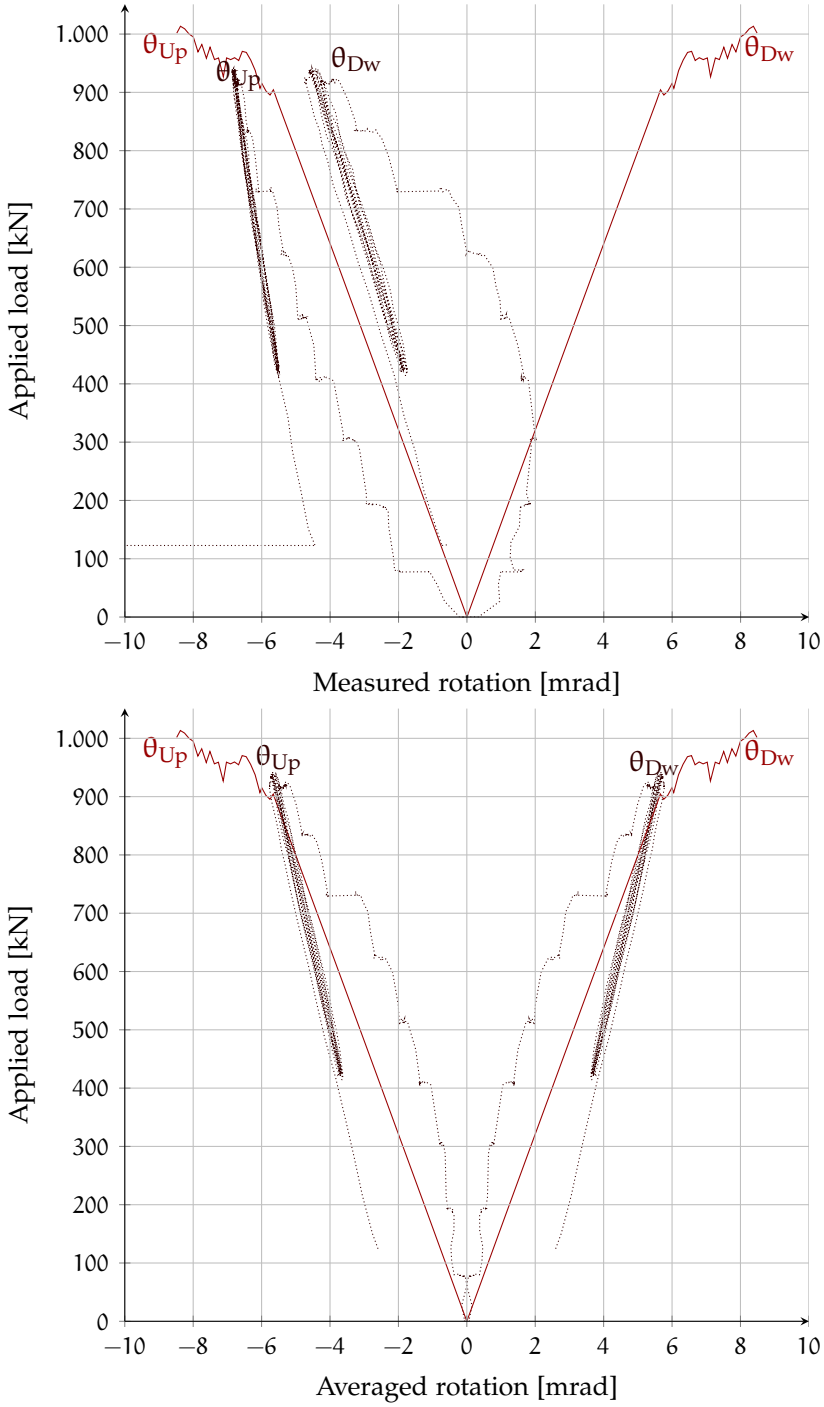

Figure D.57: Applied load Vs measured (up) and averaged (down) rotations.
In solid line, the non linear theoretical estimation

D.6.6 Strain gauges

As for the other specimens, the first flexural crack was located between the core and the adjoining members, while the last cracks developed within the joint. Gauges U5 and D5 were first reaching a

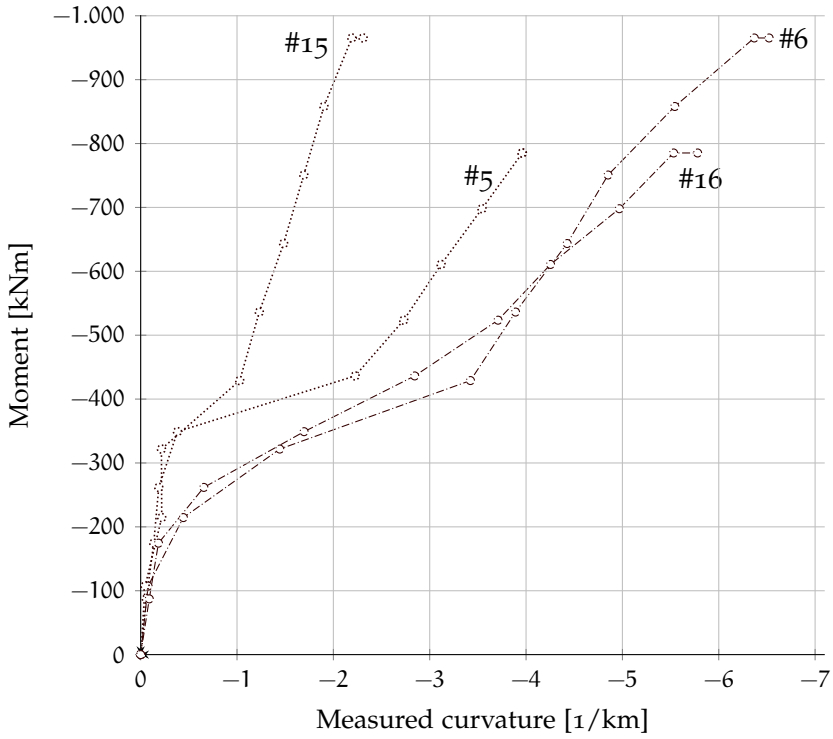

Figure D.58: 45-TH-25. Average (side A and B) measured M–χ diagram for some relevant sections

high strain, as can be observed in Figures D.61–D.62. At the ultimate load, U1, U2 and D1 gauges measured a strain of 2,0‰, while D2, U3 and D3 measured strains around 1,0‰.

D.6.6.1 *Hysteresis curves*

The same graph of the previous paragraph is reported in Figure D.63 for gauges 1 and 2 including the measurements during the cyclic loading[15]: gauge D1 measured a strain ranging between 1,5‰and 2‰, while gauge U1 oscillated from 1,5‰to 2,5‰.

D.6.7 Compression Strut

The recorded compressive strain was maximum in the strut axis with a mean compressive strain around −300 με at a load of 900 kN. Maximum strains were measured in segment H4 (−440 με; −280 με respectively in side A and side B). On both sides cracks parallel to the central strut intercept some segments: the wider cracks were measured on the outer edge (segment 4V and 8V). Full data are reported in Figure D.64–D.65.

[15]Loading-unloading cycles aimed at increase damage once the maximum capacity of the jack was reached.

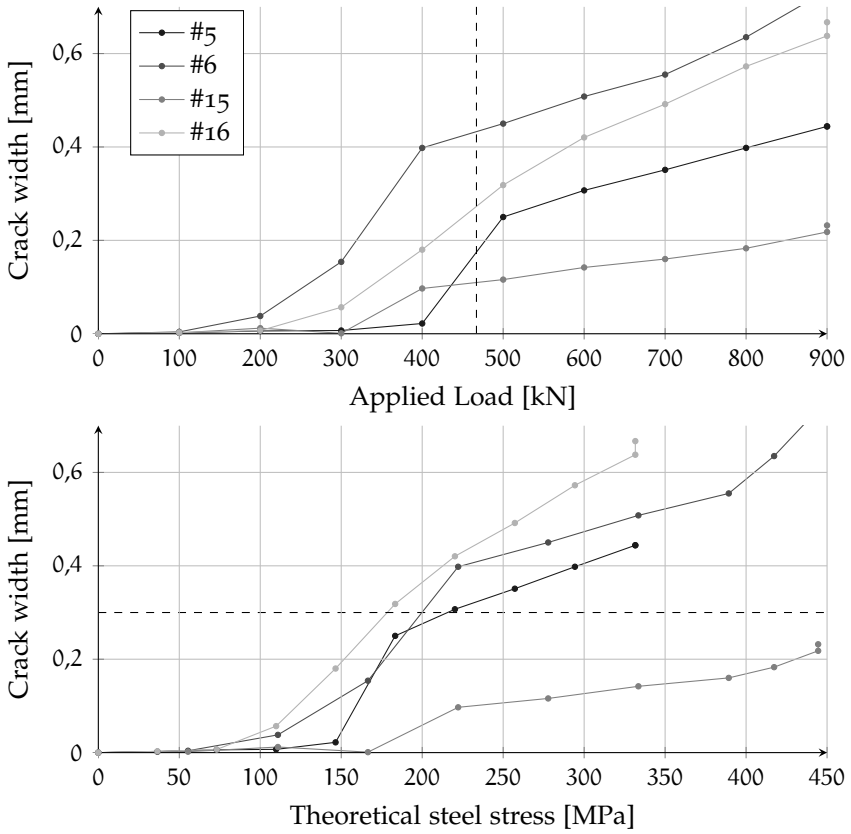

Figure D.59: 45-TH-25. Average (A and B sides) of measured crack width as a function of the applied load (top) and theoretical steel stress (bottom). The serviceability load and a crack width reference value of 0,3 mm are represented in dashed lines

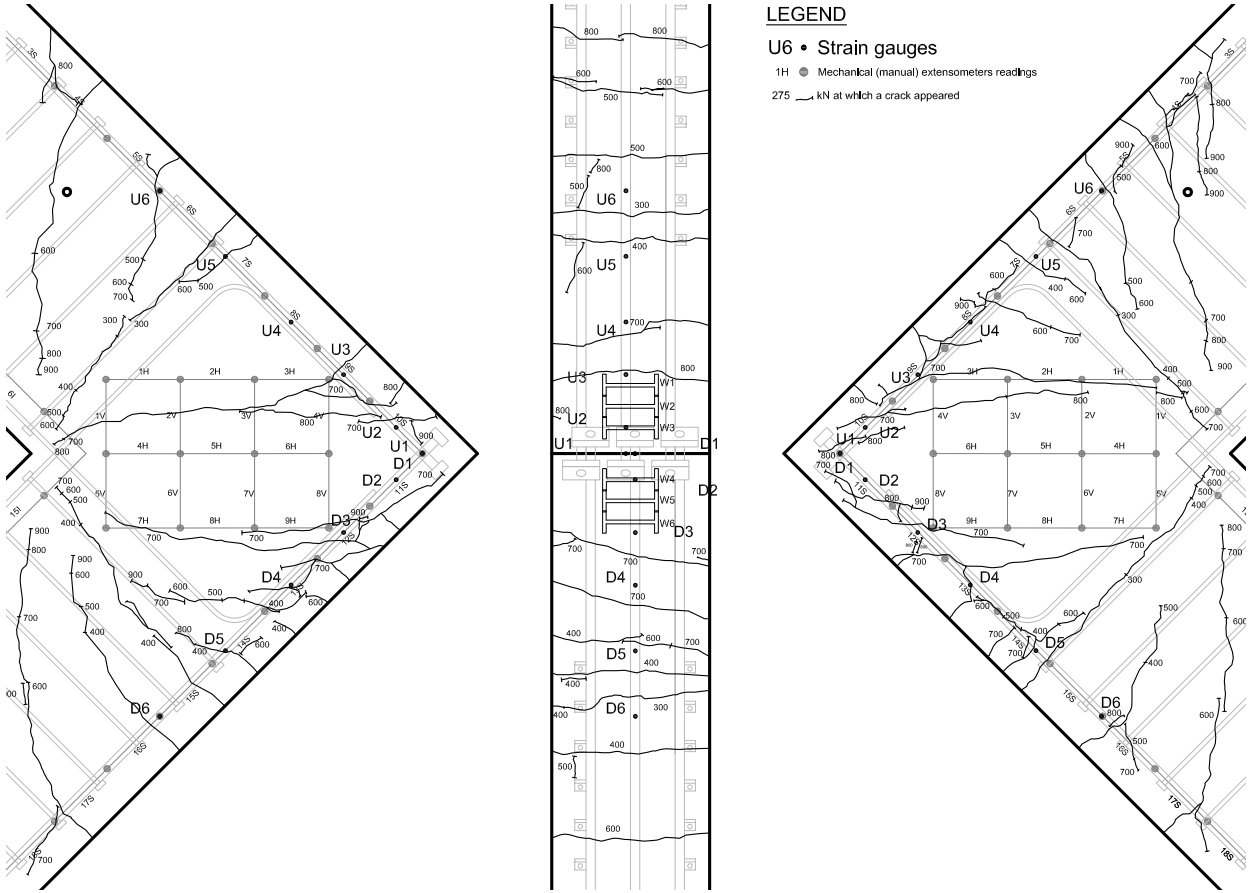

Figure D.60: 45-TH-25. Crack pattern. From left to right: front view (A), side view, front view (B)

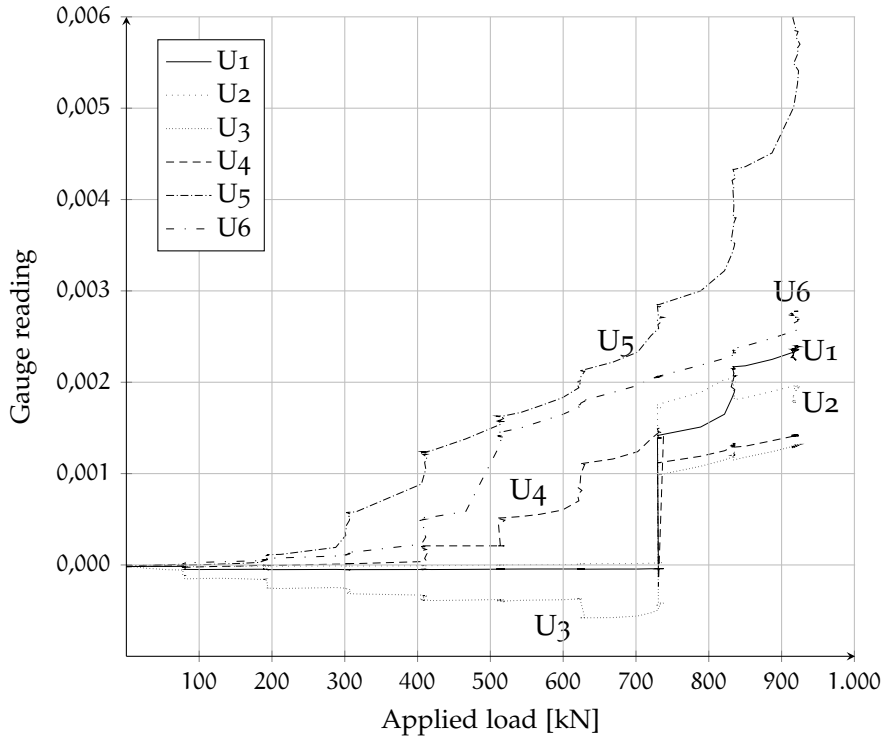

Figure D.61: 45-TH-25. Gauge readings (U)

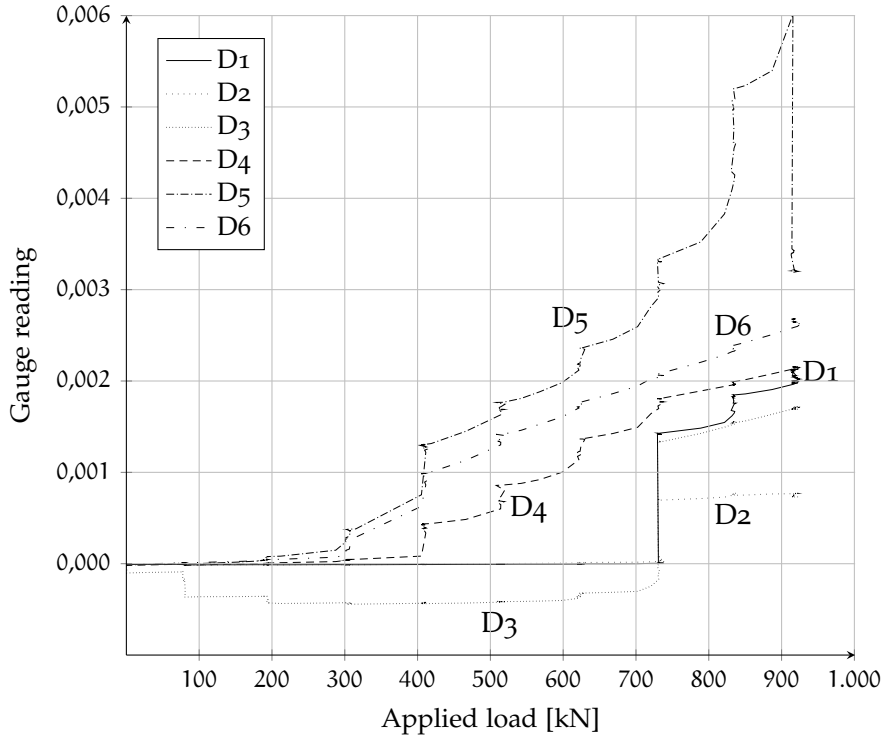

Figure D.62: 45-TH-25. Gauge readings (D)

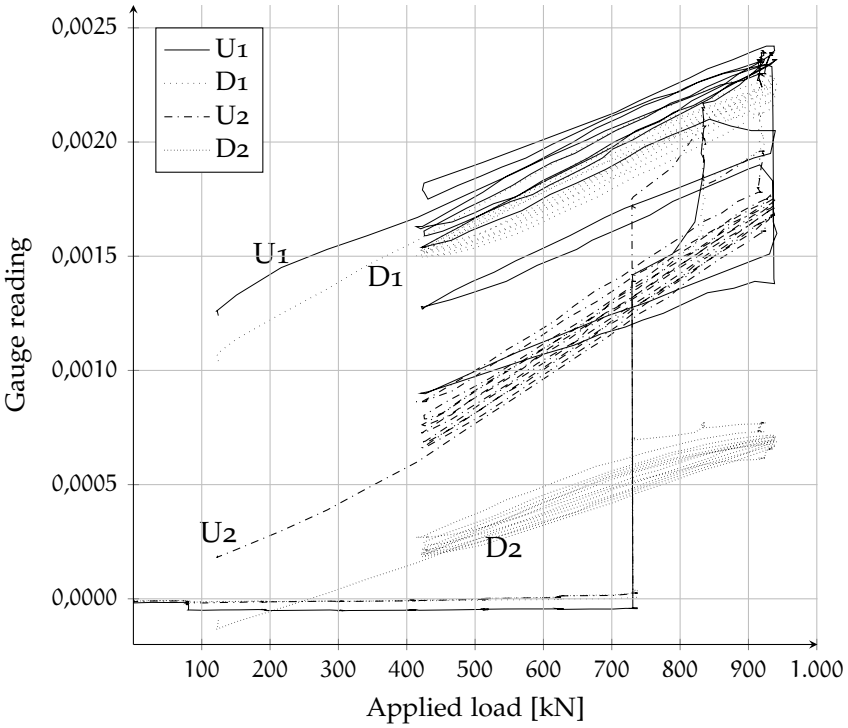

Figure D.63: 45-TH-25. Hysteresis curves for gauges 1 and 2

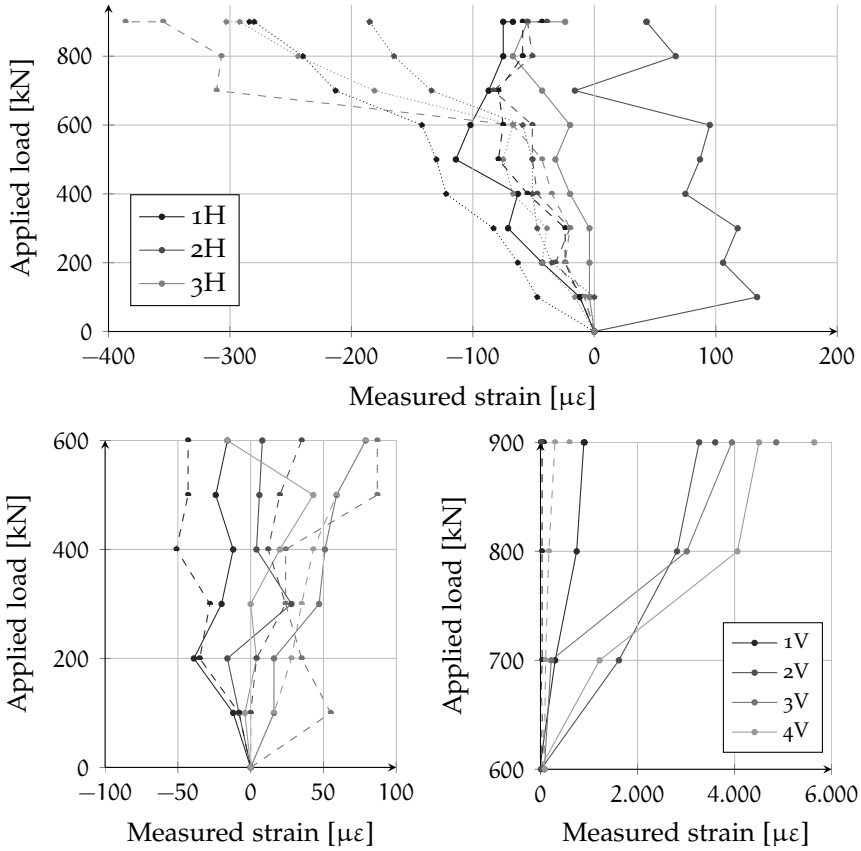

Figure D.64: 45-TH-25 – A side. Top: measured horizontal strains compared to the applied load. In dotted lines values for segments 4H to 6H, in dashed lines values for segments 7H to 9H; Bottom: vertical measured strains compared to the applied load. In dashed lines values for segments 5V to 8V

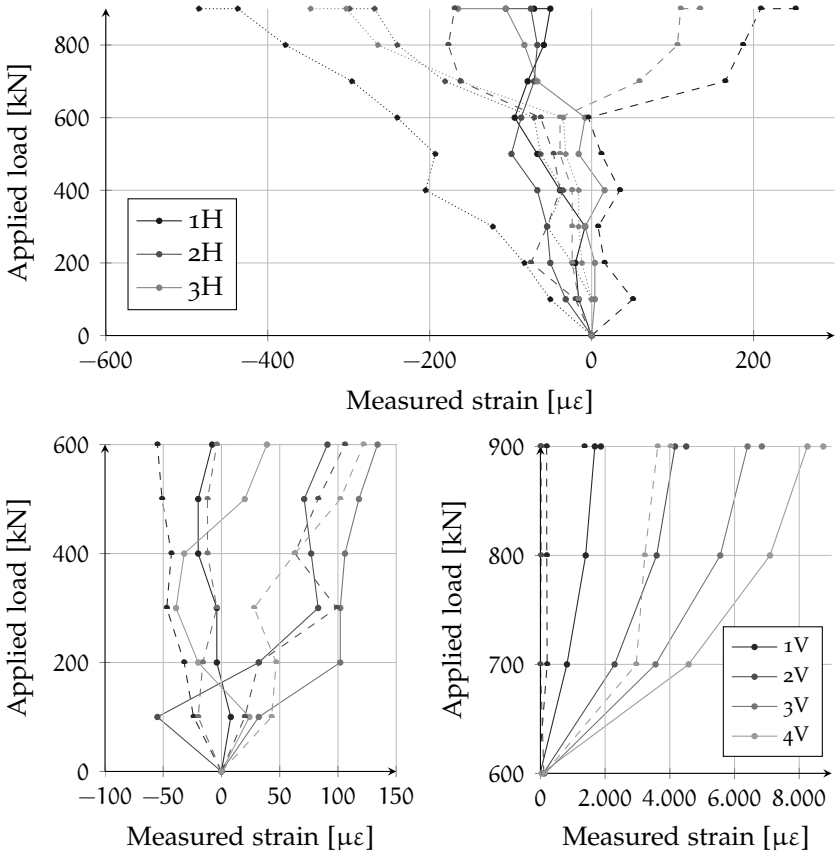

Figure D.65: 45-TH-25 – B side. Top: measured horizontal strains compared to the applied load. In dotted lines values for segments 4H to 6H, in dashed lines values for segments 7H to 9H; Bottom: vertical measured strains compared to the applied load. In dashed lines values for segments 5V to 8V

D.6.8 Vibrating wire strain gauges

In this specimen a lateral strain originated by the presence of bursting forces acting along the bar axis was observed.

The bottom wires, which measure the influence of the upper middle plate, recorded a strain larger than 500 με (Figure D.66).

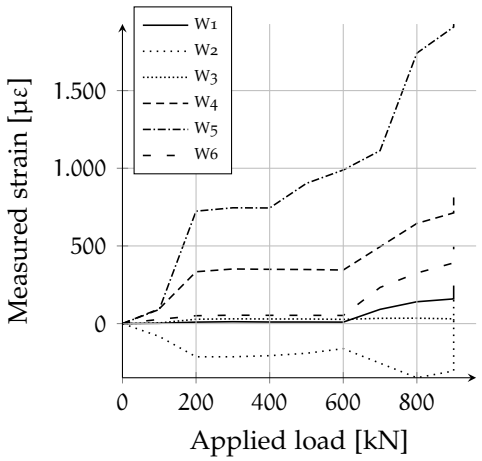

Figure D.66: 45-TH-25. Vibrating wires

D.6.9 Head slip

A slip of the central heads was measured during the test by the upper fleximeter (LVDT 1), starting from a load of 700 kN. The slip increased progressively up to almost 0,6 mm, as shown in Figure D.67.

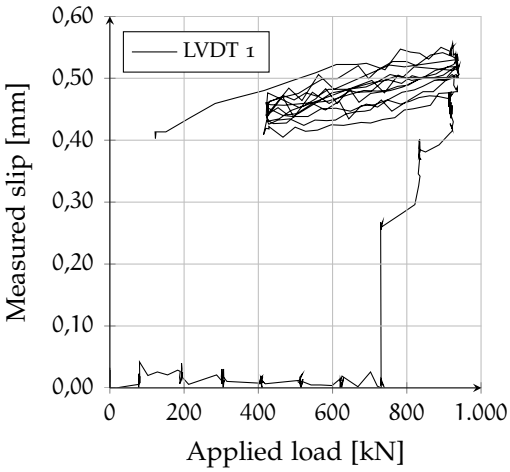

Figure D.67: 45-TH-25. Head slip

D.7 SPECIMEN 45-CV-16

The test took place 35 days after concrete pouring. The day after the test three concrete cylinders were tested: the mean compressive strength was 51,1 MPa, although the mean compressive strength of the concrete batch was more likely around 50 MPa (see Section 5.2.1.2).

D.7.1 General behavior

The applied load was increased step by step (see Table D.7) and manual measurements were taken at each step. Once a load of 450 kN was reached no measurements were taken close to the specimen for safety reasons.

Double headed shear reinforcement did not shown any sign of weakening during the test and no significant strain was observed by means of the vibrating wire gauges.

Step	Load [kN]	Notes
1	50	
2	100	
3	150	
4	200	
5	250	First flexural crack
6	300	Formation and growth of flexural cracks
7	350	Formation of bond-related cracks
8	375	
9	400	
10	425	
11	450	
12	475	Formation of cracks parallel to the central strut
13	500	
14	525	
15	550	

Table D.7: 45-CV-16. Load steps

The first flexural crack was observed at 200 kN and other flexural cracks soon developed close to the first one. Some bond-related cracks (parallel to the rebars) formed just inside the corner, starting from a load of 350 kN, while the last cracks to be formed were parallel to the central strut.

Failure was due to the excessive strain in the reinforcement, occurring at a load of 560 kN (see Figure D.68).

D.7.2 Load-displacement

The load-displacement graph presented in Figure D.69 represents the applied load and the measured displacement of the load application

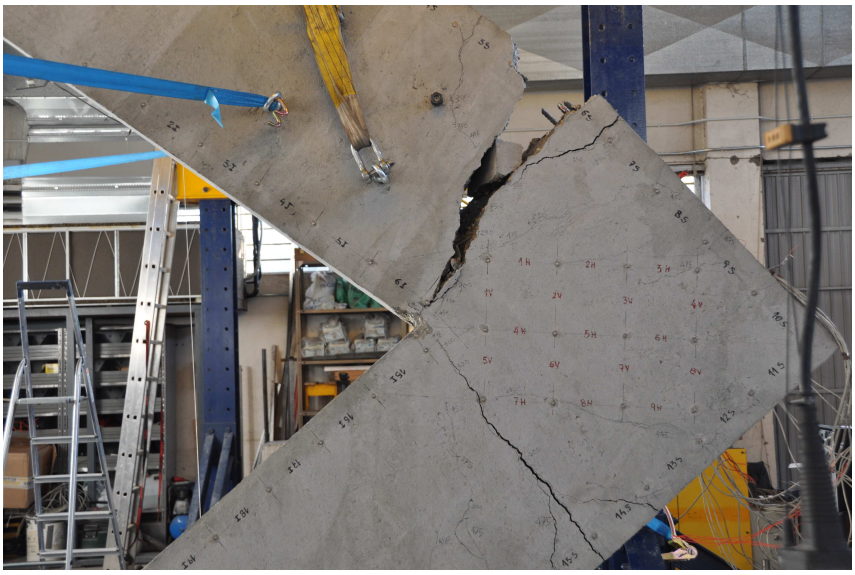

Figure D.68: The final configuration after failure: a rupture of the tensile reinforcement was observed (see also Figure D.1)

point during the test. Three different predictions are superposed on the graph, a simple sectional analysis, a non-linear analysis, and a more sofisticated non-linear finite element analysis performed with ATENA (as previously described in Section 5.3.6).

A similar graph is provided in Figure D.70 for the horizontal displacement measured by the probe indicator. As for specimen 45-TH-25, the measured horizontal displacement has not been corrected taking into account a supposed rigid rotation of the specimen (see Section D.7.3).

D.7.3 Load-rotation

Unclear data were obtained using the clinometers, making a compensation similar to that obtained for other specimens hard to obtain. In this case, a corrected graph can be obtain performing an average of the two measurements. The original data are presented in the upper graph of Figure D.71, while in the lower graph is presented the average, which is represented symmetrically.

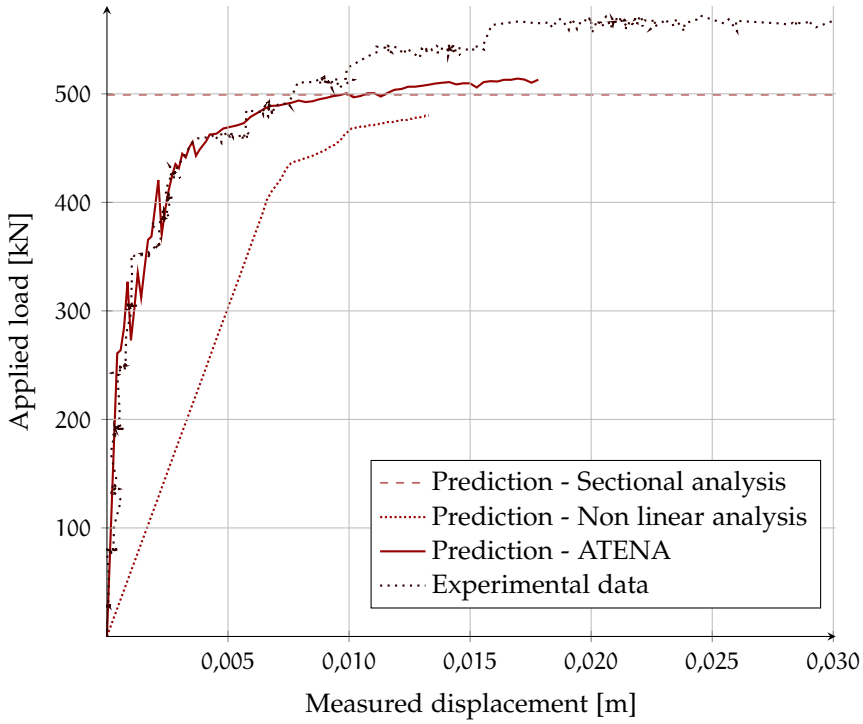

Figure D.69: Applied load Vs displacement of the load application point. In red lines the theoretical estimations

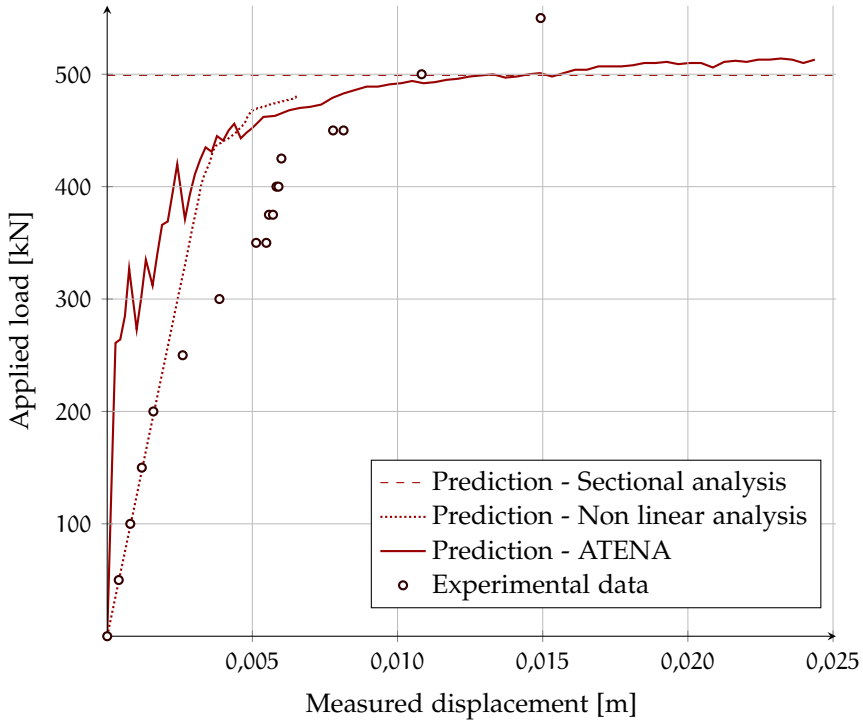

Figure D.70: Applied load Vs horizontal displacement (probe indicator). In red lines the theoretical estimations

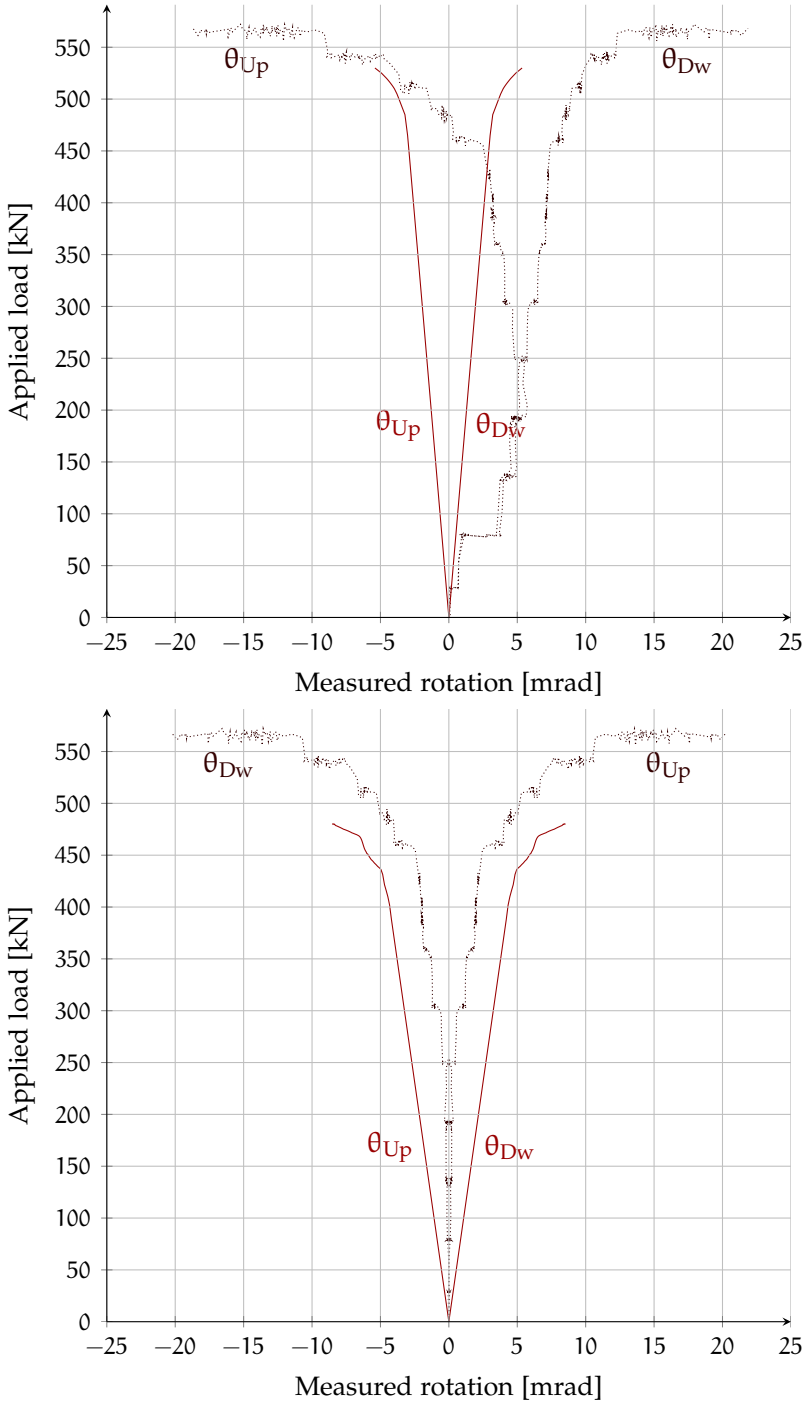

Figure D.71: Applied load Vs measured (up) and adjusted (down) rotations. In solid line, the non linear theoretical estimation

D.7.4 Moment-curvature

The experimental moment-curvature for some sections (see Figure 5.13) is shown in Figure D.72.

The experimental curvatures are calculated, for each section, as the substraction of strains measured by targets on the reinforcement axes in that section divided by the distance between the two lines[16]; the experimental moments are computed as the force perpendicular to the beam axis multiplied by the distance of the segment axis to the point of application of the load (1,075 m for sections 6-15 and 0,875 m for sections 5-16).

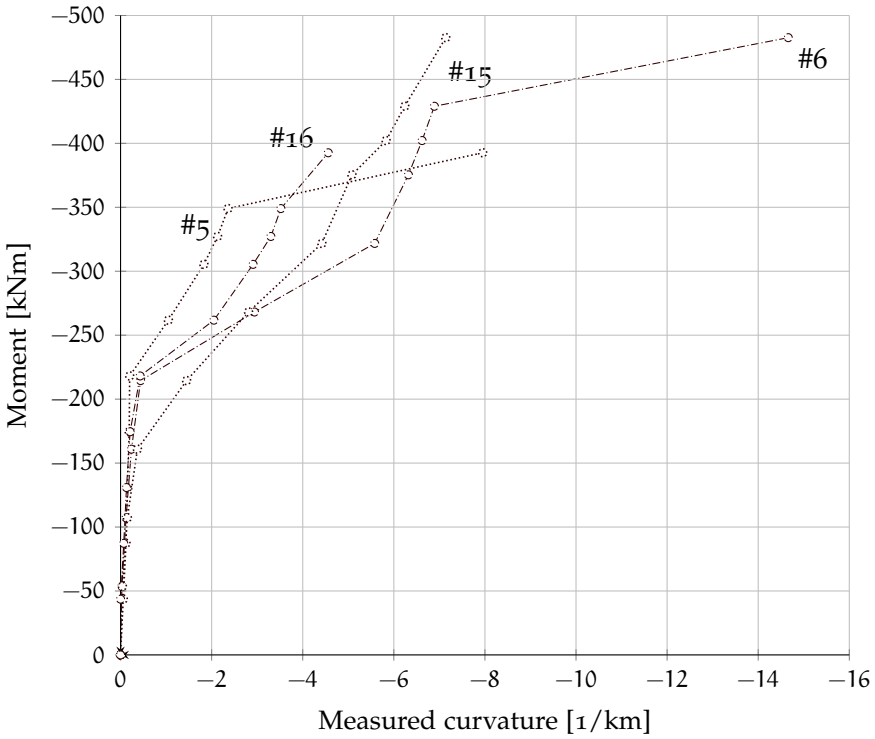

Figure D.72: 45-CV-16. Average (side A and B) measured M–χ diagram for some relevant sections

[16] $1/r = \frac{\varepsilon_s - \varepsilon_i}{d - 2d'}$

D.7.5 Crack pattern

Crack evolution described in Section D.7.1 is carefully reproduced in Figure D.74, where the position of the mechanical strain gauges is also represented. At the top of Figure D.73 is shown the measured crack width compared to the applied load, while at the bottom is provided the measured crack width compared to the theoretical steel stress, calculated at the middle of each segment.

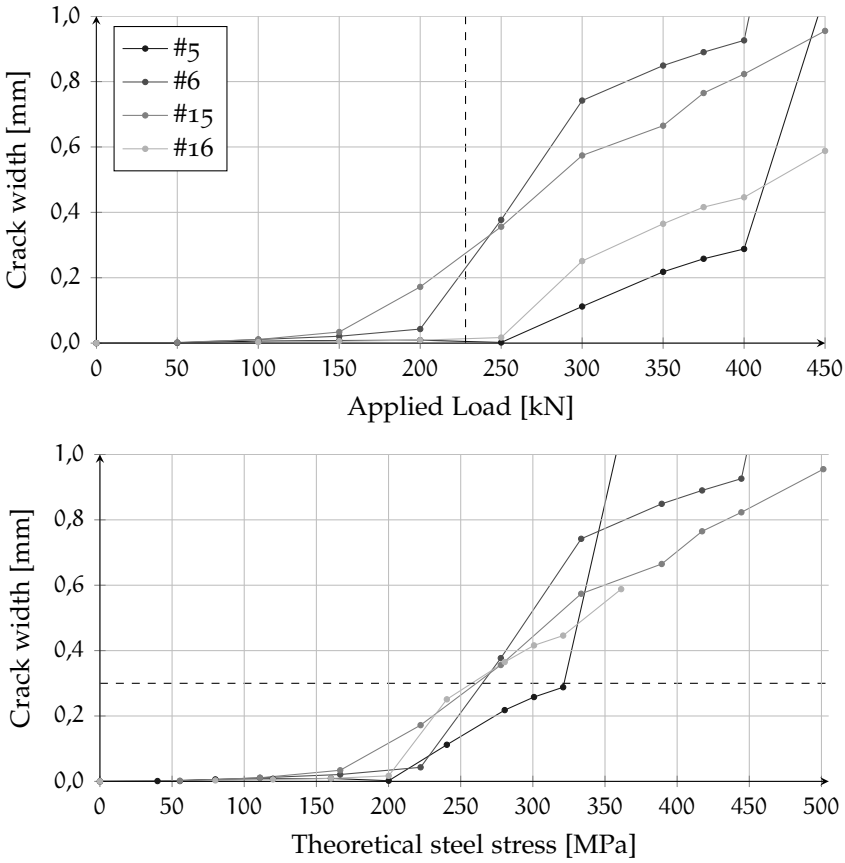

Figure D.73: 45-CV-16. Average (A and B sides) of measured crack width as a function of the applied load (top) and theoretical steel stress (bottom). The serviceability load and a crack width reference value of 0,3 mm are represented in dashed lines

D.7.6 Strain gauges

The first flexural crack was located between the core and the adjoining members, while the last cracks developed within the joint. This sequence is corroborated, for instance, by the D5 gauge reading, which is the first measuring a rise in strain. Gauge U2b measured significant strains only before failure, with a load of 550 kN. Strains higher

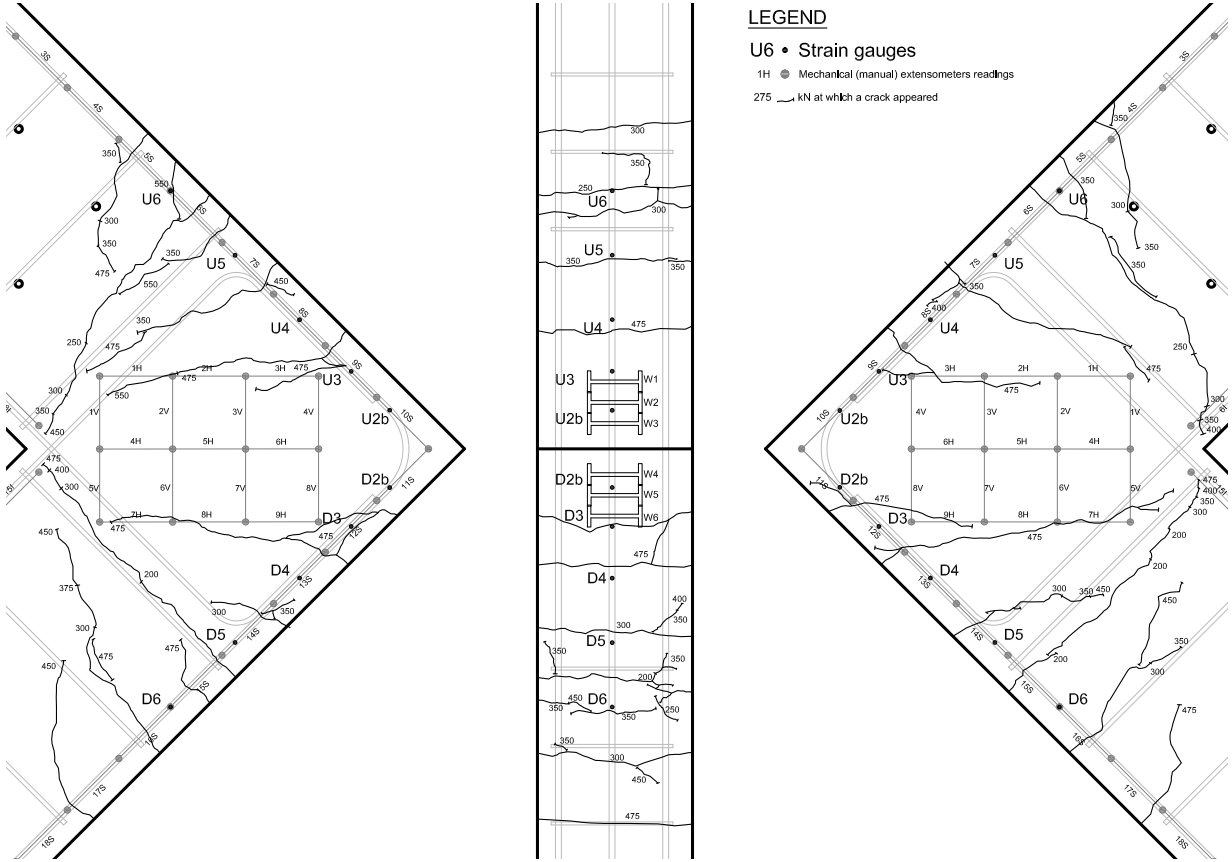

Figure D.74: 45-CV-16. Crack pattern before failure. From left to right: front view (A), side view, front view (B)

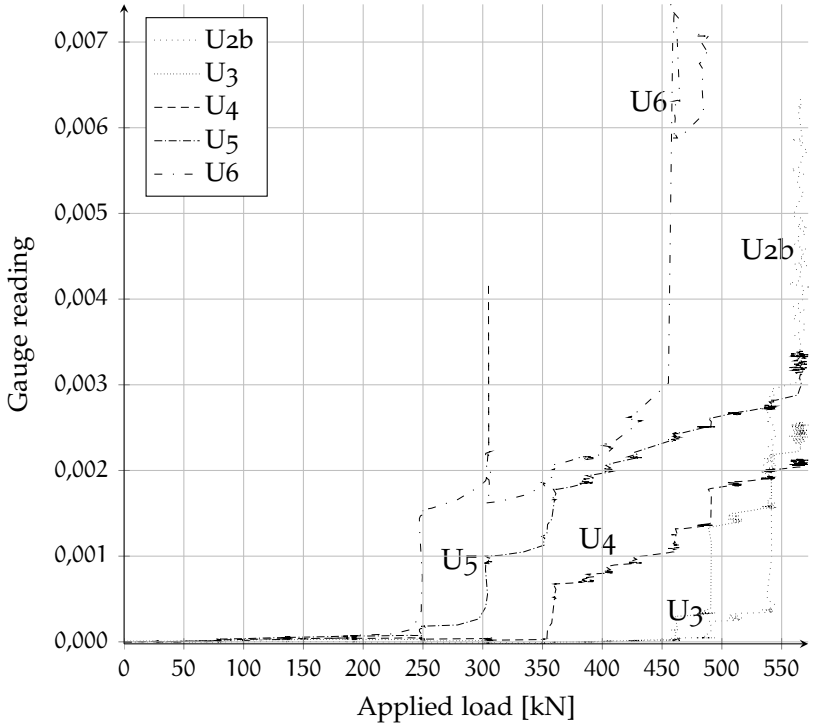

Figure D.75: 45-CV-16. Gauge readings (U)

than 2,5‰ were recorded in all gauges except U4 and D2, as shown in Figures D.75–D.76.

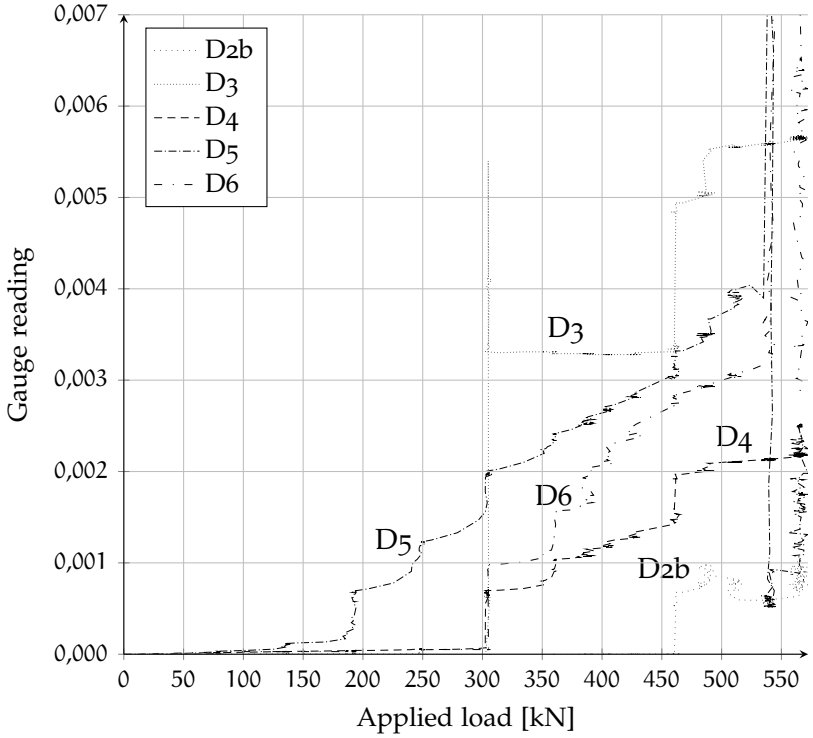

Figure D.76: 45-CV-16. Gauge readings (D)

D.7.7 Compression Strut

The recorded compressive strain was maximum in segments 4H (both sides). Segments 4V (A side) and 8V (B side) measured the largest tensile strains. No cracks were formed parallel to the central strut in this specimen before a load of 475 kN was reached. Full data are reported in Figure D.77–D.78.

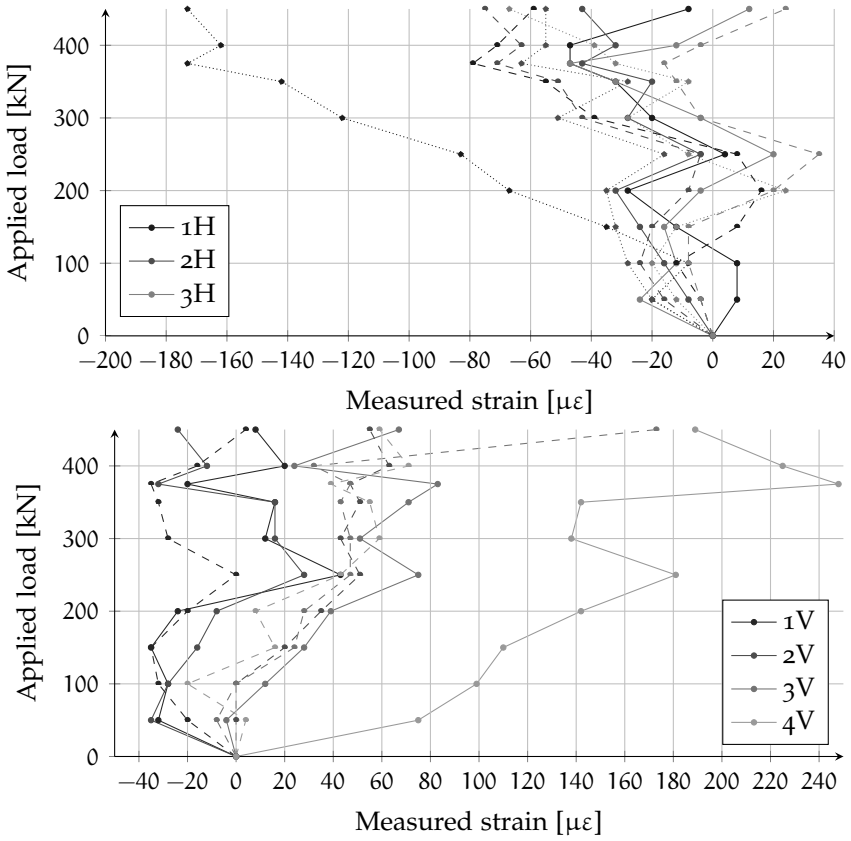

Figure D.77: 45-CV-16 – A side. Top: measured horizontal strains compared to the applied load. In dotted lines values for segments 4H to 6H, in dashed lines values for segments 7H to 9H; Bottom: vertical measured strains compared to the applied load. In dashed lines values for segments 5V to 8V

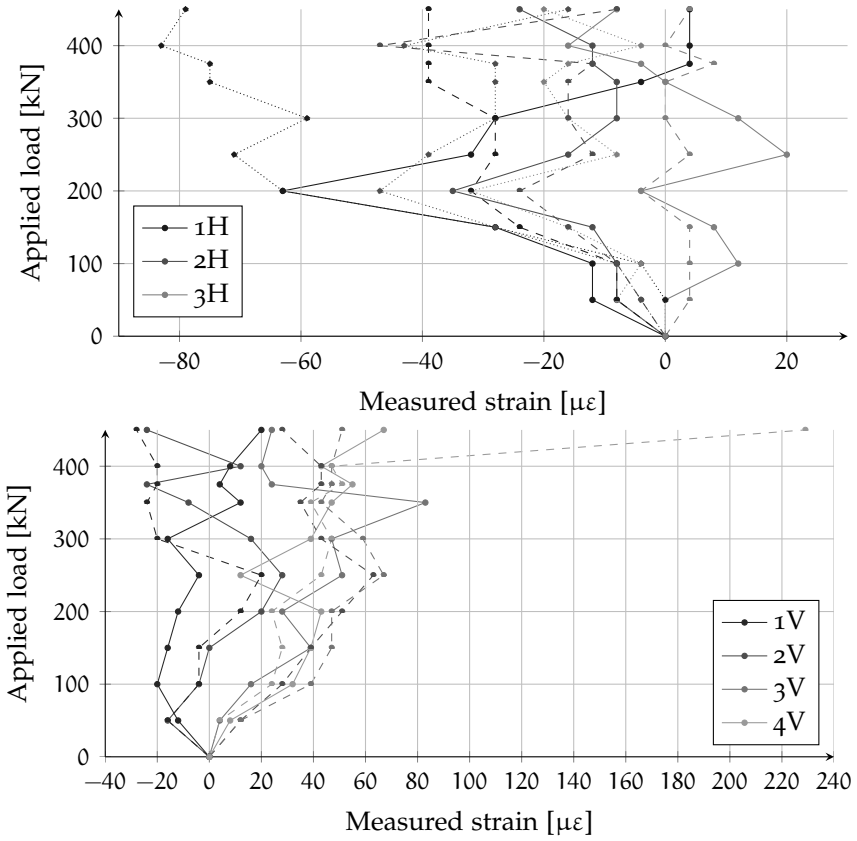

Figure D.78: 45-CV-16 – B side. Top: measured horizontal strains compared to the applied load. In dotted lines values for segments 4H to 6H, in dashed lines values for segments 7H to 9H; Bottom: vertical measured strains compared to the applied load. In dashed lines values for segments 5V to 8V

D.8 SPECIMEN 45-CV-25

The test took place 44 days after concrete pouring. The day before the test three concrete cylinders were tested: the mean compressive strength was 49,9 MPa, although the mean compressive strength of the concrete batch was more likely around 51 MPa (see Section 5.2.1.2).

D.8.1 General behavior

The applied load was increased step by step (see Table D.8) and manual measurements were taken on each step. As were no safety concerns, a final manual measurement was taken at the end of the test.

The first flexural crack was observed at a load of 300 kN. Other flexural cracks soon developed nearby between 400 and 600 kN, while bond-related cracks (parallel to the rebars) started developing at 400 kN, the same load at which first cracks along the central strut appeared.

The maximum available load was not sufficient to reach a complete rupture of the specimen, however, a state of extensive cracking of concrete and yielding of reinforcement was reached and the gauge closest to the plate measured a strain larger than 3‰. After the maximum available load was reached, six load cycles were applied to increase damage.

D.8.2 Load-displacement

The load-displacement graph presented in Figure D.79 represents the applied load and the measured displacement of the load application point during the test. Three different predictions are superposed on the graph, a simple sectional analysis, a non-linear analysis, and a more sofisticated non-linear finite element analysis performed with ATENA (as previously described in Section 5.3.6). In this case, the

Step	Load [kN]	Notes
1	100	
2	200	
3	300	First flexural crack
4	400	Formation of bond-related cracks
5	500	Formation of cracks parallel to the central strut
6	600	
7	700	
8	800	
9	900	
10	933	Capacity of loading system is reached
11	–	Six cycles 400-933 kN to increase damage

Table D.8: 45-CV-25. Load steps

measured horizontal displacement has not been corrected taking into account a supposed rigid rotation of the specimen (see Section D.8.3).

Again, a good correspondance between theoretical and experimental curves can be observed.

D.8.3 Load-rotation

Unclear data were obtained using the clinometers, making a compensation similar to that obtained for other specimens hard to obtain. In this case, a corrected graph can be obtain performing an average of the two measurements. The original data are presented in the upper graph of Figure D.80, while in the lower graph is presented the average, which is represented symmetrically.

D.8.4 Moment-curvature

The experimental moment-curvature for some sections (see Figure 5.13) is shown in Figure D.81.

The experimental curvatures are calculated, for each section, as the substraction of strains measured by targets on the reinforcement axes in that section divided by the distance between the two lines[17]; the experimental moments are computed as the force perpendicular to the beam axis multiplied by the distance of the segment axis to the point of application of the load (1,075 m for sections 6-15 and 0,875 m of sections 5-16).

D.8.5 Crack pattern

Crack evolution described in Section D.8.1 is carefully reproduced in Figure D.83, where the position of the mechanical strain gauges is also represented.

At the top of Figure D.82 is shown the measured crack width compared to the applied load, while at the bottom is provided the measured crack width compared to the theoretical steel stress, calculated at the middle of each segment.

D.8.6 Strain gauges

As for the other specimens, the U5 and D5 gauge readings were the first reaching a high strain, although in this specimen the U6 gauge recorded a moderate strain since the beginning of the test. Gauge D6 was broken and provided no data. At the ultimate load, U2b and D2b gauges measured a strain of 3,0‰and 4,0‰, as can be observed in Figures D.84–D.85.

[17] $1/r = \frac{\varepsilon_s - \varepsilon_i}{d - 2d'}$

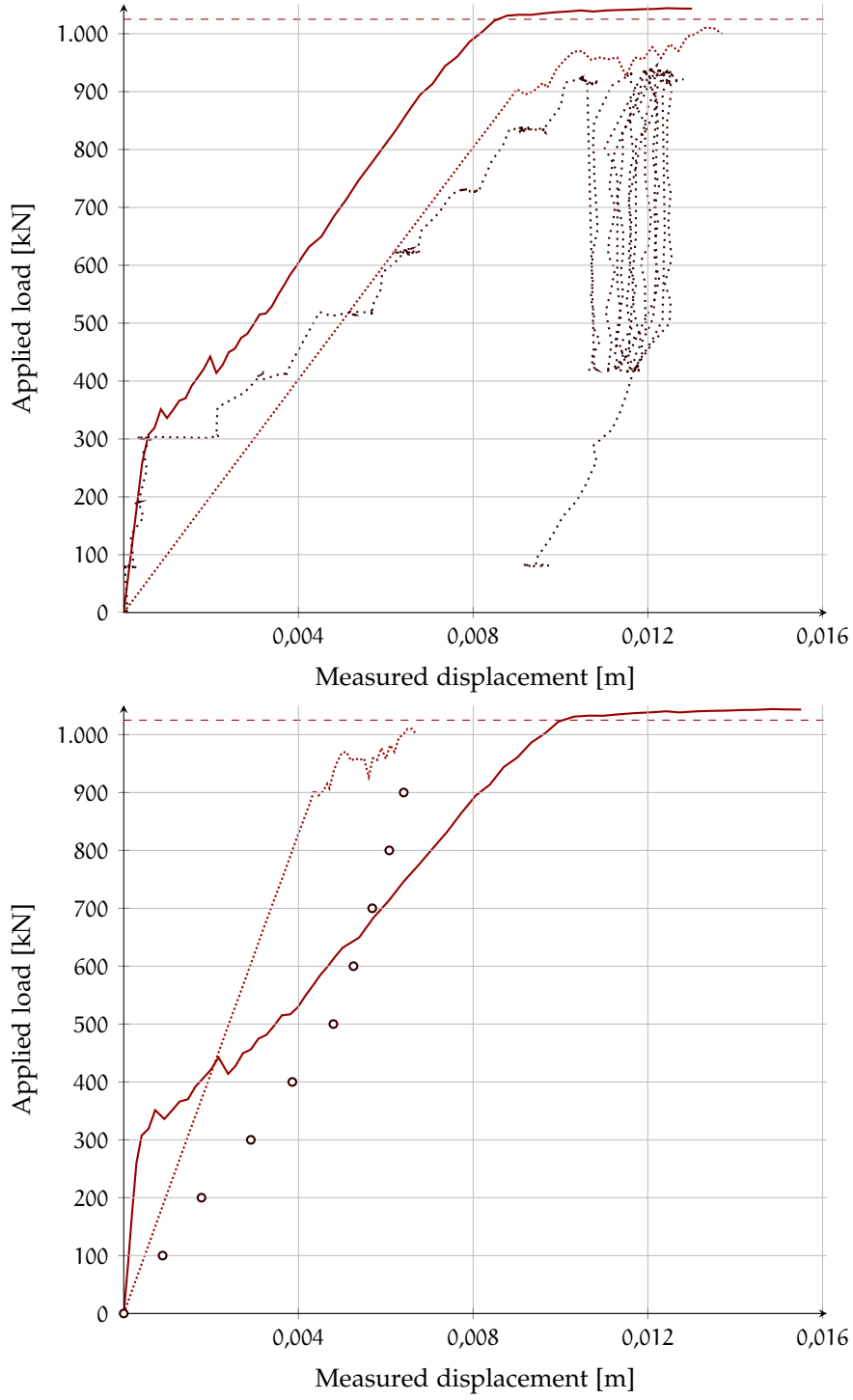

Figure D.79: Vertical displacement of the load application point (up) and horizontal displacement measured by the probe indicator (down). Experimental data (·····)(··) and predictions by sectional analysis (- - -), non–linear analysis (·····) and ATENA (——)

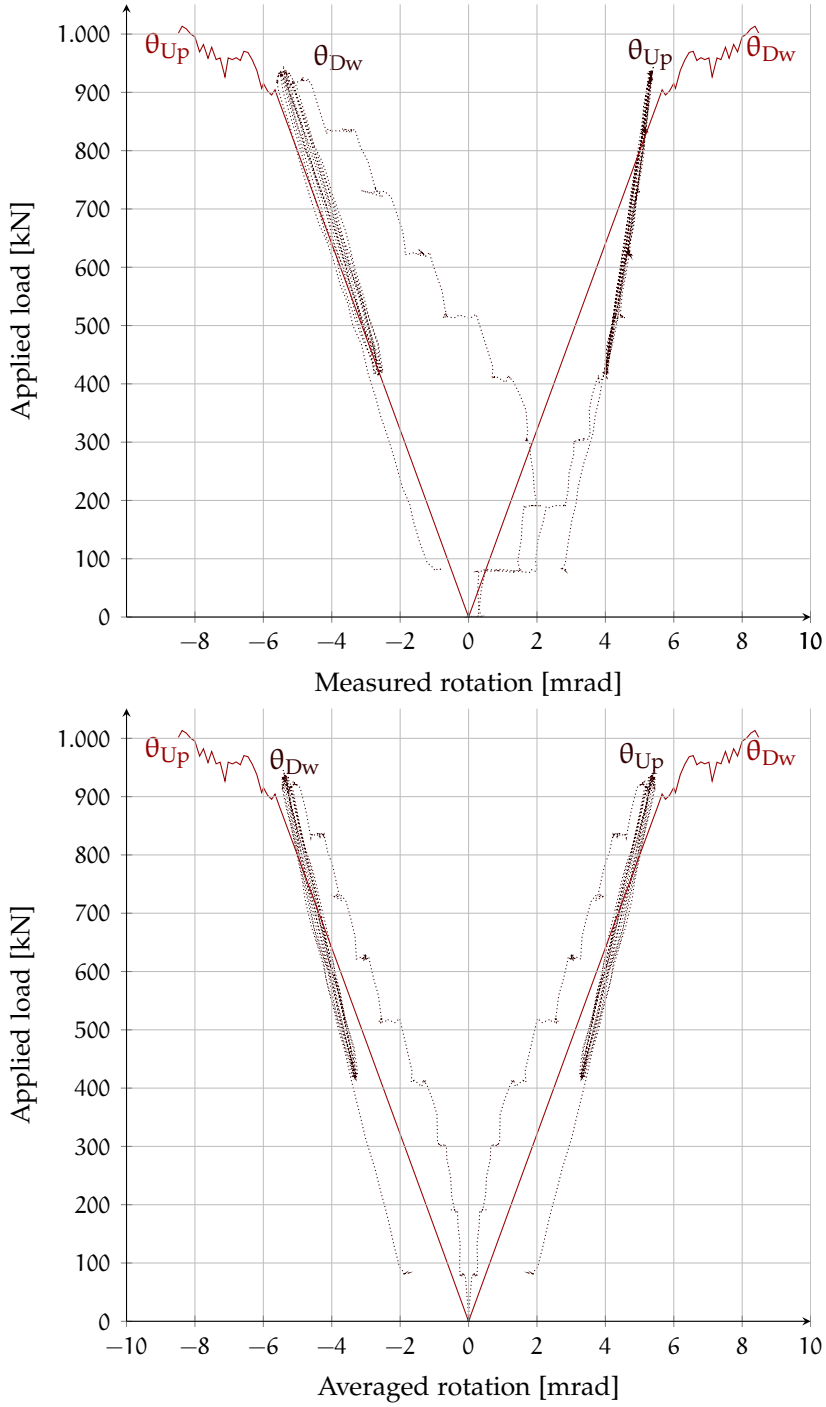

Figure D.80: Applied load Vs measured (up) and averaged (down) rotations.
In solid line, the non linear theoretical estimation

D.8.6.1 *Hysteresis curves*

The same graph of the previous paragraph is reported in Figure D.86 for gauges 2b including the measurements during the cycling load.

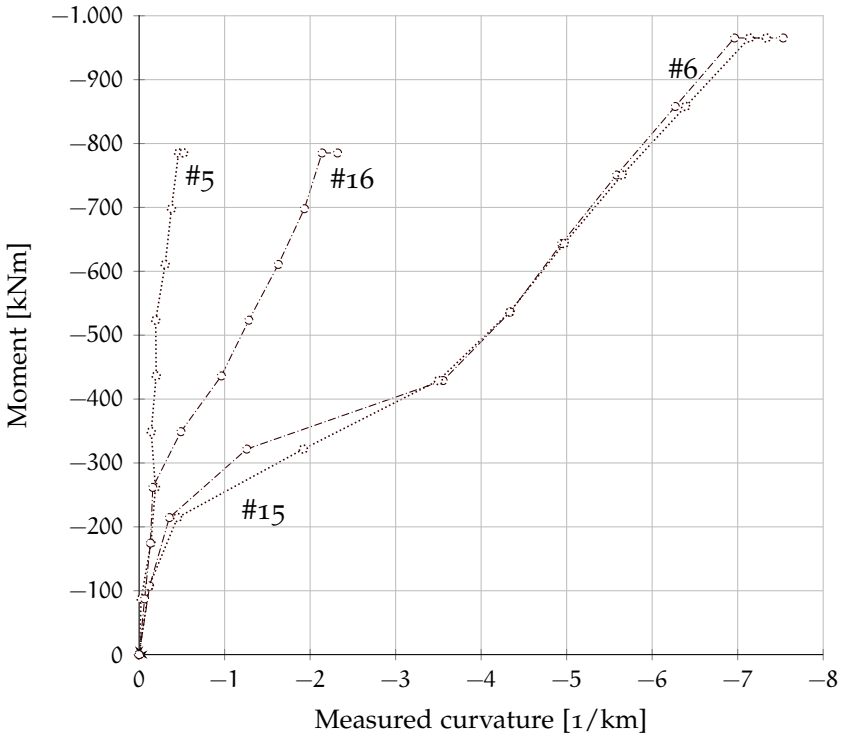

Figure D.81: 45-CV-25. Average (side A and B) measured M–χ diagram for some relevant sections compared to the theoretical prediction

D.8.7 Compression Strut

The recorded compressive strain was maximum in the strut axis with a mean compressive strain around −350 με at a load of 900 kN. Maximum strains were measured in segment H4 (−500 με). On both sides cracks intercept some segments: the wider cracks were measured on the outer edge (segment 4V and 8V). Full data are reported in Figure D.87–D.88.

D.8.8 Vibrating wire strain gauges

In this specimen was observed a moderate lateral strain only by the W5 gauge. Complete data are reported in Figure D.89.

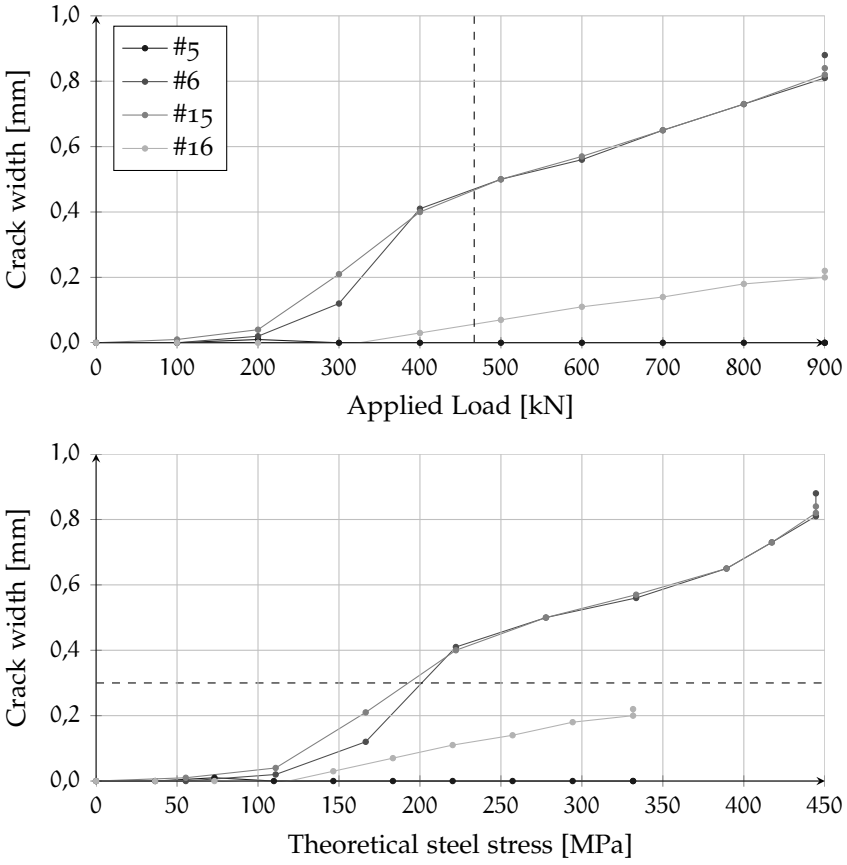

Figure D.82: 45-CV-25. Average (A and B sides) of measured crack width as a function of the applied load (top) and theoretical steel stress (bottom). The serviceability load and a crack width reference value of 0,3 mm are represented in dashed lines

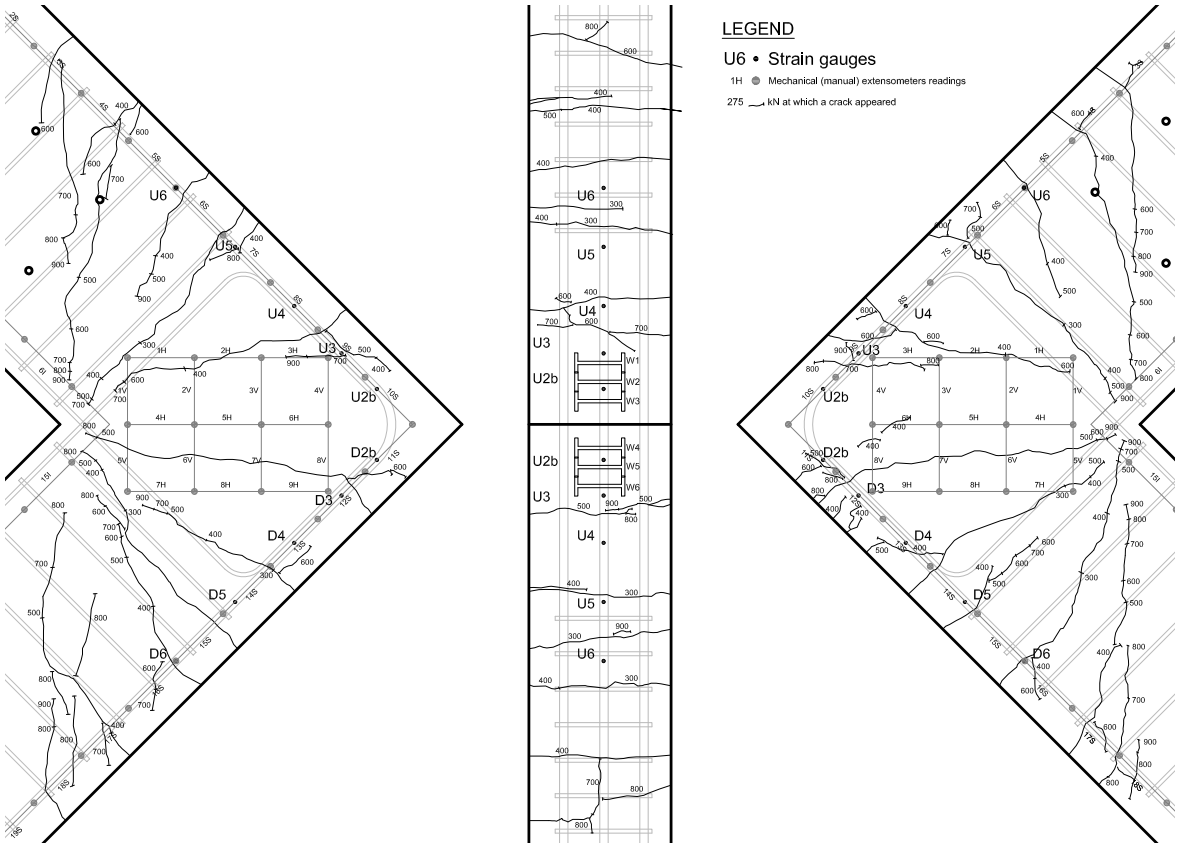

Figure D.83: 45-CV-25. Crack pattern. From left to right: front view (A), side view, front view (B)

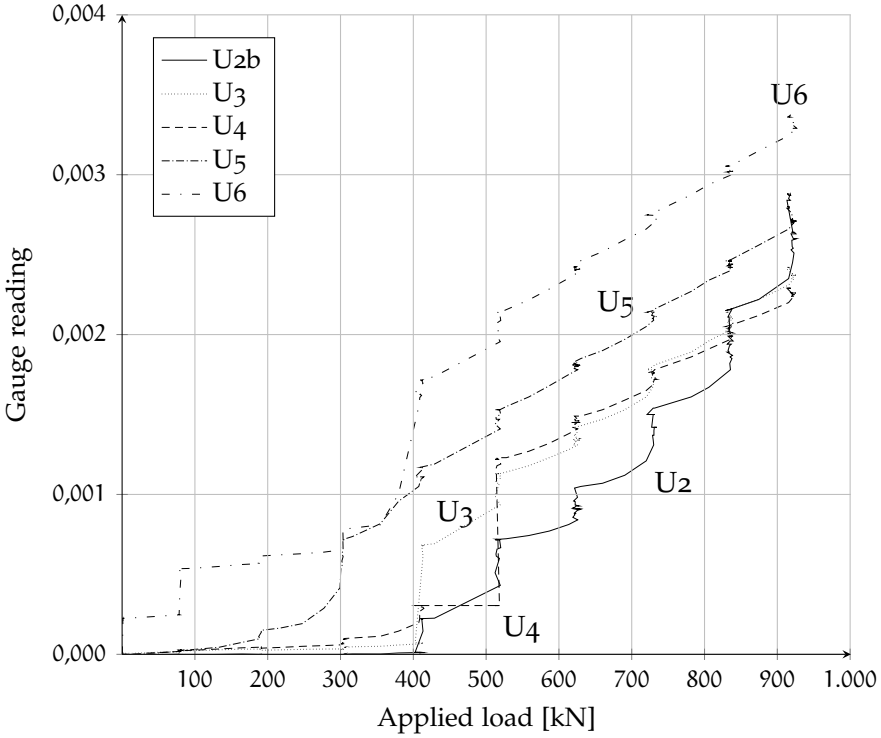

Figure D.84: 45-CV-25. Gauge readings (U)

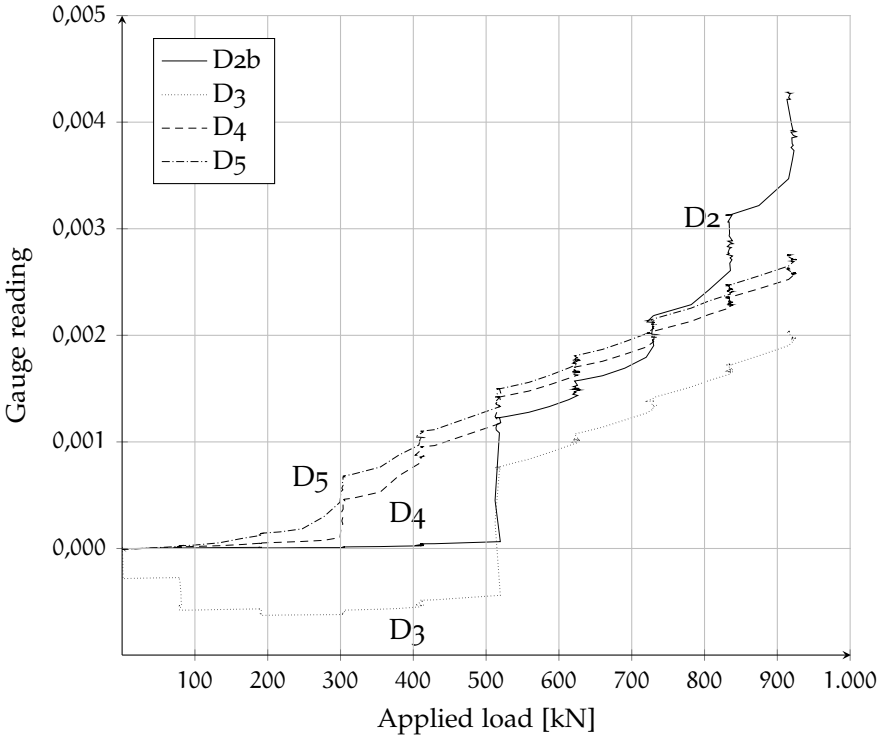

Figure D.85: 45-CV-25. Gauge readings (D)

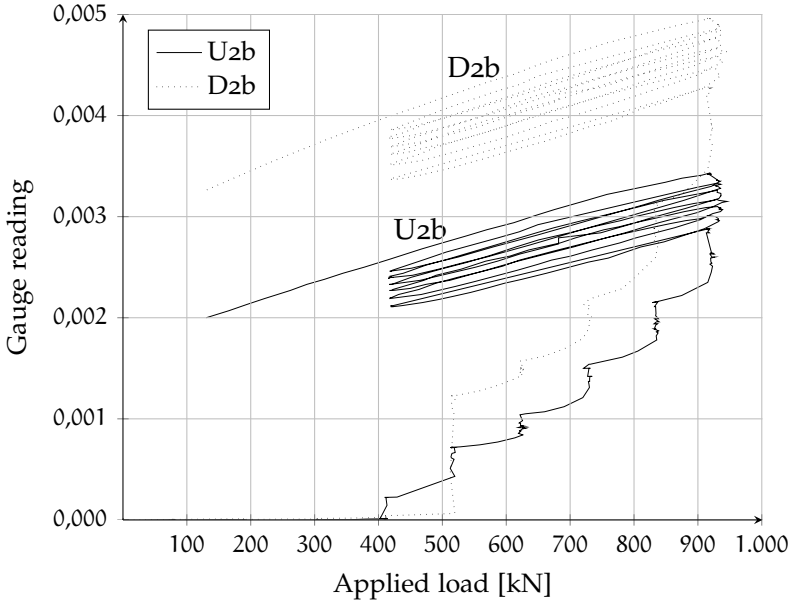

Figure D.86: 45-CV-25. Hysteresis curves for gauge 2b

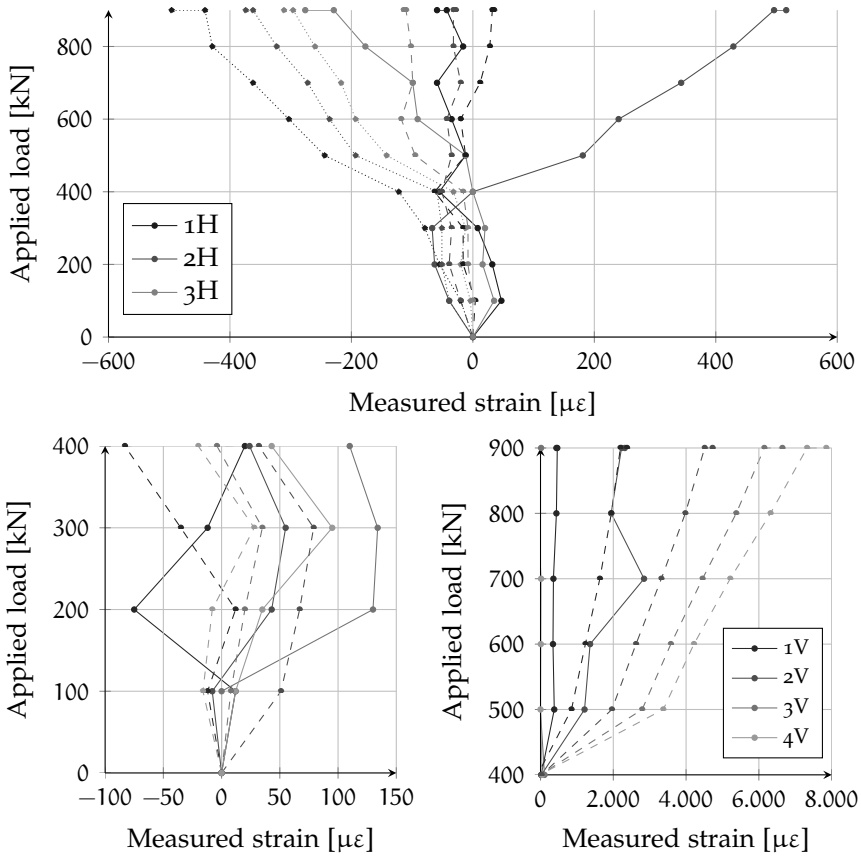

Figure D.87: 45-CV-25 – A side. Top: measured horizontal strains compared to the applied load. In dotted lines values for segments 4H to 6H, in dashed lines values for segments 7H to 9H; Bottom: vertical measured strains compared to the applied load. In dashed lines values for segments 5V to 8V

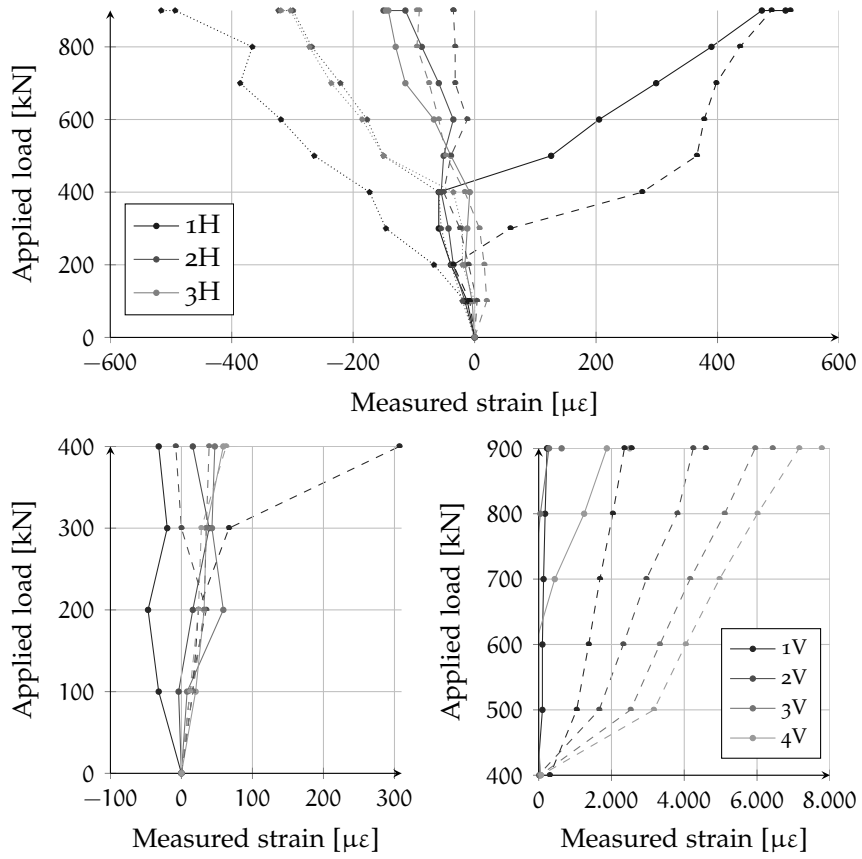

Figure D.88: 45-CV-25 – B side. Top: measured horizontal strains compared to the applied load. In dotted lines values for segments 4H to 6H, in dashed lines values for segments 7H to 9H; Bottom: vertical measured strains compared to the applied load. In dashed lines values for segments 5V to 8V

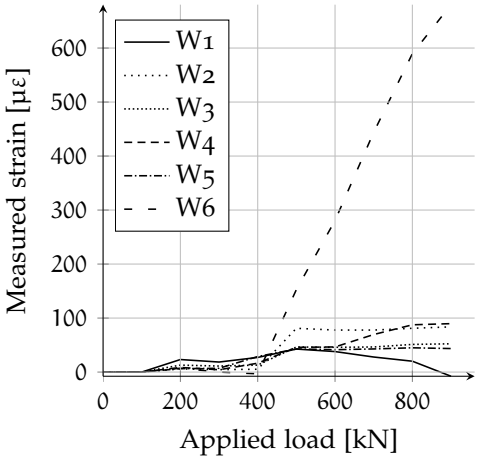

Figure D.89: 45-CV-25. Vibrating wires

BIBLIOGRAPHY

[1] fib Bulletin 10: Bond of Reinforcement in Concrete. State-of-Art Report, August 2000. (Cited on pages 6 and 8)

[2] fib Bulletin 45: Practictioner's Guide to Finite Element Modelling of Reinforced Concrete Structures: State-of-art Report marine environment, June 2008. (Cited on pages 79 and 80)

[3] fib Bulletin 50: Concrete structures for oil and gas fields in hostile marine environment, October 2009. (Cited on pages 16, 67, and 68)

[4] fib Bulletin 65-66: Model Code 2010 - Final Draft, 2012. (Cited on pages 8 and 11)

[5] ACI Commitee 318. *Building Code Requirements for Structural Concrete and Commentary.* American Concrete Institute, Farmington Hills, Michigan, January 2008. (Cited on pages 8, 10, 95, and 104)

[6] ACI Commitee 352. *Recommendations for Design of Beam-Column Connections in Monolithic Reinforced Concrete Structures*. American Concrete Institute, Farmington Hills, Michigan, June 2002. (Cited on page 37)

[7] ASTM. *Standard A970 – Standard Specification for Headed Steel Bars for Concrete Reinforcement*. , West Conshohocken, PA 19428-2959, United States., 04a$^{\epsilon 1}$ edition, February 2004. Editorial corrections were made throughout the standard in March 2004. (Cited on page 46)

[8] CEB. *Design of Fastenings in Concrete - Draft CEB Guide - Part 1 to 3*. CEB, bulletin 226 edition, August 1995. (Cited on pages 24, 25, 51, 52, and 102)

[9] European Committee for Standardization: Eurocode 2 (CEN). *Design of concrete structures. Part 1.1: General rules and rules for buildings*, en 1992-1-1 edition, December 2004. (Cited on pages 8 and 12)

[10] Paul William Abeles, B. K. Bardhan-Roy, and Frederick Henry Turner. *Prestressed concrete designer's handbook*. Cement and Concrete Association, London, 1976. (Cited on page 57)

[11] Bill Angelakos. *The Behavior of Reinforced Concrete Knee Joints Under Earthquake*. PhD thesis, University of Toronto, Toronto, 1999. (Cited on page 60)

[12] A.R. Azami and A.R. Khoei. 3D computational modeling of powder compaction processes using a three-invariant hardening cap plasticity model. *Finite Elements in Analysis and Design*, 42(8–9):792 – 807, 2006. ISSN 0168-874X. doi: http://dx.doi.org/10.1016/j.finel.2006.01.011. URL http://www.sciencedirect.com/science/article/pii/S0168874X06000187. (Cited on page 223)

[13] G. D. Base. An investigation of the use of strand in pre–tensioned prestressed concrete beams. Research Report 11, Cement and Concrete Association, London, January 1958. (Cited on page 57)

[14] Tarek Refaat Bashandy. *Application of Headed Bars in Concrete Members*. PhD thesis, The University of Texas at Austin, 1996. (Cited on pages 25, 27, 41, and 124)

[15] Dale E. Berner, Gen C. Gerwick, and George C. Hoff. T–headed stirrup bars. *Concrete International*, 13(5):49–53, May 1991. (Cited on pages 16, 69, 77, 78, and 80)

[16] Ronaldo I. Borja and Atilla Aydin. Computational modeling of deformation bands in granular media. Geological and mathematical framework. *Computer Methods in Applied Mechanics and Engineering*, 193(27-29):2667 – 2698, 2004. ISSN 0045-7825. Computational Failure Mechanics for Geomaterials. (Cited on page 222)

[17] P. T. Brown. Numerical analysis of uniformly loaded circular rafts on deep elastic foundations. *Geotechnique*, 19(3):399–404, 1969. doi: 10.1680/geot.1969.19.3.399. (Cited on page 95)

[18] Thomas Brown. *Confederation Bridge Ice Force Monitoring*, chapter 21, pages 1–10. 2008. doi: 10.1061/41016(314)118. URL http://ascelibrary.org/doi/abs/10.1061/41016%28314%29118. (Cited on page 68)

[19] J. Calavera Ruiz. Cinco accidentes célebres en la historia de la construcción. In *Primer Congreso Uruguayo de Gestión de la Calidad, Patología y Recuperaciónde la Construcción*, Montevideo, 2004. ALCONPAT. (Cited on page 79)

[20] Luigi Cedolin and Gianluca Cusatis. Identification of concrete fracture parameters through size effect experiments. *Cement and Concrete Composites*, 30(9):788 – 797, 2008. ISSN 0958-9465. doi: 10.1016/j.cemconcomp.2008.05.007. URL http://www.sciencedirect.com/science/article/pii/S0958946508000607. (Cited on page 92)

[21] Jan Ĉervenka and Vassilis K. Papanikolaou. Three dimensional combined fracture–plastic material model for concrete. *International Journal of Plasticity*, 24(12):2192 – 2220, 2008. ISSN 0749-6419. doi: 10.1016/j.ijplas.2008.01.004. URL http://www.sciencedirect.com/science/article/pii/S0749641908000259. (Cited on page 223)

[22] V. Ĉervenka, V. Novák, D. Lehký, and R. Pukl. Identification of shear wall failure mode. In *ICF XI, International Conference on Fracture*, Torino, March 2005. (Cited on page 174)

[23] Vladimir Ĉervenka, Jan Ĉervenka, and Libor Jendele. *ATENA Program Documentation – Part 1 – Theory*. Ĉervenka Consulting, Prague, October 2013. (Cited on page 224)

[24] W.F. Chen and D.J. Han. *Plasticity for Structural Engineers*. J. Ross Publishing classics. J ROSS PUB Incorporated, 2007. ISBN 9781932159752. (Cited on page 125)

[25] J. Chinn. The use of Nelson studs with idealite light-wight aggregate concrete in composite construction. Part I. Report, University of Colorado, Engineering Experiment Station, April 1961. (Cited on page 15)

[26] Chien Kuo Chiu, Kai Ning Chi, and Ker Chun Lin. Strength Performance of T-Headed Rebar in Concrete. *Applied Mechanics and Materials*, 284-287:1401–1408, 2013. (Cited on page 21)

[27] Dong-Uk Choi. Test of Headed Reinforcement in Pullout II: Deep Embedment. *International Journal of Conrete Structures and Materials*, 18(3E):151–159, December 2006. (Cited on pages 21, 35, and 47)

[28] S. C. Chun and J. G. Lee. Anchorage Strengths of Lap Splices Anchored by High-Strength Headed Bars. In *FraMCos (International Association of Fracture Mechanics for Concrete and Concrete Structures) 8*, 2013. (Cited on pages 21, 46, and 195)

[29] Sung-Chul Chun and Dae-Young Kim. Evaluation of mechanical anchorage of reinforcement by exterior beam–column joint experiments. In *Proceedings of 13th World Conference on Earthquake Engineering*, number 0326, Vancouver, Canada, August 2004. (Cited on pages 21, 36, 39, and 124)

[30] Sung Chul Chun, Sung Ho Lee, Thomas H.K. Kang, Bohwan Oh, and John W. Wallace. Mechanical anchorage in exterior beam–column joints subjected to cyclic loading. *ACI Structural Journal*, 104(1):102–113, January 2007. (Cited on pages 21 and 37)

[31] M. P. Collins, F. J. Vecchio, and G. Mehlhorn. An international competition to predict the response of reinforced concrete panels. *Canadian Journal of Civil Engineering*, 12:624–644, 1985. doi: 10.1139/l85-070. (Cited on page 222)

[32] M. P. Collins, F. J. Vecchio, and R. G. Selby. The failure of an offshore platform. *Concrete International*, 19(8):28–35, August 1997. (Cited on pages 79 and 80)

[33] Karl Culmann. *Die Graphische Statik*. Meyer & Zeller, 1875. (Cited on page 59)

[34] René De Borst. *Non-linear analysis of frictional materials*. PhD thesis, Technische Universiteit Delft, April 1986. (Cited on page 223)

[35] Richard Alan DeVries. *Anchorage of Headed Reinforcement in Concrete*. PhD thesis, The University of Texas at Austin, December 1996. (Cited on pages 21, 25, 33, 92, 95, 96, 97, 98, 99, 102, 107, and 124)

[36] W. H. Dilger and A. Ghali. Shear reinforcement for concrete slabs. *ASCE Journal of Structural Engineering*, 107-12:2403–2420, 1981. (Cited on page 15)

[37] W. H. Dilger and A. Ghali. Double head studs as ties in concrete walls and columns. *Concrete International*, 19(6):59–66, June 1997. (Cited on pages 15 and 41)

[38] Manuel Durán Fuentes. La obra del puente: fuente primaria para su conocimiento e identificación. In *Actas del Cuarto Congreso Nacional de Historia de la Construcción.*, Cádiz, 27-29 January 2005. Sociedad Española de Historia de la Construcción. (Cited on page 66)

[39] R. Eligehausen, Rainer Mallée, and J. F. Silva. *Anchorage in Concrete Construction, Volume 10*. John Wiley & Sons, March 2006. (Cited on pages 52 and 102)

[40] *Lenton Terminator for Rebar Anchorage*. ERICO International Corporation, 2011 edition, 2013. URL `http://www.erico.com/public/library/concrete/lt0434.pdf`. URL retrieved on december 12, 2013. (Cited on page 19)

[41] Carlos Fernández Casado. Fotoelasticimetría. *Revista de Obras Públicas*, 80(2589-2590-2595-2602):(2602): 353–355; (2595): 185–191; (2590): 55–61; (2589): 29–35, 1932. (Cited on page 56)

[42] W. Fuchs, R. Eligehausen, and J. E. Breen. Concrete capacity design (CCD) approach for fastening to concrete. *Structural Journal*, 92(1):73–94, January 1995. (Cited on pages 22 and 109)

[43] Y.Y. Fung and P. Tong. *Classical and Computational Solid Mechanics*. Advanced Series in Engineering Science. World Scientific Publishing Company, Incorporated, 2001. ISBN 9789810239121. (Cited on page 125)

[44] J. Furche and R. Eligehausen. Lateral blow–out failure of headed studs near a free edge. In ACI International, editor, *Anchors in Concrete - Design and Behavior*, volume SP-130, pages 235–252, Farmington Hills, Michigan, 1991. (Cited on pages 46, 50, 51, 52, 54, and 113)

[45] C. C. Fynboe and E. Thorenfeldt. SP1: Static Pullout Tests. Technical Report STF65 F86083 (Proprietary Report), SINTEF, 1986. (Cited on page 16)

[46] Pietro G. Gambarova. Bond in reinforced concrete: where do we stand today? In *General aspects of bond*, volume 1, pages 1–13. Bond in concrete 2012: Bond, Anchorage, Detailing. Fourth international simposium, June 2012. (Cited on page 6)

[47] Ben C. Jr. Gerwick. *Construction of Marine and Offshore Structures, Third Edition*. Taylor & Francis, 2007. ISBN 9781420004571. URL http://books.google.es/books?id=2lm5zXTivm4C. (Cited on page 80)

[48] Amin Ghali and Ramez B. Gayed. Bundling of headed bars in concrete. *Canadian Journal of Civil Engineering*, 39(7):849–853, 2012-07-20T00:00:00. doi: doi:10.1139/l2012-068. URL http://www.ingentaconnect.com/content/nrc/cjce/2012/00000039/00000007/art00012. (Cited on page 48)

[49] G. B. Hasselwander, J. O. Jirsa, J. E. Breen, and K. Lo. Strenght and behavior of anchor bolts embedded near edges of concrete piers. Research Project 3-5-74-29, Center for Highway Research. The University of Texas, Austin, May 1977. (Cited on pages 50, 109, and 113)

[50] N. M. Hawkins. The Bearing Strength of Concrete. Loading through rigid plates covering part of the full supporting area. Research Report R 54, The University of Sidney, March 1967. (Cited on pages 54, 94, 109, and 112)

[51] J. Hofmann and R. Eligehausen. Tragverhalten und bemessung von kopfbolzenverankerungen am bauteilrand unter beliebiger belastungsrichtung. *Beton und Stahlbetonbau*, 96(4):280, 2001. (Cited on page 52)

[52] D.A. Hordijk. *Local Approach to Fatigue of Concrete*. PhD thesis, Delft University of Technology, 1991. (Cited on page 224)

[53] *Product Catalogue*. HRC – Metalock Industrier AS, PO box 591, N-3412 Lierstranda, Norway, 2013. URL http://www.hrc-europe.com/pdf/catalogue.pdf. URL retrieved on february 11, 2013. (Cited on pages 18, 19, 42, 77, and 102)

[54] J. M. Ingham, M. J. N. Priestley, and F. Seible. Bridge knee joint with headed reinforcement. In *Pacific Conference on Earthquake Engineering*, San Diego, CA, 1995. (Cited on page 35)

[55] R. S. K. T. Iyengar and M. K. Prabhakara. A three dimensional elasticity solution for rectangular prism under end loads. *Zeitschrift für Angewandte Mathematik und Mechanik*, 49(6):321–384, 1969. (Cited on page 57)

[56] B. Jakobsen, E. Gausel, H. Stemland, and A. Tomaszewicz. Sleipner A GBS Loss Report 15: Full Scale Test of Tri-Cell Walls, Test Plan and Preparation Work. Research Report STF22 A97859, SINTEF, 1997. (Cited on page 42)

[57] M. Jirasek and Z.P. Bazant. *Inelastic Analysis of Structures*. John Wiley & Sons, 2002. ISBN 9780471987161. (Cited on page 125)

[58] J. O. Jirsa and Jose L. G. Marques. A study of hooked bar anchorages in beam-column joints. Final Report Project 33, Reinforced Concrete Research Council, Structural Research Laboratory. The Univesity of Texas at Austin, July 1972. (Cited on pages 11 and 27)

[59] Morgan Johansson. *Structural Behaviour in Concrete Frame Corners of Civil Defence Shelter*. PhD thesis, Chalmers University of Technology, Division of Conrete Structures, Department of Structural Engineering. Göteborg, Sweden, 2000. (Cited on pages 60 and 63)

[60] Driscoll G. C. Jr. and R. G. Slutter. Research on composite design at lehigh university. Fritz Laboratory reprint 180, Leigh University, Fritz Engineering Laboratory, 1961. (Cited on page 15)

[61] Thomas H.-K. Kang, M. Shin, and N. Mitra. Headed reinforcement applications for reinforced concrete beam-column connections. In *Structures Congress 2009: Don't Mess with Structural Engineers: Expanding Our Role*, 2009. doi: 10.1061/41031(341)164. (Cited on page 21)

[62] Thomas H.-K. Kang, Sang-Su Ha, and Dong-Uk Choi. Bar pullout tests and seismic tests of small-headed bars in beam-column joints. *ACI Structural Journal*, 107(1):32–42, January 2010. (Cited on pages 21 and 47)

[63] E.L. Kemp and P.R. Mukherjee. Inelastic behavior of concrete knee-joints. *The Consulting Engineer*, pages 44–48, October 1968. (Cited on page 62)

[64] Y. Kim, Y. Yoon, W. Cook, and D. Mitchell. Repeated loading tests of concrete walls containing headed shear reinforcement. *Journal of Structural Engineering*, 130(8): 1233–1241, 2004. doi: 10.1061/(ASCE)0733-9445(2004)130:8(1233). URL http://ascelibrary.org/doi/abs/10.1061/%28ASCE%290733-9445%282004%29130%3A8%281233%29. (Cited on pages 21 and 43)

[65] Helmut Kupfer, Hubert K. Hilsdorf, and Hubert Rusch. Behavior of concrete under biaxial stresses. *Journal Proceedings*, 66(8): 656–666, August 1969. (Cited on page 225)

[66] D. W. Lee and J. E. Breen. Factors affecting anchor bolt development. Research Project 3-5-65-88 Anchor Bolt Development, Center for Highway Research. The University of Texas, Austin., August 1966. (Cited on page 50)

[67] H.-J. Lee and S.-J. Hwang. High-strength concrete and reinforcing steel in beam-column connections. In *Structures Congress 2013: Bridging Your Passion with Your Profession*, 2013. doi: 10.1061/9780784412848.140. (Cited on page 21)

[68] D. Lehman, C. Roeder, and R. Larsen. Design of cotton duck bridge bearing pads. *Journal of Bridge Engineering*, 10(5):555–563, 2005. doi: 10.1061/(ASCE)1084-0702(2005)10:5(555). URL http://ascelibrary.org/doi/abs/10.1061/%28ASCE%291084-0702%282005%2910%3A5%28555%29. (Cited on page 41)

[69] Dawn E. Lehman, Sharon E. Gookin, Adrian M. Nacamuli, and Jack P. Moehle. Repair of earthquake–damaged bridge columns. *ACI Structural Journal*, 98(2):233–242, March 2001. (Cited on page 44)

[70] Dawn E. Lehman, Emily Brackmann, Amanda Jellin, and Charles W. Roeder. *Seismic Performance of Pile–Wharf Connections*, volume TCLEE 2009: Lifeline Earthquake Engineering in a Multihazard Environment, chapter 122, pages 1–13. Oakland, CA, July 2009. doi: 10.1061/41050(357)82. URL http://ascelibrary.org/doi/abs/10.1061/41050%28357%2982. (Cited on pages 40 and 41)

[71] Fritz Leonhardt. Reducing the shear reinforcement in reinforced concrete beams and slabs. *Magazine of Concrete Research*, 17(53):187–198, 1965. (Cited on page 59)

[72] Fritz Leonhardt and E. Mönnig. *Vorlesungen über Massivbau: Teil 2 Sonderfälle der Bemessung im Stahlbetonbau*. Springer, 1975. (Cited on pages 57, 90, 91, and 93)

[73] W. Lode. Versuche über den einfluß der mittleren hauptspannung auf das fließen der metalle eisen, kupfer und nickel. *Zeitschrift für Physik*, 36(11-12):913–939, 1926. doi: 10.1007/BF01400222. (Cited on page 219)

[74] Hannes Ludescher, S. A. Haugerud, and Miguel Fernández Ruiz. Detail design of the MPU Heavy Lifter. *fib Symposium*, pages 931–937, 2008. (Cited on pages 82 and 83)

[75] Karin Lundgren. *Three-Dimensional Modelling of Bond in Reinforced Concrete*. PhD thesis, Chalmers University of Technology, Division of Concrete Structures, Department of Structural Engineering. Göteborg, Sweden, 1999. (Cited on page 63)

[76] Y. H. Luo, A. J. Durrani, Shaoliang Bai, and Jixing Yuan. Study of reinforcing detail of tension bars in frame corner connections. *ACI Structural Journal*, 91(4):486–496, July 1994. (Cited on page 62)

[77] G. Magnel. Design of the ends of prestressed concrete beams. Technical Report 2, Concrete and constructional engineering, May 1949. (Cited on page 55)

[78] Yann Malecot, Laurent Daudeville, Fabrice Dupray, Cédric Poinard, and Eric Buzaud. Strength and damage of concrete under high triaxial loading. *European Journal of Environmental and Civil Engineering*, 14(6-7):777–803, 2010. doi: 10.1080/19648189.2010.9693262. URL http://www.tandfonline.com/doi/abs/10.1080/19648189.2010.9693262. (Cited on page 58)

[79] R. Mark. *Architectural technology up to the scientific revolution: the art and structure of large-scale buildings*. New liberal arts series. MIT Press, 1993. ISBN 9780262132879. (Cited on pages 65 and 66)

[80] Peter Marti. Basic tools of reinforced concrete beam design. *ACI Journal*, 82(82-4):11, January-February 1985. (Cited on page 59)

[81] Eric Eiji Matsumoto. *Development of a Precast Bent System*. PhD thesis, The Univesity of Texas at Austin, December 2000. (Cited on page 39)

[82] Bryan Mayfield, Fung-Kew Kong, Alan Bennison, and Julian C. D. Twiston Davies. Corner joint details in structural lightweight concrete. *ACI Structural Journal*, 68(5):366–372, May 1971. (Cited on page 62)

[83] S.W. McConnell and J.W. Wallace. Use of t-headed bars in reinforced concrete knee-joints subjected to cyclic lateral loading. Research Report CU/CEE-94/10, Clarkson University, Potsdam, NY, June 1994. (Cited on pages 34 and 38)

[84] P. J. McMackin, R. G. Slutter, and J. W. Fisher. Headed steel anchor under combined loading. *AISC Engineeging Journal*, 10-2:43–52, 1973. (Cited on page 15)

[85] R.E. Melchers and R. Hough. *Modeling Complex Engineering Structures*. American Society of Civil Engineers, 2007. ISBN 9780784471531. URL http://books.google.es/books?id=Y_QKNDGobC0C. (Cited on pages 69 and 78)

[86] P. Menétrey and K. J. Willam. Triaxial failure criterion for concrete and its generalization. *ACI Structural Journal*, 92(3):311–318, 1995. (Cited on pages 58, 93, and 224)

[87] Boyan I. Mihaylov, Evan C. Bentz, and Michael P. Collins. Behavior of deep beams with large headed bars. *ACI Structural Journal*, 110(6):1013–1022, November-December 2013. (Cited on page 47)

[88] John Minor. *A study of bent bar anchorages in concrete*. PhD thesis, Rice University, Houston, Texas, December 1971. (Cited on page 10)

[89] D. Mitchell, D., W. Cook, Y. Deng, and J. Liu. Confinement of columns and wall boundary elements using headed bars. *Journal of Structural Engineering*, page 04013080, April 2013. doi: 10.1061/(ASCE)ST.1943-541X.0000850. URL http://ascelibrary.org/doi/abs/10.1061/%28ASCE%29ST.1943-541X.0000850. (Cited on page 44)

[90] Esneyder Montoya, Frank J. Vecchio, and Shamim A. Sheikh. Compression field modeling of confined concrete: Constitutive models. *Journal of Materials in Civil Engineering*, 18(4):510–517, July/August 2006. (Cited on pages 58 and 93)

[91] Emil Mörsch. *Der Eisenbetonbau, seine Theorie und Anwendung*. Stuttgart, K. Wittwer, 1908. (Cited on page 59)

[92] Emil Mörsch. Über die berechnung der gelenkquader. *Beton und Eisen*, 23(12):156–161, 1924. (Cited on page 55)

[93] A. Muttoni, J. Schwartz, and B. Thürlimann. *Design of Concrete Structures With Stress Fields*. Birkhäuser, 1997. ISBN 9783764354916. (Cited on page 59)

[94] Aurelio Muttoni and Miguel Fernández Ruiz. Dimensionamiento y verificación del hormigón estructural mediante el

método de los campos de tensiones. *Hormigón y Acero*, 243: 93–102, 2007. (Cited on page 59)

[95] Clay J. Naito, J. P. Moehle, and Khalid M. Mosalam. Evaluation of bridge beam–column joints under simulated seismic loading. *ACI Structural Journal*, 99(1):62–71, January 2002. (Cited on page 35)

[96] E.G. Nawy. *Concrete Construction Engineering Handbook*. Taylor & Francis, 2010. ISBN 9781420007657. URL http://books.google.es/books?id=1OwkUrXuhjQC. (Cited on page 69)

[97] Sanat K. Niyogi. Bearing strength of concrete — geometric variations. *Journal of the Structural Division*, 99(7):1471–1490, July 1973. (Cited on pages 54, 94, 96, 109, and 110)

[98] Sanat K. Niyogi. Concrete bearing strength — support, mix, size effect. *Journal of the Structural Division*, 100(8):1685–1702, August 1974. (Cited on pages 54, 111, and 206)

[99] Vassilis K. Papanikolaou and Andreas J. Kappos. Confinement-sensitive plasticity constitutive model for concrete in triaxial compression. *International Journal of Solids and Structures*, 44(21): 7021 – 7048, 2007. ISSN 0020-7683. doi: 10.1016/j.ijsolstr.2007.03.022. URL http://www.sciencedirect.com/science/article/pii/S0020768307001783. (Cited on pages 58 and 225)

[100] J. Paterson and D. Mitchell. Seismic Retrofit of Shear Walls with Headed Bars and Carbon Fiber Wrap. *Journal of Structural Engineering*, 129(5):606–614, 2003. doi: 10.1061/(ASCE)0733-9445(2003)129:5(606). URL http://ascelibrary.org/doi/abs/10.1061/%28ASCE%290733-9445%282003%29129%3A5%28606%29. (Cited on page 44)

[101] Ruben Mario Salas Pereira. *Behavior of Structural Concrete Cantilever Piers Using T-Headed Reinforcing Bars and Varied Prestressing Design Criteria*. PhD thesis, The University of Texas at Austin, August 1994. (Cited on page 38)

[102] Frank E. Richart, Anton Brandtzaeg, and Rex L. Brown. *A study of the failure of concrete under combined compressive stresses*, volume XXVI of *Bulletin 185*. University of Illinois, Urbana, November 1928. (Cited on page 58)

[103] Karl Wilhelm Ritter. Die bauweise hennebique. *Schweizerische Bauzeitung*, 33(5, 6, 7):41–43, 49–52, 59–61, 1899. (Cited on page 59)

[104] Charles W. Roeder, Robert Graff, Jennifer L. Soderstrom, and Junh han Yoo. Seismic performance of pile–wharf connections.

Peer report 2002/07, University of California, Berkeley, Pacific Earthquake Engineering Research Center, December 2001. (Cited on pages 39 and 40)

[105] Miguel Fernández Ruiz and Aurelio Muttoni. On development of suitable stress fields for structural concrete. *Structural Journal*, 104(4):495–502, July 2007. (Cited on page 59)

[106] Ali Khajeh Samani and Mario M. Attard. A stress-strain model for uniaxial and confined concrete under compression. *Engineering Structures*, 41(0):335 – 349, 2012. ISSN 0141-0296. doi: 10.1016/j.engstruct.2012.03.027. URL http://www.sciencedirect.com/science/article/pii/S0141029612001459. (Cited on pages 58 and 93)

[107] Knut Sandvik, Jan-Diederik Advocaat, Arnstein Godejord, Kåre O.Hæreid, Kolbjørn Høyland, and Tor Ole Olsen. Offshore structures — a new challenge. In *XIV National Conference on Structural Engineering*, Acapulco, 2004. (Cited on page 77)

[108] Jörg Schlaich, Kurt Schäfer, and Mattias Jennewein. Toward a consistent design of structural concrete. Technical Report Vol. 32 No. 3, PCI Journal, May-June 1987. (Cited on page 59)

[109] Toshiyuki Shioya, Yoshihiro Higuchi, Hideyo Shiokawa, and Masaaki Takagishi. RC Beam Test Using T-Headed Bars Under Shear, Flexure and Compression. In Japan Prestressed Concrete Engineering Association, editor, *Concrete structures in the 21st century : proceedings of the first fib congress*, October 2002. (Cited on pages 21 and 43)

[110] R. G. Slutter. Pushout tests of welded stud shear connectors in lightweight concrete. Report 200.63.409.1, Leigh University, Fritz Engineering Laboratory, June 1963. (Cited on page 15)

[111] R. G. Slutter. Pushout tests of stud shear connectors in lightweight concrete. Report 200.65.360.1 and 200.66.360.1, Leigh University, Fritz Engineering Laboratory, 1966. (Cited on page 15)

[112] Hans-Peter Spieth. Das verhalten von beton unter hoher örtlicher pressung. *Beton und Stahlbetonbau*, 56(11):257–263, November 1961. (Cited on pages 58 and 93)

[113] J.R. Stoker, R.L. Boulware, W.F. Crozier, and R.A. Swirsky. Anchorage devices for large diameter reinforcing bars. Monograph D-4-99, California Department of Transportation, September 1974. (Cited on page 15)

[114] J. Stroband and J.J. Kolpa. The behaviour of reinforced concrete column-to-beam joints. Part 1: concrete joints subjected to

a negative moment. Technical report, Stevin Laboratory. Technische Hogeschool Delft, 1983. (Cited on pages 60 and 162)

[115] B. Svensvik and B. Kepp. The concrete gravity base structure of the Gullfaks C platform: Examples of applied technical development. pages 263–272, Houston, Texas, May 1989. Offshore Technology Conference. (Cited on pages 69 and 78)

[116] R.A. Swann. *Flexural Strength of Corners of Reinforced Concrete Portal Frames*, volume Tech Rept TRA 434. Cement and Concrete Association, November 1969. (Cited on page 62)

[117] M.K. Thompson. *The Anchorage Behavior of Headed Reinforcement in CCT Nodes and Lap Splices*. PhD thesis, The University of Texas at Austin, May 2002. (Cited on pages 28, 29, 31, 32, 33, 46, 77, 124, 129, 195, and 237)

[118] M.K. Thompson, J. O. Jirsa, J. E. Breen, and R.E. Klingner. Anchorage behavior of headed reinforcement: Literature review. Research Report 1855-1, Center for transportation research, Austin, TX, May 2002. (Cited on pages 11, 16, and 31)

[119] Mark Clinton Waggoner. Reinforcement anchorage in grouted connections for precast bridge bent cap systems. MsC in Engineering, The Univesity of Texas at Austin, May 1999. (Cited on page 39)

[120] W. A. Welsh and M. A. Sozen. Investigation of prestressed reinforced concrete for highway bridges. Part V: Analysis and control of anchorage–zone cracking in prestressed concrete. Private Communication Structural Research Series No. 309, Engineering Experiment Station at University of Illinois, June 1966. (Cited on page 57)

[121] A. Williams. The bearing capacity of concrete loaded over a limited area. Technical Report 526, Cement and Concrete Association, Wexham Springs, U.K., August 1979. (Cited on pages 55, 109, 112, and 113)

[122] J.L. Wright and S.L. McCabe. The development length and anchorage behavior of headed reinforcing bars. SM Report 44, University of Kansas Center for Research, Lawrence, Kansas, September 1997. (Cited on pages 32, 33, 34, and 124)

[123] J.M. Yang, K.H. Min, H.O. Shin, and Yoon Y.S. The use of T-headed bars in high-strength concrete members. In *FraMCos (International Association of Fracture Mechanics for Concrete and Concrete Structures)* 7, 2010. (Cited on page 21)

[124] K. Yoshitake, A. Ogawa, K. Dewa, T. Maenosomo, M. Takagishi, and Kimura. K. Structural performance of RC beams using T-headed bars as shear reinforcement under static and fatigue loading. In *Sustainable Concrete Technology & Structures in Local Climate and Environment Conditions*, number C.05, Vietnam, November 2008. 3rd ACF (Asian Concrete Federation) International Conference. (Cited on pages 21, 43, and 195)

[125] A. Zouzou and D. Haldane. Detailing reinforced concrete closing corner joints for ductility. *Structures and Buildings*, 99(1): 43–48, 1993. (Cited on page 62)

COLOPHON

This document was typeset using LaTeX with the typographical look-and-feel `classicthesis` developed by André Miede. A special thanks goes to Lorenzo Pantieri for his version of the package, `ArsClassica`, that changes some typographical points of the ClassicThesis style and for his well draft guide *The Art of Writing with LaTeX*.

☞ http://www.ctan.org/tex-archive/macros/latex/contrib/classicthesis/
☞ http://www.ctan.org/tex-archive/macros/latex/contrib/arsclassica/

CONTACTS

☞ http://www.he-upm.com
☞ francisco83pv@gmail.com

Final Version as of April 8, 2015.